Plasma Physics Reports, Vol. 26, No. 2, 2000, pp. 109–114. Translated from Fizika Plazmy, Vol. 26, No. 2, 2000, pp. 122–127.

Evaluation of the Ion Temperature Profile from Measurements of the DD Fusion Products in the T-10 Tokamak

V. S. Zaveryaev*, V. D. Maĭsyukov†, S. V. Popovichev*, A. V. Khramenkov*, and A. P. Shevchenko****

**Russian Research Centre Kurchatov Institute, Institute of Nuclear Fusion, pl. Kurchatova 1, Moscow, 123182 Russia*

***SNIIP Scientific and Engineering Center, ul. Raspletina 5, Moscow, 123060 Russia*

Received December 23, 1998; in final form, July 7, 1999

Abstract—Results are presented from measurements of the energy spectra and fluxes of the escaping charged fusion products and fluxes of fusion neutrons in ohmic regimes of the T-10 tokamak. The central temperature of the plasma ions is determined from the broadening of the energy spectra of thermonuclear protons and tritons. The ion temperature profile is evaluated from the dependence of the fluxes of charged fusion products on the radial plasma shift. It is proposed to use a single spectrometric detector with several collimators and slowing-down foils to measure the distribution of charged fusion products over pitch angles, which permits the determination of the ion temperature profile in a single shot. The feasibility of the method proposed is proved experimentally. © *2000 MAIK "Nauka/Interperiodica".*

1. INTRODUCTION

Measurements of the ion temperature in a tokamak plasma are of great importance, because the ion temperature is one of the main parameters determining the plasma energy balance.

There is a variety of methods for measuring the ion temperature: passive and active neutral-particle diagnostics, measurements of the Doppler broadening of the spectral lines of impurity ions, diagnostics based on the excitation of the resonant lines of hydrogen ions by a neutral-particle probing beam, high-resolution X-ray spectroscopy, and neutron spectrometry.

In the experiments described below, in order to measure the value and profile of the ion temperature in the T-10 tokamak, we measured the products of the thermonuclear DD reaction: neutrons, protons, and tritons.

The measurements were carried out with the toroidal magnetic field B_t = 2.2–3.0 T, plasma current I_p = 200–360 kA, and average electron density $\langle n_e \rangle$ = $(2–5.5) \times 10^{13}$ cm^{-3}.

2. DIAGNOSTICS OF THE PRODUCTS OF THERMONUCLEAR REACTIONS

2.1. Neutron Diagnostics

Since the intensity of the thermonuclear DD reaction in the T-10 tokamak is less than 5×10^9 s^{-1}, we used highly efficient boron and helium SNM-11, SNM-17, and SNM-18 neutron counters to detect neutron radiation. The total number of neutron detectors was ten; eight of them (four SNM-11 detectors and four SNM-17 detectors) were located symmetrically around the device in order to observe the possible anisotropy of neutron radiation (Fig. 1). The more sensitive ninth detector (SNM-18) was positioned as close to the plasma as possible and was used for measurements in the regimes with a low neutron yield. Measurements showed the absence of anisotropy; therefore, we carried out the absolute calibration (using a ^{252}Cf neutron source) of the tenth detector (SNM-18), which was placed on top of the device symmetrically about the

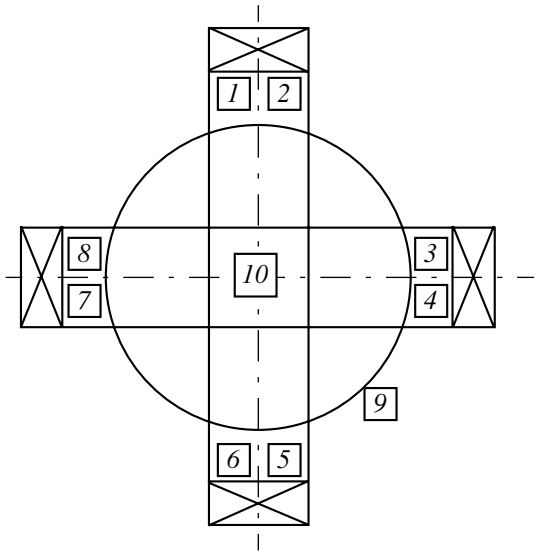

Fig. 1. Arrangement of the neutron detectors in the T-10 tokamak experiments: (*1–10*) neutron detectors.

† Deceased.

1063-780X/00/2602-0109$20.00 © 2000 MAIK "Nauka/Interperiodica"

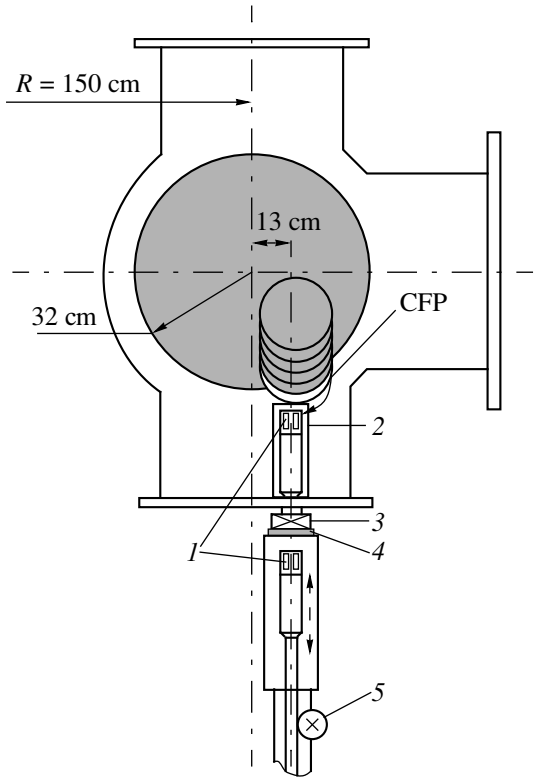

Fig. 2. Schematic of the CFP diagnostics: (*1*) detector unit, (*2*) electrostatic shielding, (*3*) valve, (*4*) Teflon insulator, and (*5*) arrangement for moving the detector unit.

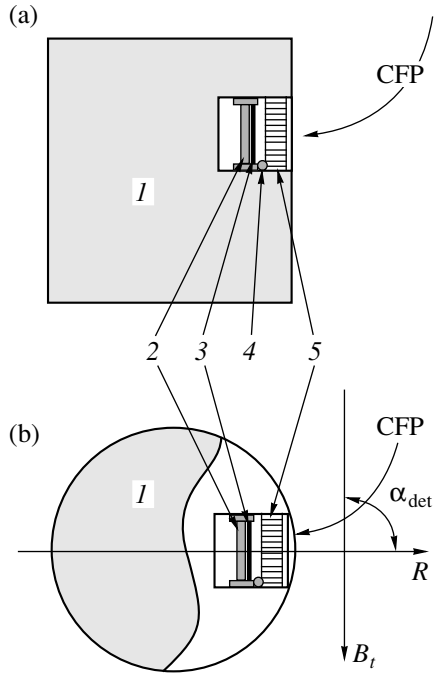

Fig. 3. Detector unit: (*1*) case of the detector unit, (*2*) semiconductor detector, (*3*) light-protecting film, (*4*) alpha-particle source, and (*5*) collimator; (a) side view and (b) top view.

plasma column. This allowed us to obtain the neutron yield with an accuracy of approximately 50%.

The neutron signal was used as a normalizing factor in the treatment of the measured fluxes of charged fusion products (CFPs).

2.2. CFP Diagnostics

Basic characteristics of the diagnostic facilities used in the T-10 tokamak to detect the escaping CFPs are described in detail in [1]. Here, we only describe the following main elements of the diagnostics.

The measurement of fluxes and energy spectra of the thermonuclear 1-MeV tritons and 3-MeV protons were carried out with an uncooled silicon surface-barrier detector (SBD) located near the lower plasma boundary (Fig. 2). The case of the detector unit was made of a WND alloy containing 80% tungsten and served to protect the detector against hard X-ray plasma emission. The arrangement of basic elements of the CFP diagnostics in the detector unit is shown in Fig. 3. The sensitive surface of the detector (0.5 cm^2) was protected against the optical plasma radiation by a thin aluminum foil deposited directly on the detector; the foil had little or no effect on the energy spectra of tritons and protons. A collimator consisting of a system of nickel pipes was located in front of the detector. The geometrical transparency of the collimator was 75%, and the collimation angle was 14°. A ^{238}Pu alpha-particle source was placed between the light-protective film and the collimator. The source continuously irradiated the detector with an intensity of 6–8 particle/s and was used to test the efficiency of the detector and provide the energy calibration of the measuring system between the tokamak shots.

3. DETERMINATION OF THE ABSOLUTE VALUE OF THE CENTRAL ION TEMPERATURE

For the Maxwellian distribution function of deuterons, the energy spectra of the thermonuclear tritons and protons must have maximums at 1 and 3 MeV, respectively; the half-width of these peaks depends on the plasma-ion temperature T_i as $91.6 \times (T_i\ [\mathrm{keV}])^{1/2}$.

As was expected, the triton and proton spectra measured in the T-10 tokamak always had peaks at 1 and 3 MeV. Accurate measuring of the shape of these peaks requires that the spectrometer energy resolution should be several times better than the peak half-width. The ion temperature in the central plasma region of the T-10 tokamak is in the 0.5–0.8-keV range; therefore, it was necessary to ensure a spectrometer energy resolution of 20–30 keV. The testing experiments with the use of an alpha-particle source showed that, in the absence of the plasma, the energy resolution of the spectrometer was ~30 keV. Under the experimental conditions (i.e., in the presence of the plasma), the resolution was lower because of the presence of both the electromagnetic

fields and the plasma radiation incompletely eliminated by shielding. This resolution was measured to be 50–60 keV from the broadening of the line of a generator with a stable amplitude and frequency, whose signal was added to the spectrometric signal.

The energy spectra were measured over time intervals of 100 ms. The time evolution of the plasma current, electron density, neutron emission, and the CFP energy spectra in one of the shots is shown in Fig. 4.

The energy spectra of protons and tritons that were measured in the steady stage of another regime of tokamak operation is presented in more detail in Fig. 5. The ion temperature evaluated from the half-width of the proton peak was 810 ± 70 eV.

The accuracy of determining the ion temperature from the CFP energy spectra was evaluated with the use of the expression obtained in [2] for the accuracy of determining T_i from the spectral measurements of neutrons:

$$\frac{\Delta T_i}{T_i} = \sqrt{\frac{2}{N}}\left[1 + \frac{\sigma_{\text{gen}}^2}{\sigma_{\text{dop}}^2}\right],$$

where N is the total number of counts in the individual measured CFP peak, σ_{gen} is the broadening of the generator line, and σ_{dop} is the Doppler broadening of the CFP line.

Note that the measured ion temperature is the temperature of ions in the plasma core. Taking into account the measurement accuracy of CFP spectra and the accuracy of the absolute calibration of neutron detectors, we can assume that the measured ion temperature does not contradict the observed neutron emission.

4. EVALUATION OF THE ION TEMPERATURE PROFILE FROM THE ANGULAR DISTRIBUTION OF CFP FLUXES

The pitch-angle distribution of CFP fluxes on the wall depends on the radial profiles of both the fusion source and the density of the plasma current [3]. However, calculations show that, in the given measurement geometry (the detector is located near the lower plasma boundary), the current profile has a small effect on the angular distribution of CFPs; this distribution is mainly determined by the radial distribution of the ion temperature in the central region of the plasma.

In order to measure the angular CFP distribution by a single collimated detector, we have to turn the detector around its axis. In the spectrometer in use, this procedure requires air let into the diagnostic system. Therefore, the detector can be readjusted only in intervals between the series of measurements. Evidently, the ion temperature distribution can be determined only if the plasma parameters in different shots are identical.

Nevertheless, there is the possibility of measuring the angular CFP distribution in a single shot with the use of a single detector. For this purpose, it is necessary to convert the angular distribution into the energy distribution. From a technological standpoint, this can be achieved by placing several foils of different thicknesses with individual collimators in front of the detector. The CFPs passing through the foil will decelerate, and their spectrum will insignificantly broaden as a result of straggling. Additional CFP peaks shifted toward lower energies with respect to the initial CFP

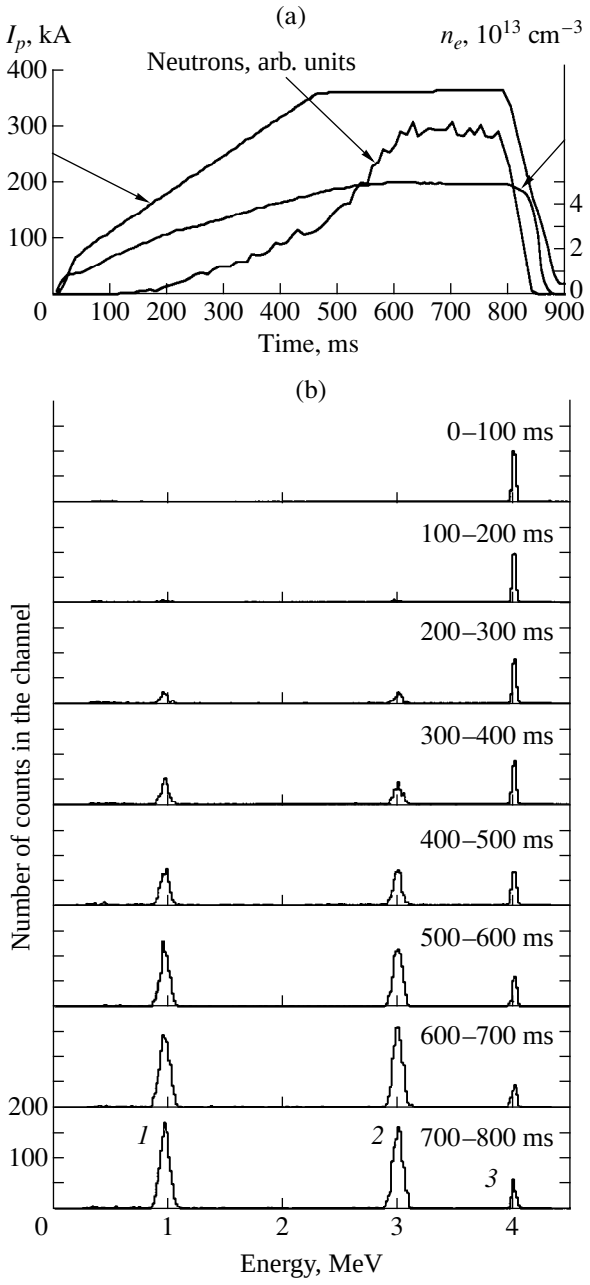

Fig. 4. (a) Time evolution of the plasma parameters and (b) CFP energy spectra. The measurements were carried out in shot no. 63872 (B_t = 2.65 T): (*1*) tritons, (*2*) protons, and (*3*) generator pulse.

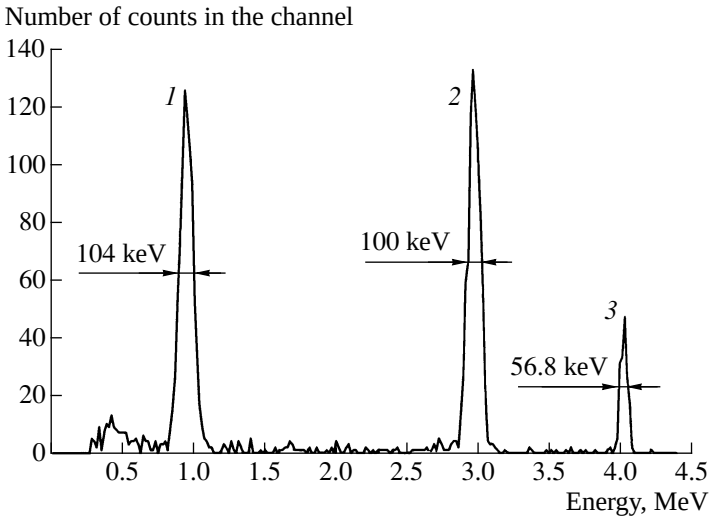

Fig. 5. CFP energy spectrum measured in 0.1-s time intervals in the steady stage of shot no. 64317 (B_t = 2.6 T, I_p = 250 kA, and $\langle n_e \rangle = 5.4 \times 10^{13}$ cm^{-3}): (*1*) tritons, (*2*) protons, and (*3*) generator pulse.

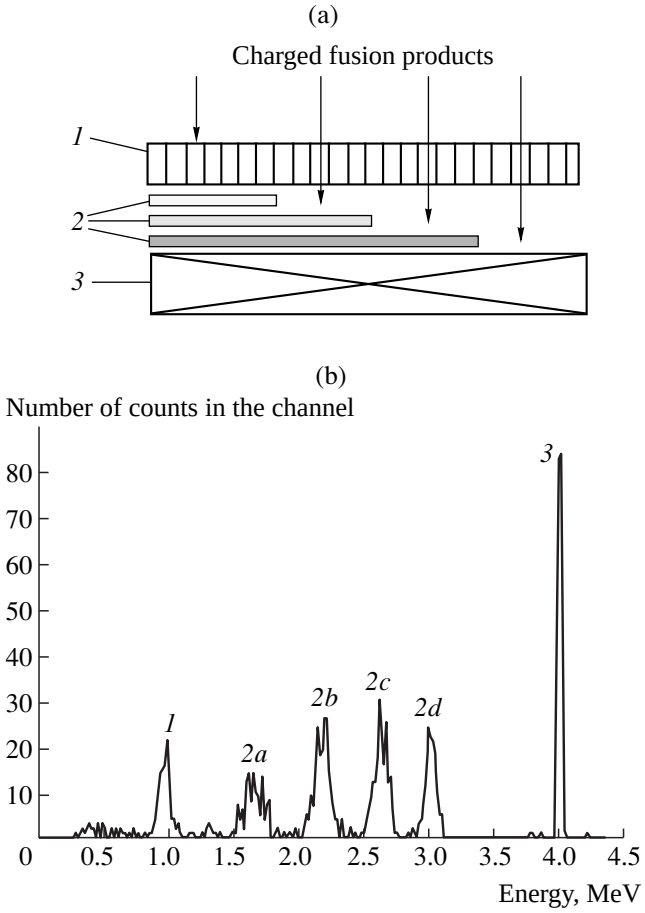

Fig. 6. (a) Single detector with decelerating foils: (*1*) collimator, (*2*) decelerating foils, and (*3*) SBD. (b) CFP energy spectrum: (*1*) tritons; (*2a*) 1.65, (*2b*) 2.2, (*2c*) 2.6, and (*2d*) 3.0 MeV protons; and (*3*) generator pulse.

energy should emerge in the energy spectrum. The value of the shift depends on the thickness of the foil; i.e., it is determined by the collimator specifying the pitch angle.

The feasibility of this idea was proved in the T-10 tokamak experimentally. The detector surface was partially covered with three foils so that the total thickness of the foils in different regions was 20, 40, and 60 μm (see Fig. 6a). A common collimator was installed in front of the detector; i.e., the measurement signal was unresolved in the pitch angle. The CFP energy spectra measured in the T-10 tokamak with the use of this system are presented in Fig. 6b.

Passing through the foils of different thicknesses, protons lost an energy of 390, 810, or 1350 keV and reached the detector surface with an energy of 2610, 2190, or 1650 keV, respectively, which agreed with the calculated values. Tritons with an energy of 1 MeV were completely absorbed by even the thinnest foil. A fraction of the surface was uncovered and received the protons and tritons that did not undergo deceleration. Thus, the possibility still exists of measuring the ion temperature from the energy spectra of 1-MeV tritons and 3-MeV protons, although the number of counts falling within these peaks is lower because of a decrease in the uncovered detector surface.

These test experiments in the T-10 tokamak showed that it is possible to place at least three foils on the surface of a single detector. Consequently, it is possible to measure the CFP fluxes for no less than four values of the pitch angle in a single shot. This method has an evident advantage over that using four independent detectors and four spectrometric channels.

At present, we are producing a detector unit with three spectrometric silicon semiconductor detectors

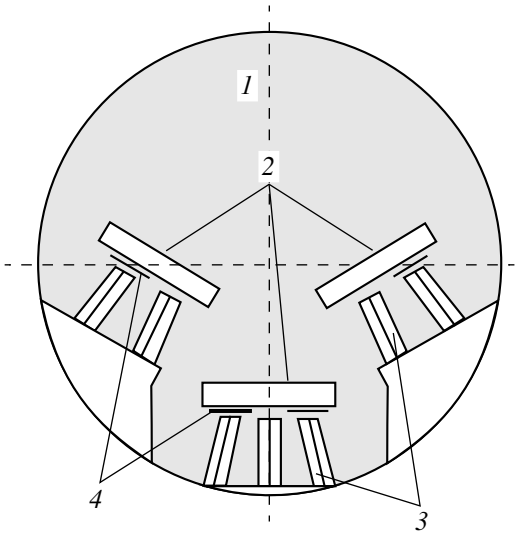

Fig. 7. Detector unit (top view): (*1*) case of the detector unit, (*2*) SBD, (*3*) collimators, and (*4*) decelerating filters.

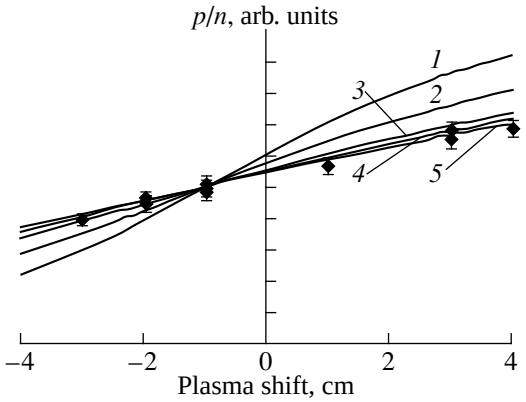

Fig. 8. The ratio of the proton flux (p) to the neutron flux (n) as a function of the radial plasma shift; experimental results (points) and calculated curves for different $T_i(r)$ profiles: (*1*) $T_i(r) \sim (1 - (r/a)^2)^2$, (*2*) $T_i(r) \sim (1 - (r/a)^2)$, (*3*) $T_i(r) \sim (1 - (r/a)^4)$, (*4*) $T_i(r) \sim (1 - (r/a)^4)^2$, and (*5*) $T_i(r) \sim (1 - (r/a)^4)^{1/2}$.

(SBDs) (Fig. 7). In order to resolve CFP particles by the pitch angle, three collimators consisting of sets of thin nickel pipes were placed in front of the central detector and two collimators were placed in front of each of the other detectors. For the unambiguous identification of protons passing through each collimator, we use decelerating foils: two foils of different thicknesses in front of the central detector and one in front of each of the other (second and third) SBDs.

Thus, the new diagnostic system allows direct measurements of the pitch-angle distribution of fluxes of the escaping CFPs in each shot. The measured pitch angles range from 50° to 130°.

5. EVALUATION OF THE ION TEMPERATURE PROFILE FROM THE DEPENDENCE OF THE CFP FLUX ON THE RADIAL SHIFT OF THE PLASMA

The measured CFP flux is formed along a certain helical trajectory determining the detector line of sight. When the plasma column shifts inward or outward along the major radius, the line of sight passes through the different plasma regions; consequently, the measured CFP flux changes.

In our experiment, the orbits of particles falling on the detector oriented at the angle $\alpha_{det} = 90°$ are close to the central, hottest plasma region because of the large Larmor radius (~10 cm). When the plasma column shifts inward or outward, the detector sees the plasma regions at a greater or lesser distance from the center, respectively. In the first case, the value of the measured CFP fluxes decreases, and, in the second case, it increases. The sharper the fusion source profile, the larger a relative change in the fluxes. This idea was first realized in experiments in the PLT device [4] in order to measure the ion temperature gradient.

In our experiments, the plasma position was varied from shot to shot from –3 cm (inward shift) to +4 cm (outward shift). Figure 8 presents both the experimental data (for $\alpha_{det} = 90°$) and the calculated dependences obtained for different shapes of the $T_i(r)$ profile. Each experimental point corresponds to an individual shot, in which the proton fluxes were averaged over a period of 0.2 s in the steady-state stage of the discharge. Experimental and calculated values are normalized to the –1-cm position, which is standard for the T-10 tokamak.

From the data presented, it follows that the ion temperature profile in the T-10 tokamak is fairly flat, at least in the central region of the plasma, which is the main source of the measured CFP flux.

Plasma-shift experiments were also carried out for the detector oriented at the angle $\alpha_{det} = 65°$. In this case, the measured dependence of CFP fluxes on the plasma shift behaves even more smoothly, which is also in agreement with calculations.

6. CONCLUSION

The ion temperature in the T-10 tokamak plasma is measured in different operating modes of the device from the broadening of the energy spectra of thermonuclear protons and tritons. Within the measurement accuracy (10–15%), the obtained values of the ion temperature agree with the measured neutron yield.

The ion temperature profile is evaluated from the dependence of CFP fluxes on the radial plasma shift. It is found that, in the T-10 ohmic regimes, the ion tem-

perature profile is relatively flat and is shaped as $T_i(r) \sim (1 - (r/a)^4)^2$.

It is proposed to use a single spectrometric detector with several collimators and slowing-down foils to measure the CFP distribution over pitch angles, which allows the determination of the ion temperature profile in a single shot. The feasibility of the method proposed is proved experimentally.

ACKNOWLEDGMENTS

This work was supported by the Russian Foundation for Basic Research, project no. 97-02-16595.

REFERENCES

1. V. S. Zaveryaev, V. D. Maĭsyukov, S. V. Popovichev, *et al.*, Fiz. Plazmy **20**, 199 (1994) [Plasma Phys. Rep. **20**, 185 (1994)].
2. O. N. Jarvis, in *Proceedings of the Course "Diagnostics for Fusion Reactor Conditions," Varenna, Italy, 1982*, Vol. 1, paper EUR 8351-1 EN.
3. N. E. Karulin and S. V. Putvinskij, Nucl. Fusion **25**, 961 (1985).
4. W. W. Heidbrink, J. Lovberg, J. D. Strachan, *et al.*, Nucl. Fusion **27**, 129 (1987).

Translated by A. D. Smirnova

Plasma Physics Reports, Vol. 26, No. 2, 2000, pp. 115–118. Translated from Fizika Plazmy, Vol. 26, No. 2, 2000, pp. 128–131.

MAGNETIC CONFINEMENT SYSTEMS

Formation of the Flow of Fast Electrons in the Plasma of the AMBAL-M Device

S. Yu. Taskaev

Budker Institute of Nuclear Physics, Siberian Division, Russian Academy of Sciences, pr. akademika Lavrent'eva 11, Novosibirsk, 630090 Russia

Received March 12, 1999; in final form, May 20, 1999

Abstract—A hot target plasma is obtained in the end cell of the AMBAL-M device with the use of an end gas-discharge plasma source. A fairly high longitudinal electron current flowing from the plasma source to the plasma receiver is detected experimentally. The electron current is studied in the region in front of the input magnetic mirror, where the longitudinal electric field is directed outward from the mirror. Different models for plasma description are considered, and possible plasma instabilities are discussed. It is shown that a fairly high longitudinal electron current in the region where the electric field accelerates electrons results in the generation of the flow of fast electrons responsible for the current in the mirror system. © *2000 MAIK "Nauka/Interperiodica".*

1. INTRODUCTION

A hot target plasma is obtained [2], and a fairly high longitudinal electric current [3] flowing through the plasma from the plasma source to the plasma receiver is detected in the end cell of the AMBAL-M device with the use of an end gas-discharge plasma source [1]. It is shown that the longitudinal current owes it existence to the method for the plasma production and is a fraction of the discharge current of the plasma source [4]. It is found that, as the distance from the magnetic mirror (on the plasma-source side) decreases, the plasma potential increases along the magnetic field lines (along which the current flows) [2, 5] but does not decrease, as in the case of a thermal barrier. In this paper, we study the electron current in this particular region of the electric field in front of the input magnetic mirror.

After a brief description of the experimental setup and formulation of the problem, numerical models are considered and the conclusion is drawn that a fast- electron flow is produced in the system, which is confirmed by direct measurements of the electron distribution function. In the Conclusion, we give a summary of the results obtained.

2. BRIEF DESCRIPTION OF THE EXPERIMENTAL SETUP

The schematic of the experiment is shown in Fig. 1. An annular gas-discharge plasma source[1] [1] generates a cold dense plasma flow and specifies a nonequilibrium profile of the radial electric field. The Kelvin–Helmholtz instability [6] and the longitudinal current [7] lead to an increase in the transverse ion temperature; as a result, the ion mean free path increases, a substantial fraction of the plasma flow is reflected by the magnetic field of the mirror, the plasma density decreases, and a thermal barrier is produced in the region of the input magnetic mirror. In the magnetic mirror system, the ions (whose temperature continues to grow) are confined by the magnetic field, whereas the electrons are confined by the ambipolar potential and are heated by the current and collisions with ions. The basic plasma parameters in the center of the magnetic mirror system are the following: the plasma diam-

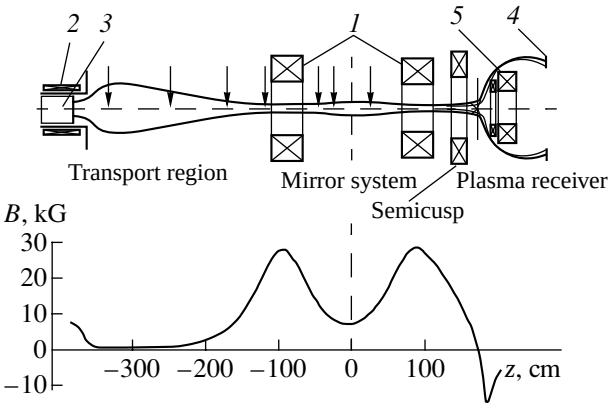

Fig. 1. Schematic of the end cell of the AMBAL-M device and the magnetic field line emerging from the plasma source: (*1*) coils of the mirror system, (*2*) plasma-source solenoid, (*3*) gas-discharge plasma source, (*4*) plasma receiver, and (*5*) semicusp coils. Arrows mark the cross sections in which the Langmuir probe measurements were carried out. At the bottom, the profile of the magnetic field on the axis is shown.

[1] The gas-discharge plasma source is shaped as a ring 11 cm in the inner diameter and 13 cm in the outer diameter.

1063-780X/00/2602-0115$20.00 © 2000 MAIK "Nauka/Interperiodica"

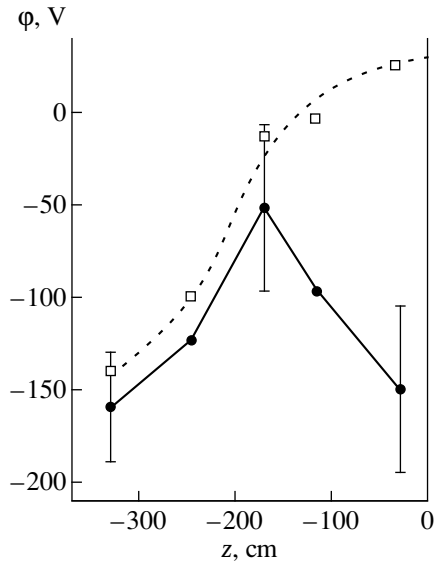

Fig. 2. Longitudinal profile of the floating potential of the Langmuir probe (solid line) and space potential (dashed line) along the magnetic field (at a 3.4-cm radius in the central plane of the mirror system) at the instant 1.4 ms.

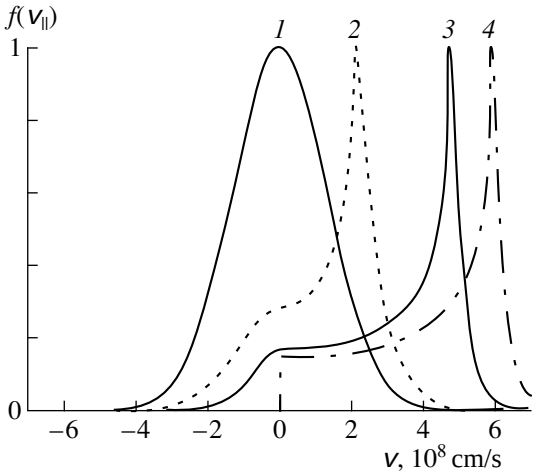

Fig. 3. Electron distribution functions over longitudinal velocities at z = (*1*) –243, (*2*) –168, (*3*) –115 cm, and (*4*) in the magnetic mirror region. The potential difference between the input magnetic mirror and the z = –243-cm cross section is 100 V.

eter is 20 cm, the plasma density is 6×10^{12} cm^{-3}, the electron temperature is 50 eV, and the ion temperature is 200 eV. A detailed description of the device and the experimental results are presented in [2–5].

3. FORMULATION OF THE PROBLEM

One of the most important and interesting results obtained in the AMBAL-M experiments is the presence of the longitudinal electric field accelerating the electrons toward the mirror system. This field was observed in the transport region in front of the input magnetic mirror at a radius approximately equal to the half-radius of the plasma stream flowing from the gas-discharge plasma source. The electric field at other radii decelerates electrons, which is typical of the formation of the thermal barrier [2, 5]. The measured longitudinal profiles of the floating potential of the Langmuir probe and the space potential are presented in Fig. 2. The space potential is determined by the point of inflection of the electron part of the I–V characteristic of an asymmetric double probe [8]. The value of the excess of the space potential above the floating potential of the probe for the Maxwellian particle distribution is well known. In the case in question, the excess is approximately $(2–3)T_e$ because of a higher ion temperature. Such an excess potential is observed near the plasma source (z < –240 cm), where the plasma is dense and cold ($T_e \approx 8$ eV). The difference between the space potential and floating potential increases with distance from the plasma source (see [5], Figs. 9, 11) because of the increase in the electron temperature (see [2], Fig. 6). The presence of the electric field (up to 0.7 V/cm) accelerating the electrons and extending over two meters in front of the input magnetic mirror is seen in Fig. 2. In [5], it was assumed that a fairly high electron current flows just in this region rather than along the magnetic lines coming out of the gas-discharge plasma source. Later, this assumption was confirmed experimentally in [3].

The problem of the electron current flowing in the region of the accelerating electric field is of great interest. Let us consider several models for this phenomenon.

4. SIMULATION

4.1. Two-Fluid Magnetohydrodynamics

Because of the small plasma density in the magnetic-mirror region, the electron mean free path determined by the Coulomb collisions reaches several meters and is 3–10 times the magnetic-field-variation scale length $L = B/(\partial B/\partial z)$. Therefore, the hydrodynamic approximation is invalid. However, if the electrons are scattered on the turbulent oscillations arising due to instabilities, the hydrodynamic approach is applicable. The electron distribution function can be represented as the Maxwellian distribution shifted by the flow velocity. However, the existence of such a collisional flow generates the problems of how to fit the calculated potential distribution to the measured one and how to explain the high electron temperature [5]. To achieve an agreement with the measured electron temperature, a very high heating power is required, because the energy carried away due to convection and heat conduction increases substantially. With such high energy losses, it is hardly possible to heat this turbulent plasma flow by injecting available neutral beams.

Although it seems that scattering by waves does not lead to the turbulent collisional flow of the plasma jet, only experiments can confirm this assumption—whether it will be the injection of neutral beams or the measurements of the electron distribution function in the mirror system.

4.2. Kinetic Model

Another method for studying the current flowing in the plasma is the kinetic approach [9]. Let us consider a collisionless plasma described by the Vlasov equation [10]. We assume that the electrons move from the initial point denoted by the index 0, where their distribution is Maxwellian, toward the higher magnetic field. In addition, the electrons are in the accelerating electric field. The electron distribution function f is found from the laws of conservation of energy and the magnetic moment. In the absence of collisions, the total time derivative is $df/dt = 0$. In phase space, the particles move along the lines at which f is constant. The electron distribution function is Maxwellian but has a sharp boundary, beyond which the distribution function vanishes. In the plane $(v_\parallel, v_\perp)$, the contours of the distribution function are circles and the boundary beyond which the distribution function vanishes is an ellipse

$$\frac{mv_\perp^2}{2}\left(1-\frac{B_0}{B}\right)+\frac{mv_\parallel^2}{2}=e\varphi-e\varphi_0$$

for $v_\parallel > 0$ and a hyperbola

$$\frac{mv_\perp^2}{2}\left(1-\frac{B_m}{B}\right)+\frac{mv_\parallel^2}{2}=e\varphi-e\varphi_m$$

for $v_\parallel < 0$. Here, the index m refers to the quantity in the magnetic mirror region. In order for these boundaries to be joined at the point $v_\parallel = 0$, the dependence of the potential on the magnetic field must be linear.

Let the electron acceleration by the electric field start near the point where the probe is located ($z = -243$ cm) and terminate in the mirror system, the potential difference being 100 V. The corresponding evolution of the electron distribution function $f(v_\parallel)$ over longitudinal velocities with decreasing distance from the magnetic mirror is shown in Fig. 3.

4.3. Runaway Electrons

It is difficult to model the real experimental situation, because the plasma flow is collisional near the plasma source and collisionless in the mirror region. It is well known that, in the presence of an accelerating electric field, runaway electrons can be generated in the collisional plasma. Runaway electrons are fast electrons that on average accelerate rather than decelerate, because the friction force $(\sim 1/v)$ decreases with increasing the electron velocity. In the electric field E, the electrons with velocity v_z become runaways if $v_z > \sqrt{4\pi e^3 \lambda n/mE}$ [11]. As the distance from the magnetic mirror decreases, the plasma density decreases and the boundary of the runaway region shifts to lower velocities; as a result, more and more electrons become runaways. Near the mirror region, the runaway boundary corresponds to the velocity $v_z \approx 2 \times 10^8$ cm/s, which is close to the thermal electron velocity; therefore, a substantial fraction of electrons become runaways.

4.4. Summary

When the accelerating potential is much greater than the initial temperature (as in our case), the collisionless acceleration in the constant magnetic field leads to the formation of a beam of electrons with close longitudinal velocities. In the increasing magnetic field, there is energy transfer between the degrees of freedom because of the conservation of the adiabatic invariant. As a result, for a given potential difference, electrons with different transverse momentums gain different longitudinal velocities, as is seen in Fig. 3. An even greater dispersion of the fast-electron beam in longitudinal velocities results from the absence of a sharp acceleration boundary in velocity space because of a smooth decrease in the plasma density with decreasing distance from the magnetic mirror.

The onset of the Buneman instability [12] and the build-up of Langmuir oscillations can also contribute to the broadening of the electron beam in energy space. According to the estimate from [13], the formation of a plateau in the electron distribution function due to Langmuir turbulence must proceed rather rapidly (on a space scale of ~1 cm). Therefore, there can exist a situation similar to the propagation of a monoenergetic electron beam in a plasma, which was considered in [14]. In that paper, it was shown that an electron distribution with a plateau is established at each point, the maximum velocity in the plateau being constant.

5. EXPERIMENTAL RESULTS

The presence of the fast-electron flow in the mirror system is seen from the I–V characteristic of the Langmuir probe placed in the region where the current flows. The I–V characteristic shows the presence of both regions with the positive derivative $\partial f(\mathscr{E})/\partial\mathscr{E}$ and the plateau (linear dependence of the current on the voltage) in the electron energy distribution function. However, an accurate interpretation of these results leaves unclear the problems associated with the secondary electron emission, a possible change in the potential jump near the surface [15], and the possible existence of the linear transient region in the I–V characteristic [16]. Therefore, we designed a special small-size movable electron-energy analyzer and used it to measure the electron distribution function over longitu-

dinal energies in the mirror system. A detailed description of the analyzer and obtained experimental results are presented in [17]. The analyzer measurements show that, in the current channel, the electron distribution function of the arriving electrons over longitudinal velocities differs from the Maxwellian distribution function and, in the energy range from 150 to 350 eV, is shaped like a plateau. Fast electrons with the density $\sim 10^{11}$ cm^{-3} are responsible for the transport of the main part of the detected longitudinal current [3]. Thus, the experimental results show that the longitudinal electron current in the mirror system is carried by fast electrons that are produced in the region of the accelerating electric field, in front of the magnetic mirror.

6. CONCLUSION

In the previous experiments with a target plasma in the AMBAL-M device, it was found that, in front of the input magnetic mirror, there is a longitudinal electric field directed outward from the magnetic mirror. It was shown that a high electron current flowing into the mirror system exists in this region.

In this paper, we have considered various models for a plasma description and have shown that the presence of an electron current in the region of the accelerating electric field leads to the generation of a flow of fast electrons that carry the current in the mirror system. The fast-electron flow is recorded experimentally.

The production of a fast-electron flow is not characteristic of open magnetic confinement systems. Further investigations of the processes related to this phenomenon (in particular, the formation of an accelerating electric field and the influence of the fast-electron flow on the confinement and heating of the plasma in the mirror system) are of considerable interest.

ACKNOWLEDGMENTS

We thank the AMBAL-M team for assistance in experiments. This work was supported by the Russian Foundation for Basic Research, project no. 98-02-17801.

REFERENCES

1. G. I. Dimov, A. A. Ivanov, and G. V. Roslyakov, Fiz. Plazmy **8**, 970 (1982) [Sov. J. Plasma Phys. **8**, 546 (1982)].
2. T. D. Akhmetov, V. S. Belkin, E. D. Bender, *et al.*, Fiz. Plazmy **23**, 988 (1997) [Plasma Phys. Rep. **23**, 911 (1997)].
3. T. D. Akhmetov, V. I. Davydenko, A. A. Kabantsev, *et al.*, Fiz. Plazmy **24**, 1065 (1998) [Plasma Phys. Rep. **24**, 995 (1998)].
4. S. Yu. Taskaev, Fiz. Plazmy **25**, 510 (1999) [Plasma Phys. Rep. **25**, 461 (1999)].
5. S. Yu. Taskaev, Preprint No. 95-92, IYaF SO RAN (Budker Institute of Nuclear Physics, Siberian Division, Russian Academy of Sciences, Novosibirsk, 1995).
6. A. A. Kabantsev and S. Yu. Taskaev, Fiz. Plazmy **16**, 700 (1990) [Sov. J. Plasma Phys. **16**, 406 (1990)].
7. K. J. Reitzel and G. J. Morales, Phys. Plasmas **5**, 3806 (1998).
8. Yu. P. Raizer, *Gas Discharge Physics* (Nauka, Moscow, 1987; Springer-Verlag, Berlin, 1991).
9. S. I. Braginskii, in *Reviews of Plasma Physics*, Ed. by M. A. Leontovich (Gosatomizdat, Moscow, 1963; Consultants Bureau, New York, 1965), Vol. 1.
10. D. V. Sivukhin, in *Reviews of Plasma Physics*, Ed. by M. A. Leontovich (Gosatomizdat, Moscow, 1963; Consultants Bureau, New York, 1965), Vol. 1.
11. D. V. Sivukhin, in *Reviews of Plasma Physics*, Ed. by M. A. Leontovich (Atomizdat, Moscow, 1964; Consultants Bureau, New York, 1968), Vol. 4.
12. B. B. Kadomtsev, in *Reviews of Plasma Physics*, Ed. by M. A. Leontovich (Atomizdat, Moscow, 1964; Consultants Bureau, New York, 1968), Vol. 4.
13. A. A. Vedenov and D. D. Ryutov, in *Reviews of Plasma Physics*, Ed. by M. A. Leontovich (Atomizdat, Moscow, 1972; Consultants Bureau, New York, 1975), Vol. 6.
14. É. P. Kontar', V. I. Lapshin, and V. N. Mel'nik, Fiz. Plazmy **24**, 832 (1998) [Plasma Phys. Rep. **24**, 772 (1998)].
15. S. Ishiguro and N. J. Sato, J. Phys. Soc. Jpn. **60**, 2218 (1991).
16. V. A. Rozhanskiĭ, A. A. Ushakov, and S. P. Voskoboĭnikov, Fiz. Plazmy **24**, 837 (1998) [Plasma Phys. Rep. **24**, 777 (1998)].
17. T. D. Akhmetov, V. I. Davydenko, and S. Yu. Taskaev, Fiz. Plazmy **26**, 166 (2000) [Plasma Phys. Rep. **26**, 152 (2000)].

Translated by A. D. Smirnova

Plasma Physics Reports, Vol. 26, No. 2, 2000, pp. 119–128. Translated from Fizika Plazmy, Vol. 26, No. 2, 2000, pp. 132–141.

PLASMA OSCILLATIONS AND WAVES

Resonance of the Larmor Drift with Plasma Oscillations

A. V. Timofeev

Russian Research Centre Kurchatov Institute, pl. Kurchatova 1, Moscow, 123182 Russia

Received March 18, 1999; in final form, May 20, 1999

Abstract—Resonance phenomena arising when the Larmor drift velocity is locally equal to the phase velocity of plasma oscillations are analyzed. It is shown that, in a plasma with a nonuniform temperature, the wavelength of the oscillations sharply reduces at the resonant point, so that the oscillations convert into small-scale waves. In a plasma with a uniform temperature, Coulomb collisions cause the oscillations to dissipate at the resonant point. It is noted that a resonance with the Larmor drift can be used to heat the plasma. © *2000 MAIK "Nauka/Interperiodica".*

1. INTRODUCTION

The stability of the plasma that executes a nonuniform motion is in large measure governed by the phenomenon of hydrodynamic resonant interaction [1]. In an inhomogeneous plasma in a magnetic field, the so-called Larmor drift (or a flowing-around stream), which is a hydrodynamic motion unrelated to the displacement of Larmor circles, occurs. This phenomenon is also known as a diamagnetic current or gradient current. The Larmor drift velocity is $\mathbf{V}_L = \frac{c}{eB^2n}[\mathbf{B}\nabla p]$. In earlier papers [2, 3], I noted that, at a resonance with the Larmor drift, the wave phase along particle trajectories changes in time, thereby preventing direct energy and momentum exchange between waves and particles (it is well known that such an exchange is peculiar to resonant interaction). It sill remains unclear how the energy and momentum exchange between particles and waves can occur at resonances with the Larmor drift and whether this happens in reality. In order to answer this question, we must take into account local physical processes occurring in the vicinity of the resonant point, which are unimportant far away from this point, where they are usually neglected. However, this approach to describing various plasma waves yields singular wave equations having a singularity at the point of the Larmor resonance.

It was found that, in a plasma in which the density and temperature gradients are both nonzero, the higher order (fourth-order) effects in the ion Larmor radius become important near the resonant point. Taking into account these effects raises the order of the wave equation. The refined wave equation describes how comparatively large-scale (e.g., flute or drift) oscillations convert into smaller scale waves propagating away from the Larmor resonance point. However, this phenomenon can be correctly described using a simplified wave equation supplemented with the Landau rule for circumventing the resonant point. Small-scale waves travel toward the point at which the resonance condition is satisfied for the Larmor drift velocity calculated solely in terms of the density gradient, $\mathbf{V}_L' = \frac{cT}{eB^2n}[\mathbf{B}\nabla n]$. In the vicinity of this point, the wavelength of the small-scale waves approaches zero; i.e., the waves stop propagating. Then, the waves will evolve depending on the sign of the temperature gradient. If the temperature and density gradients are equidirectional, then the oscillations will be damped by ion–ion (i–i) collisions. If the gradients are oppositely directed, then i–i collisions can cause small-scale waves to grow.

In a plasma with a uniform temperature and nonzero density gradient, the energy of large-scale waves increases in the vicinity of the point of Larmor resonance until the effects of ion–electron (i–e) friction, which are responsible for wave absorption, come into play. Along with the wave conversion in a plasma with $\nabla T \neq 0$, this phenomenon can also be correctly described using a simplified singular wave equation supplemented with the Landau circumvention rule.

Our analysis shows that the energy of the plasma waves decreases due to resonant interaction with the Larmor drift. Since the energy lost by the waves is finally converted into thermal energy, the Larmor resonance phenomenon can be used to heat the plasma.

2. PLASMA WITH NONUNIFORM TEMPERATURE AND DENSITY

2.1. Basic Equations

The Larmor resonance phenomenon, which has a substantial impact on various kinds of plasma oscillations, may, in particular, enlarge the domain in which flute perturbations are unstable because of the diamagnetic nature of the plasma [4]. We will study the problem at hand using as an example flute oscillations, which are a simple and convenient object for demonstrating the general features of the Larmor resonance

1063-780X/00/2602-0119$20.00

phenomenon. In the simplest formulation (which implies a plane symmetry, a uniform magnetic field, the use of the potential approximation, and modeling of the nonuniform part of the magnetic field by the effective gravity acceleration g), flute oscillations are described by the equation (see, e.g., [5, 6])

$$\frac{d}{dx}n_0(\omega-\Omega_i)\frac{d\varphi_1}{dx}-k_y^2 n_0(\omega-\Omega_i)\varphi_1+\frac{k_y^2 g}{\omega}\frac{dn_0}{dx}\varphi_1=0, \quad (1)$$

where $\Omega_i = \frac{k_y c}{eB_0}\frac{1}{n_0}\frac{dp_0}{dx}$, $g = \frac{T_0}{m_i R}$, R is the scale on which the magnetic field varies, and the perturbed electric potential is chosen to be $\varphi_1(\mathbf{r}, t) = \varphi_1(x)\exp(-i\omega t + ik_y y)$. Equation (1) is written in Cartesian coordinates with the x-axis directed along the unperturbed density and temperature gradients and the z-axis directed along the magnetic field.

The point of the Larmor resonance is a singular point of equation (1), which was derived under the assumption that the ion Larmor radius ρ_i is small. This equation is correct up to terms on the order of ρ_i^2. In order to regularize the wave equation, we must incorporate the finite-Larmor-radius effects more completely.

In the potential approximation, the wave equation can be derived from the condition that the plasma is quasineutral. The perturbed ion density into which the finite-Larmor-radius effects are completely incorporated is found by solving the kinetic equation by the standard method of integration along the trajectories:

$$n_{1i} = e\int dk_x \exp(ik_x x)\varphi_1(k_x)$$
$$\times\int d\mathbf{v}\left[\frac{\partial f_0}{\partial\varepsilon}-\left(\frac{\partial f_0}{\partial\varepsilon}+\frac{k_y}{m_i\omega_i(\omega+k_y g/\omega_i)}\frac{\partial f_0}{\partial\zeta}\right)\right. \quad (2)$$
$$\left.\times J_0(\xi)\exp(i\xi\sin(\theta-\chi))\right],$$

where $f_0(\mathbf{v}) = n_0(\zeta)\left(\frac{m_i}{2\pi T_0(\zeta)}\right)^{3/2}\exp\left(-\frac{m_i v^2}{2T_0(\zeta)}\right)$ is the initial ion distribution function, $\zeta = x + v_y/\omega_i$, ω_i is the ion cyclotron frequency, θ is the phase of the ion cyclotron gyration, $\chi = \arctan(k_y/k_x)$, $\xi = kv_\perp/\omega_i$, and J_0 is the zero-order Bessel function.

Because of a reduction in the characteristic spatial scale of the flute perturbations in the vicinity of the resonant point, the dominant terms in the expansion in ρ_i in the expression for n_{1i} are the terms containing the fourth-order derivative of φ_1 ($k_x \longrightarrow -id/dx$). Incorporating these terms into the quasineutrality condition makes it possible to generalize equation (1):

$$-\frac{3}{4}n_0\Omega_{Ti}\rho_i^2\frac{d^4\varphi_1}{dx^4}+\frac{d}{dx}n_0(\omega-\Omega_i)\frac{d\varphi_1}{dx}$$
$$-k_y^2 n_0(\omega-\Omega_i)\varphi_1+\frac{k_y^2 g}{\omega}\frac{dn_0}{dx}\varphi_1 = 0, \quad (3)$$

where

$$\Omega_{Ti} = \frac{k_y c}{eB}\frac{dT_0}{dx}, \quad \rho_i^2 = \frac{T_0}{m_i\omega_i}.$$

We set the origin for the coordinates at the resonant point, change the variables $\omega - \Omega_i(x) \approx -\Omega'_{i,x}x$, and omit the small term proportional to $\propto x\varphi_1$ in the fourth-order equation (3) in order to reduce this equation to the standard form with a small coefficient in front of the highest derivative (see, e.g., [7]):

$$\frac{1}{\Lambda}\frac{d^4\varphi_1}{dx^4}+\frac{d}{dx}x\frac{d\varphi_1}{dx}+P\varphi_1 = 0, \quad (4)$$

where $\Lambda = \frac{4}{3}\frac{\Omega'_{i,x}}{\rho_i^2\Omega_{Ti}}$. The quantity P, which is equal to $P = -\frac{k_y^2 g}{\omega\Omega'_{i,x}}\frac{1}{n_0}\frac{dn_0}{dx}$, is assumed to be positive, which corresponds to a plasma that is unstable against flute perturbations. For definiteness, we also set $\Omega'_{i,x} > 0$.

2.2. Wave Conversion and Landau Circumvention Rule

The theory for solving equations of the form of (4) is well developed: they are usually solved by taking the Fourier transformation at complex values of k_x,

$$\varphi_1(x) = \int_C dk_x \exp(ik_x x)\varphi_1(k_x). \quad (5)$$

The integration contours for this expression can be divided into two groups: closed contours and contours on which $\varphi_1(k_x) \xrightarrow[|k_x|\to\infty]{} 0$.

For the Fourier transform $\varphi_1(k_x)$, we obtain from (4)

$$\varphi_1(k_x) = \frac{1}{k_x}\exp\left(-\frac{ik_x^3}{3\Lambda}+\frac{iP}{k_x}\right). \quad (6)$$

Although equation (4) has only four linearly independent solutions, it is convenient to introduce seven functions. The relevant contours of integration over k_x are shown in Fig. 1, in which the "forbidden" regions where $|\varphi_1(k_x) \xrightarrow[|k_x|\to\infty]{} \infty$ are hatched. From Fig. 1, one

can see that the seven functions we have just introduced are related by

$$\begin{aligned} U_3 - U_2 &= A_1, \\ U_1 - U_3 &= A_2, \\ U_2 - U_1 + V &= A_3. \end{aligned} \tag{7}$$

Taking the sum of these expressions yields

$$V = A_1 + A_2 + A_3. \tag{8}$$

The functions V and U_i can be regarded as long-wavelength, because, in the limit $\Lambda \longrightarrow \infty$, they pass over to the solution to the reduced equation (4) without the term containing the fourth-order derivative. In the same limit, the short-wavelength functions A_i can be obtained from (4) in which the last term on the left-hand side is omitted.

To obtain the function V, we consider the range $P^{-1} \gg |x| \gg \Lambda^{-1/3}$ and choose the integration contour in the region $\Lambda^{1/3} \gg |k_x| \gg P$, in which we have $\varphi_1(k_x) \approx 1/k_x$ and, accordingly, $V \approx 2\pi i$. Consequently, in this range of $|x|$ values, the desired solution to equation (4) in which we omit the term containing the fourth-order derivative is a solution that is regular at the resonant point and has the form

$$V \approx 2\pi i J_0(2\sqrt{Px}).$$

As a second linearly independent solution to the reduced equation, we can choose, e.g., the function U_2. If $0 > \arg x > -4\pi/3$, then the sector in which contour U_2 approaches infinity in the plane of the complex variable k_x ($\pi < \arg k_x < 5\pi/3$) intersects the half-plane $\mathrm{Im}(k_x x) > 0$. For such values of $\arg x$, the integral in (5) converges, because it contains the factor $\exp(ik_x x)$. If $|x| \gg \Lambda^{-1/3}$, then the first term in the exponential index in (6) is unimportant, in which case the function U_2 passes over to the solution to the reduced equation (4). Setting $|x| \gg P^{-1}, \Lambda^{-1/3}$ and evaluating (5) by the saddle point method yields

$$U_2 \approx \frac{\pi^{1/2}}{(Px)^{1/4}} \exp(-2i\sqrt{Px} - i\pi/4). \tag{9}$$

This asymptotic behavior is characteristic of the following solution to the reduced equation:

$$U_2 \approx -\pi i H_0^{(2)}(2\sqrt{Px}).$$

If $\arg x = 0$, then the half-plane $\mathrm{Im}(k_x x) > 0$ on the plane of the complex variable k_x only borders the sector $\pi < \arg k_x < 5\pi/3$, without intersecting it. Consequently, for $\arg x = 0$, the main contribution to the integral in (5) comes from the region where $|k_x|$ values are large and in which the first term in the exponential index in (6) should be taken into account. In this case, the function U_2 can be found from the third expression in (7), in which the function A_3 is evaluated by the saddle point method. For $\arg x \neq 2\pi/3$, contour A_3 intersects only one saddle point $k_{x,s} = -(x\Lambda)^{1/2}$. The corresponding calculations give

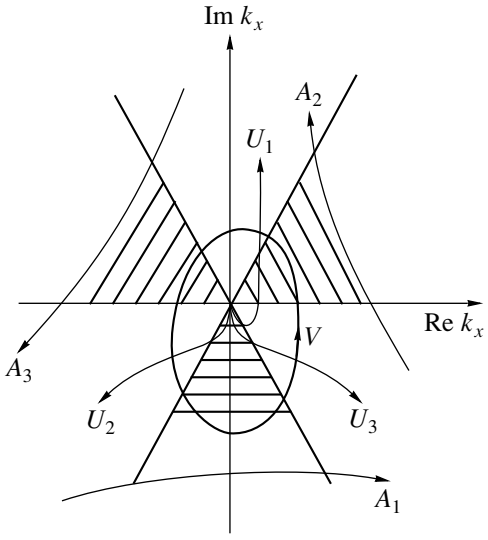

Fig. 1. Integration contours in (5) corresponding to solutions to equation (3). The sectors in which the integrand increases without bound as $|k_x| \longrightarrow \infty$ are hatched.

$$\begin{aligned} U_2 \approx &-\pi i H_0^{(2)}(2\sqrt{Px}) \\ &+ \frac{\pi^{1/2}}{x^{3/4}\Lambda^{1/4}} \exp\left(-\frac{2i}{3}x^{3/2}\Lambda^{1/2} + \frac{i\pi}{4}\right). \end{aligned} \tag{10}$$

The existence of the asymptotic solution (10), which is valid along the positive real semiaxis and contains an exponential function whose index varies on a short scale, indicates the conversion of large-scale waves into small-scale waves at a Larmor resonance.

The last term in (10) should be taken into account not only at $\arg x = 0$ but also in the sector $0 < \arg x < 2\pi/3$, where it grows exponentially and plays the dominant role. Hence, we arrive at the conclusion that the nonanalytic solution to the reduced equation (1) coincides approximately with the solution to equation (3) only in the sector $0 > \arg x > -4\pi/3$, which contains the lower half-plane. Therefore, if we wish to operate with the simplified equation (1), then we must choose the integration contour that lies below the resonant point (Fig. 2). Since we are working under the assumption $\Omega'_{i,x} > 0$, the integration contour is chosen in accordance with the Landau rule. Consequently, the Landau circumvention rule appears to be a consequence of the Stokes phenomenon, which implies that the asymptotics of an analytic function are different in different regions on the plane of a complex variable [cf. (9), (10)].

A similar analysis shows that the functions

$$U_{1,3} \approx \pi i H_0^{(1)}(2\sqrt{Px})$$

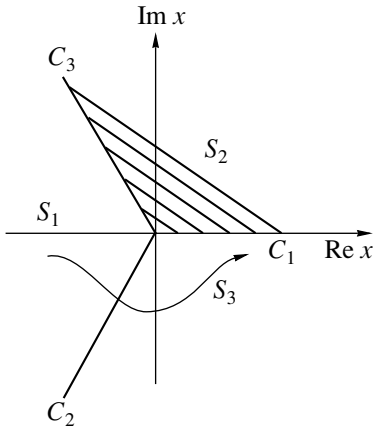

Fig. 2. Plane of the complex variable x for the function U_2. The sector in which this function transforms into a short-wavelength function is hatched. The contour for circumventing the Larmor resonance point according to the Landau rule is marked by an arrow.

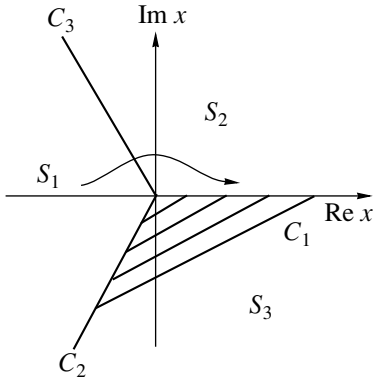

Fig. 3. The same as in Fig. 2, but for the function U_3. The arrow indicates the contour for circumventing the resonant point in the sense of the "anti-Landau" rule.

differ from U_2 only with regard to the positions of the sectors of the complex variable x in which they transform into the corresponding short-wavelength exponentially growing solutions to the complete equation (4). In Figs. 2 and 3, these sectors are denoted by S_i with the same subscripts as in U_i. Figure 3 implies that, if we choose the function U_3 as a second linearly independent long-wavelength solution, then the integration contour should lie above the singular point in the complex plane, which corresponds to the "anti-Landau" circumvention rule. In fact, the positive real semiaxis coincides with the upper boundary of sector S_3, in which, in accordance with the second relationship in (7), the function U_3 transforms into the short-wavelength solution A_2:

$$U_3 \approx \pi i H_0^{(1)}(2\sqrt{Px}) + \frac{\pi^{1/2}}{x^{3/4}\Lambda^{1/4}}\exp\left(\frac{2i}{3}x^{3/2}\Lambda^{1/2} - \frac{i\pi}{4}\right). \quad (11)$$

As for the solution U_1, the last two relationships in (7) imply that it is rapidly growing in sector S_1, which contains a negative real semiaxis. It is hardly conceivable that this solution reflects a real physical situation.

The answer to the question of which solution (U_2 or U_3) should be used (and, accordingly, the question of whether the Landau circumvention rule is valid) depends on the particular problem that is to be solved. To clarify this point, we turn to the dispersion relation for small-scale waves, which can be obtained from equation (3) without the last two terms:

$$\omega \approx \Omega_i - \frac{3}{4}\Omega_{Ti}\rho_i^2 k_x^2. \quad (12)$$

This relation implies that the group and phase velocities of the small-scale waves have different signs. Consequently, the phase of the second term in (10) decreases as x increases, so that this term describes the wave that carries the energy away from the resonant point. On the other hand, the second term in (11) describes small-scale waves that propagate toward the point of Larmor resonance.

Large-scale waves are characterized by a normal dispersion: in the vicinity of the resonant point, the approximate dispersion relation has the form

$$\omega \approx \Omega_i - \frac{k_y^2}{k_x^2\Omega_i}\left|\frac{g}{n_0}\frac{dn_0}{dx}\right|.$$

Consequently, the first terms in (10) and (11) describe large-scale waves propagating oppositely to small-scale waves, which corresponds to the complete conversion of large-scale waves into small-scale waves and back at the point of the Larmor resonance.

Below, we will show that, during the flute instability, large-scale waves are generated on the outside of the vicinity of the resonant point. Large-scale waves propagating toward the point of Larmor resonance should be described by the solution U_2, which corresponds to the Landau circumvention rule.

On the other hand, we can imagine situations in which small-scale waves also propagate toward the resonant point. Below, we will show that the energy of the small-scale waves into which large-scale waves are converted increases in the vicinity of the point at which the resonance condition is satisfied for the Larmor drift velocity calculated solely in terms of the density gradient. However, for some density profiles, no such point exists, in which case small-scale waves should return to the point of Larmor resonance after they have been reflected from the boundary. The solution describing small-scale waves that approach the resonant point is determined by the function U_3 with the "anti-Landau" rule for circumventing the singular point (see above). Note that both of the long-wavelength solutions decrease exponentially behind the point of Larmor resonance, i.e., in the region $x < 0$, in which $U_{2,3} \propto \exp(-2\sqrt{P|x|})$.

If the Larmor drift velocity is a nonmonotonic function of the coordinate, then there can exist eigenmodes between two points of the Larmor resonance in a plasma. The eigenmodes are a superposition of the oppositely propagating large-scale and small-scale waves. At the points of Larmor resonance, the reflection of these waves is accompanied by their conversion: large-scale waves are converted into small-scale waves and back. The spatial structure of these waves is illustrated in Fig. 4. Presumably, these are the waves that were found to be unstable in the problems treated in [8, 9].

Along with the solutions that we have already discussed, it is of interest to consider the solution A_1, which decreases sharply behind the resonant point:

$$A_1 \approx \frac{\pi^{1/2}}{|x|^{3/4}\Lambda^{1/4}}\exp\left(-\frac{2}{3}|x|^{3/2}\Lambda^{1/2} + \frac{i\pi}{2}\right).$$

It is convenient to find the solution at the positive real semiaxis (line C_1) from relationship (8). This is related, in particular, to the following circumstance: if x lies on lines C_i, then contours A_i pass through both of the saddle points $k_{x,s} = \pm(x\Lambda)^{1/2}$ of the integral in (5). Relationship (8) shows that, in the region ahead of the resonant point ($x > 0$), the solution A_1 describes the standing large-scale and small-scale waves that are somehow coupled to each other.

2.3. Wave Energy Flux and Flute Instability

The reduced equation (1) enables us to consider the flute instability that may occur in a gravitational field directed outward from the plasma, $g\frac{dn_0}{dx} < 0$. Rosenbluth *et al.* [5] showed that the flute instability is suppressed if the Larmor drift velocity is sufficiently high, $\Omega_i^2 \geq \left|g\frac{1}{n_0}\frac{dn_0}{dx}\right|$. However, in [4], it was shown that, even in the regime in which the flute instability is suppressed, flute oscillations may nevertheless grow as a result of resonant interaction with the Larmor drift.

If the growth rate of such a resonant flute instability is not high, it can be estimated from the quadratic form obtained by multiplying (1) by φ_1^* and by integrating the resulting equation over the interval (x_1, x_2), which we are considering here. With allowance for the boundary condition $\varphi_1(x_{1,2}) = 0$, the imaginary part of the quadratic form is

$$Q = \int_{x_1}^{x_2} dx\left(\operatorname{Im}\omega n_0|\nabla\varphi_1|^2 + \operatorname{Im}\omega\frac{k_y^2 g}{\omega^2}\frac{dn_0}{dx}|\varphi_1|^2\right) = 0. \quad (13)$$

The main contribution to the integral of the first term (which will be denoted by Q_1) comes from the vicinity of the resonant point at which the solution has

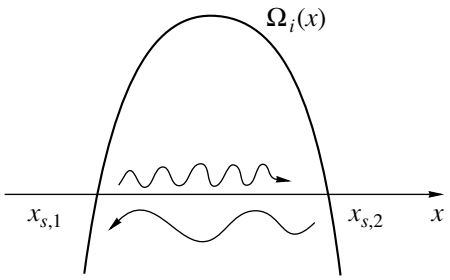

Fig. 4. Spatial structure of the eigenmodes excited between the points of Larmor resonance: the Larmor drift velocity versus the coordinate ($x_{s;\,1,\,2}$ are the resonant points). The wavy arrows show the wave propagation directions that lead to the establishment of eigenmodes (the propagation directions of the long- and short-wavelength oscillations can be reversed simultaneously).

a logarithmic singularity $\varphi_1 \underset{x\to x_s}{\approx} \ln(x - x_s - i\gamma/\Omega'_{i,x})$ in the limit $\gamma = \operatorname{Im}\omega \longrightarrow 0$. Using the familiar equality $\int_{-\infty}^{\infty} dx\frac{\delta}{x^2+\delta^2} = \pi$, we obtain

$$Q_1 \underset{\operatorname{Im}\omega\to 0}{\approx} \pi|\Omega'_{i,x}|_{x=x_s} n_0(x_s).$$

With allowance for this relationship, expression (13) implies that, if $g\frac{dn_0}{dx} < 0$, then the flute oscillations are unstable,

$$\gamma \approx -\omega^2(k_y^2 g\langle n'_{0,x}\rangle)^{-1} n_0(x_s)|\Omega'_{i,x}|_{x=x_s}\Delta x/\Omega_i^2,$$

where $\langle n'_{0,x}\rangle$ is a certain mean value of $n'_{0,x}$ and Δx is the plasma dimension.

Let us analyze the energy balance in unstable oscillations. It is convenient to evaluate the energy density of the potential waves,

$$W = \frac{1}{8\pi}\frac{d}{d\omega}\omega\varepsilon_{ik}\frac{\partial\varphi_1^*}{\partial x_i}\frac{\partial\varphi_1}{\partial x_k},$$

from the wave equation

$$\frac{\partial}{\partial x_i}\varepsilon_{ik}\frac{\partial\varphi_1}{\partial x_k} = 0, \quad (14)$$

which is valid for any potential oscillations.

We integrate (14) multiplied by φ_1^* by parts assuming that, at the boundary, the potential is unperturbed. As a result, we obtain

$$\int d\mathbf{r}\varepsilon_{ik}\frac{\partial\varphi_1^*}{\partial x_i}\frac{\partial\varphi_1}{\partial x_k} = 0. \quad (15)$$

We also assume that the tensor ε_{ik} is Hermitian and that the waves grow at a low rate ($\omega \gg \gamma$). Both of these assumptions are valid for the unstable waves we are

going to analyze. In (15), we single out the imaginary part by expanding ε_{ik} in powers of the small ratio $i\gamma/\omega$ and add the resulting expression to the real part multiplied by $i\gamma/\omega$. This yields the following equality, which describes the time evolution of the wave energy:

$$\int d\mathbf{r}\dot{W} = \text{Const} \times Q.$$

The constant can be found by comparing equations (1) and (14) in the simplest case of a homogeneous plasma:

$$\text{Const} = \frac{1}{4\pi n_0}\left(\frac{\omega_{pi}}{\omega_i}\right)^2.$$

Thus, we have found that the net wave energy is equal to zero. This result is quite natural, because we are considering a closed conservative system. In the course of instability, the net wave energy does not change: it is only redistributed between different regions. In the case of waves with low frequencies $\omega \ll \left|\frac{g}{n_0}\frac{dn_0}{dx}\right|^{1/2}$, the second term in the integrand in (13) dominates everywhere except for a small vicinity of the resonant point. For radially decreasing density profiles, this term is negative. This indicates that, as the wave amplitude grows, the plasma loses thermal energy, which is accumulated in the resonance region, where it is converted into oscillatory ion energy. In the resonance region, the first term in the integrand in (13) increases sharply (see the discussion above).

Let us show that the waves lose the same energy as at $\mathrm{Im}\,\omega = 0$, in which case it is converted into the energy of small-scale waves running away from the resonant point. To take into account small-scale waves, we turn to equation (3). Multiplying this equation by φ_1^* and integrating by parts gives the imaginary part of the quadratic form at $\mathrm{Im}\,\omega = 0$:

$$Q = -\frac{3}{4}n_0\Omega_{Ti}\rho_i^2(\varphi_{1,sw}^*\varphi_{1,sw}''' - \varphi_{1,sw}'^*\varphi_{1,sw}'')^{x=\infty} - n_0(\omega-\Omega_i)\varphi_{1,sw}^*\varphi_{1,sw}'|^{x=\infty}. \quad (16)$$

Here, $\varphi_{1,sw}$ is the short-wavelength part of the solution U_2 and account is taken of the fact that small-scale waves run toward the region $x > x_s$. Since, in a dissipationless plasma, the energy flux is independent of distance, it can be found by solving equation (4), which is valid at short distances from the resonant point. Using the relationship $\varphi_{1,sw}' \approx -ik_x\varphi_{1,sw}$ with $k_x \approx (x\Lambda)^{1/2}$, which is valid for the short-wavelength part of solution (10), we can see that (16) is exactly equal to Q_1.

2.4. Effect of Ion–Ion Collisions on Small-Scale Waves

Now, we consider the time evolution of the small-scale waves into which large-scale waves are converted at the point of Larmor resonance. The spatial structure of the small-scale waves can be described in a quasi-classical fashion, $\varphi_1(x) \propto \exp(i\int^x dx\, k_x(x, \omega))$. The small-scale waves can be analyzed from relationship (2) by setting $\varphi_1(k_x) \propto \delta(k_x - k_x(x, \omega))$, in which case we obtain

$$n_{1i} \approx \left[-1 + \left(1 - \frac{\Omega_{ni}}{\omega}\right)F_i - \frac{\Omega_{Ti}}{\omega}b_iF_i'\right]n_0\frac{e\varphi_1}{T_0},$$

where $F_i = \exp(-b_i)I_0(b_i)$, $b = (k_x\rho_i)^2$.

The perturbed electron density can be found in the hydrodynamic approximation:

$$n_{1e} \approx -\frac{\Omega_{ni}}{\omega}n_0\frac{e\varphi_1}{T}.$$

The condition that the plasma be quasineutral yields the following local dispersion relation, which describes small-scale waves and is a generalization of (12):

$$\omega \approx \Omega_{ni}(x) + \frac{b_iF_i'}{F_i - 1}\Omega_{Ti}(x). \quad (17)$$

Above, we have shown that the wavenumber of the waves increases as they propagate away from the point of Larmor resonance at which $\omega = \Omega_i = \Omega_{ni} + \Omega_{Ti}$. According to (17), the wavenumber tends to infinity as the waves approach the point at which $\omega = \Omega_{ni}\left(F_i \xrightarrow[b_i\to\infty]{} \frac{1}{\sqrt{2\pi b_i}}\right)$. In the region near this point, the wave energy grows.

In this region, i–i collisions may have a strong impact on the small-scale waves. The i–i collisions can be taken into account by introducing the Bhatnagar–Gross–Krook (BGK) collision term (which conserves the number of particles and their momentum and energy) into the kinetic equation:

$$\mathrm{St}(f) = -\nu_{ii}f_1 + \nu_{ii}\left(\frac{n_1}{n_0} + \frac{m_i(\mathbf{v}\mathbf{V}_1)}{T_0} + \left(\frac{m_iv^2}{2T_0} - \frac{3}{2}\right)\frac{T_1}{T_0}\right)f_0,$$

where $\mathbf{V}_1$ is the perturbed velocity and T_1 is the perturbed temperature.

Integrating the kinetic equation along the trajectories, we obtain

$$f_{1i} = \frac{\partial f_0}{\partial\varepsilon} - \left(\frac{\partial f_0}{\partial\varepsilon} + \frac{k_y}{m_i\omega_i(\omega + i\nu_{ii} + k_yg/\omega_i)}\frac{\partial f_0}{\partial\zeta}\right) \times J_0(\xi)\exp(i\xi\sin(\theta-\chi)) + \frac{i\nu_{ii}}{\omega}\left(\frac{n_1}{n_0}J_0(\xi) + i\frac{m_iv_\perp}{T_0}(V_{1x}\sin\chi - V_{1y}\cos\chi)J_1(\xi) + \left(\frac{m_iv^2}{2T_0} - \frac{3}{2}\right)\frac{T_1}{T_0}J_0(\xi)\right)\exp(i\xi\sin(\theta-\chi))f_0.$$

We will find the corrections related to collisions, assuming that the collision frequency is sufficiently low. For small-scale waves in the collisionless approximation, we obtain

$$n_1 \approx n_0\left(-1+\left(1-\frac{\Omega_{ni}}{\omega}\right)F_i-\frac{\Omega_{Ti}}{\omega}b_iF_i'\right)\frac{e\varphi_1}{T_0},$$

$$V_{1x}\sin\chi - V_{1y}\cos\chi$$
$$\approx i\frac{\omega}{k}\left(\left(1-\frac{\Omega_{ni}}{\omega}\right)b_iF_i'-\frac{\Omega_{Ti}}{\omega}b_i(b_iF_i''+F_i')\right)\frac{e\varphi_1}{T_0},$$

$$T_1 \approx \frac{2}{3}T_0\left(\left(1-\frac{\Omega_{ni}}{\omega}\right)b_iF_i'\right.$$
$$\left.-\frac{\Omega_{Ti}}{\omega}\left(b_i^2F_i''+2b_iF_i'+\frac{3}{2}F_i\right)\right)\frac{e\varphi_1}{T_0}.$$

The collisional correction to the perturbed ion density has the form

$$\delta n_{1i} \approx \frac{i\nu_{ii}}{\omega}\left[\left(1-\frac{\Omega_{ni}}{\omega}\right)\left(F_i(F_i-1)+b_i\left(1+\frac{2}{3}b_i\right)F_i'^2\right)\right.$$
$$\left.+\frac{\Omega_{Ti}}{\omega}b_iF_i'\left(1-2F_i-\left(1+\frac{4}{3}b_i\right)F_i'-b_i\left(1+\frac{2}{3}b_i\right)F_i''\right)\right]$$
$$\times n_0\frac{e\varphi_1}{T_0}.$$

Incorporating this correction into the quasineutrality condition and using the "collisionless" dispersion relation (17), we obtain the correction to the frequency of the small-scale natural waves introduced by i–i collisions:

$$\delta\omega \approx -i\nu_{ii}\frac{\Omega_{Ti}}{\Omega_{ni}+\dfrac{b_iF_i'}{F_i-1}\Omega_{Ti}}\left((-1+F_i)\right.$$
$$\left.\times\left(1+\frac{2}{3}b_iF_i+\frac{4}{3}b_i(1+b_i)F_i'\right)+b_i\left(1+\frac{2}{3}b_i\right)F_i'^2\right).$$

This expression shows that small-scale waves are stable when the quantities $\Omega_{ni}\propto\dfrac{dn_0}{dx}$ and $\Omega_{Ti}\propto\dfrac{dT_0}{dx}$ have the same signs. Otherwise, small-scale waves may be unstable.

In the limits of small and large values of b_i, the correction $\delta\omega$ becomes

$$\delta\omega \underset{b_i\ll 1}{\approx} -i\nu_{ii}\frac{\Omega_{Ti}}{\Omega_i}\frac{11}{12}b_i,$$

$$\delta\omega \underset{b_i\gg 1}{\approx} -i\nu_{ii}\frac{\Omega_{Ti}}{\Omega_{ni}}\frac{1}{2\sqrt{2\pi b_i}}.$$

If the small-scale waves are excited by an external source, then i–i collisions cause the wave amplitude to change in space according to $\mathrm{Im}\,k_x=\left(\dfrac{\partial\omega}{\partial k_x}\right)^{-1}\delta\omega$. Small-scale waves are difficult to excite externally. It is more convenient to initiate them via the conversion of large-scale waves at the Larmor resonance point. Since the energy of small-scale waves is converted into the thermal energy, we can imagine a scheme of "Larmor" plasma heating similar to the scheme of Alfvén heating of a weakly collisional plasma, which is also based on the conversion of large-scale waves into small-scale waves. Note that the equations for large-scale flute oscillations are similar to those for Alfvén waves (see, e.g., [10]): the point of the Alfvén resonance, at which large-scale waves are also converted into small-scale waves, is a singular point for the latter equations.

3. PLASMA WITH A NONUNIFORM DENSITY AND A UNIFORM TEMPERATURE

3.1. "Stability" of the Larmor Resonance against Certain Factors

In the simpler case of a uniform temperature, we can use relationship (2) to obtain n_{1i} in a fairly compact form with allowance for the effects of all orders in $k\rho_i$ and the first order in the ratio ρ_i/L, where L is the scale on which the plasma density varies. The effects of the first order in this ratio should be taken into account, because, in the limit $\rho_i \ll 1$, we must correctly pass over to equation (1), which contains the term proportional to $\propto\dfrac{1}{L}\dfrac{d\varphi_1}{dx}$. The corresponding quasineutrality condition can be written as

$$0 = n_{1i}-n_{1e} = \frac{e}{T_0}\int dk_x\exp(ik_xx)\varphi_1(k_x)$$
$$\times\left(G_i(x)(F_i-1)+\frac{i}{2}G_i'(x)\frac{dF_i}{dk_x}\right), \qquad (18)$$

where $G_i(x)=n_0(x)\left(1-\dfrac{\Omega_i(x)}{\omega}\right)$.

To derive a differential wave equation for $\varphi_1(x)$, we must replace k_x in (18) by the operator id/dx and apply this operator to $\varphi_1(x)=\int dk_x\,\varphi_1(k_x)e^{ik_xx}$. If we expand the function F_i from (18) in powers of $k_x\rho_i$, retaining terms up to a certain finite order, then the order of the desired differential equation will coincide with the order of the expansion. Moreover, regardless of the order of the expansion, the coefficient in front of the highest derivative in the wave equation will vanish at

the point of the Larmor resonance. Relationship (2) implies that, at this point, the ions obey a Boltzmann distribution, which is obviously unaffected by i–i collisions. This assertion is supported by the analysis of the preceding section. Hence, we can conclude that, in a plasma with a uniform temperature, the wave equation cannot be regularized by taking into account the effects of the finite ion Larmor radius and i–i collisions.

Above, we assumed that the plasma is quasineutral and the plasma waves are potential. If the wave electric field contains a nonpotential component, $\mathbf{E}_1 = -\nabla\varphi_1 + \frac{i\omega}{c}\mathbf{A}_1$, then we can readily show that, at the point of Larmor resonance, the perturbed ion distribution function has the form $f_{i1} = \frac{ie}{k_y T} E_{y1} f_0$, which is a generalization of the distribution function in a Boltzmann equilibrium state. The terms proportional to the derivatives $d^n\varphi_1/dx^n$ of the electric field vanish at the resonant point, as is the case with the potential waves.

The effects of plasma nonquasineutrality can be incorporated into (18) through the change $G_i \longrightarrow n_0\left(1 + \frac{\omega_i^2}{\omega_{pi}^2} - \frac{\Omega_i}{\omega}\right)$, in which case the terms containing the derivatives beyond the second order remain unchanged. Consequently, allowing for the nonquasineutrality and nonpotentiality effects also fails to regularize the problem.

Since the spatial scale of perturbations becomes shorter as the resonant point is approached, the wave electric field grows. Consequently, we cannot exclude that, in the vicinity of the resonant point, nonlinear effects may be important. Let us derive a nonlinear equation for the case of neutral oscillations with $\mathrm{Im}\,\omega = 0$. To do this, it is convenient to pass over to a frame moving with the wave. In this frame, an additional inductive electric field $\frac{d\varphi}{dx} = -\frac{\omega}{k_y c} B$ appears and the plasma moves as a steady stream. Moreover, at the point of Larmor resonance, the unperturbed hydrodynamic velocity $V_{0y} = \frac{c}{B}\left(\frac{d\varphi_0}{dx} + \frac{T_0}{e}\frac{1}{n_0}\frac{dn_0}{dx}\right)$ vanishes, so that the ions obey a local Boltzmann distribution.

In analyzing the electron motion, we can assume that the electric field causes the electrons to drift with the velocity $\mathbf{V} = \frac{c}{B^2}[\mathbf{B}\nabla\varphi]$. From the continuity equation, we find $n(\mathbf{r}) = n(\varphi(\mathbf{r}))$, where $n(\varphi)$ is an arbitrary function.

For the desired nonlinear wave equation to be informative, we must retain the inertial force in the equation of ion motion and supplement it with the force associated with collisionless viscosity. It is well known (see, e.g., [6]) that the viscous force makes it possible to incorporate the effects of the finite ion Larmor radius to the lowest order in the small parameter $\rho_i d/dx$. Omitting the intermediate manipulations, we write out the nonlinear wave equation, which follows from the quasineutrality condition:

$$\nabla\left(n\frac{d\Phi}{d\varphi}\left(\frac{d\varphi}{dx}\right)^2\nabla\left(\frac{d\varphi}{dy}\Big/\frac{d\varphi}{dx}\right)\right) - \frac{1}{\omega_i}\nabla\left(n\left[\mathbf{g}\frac{\mathbf{B}}{B}\right]\right) = 0, \quad (19)$$

where $\Phi = \frac{cT}{eB}\ln\left(n\exp\left(\frac{e\varphi}{T}\right)\right)$.

In a linear approximation such that the condition $|d\varphi/dy| \ll |d\varphi/dx|$ holds, equation (19) coincides with the equation derived by Rosenbluth and Simon [11] for plasmas with arbitrary steady electric fields if we set $\omega = 0$ in it. On the other hand, at $T = 0$, equation (19) passes over to the nonlinear equation presented in [12].

Recall that, in the linear approximation, the stationary point in the comoving frame (a line on the xy plane) corresponds to the point of Larmor resonance in the laboratory frame. In the nonlinear approximation, this line transforms into a "Boltzmann" current line along which we have $n(\varphi) = C\exp\left(-\frac{e\varphi}{T}\right)$. It is easy to see that the coefficient in front of the highest derivative in (19) vanishes on this line. Hence, along with the linear equations we have analyzed above, the point of Larmor resonance is also a singularity of the nonlinear equation (19).

3.2. Effect of Ion–Electron Friction

Since the effects that appear, at first glance, to be most important do not play a role at a Larmor resonance, we must focus our attention on the effects that are usually ignored. Let us provide insight into the consequences of i–e friction. In the kinetic equation, i–e collisions can be described by the BGK collision term in a form that conserves the number of particles and allows for the momentum exchange between electrons and ions:

$$\mathrm{St}(f) = -\nu_{ie} f_1 + \nu_{ie}\left(\frac{n_1}{n_0} + \frac{m_i(\mathbf{v}\mathbf{V}_{1e})}{T}\right) f_0, \quad (20)$$

where ν_{ie} is the rate with which the ions are scattered by the electrons and $\mathbf{V}_{1e} = \frac{c}{B^2}\left[\mathbf{B}\left(\nabla\varphi - \frac{T_0}{en}\nabla n\right)_1\right]$ is the hydrodynamic electron velocity. In (20), the temperature remains unperturbed, because the perturbed electron temperature is proportional to the small parameter $(k\rho_e)^2$ and, for $\nabla T = 0$, we have $T_{1i} \longrightarrow 0$ as $x \longrightarrow x_s$ (see the discussion of the preceding section).

As in the preceding section, the collisional correction to n_{1i} can be obtained by the method of integration along the trajectories:

$$\delta n_{1i} = \frac{i\nu_{ie}}{\omega}\frac{e}{T_0}\int dk_x \exp(ik_x x)\varphi_1(k_x) \times (G_i(x)F_i(F_i-1) - G_e(x)b_iF_i'), \quad (21)$$

where $G_e(x) = n_0(x)\left(1 + \frac{\Omega_e(x)}{\omega}\right)$.

In order for the analysis of the effects associated with the i–e friction to be consistent, it is necessary to incorporate the electron scattering by the ions into the equation of electron motion. The collisional correction to the perturbed electron density can be represented in an integral form (as was done for δn_{1i}):

$$\delta n_{1e} = \frac{i\nu_{ie}}{\omega}\frac{e}{T}\int dk_x \exp(ik_x x)\varphi_1(k_x)(G_e(x) - G_i(x))b_i. \quad (22)$$

From (18), (21), and (22), we find the complete quasineutrality condition allowing for the effects of i–e friction:

$$\int dk_x \exp(ik_x x)\varphi_1(k_x)\left(G_i(x)(F_i-1) + \frac{i}{2}G_i'(x)\frac{dF_i}{dk_x} - SF_i + \frac{i\nu_{ie}}{\omega}(G_i(x)F_i(F_i-1) - G_e(x)b_i(F_i'+1))\right) = 0, \quad (23)$$

where $S = P\rho_i^2$.

We restrict ourselves to considering the vicinity of the Larmor resonance point. We set $G_i(x) \approx -n_0(x_s)\frac{\Omega_{i,x}'}{\omega}(x - x_s)$ and $\Omega_e(x) = \text{const}$. We apply the operation of translation $x - x_s \longrightarrow x$ to (23) and switch to a new variable $x \longrightarrow i\partial/\partial k_x$. Then, from the condition for the integrand to vanish, we obtain the following equation for $\varphi_1(k_x)$:

$$\sqrt{1-F_i}\frac{d}{dk_x}(\sqrt{1-F_i}\varphi_1) + (-iSF_i - \sigma b_i(F_i'+1))\varphi_1 = 0, \quad (24)$$

where $\sigma = \frac{\nu_{ie}}{\omega}\frac{\Omega_i + \Omega_e}{\Omega_{i,x}'}$.

The solution to (24) is

$$\varphi_1(k_x) = \frac{1}{\sqrt{1-F_i}} \times \exp\left(iS\int^{k_x} dk_x \frac{F_i}{1-F_i} + \sigma\int^{k_x} dk_x \frac{b_i(1+F_i')}{1-F_i}\right). \quad (25)$$

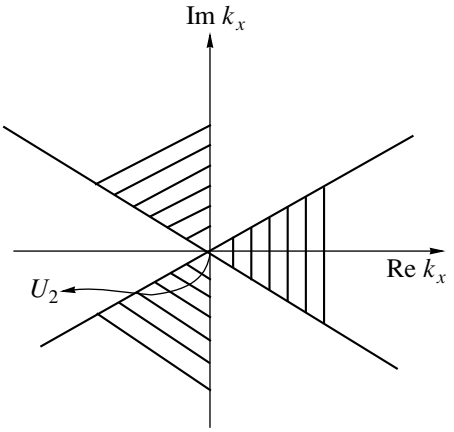

Fig. 5. Integration contour in (5) that corresponds to one of the solutions to equation (23). The sectors in which the integrand increases without bound as $|k_x| \longrightarrow \infty$ are hatched.

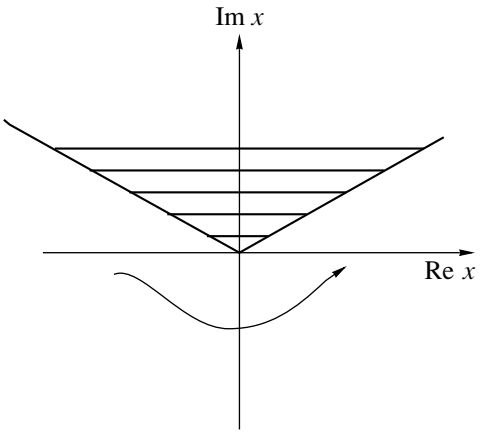

Fig. 6. Plane of the complex variable x for a long-wavelength solution to equation (23) that grows asymptotically without bound. The sector in which this function transforms into a short-wavelength function is hatched. The contour for circumventing the Larmor resonance point according to the Landau rule is marked by an arrow.

We restrict ourselves to analyzing such solutions to the wave equation that pass over to the solutions to the reduced equation (1) far away from the resonant point. In the collisionless limit ($\sigma = 0$), expression (24) coincides with (6) at $k_x \longrightarrow 0$. We take the integral over k_x in (5) using the same integration contours as in Section 2.2. Effects that occur on short scales and come into play in the vicinity of the resonant point have an insignificant impact on the solution V, which is regular at this point. We consider the function U_3, which has a logarithmic singularity at the resonant point, over the range of distances $|x| \gg \rho_i$. In this case, the main contribution to the integral in (5) comes from the k_x region where $\varphi_1(k_x)$ can be described by expression (6), in which the first term in the exponential index is unimportant. In the region $|k_x| \longrightarrow \infty$, the behavior of $\varphi_1(k_x)$

is determined by the second term in the exponential function in (25); it is this term that accounts for i–e friction: $\varphi_1(k_x) \propto \exp\left(\frac{1}{3}\sigma\rho_i^2 k_x^3\right)$. The contribution of this region to the integral in (5) is insignificant if the integration contour on the plane of the complex variable k_x approaches infinity in the unhatched sectors in Fig. 5. We emphasize that, in Fig. 5, the forbidden sectors are rotated through the angle $-\pi/6$ with respect to those in Fig. 1. An analysis similar to that carried out in Section 2.2 shows that, on the plane of the complex variable x, the sector in which the long-wavelength solution to the wave equation transforms into the short-wavelength solution is rotated precisely through the same angle. In Fig. 6, this sector lies entirely within the upper half-plane. Consequently, the Landau circumvention rule is valid for the solutions to the reduced equation (1); moreover, for real values of the argument, the solution to the complete wave equation remains long-wavelength.

Our analysis shows that, for $\nabla T = 0$, the energy of the large-scale flute oscillations increases near the point of Larmor resonance until the effects of i–e friction cause them to damp. The characteristic spatial scale on which these effects come into play can be estimated by comparing the terms in the exponential index in (25): $|x| \approx |k_x|^{-1} \approx \left(\frac{\nu_{ie}}{\omega_i}\frac{R\rho_i}{k_y}\right)^{1/3}$.

4. CONCLUSION

We have analyzed the physical processes that are important near the point of Larmor resonance. We have established rules for continuing solutions through a singular point corresponding to the resonant point in the simplified wave equation. We have shown that the phenomenon of Larmor resonance can be used to heat the plasma.

ACKNOWLEDGMENTS

The work was supported in part by the Russian Foundation for Basic Research, project nos. 99-02-16615 and 96-15-96815 (under the program “Leading Scientific Schools”).

REFERENCES

1. A. V. Timofeev, in *Reviews of Plasma Physics*, Ed. by B. B. Kadomtsev (Énergoatomizdat, Moscow, 1989; Consultants Bureau, New York, 1992), Vol. 17.
2. A. V. Timofeev, Nucl. Fusion **6**, 93 (1966).
3. A. V. Timofeev, Nucl. Fusion **8**, 99 (1968).
4. A. V. Timofeev, Fiz. Plazmy **25**, 573 (1999) [Plasma Phys. Rep. **25**, 522 (1999)].
5. M. N. Rosenbluth, N. A. Krall, and N. Rostoker, Nucl. Fusion Suppl. **1**, 143 (1962).
6. A. B. Mikhaĭlovskiĭ, *Theory of Plasma Instabilities* (Atomizdat, Moscow, 1977; Consultants Bureau, New York, 1974), Vol. 2.
7. C.-C. Lin, *The Theory of Hydrodynamic Stability* (Cambridge University Press, Cambridge, 1966).
8. B. N. Breizman and S. E. Sharapov, Plasma Phys. Controlled Fusion **37**, 1057 (1995).
9. A. B. Mikhaĭlovskiĭ and S. E. Sharapov, Fiz. Plazmy **25**, 872 (1999) [Plasma Phys. Rep. **25**, 803 (1999)].
10. A. G. Elfimov, A. G. Kirov, and V. P. Sidorov, in *High-Frequency Plasma Heating*, Ed. by A. G. Litvak (IPFAN, Gorki, 1983), p. 211.
11. M. N. Rosenbluth and A. Simon, Phys. Fluids **8**, 1300 (1965).
12. V. I. Petviashvili and V. V. Yan’kov, in *Reviews of Plasma Physics*, Ed. by B. B. Kadomtsev (Énergoatomizdat, Moscow, 1985; Consultants Bureau, New York, 1987), Vol. 14.

Translated by O. E. Khadin

Plasma Physics Reports, Vol. 26, No. 2, 2000, pp. 129–132. Translated from Fizika Plazmy, Vol. 26, No. 2, 2000, pp. 142–145.

PLASMA DYNAMICS

Effect of the Magnetic Field on the Energy of Deuterium Ions Accelerated in the Collision of Magnetosonic Shock Waves

G. N. Dudkin, B. A. Nechaev, and V. N. Padalko

Research Institute of Nuclear Physics, Tomsk Polytechnic University, Tomsk, Russia

Received February 9, 1999; in final form, April 27, 1999

Abstract—A study is made of the effect of the initial magnetic field magnitude on the energy of deuterium ions accelerated in the collision of two magnetosonic shock waves propagating in a deuterium plasma quasi-perpendicularly to the magnetic field. Experiments were carried out at a constant plasma density of $\simeq 2.5 \times 10^{13}$ cm^{-3}. It is found that, as the external magnetic field decreases from 1.4 to 0.7 T and, accordingly, the magnetic Mach number increases from 1.02 to 2.3, the energy of accelerated ions increases from 3.2 to 7.5 MeV. The maximum number of accelerated ions attains 10^5–10^6 particles per shot. © *2000 MAIK "Nauka/Interperiodica".*

1. INTRODUCTION

Acceleration of charged particles by magnetosonic shock waves (MSWs) has been widely studied experimentally and theoretically, because it is one of the main mechanisms for the generation of high-energy particles and plasma heating in both laboratory and space plasmas.

Theoretical studies [1–4] have shown that the electric field at the MSW front is sufficient to accelerate ions to high energies at a high rate.

In laboratory experiments [5, 6], mechanisms were revealed and investigated for accelerating ions by MSWs both perpendicularly to the front (the reflection of ions from a potential jump) and along the front (resonant acceleration). In both cases, the accelerated particles move across the magnetic field, which is one of the factors limiting the energy of accelerated particles in laboratory facilities, because, e.g., even for a deuteron energy of 1 MeV, the Larmor radius is larger than the cross size of typical plasma devices.

In experiments [7–9], the possibility of accelerating plasma ions along an external magnetic field during the interaction of two MSWs propagating quasi-perpendicularly to the magnetic field toward each other was demonstrated for the first time. In those experiments, the maximum energy of accelerated deuterons was $\varepsilon_{max} \approx$ 10 MeV and the maximum number of accelerated particles per shot was 10^5–10^6. A quantitative explanation of this result encounters serious difficulties. Qualitatively, this result was explained based on the numerical calculations of the collision of two MSWs in a plasma whose density varied along the magnetic field [10]. It was assumed that the accelerating electric field E_z, directed along the magnetic field, was a superposition of the electric fields existing at the MSW fronts. The energy of accelerated deuterons in this model was estimated as $\varepsilon \sim E_z$. For a soliton MSW model [1], the accelerating electric field is $E_z \sim B_0^2 (M_A - 1)^{3/2}$ (where B_0 is the initial magnetic field and M_A is the magnetic Mach number). Here, we experimentally study the influence of the magnitude of the initial magnetic field on the maximum energy of accelerated deuterons.

In order to formulate the problem, we will clarify some points. In [11], it was shown that, when the plasma flow is decelerated by the magnetic barrier, the liberated energy efficiently converts into magnetic energy. When the plasma produced in the discharge drifts at a velocity $V_d = cE/B_0$ (where c is the speed of light and E is the electric field in the discharge) into a region with a lower electric field, the plasma flow is slowed down and the liberated energy partially converts into magnetic energy. The magnitude of the induced magnetic field is determined by the density $j \simeq Ne\beta V_d$ of the polarization current flowing while a drift channel is being formed (see [12] for details). Here, $\beta = \omega_{ce}\tau_{ei}$ determines the extent to which the electrons are magnetized, ω_{ce} is the electron cyclotron frequency, τ_{ei} is the electron–ion collision time, and N is the plasma density.

The induced magnetic field penetrates into the plasma to the depth L, determined by the duration of the polarization current $\tau \approx 1/\beta\omega_{ci} \le L/V_A$, where ω_{ci} is the ion cyclotron frequency and V_A is the Alfvén velocity. As the magnetic perturbation propagates, it converts to an MSW with the Mach number

$$M_A \le 0.5(\beta L \omega_{ci}/V_A + 1).$$

For $L \simeq R_i$ (where R_i is the ion Larmor radius over which the plasma parameters remain almost unchanged), the condition for the excitation of an MSW ($M_A > 1$) is $\beta V_d/V_A > 1$.

1063-780X/00/2602-0129$20.00

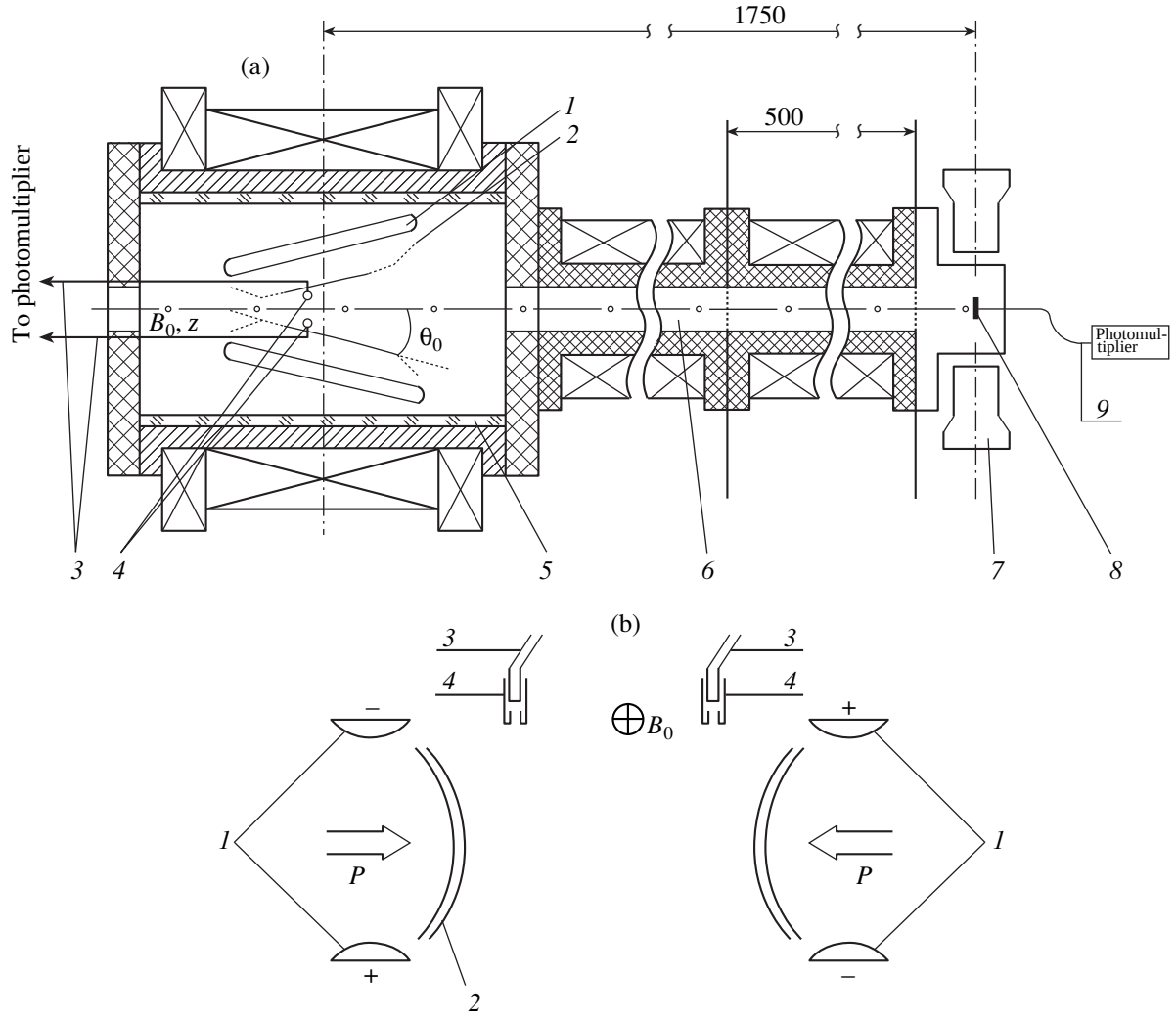

Fig. 1. (a) Experimental device and (a, b) arrangement of diagnostics in the working chamber: (*1*) electrodes, (*2*) wave front, (*3*) fibers, (*4*) collimators, (*5*) ceramic chamber, (*6*) ion-transport line, (*7*) NaI spectrometer detectors, (*8*) scintillator, and (*9*) photomultiplier with a fiber; *P* is the plasma flow.

We express the Mach number through parameters that can be controlled in the experiment:

$$M_A \simeq \frac{\pi N m_i c^2 E^2 \beta}{B_0^4} + 1,$$

where m_i is the ion mass.

It can be shown that $\beta \sim \omega_{ce}\tau_{ei} \sim B_0 V_d^3 \sim E^3/B_0^2$ and, consequently, $M_A - 1 \sim E^5/B_0^6$. From the dependence obtained and the above expression for E_z, it follows that, by varying the magnetic or electric field within relatively small intervals, it is possible to experimentally obtain the dependence of the energy of accelerated ions on the above controlled parameters, providing that the other parameters vary slightly.

Investigations showed that, when the magnetic field was varied, the energy density and plasma density distributions along the magnetic field in the plasma flowing out of the discharge remained almost unchanged. In contrast, when the discharge electric field was varied, these distributions changed significantly. For this reason, the studies were carried out at a constant value of *E*.

2. EXPERIMENT

Experiments were carried out in a TEMP plasma device, described in [7, 9]. In a ceramic chamber with an inner diameter of 18 cm and length l = 150 cm, two pairs of electrodes were installed (with a length of 30 cm, width of 4 cm, and an interelectrode gap of about 2 cm) at an angle of 6° to the symmetry axis of a magnetic mirror system, the mirror ratio being ~1.4 (Fig. 1). The

process of the formation of two counterpropagating MSWs can be divided into two steps.

2.1. Background Plasma Production

On filling the pre-evacuated chamber with a gas and applying the magnetic field, a discharge with $I_{max} \approx 5$ kA and a duration of ≈ 3 ms was initiated between two electrodes.

The working volume was filled with two plasma flows drifting toward each other from two discharge gaps. The plasma in the discharge gaps was produced in "slow" discharges in crossed **E** and **B** fields. In our case, the time needed to fill the working volume with a plasma was ≤ 50 μs. The recorded plasma-density profile along the magnetic field can be approximated by the expression $N(z) = N_0(0.74 + 0.26\cos(\alpha z))$, where $\alpha = 0.255$ cm^{-1} and N_0 is the plasma density at $z = 0$ [12].

2.2. Generation of Counterpropagating MSWs

At a certain instant, a high-power current pulse with $I > 10$ kA and a duration of 1.5 μs was generated in the discharge gaps.

Two plasma flows that were formed in the course of "fast" (when both the electric field E and the power deposition increased rapidly) discharges in crossed **E** and **B** fields propagated toward each other across the magnetic field with a drift velocity V_d. Slowing-down of these plasma flows by the background plasma led to the generation of MSWs. When investigating the mechanism for MSW generation, we measured the propagation velocity of one MSW with the help of probes and loops and obtained a qualitative agreement with dependence (1) [7]. In the case of two interacting MSWs, the probe measurements were not carried out, because, in this case, the gauges prevented ion acceleration.

A beam of accelerated ions was formed in an ion-transport line (32 mm in diameter and 100 cm in length), which was connected coaxially to the discharge chamber. The guiding magnetic field in the line was 0.3 T. At the end of the ion-transport line, a detector based on a standard polystyrene scintillator with a 15-mm diameter and 1.5-mm thickness was positioned. The light from the scintillator was fed to an FEU-115M photomultiplier through a fiber. To protect the scintillator from external light and from slow ions, it was covered with an aluminum foil with a thickness of 7 μm (which is equal to the mean free path of deuterons with an energy of ~0.7 MeV). The energy of accelerated ions was measured by the time-of-flight technique. The stop signal for the time-of-flight system was generated by the scintillator detector positioned at the end of the ion-transport line. The start signal was generated by one of two optical detectors viewing the region where two MSWs collide, the spatial resolution being 0.8 mm. Each optical detector consisted of a fiber (0.5 mm in diameter and 6 m in length), an optical collimator at the fiber entry, and an FEU-85 photomultiplier at the fiber output. Signals from photomultipliers were fed to an S8-14 high-speed storage oscillograph. Since the base distance between the light and scintillator detectors was known (175 cm), we could reconstruct the maximum energy of the bunch of accelerated ions by processing the oscillograms. The number of accelerated ions was determined from the area under the signal trace as follows. With a radioactive ^{239}Pu source, we determined the proportionality coefficient between the energy lost by one α-particle in the scintillator and the amplitude of the multiplier signal (the coefficient was expressed in units of photoelectron/MeV). Then, a correction was made for the different light outputs of the scintillator for α-particles and deuterons and also for the light attenuation in the fibers. Finally, with the use of a light diode, pulse generator, and pulse analyzer, the oscillograph scale was calibrated in photoelectrons. In the experiment, the maximum number of ions per pulse varied from 10^5 to 10^6.

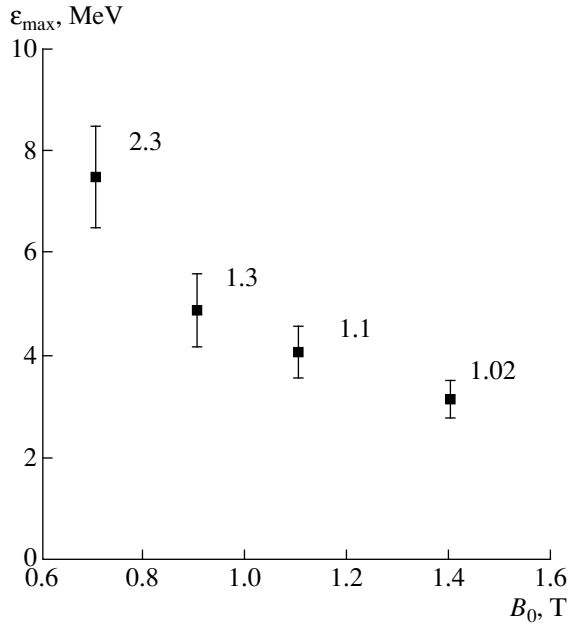

Fig. 2. Maximum energy of accelerated deuterons as a function of the initial magnitude of the magnetic field. The numerals near the points show the values of the MSW Mach number.

Since the time-of-flight system does not identify the species of accelerated ions, it was supplemented with a system of radioactivation analysis. For both systems to operate simultaneously, we employed the $^{12}C(d, n)^{13}N$ ($^{13}N \longrightarrow \beta^+$, $\tau_{1/2} = 9.9$ min) nuclear reaction, using ^{12}C nuclei that were contained in the material of the polystyrene scintillator. A γ–γ-coincidence spectrometer (based on two NaI(Tl) scintillator crystals) recorded the events corresponding to the annihilation of the positrons arising from the decay of ^{13}N. The reaction

was identified by analyzing the behavior of the measured decay curve.

The experiments were carried out at a constant electric field ($E \simeq 9$ kV/cm), $N_0 \simeq 2.5 \times 10^{13}$ cm^{-3}, and at different magnitudes of the magnetic field, which provided different MSW Mach numbers. The measurement procedure was as follows. A series of shots was produced at the same initial parameters of the device. By analyzing the delay time for the detector signals in this series, we selected the event corresponding to the maximum energy and intensity of the flux of accelerated ions. Simultaneously, the system of radioactivation analysis recorded the events corresponding to the annihilation of the positrons arising from the ^{13}N decay. This procedure was repeated for each new value of the magnetic field.

It should be noted that, for the magnetic field $B_0 <$ 0.7 T, the acceleration process is unstable.

The experimental results are shown in Fig. 2. The error bars reflect only the error of determining the ion energy by the delay of the storage-oscillograph signal. The estimated value of the Mach number $M_A = 1.02$ is presented only to demonstrate that $M_A \geq 1$ for the given E and B_0 values.

3. CONCLUSION

A comparison of the experimentally obtained dependence of the energy of accelerated ions on the magnitude of the magnetic field with the dependence prescribed by the magnetic-soliton model ($\varepsilon \sim 1/B_0^7$) shows that it is necessary to consider an alternative model of the formation of an accelerating structure and the associated accelerating field. For example, if we assume the ion-acoustic wave to be an accelerating structure that is formed in the region where two MSWs collide, then we obtain the estimate $\varepsilon \sim 1/B_0^2$. In the future, we plan to perform numerical calculations using a model allowing for the generation of ion-acoustic waves in the region where two MSWs collide.

ACKNOWLEDGMENTS

This work was supported in part by the Russian Foundation for Basic Research (project no. 97-02-17175) and the program "Universities of Russia–Basic Research."

REFERENCES

1. Y. Ohsawa, Phys. Fluids **28**, 2130 (1985).
2. Y. Ohsawa, Phys. Fluids **29**, 773 (1986); Phys. Fluids **29**, 1844 (1986).
3. S. V. Bulanov and A. S. Sakharov, Pis'ma Zh. Éksp. Teor. Fiz. **44**, 421 (1986) [JETP Lett. **44**, 543 (1986)].
4. G. N. Kichigin, Zh. Éksp. Teor. Fiz. **101**, 1487 (1992) [Sov. Phys. JETP **74**, 793 (1992)].
5. N. A. Strokin, Zh. Éksp. Teor. Fiz. **88**, 2005 (1985) [Sov. Phys. JETP **61**, 1187 (1985)].
6. A. T. Altyntsev, G. N. Kichigin, I. V. Lebedev, *et al.*, Zh. Éksp. Teor. Fiz. **96**, 574 (1989) [Sov. Phys. JETP **69**, 324 (1989)].
7. G. N. Dudkin, B. A. Nechaev, A. V. Peshkov, *et al.*, Zh. Éksp. Teor. Fiz. **105**, 1606 (1994) [JETP **78**, 865 (1994)].
8. G. N. Dudkin, V. Yu. Egorov, B. A. Nechaev, *et al.*, Pis'ma Zh. Éksp. Teor. Fiz. **61**, 617 (1995) [JETP Lett. **61**, 633 (1995)].
9. G. N. Dudkin, V. Yu. Egorov, V. K. Kononov, *et al.*, Izv. Vyssh. Uchebn. Zaved., Fiz. **4**, 119 (1998).
10. G. N. Dudkin, B. A. Nechaev, V. N. Padalko, *et al.*, Fiz. Plazmy **25**, 441 (1999) [Plasma Phys. Rep. **25**, 398 (1999)].
11. A. G. Belikov and N. A. Khizhnyak, Fiz. Plazmy **21**, 723 (1995) [Plasma Phys. Rep. **21**, 685 (1995)].
12. G. N. Dudkin, B. A. Nechaev, and V. N. Padalko, Fiz. Plazmy **23**, 258 (1997) [Plasma Phys. Rep. **23**, 237 (1997)].

Translated by N. F. Larionova

Plasma Physics Reports, Vol. 26, No. 2, 2000, pp. 133–138. Translated from Fizika Plazmy, Vol. 26, No. 2, 2000, pp. 146–152.

PLASMA DYNAMICS

Self-Consistent Electron and Ion Motion in a High-Current Plasma Channel

G. V. Karpov

Russian Federal Nuclear Center, All-Russia Research Institute of Experimental Physics, Sarov, Nizhni Novgorod oblast, 607200 Russia

Received April 24, 1997; in final form, May 5, 1999

Abstract—The problem of self-consistent motion of charged particles in a high-current plasma channel is solved using the kinetic model of a plasma with electron and ion beams whose motion is governed by the resulting electromagnetic field. It is shown that, in a high-density plasma, the ion motion makes the contribution of electrons to the current in the channel negative, in which case the ion current is higher than the net current and the plasma moves at a high speed as an electrically neutral axial stream whose direction coincides with the direction of the current in the channel. © *2000 MAIK "Nauka/Interperiodica".*

1. INTRODUCTION

In high-temperature pinchlike plasma formations [1], which have the form of plasma channels in electric discharges with a current from 10^5 to 10^6 A, the electron energy is high enough for the plasma to be magnetized. For a characteristic electron temperature of 10 keV and an electron density of 10^{19} cm^{-3}, the electron mean free path in a fully ionized hydrogen plasma is 40 cm, which exceeds the channel diameter by more than two orders of magnitude. In a collisionless current-carrying plasma, the electrons and ions can be regarded as charged-particle beams, which were investigated in detail by, e.g., Benford and Book [2]. From the standpoint of the physics of electron beams, the essential feature of electrons in a high-current plasma channel is that the current carried by them is much higher than the Alfvén current. Benford and Book [2] noted that, in such beams, the electrons move predominantly in the transverse direction (the mean axial velocity of the electrons is low in comparison with their radial velocity). Qualitatively, the electron current can be described using the model of an electron beam [3, 4], in which the electron distribution function is represented as a superposition of two δ-functions; i.e., all of the electrons are assumed to have the same energy and the same axial canonical momentum. The calculations based on this model [4] show that, for high electron densities, the radial profile of the current over the entire beam cross section is extremely nonuniform: the current flows predominantly in a thin surface layer of thickness Δ, which is equal to the collisionless skin depth and exceeds the Alfvén current by a factor of $R/2\Delta$, where R is the beam radius. The electrons move predominantly in the transverse direction with respect to the beam axis, and they are displaced in the axial direction under the action of the magnetic field only over short time intervals during which they occur in the surface current layer. The mean axial velocity $V_z = 2\Delta R^{-1}V_e$ of the electrons is low in comparison with their total velocity V_e. Consequently, in high-current channels filled with a high-density plasma, the ion current may be important, because the axial velocity of the ions can become comparable with V_z even when the ion energy is low. Our objective here is to analyze self-consistent motion of both the electron and ion plasma components in a high-current plasma channel.

2. SOLUTION OF THE PROBLEM OF ELECTRON AND ION MOTION

In the absence of binary collisions, the self-consistent motion of charged particles in a current-carrying two-species plasma is described in terms of the distribution functions f_e and f_i satisfying the kinetic equations

$$\frac{\partial f_e}{\partial t} + \mathbf{V}_e\frac{\partial f_e}{\partial \mathbf{x}} - e\left(\mathbf{E} + \frac{1}{c}[\mathbf{V}_e\mathbf{H}]\right)\frac{\partial f_e}{\partial \mathbf{p}_e} = 0, \qquad (1)$$

$$\frac{\partial f_i}{\partial t} + \mathbf{V}_i\frac{\partial f_i}{\partial \mathbf{x}} + q_i\left(\mathbf{E} + \frac{1}{c}[\mathbf{V}_i\mathbf{H}]\right)\frac{\partial f_i}{\partial \mathbf{p}_i} = 0. \qquad (2)$$

We restrict ourselves to considering a steady cylindrical channel in which the current and field distributions depend only on the radial coordinate, in which case the Maxwell equations for the self-consistent fields **E** and **H** can be written as

$$\nabla\cdot\mathbf{E} = -\nabla^2\Phi = 4\pi(-en_e + q_in_i), \qquad (3)$$

$$[\nabla\times\mathbf{H}] = [\nabla\times[\nabla\times\mathbf{A}]] = \frac{4\pi}{c}(\mathbf{j}_e + \mathbf{j}_i), \qquad (4)$$

1063-780X/00/2602-0133$20.00

where the particle and current densities have the form

$$n_e = \int f_e(r, \mathbf{p}_e) d\mathbf{p}_e, \quad n_i = \int f_i(r, \mathbf{p}_i) d\mathbf{p}_i, \tag{5}$$

$$\mathbf{j}_e = -e\int \mathbf{V}_e f_e(r, \mathbf{p}_e) d\mathbf{p}_e, \quad \mathbf{j}_i = q_i \int \mathbf{V}_i f_i(r, \mathbf{p}_i) d\mathbf{p}_i. \tag{6}$$

The integrals of motion are the net energies,

$$\begin{aligned} H_e &= c\sqrt{p_e^2 + m_e^2 c^2} - e\Phi, \\ H_i &= c\sqrt{p_i^2 + m_i^2 c^2} + q_i\Phi, \end{aligned} \tag{7}$$

and the axial components of the canonical particle momenta,

$$P_{ez} = p_{ez} - \frac{e}{c}A_z, \quad P_{iz} = p_{iz} + \frac{q_i}{c}A_z. \tag{8}$$

The distribution functions, which depend explicitly only on the constants of motion, automatically satisfy equations (1) and (2), which significantly simplifies the problem of constructing self-consistent kinetic models. We use a plasma model in which all of the particles with the same charge have the same energy and the same axial canonical momentum, so that both the electron and ion distribution functions are a superposition of two δ-functions,

$$f_e(r, \mathbf{p}_e) = \frac{n_{e0}c^2}{2\pi w_e}\delta(H_e - w_e)\delta(P_{ez} - P_{e0}), \tag{9}$$

$$f_i(r, \mathbf{p}_i) = \frac{n_{i0}c^2}{2\pi w_i}\delta(H_i - w_i)\delta(P_{iz} - P_{i0}). \tag{10}$$

Hammer and Rostoker [4] analyzed the steady state of a high-current electron beam using a similar approach to solving the Vlasov equation, but they assumed that the ions were immobile. Substituting the distribution functions (9) and (10) into (5) and (6), we can readily find the particle densities in terms of the scalar potential,

$$n_e = n_{e0}\left(1 + \frac{e\Phi}{w_e}\right), \quad n_i = n_{i0}\left(1 - \frac{q_i\Phi}{w_i}\right), \tag{11}$$

and the current densities in terms of the vector potential,

$$\begin{aligned} j_e &= -\frac{en_{e0}c^2}{w_e}\left(P_{e0} + \frac{e}{c}A_z\right), \\ j_i &= \frac{q_i n_{i0}c^2}{w_i}\left(P_{i0} - \frac{q_i}{c}A_z\right). \end{aligned} \tag{12}$$

Choosing $\Phi(0) = A_z(0) = 0$, we can see that the coefficients n_{e0} and n_{i0} and the constants P_{e0} and P_{i0} are, respectively, equal to the particle densities and the axial components of the particle momenta at the center of the channel. The solutions to equations (3) and (4) whose right-hand sides are written in terms of Φ and A_z can be expressed through a zero-order modified Bessel function:

$$\Phi(r) = 4\pi\Delta^2(q_i n_{i0} - en_{e0})\left[1 - I_0\left(\frac{r}{\Delta}\right)\right], \tag{13}$$

$$A_z(r) = 4\pi c\Delta^2\left(\frac{q_i n_{i0}P_{i0}}{w_i} - \frac{en_{e0}P_{e0}}{w_e}\right)\left[1 - I_0\left(\frac{r}{\Delta}\right)\right]. \tag{14}$$

The scale on which the potentials vary in the radial direction is equal to the collisionless skin depth,

$$\Delta = \left(\frac{4\pi e^2 n_{e0}}{w_e} + \frac{4\pi q_i^2 n_{i0}}{w_i}\right)^{-1/2} = \left(\frac{1}{\Delta_e^2} + \frac{1}{\Delta_i^2}\right)^{-1/2}. \tag{15}$$

Knowing $\Phi(r)$ and $A_z(r)$, we can readily find radial profiles of the densities, fields, and currents. However, the results obtained are difficult to interpret unambiguously, because there are a large number of unknown quantities. The main task here is to minimize this ambiguity using such illustrative parameters as the channel radius, electric current, and mean particle density. For this purpose, we consider a cylindrical region of radius R inside the channel. Let us denote the current flowing in this region by I and the magnetic field at its boundary by H_0 ($H_0 = 2I(Rc)^{-1}$). We also introduce the dimensionless parameter

$$F = \frac{\Delta}{\Delta_e\Delta_i}\left(\frac{p_{ez}c}{eH_0} + \frac{p_{iz}c}{q_i H_0}\right). \tag{16}$$

With this notation, the radial profile of the magnetic field can be described in terms of the first-order modified Bessel function,

$$H(r) = H_0\frac{I_1\left(\frac{r}{\Delta}\right)}{I_1\left(\frac{R}{\Delta}\right)}, \tag{17}$$

and the electron and ion components of the resulting current $I = I_e + I_i$ can be written as

$$\begin{aligned} I_e &= \int_0^R j_e 2\pi r dr = I\frac{\Delta^2}{\Delta_e^2}\left(1 - \frac{R}{2\Delta}F\frac{\Delta_e}{\Delta_i}\right), \\ I_i &= \int_0^R j_i 2\pi r dr = I\frac{\Delta^2}{\Delta_i^2}\left(1 + \frac{R}{2\Delta}F\frac{\Delta_i}{\Delta_e}\right). \end{aligned} \tag{18}$$

Interestingly, at high particle densities such that $R(2\Delta)^{-1} \gg 1$, the current components depend strongly on the parameter F; moreover, one of the current components and the resulting current may have opposite signs. Let us estimate the range of possible F values based on the fact that, in the region close to the channel boundary, the radial component of the magnetic

Lorentz force is directed toward the axis. However, before proceeding further, note that the potential profiles (13) and (14) are valid only in the region occupied by the electrons and ions that pass through the channel axis, rather than over the entire cross section of the channel. The radius R of this region can be generally smaller than the channel radius, $R \le R_{ch}$, because the amplitude of electron oscillations in the radial direction can differ from the amplitude of ion oscillations. In a ring layer of thickness $\varepsilon = R_{ch} - R$, the potential profiles differ from (13) and (14); moreover, the ring layer can be occupied by either particles with the same charge or both electrons and ions. In the latter case, the particles of one species do not leave the ring layer, as is the case with the drift in crossed fields or with the gradient drift in a nonuniform magnetic field. If the surface ring layer is occupied by particles with the same charge, then the layer thickness ε can be estimated from the condition that the electric field is continuous. When Δ is small in comparison with R and the particle motion in a high-density plasma is nonrelativistic, we find

$$\frac{\varepsilon}{\Delta} \simeq \frac{e\Phi(r)}{\Delta^2 4\pi e^2 n_e} \simeq \frac{e\Phi(r)}{m_e c^2} \ll 1. \tag{19}$$

In this case, we can assume that the radial components of the electron and ion momenta become zero at the same distance from the axis. To obtain the boundary values of the axial momentum components

$$p_{ez} = -\frac{eH_0\Delta}{c}\left[\frac{I_0\left(\frac{r}{\Delta}\right)}{I_1\left(\frac{R}{\Delta}\right)} - F\frac{\Delta_e}{\Delta_i}\right],$$
$$p_{iz} = \frac{q_i H_0\Delta}{c}\left[\frac{I_0\left(\frac{r}{\Delta}\right)}{I_1\left(\frac{R}{\Delta}\right)} + F\frac{\Delta_i}{\Delta_e}\right], \tag{20}$$

which follow from (8) and (14), we can set $r = R$ for both electrons and ions. In the absence of a surface layer with an unneutralized charge ($\varepsilon = 0$), the magnetic components of the Lorentz force, F_e and F_i, at the channel boundary are equal in magnitude (but opposite in direction) to the inertial forces of the electrons and ions, respectively. Since the inertial forces are positive at the boundary, we have $F_e \le 0$ and $F_i \le 0$. In the presence of a surface ring layer ($\varepsilon \ne 0$), the sign of the magnetic components of the Lorentz force remains the same. At the outer boundary of the ring layer, the inertial force of one plasma species is equal in magnitude to the magnetic force, whereas, at the inner boundary, a positively directed electric force is added to the inertial force associated with another plasma species. If a plasma species is trapped only by a transverse electric field, then the magnetic component of the Lorentz force acting upon this species vanishes. As a result, we arrive at the conclusion that, in any case, F_e and F_i cannot be positive; in other words, at $r = R$, each of the expressions in square brackets in (20) is larger than or equal to zero, which allows us to determine the range of possible F values. Setting $r = R$ and taking into account the fact that at large arguments the ratio of the modified Bessel functions in (20) is close to unity, we obtain

$$-\Delta_e\Delta_i^{-1} \le F \le \Delta_i\Delta_e^{-1}. \tag{21}$$

Assuming that $en_{e0} = q_i n_{i0}$ and introducing the notation $w_e = m_e c^2$ and $w_i = m_i c^2$, we can represent the boundaries of the interval in (21) as $-\left(\frac{q_i m_e}{e m_i}\right)^{1/2} \le F \le \left(\frac{e m_i}{q_i m_e}\right)^{1/2}$. Expressions (20) and the approximate equality $\Delta \approx \Delta_e$ enable us to rewrite (16) as $F = (r_{ic} - r_{ec})\Delta_i^{-1}$, where r_{ic} and r_{ec} are gyroradii of the particles at the channel boundary. In the nonrelativistic case (when the particle densities near the channel boundary differ from those on the axis only slightly), expressions (20) make it possible to express the kinetic energy density of each particle species and the net kinetic energy density of the particles at the channel boundary through the magnetic energy density $H_0^2/8\pi$:

$$n_e\frac{p_e^2}{2m_e} = \frac{H_0^2}{8\pi}\frac{\Delta^2}{\Delta_e^2}\left(1 - F\frac{\Delta_e}{\Delta_i}\right)^2,$$
$$n_i\frac{p_i^2}{2m_i} = \frac{H_0^2}{8\pi}\frac{\Delta^2}{\Delta_i^2}\left(1 + F\frac{\Delta_i}{\Delta_e}\right)^2, \tag{22}$$

$$n_e\frac{p_e^2}{2m_e} + n_i\frac{p_i^2}{2m_i} = \frac{H_0^2}{8\pi}(1 + F^2). \tag{23}$$

For F lying within the interval in (21), the electron energy density decreases monotonically from its maximum (which is slightly above $H_0^2/8\pi$) at the left boundary to zero at the right boundary. On the other hand, the ion energy density increases monotonically from zero at the left boundary to a very high value (much higher than the magnetic energy density) because, at the right boundary, we have $F^2 \gg 1$.

3. DISCUSSION OF THE RESULTS

A characteristic feature of a two-species current flow is that it implies the existence of such current regimes in which the electron and ion current components, I_e and I_i, have opposite signs but each of them can be much higher than the resulting current in a channel. The current components depend on the parameter F; the range of its possible values can be estimated using a steady plasma model. In the range $F < 0$, the ion

contribution to the net current may be large and negative; however, the conditions under which such regimes can occur require that the plasma density be extremely high, $R(2\Delta)^{-1} \gg m_i m_e^{-1}$. Possible regimes with a large negative contribution of the electron species are more realistic: they can occur in the range $F > 0$ at moderately high plasma densities. The effect of a negative contribution of one plasma species to the net current is not associated with the radial electric field in a current-carrying plasma but stems from the fact that the influence of the magnetic field on the electrons differs from that on the ions when the electron and ion gyroradii are different. The formation of a thin current skin layer in a plasma channel makes this effect more pronounced.

For $F = 0$, the ion current component is independent of $R\Delta^{-1}$ and is as low as $m_e m_i^{-1}$. The net current in the channel is governed by the electron species: according to (20), the electron contribution $I = I_e = \frac{R}{2\Delta}\frac{m_e c^3 V_e}{e}\frac{V_e}{c}\gamma = \frac{R}{2\Delta} I_A$ substantially exceeds the Alfvén current I_A if $2\Delta \ll R$. At the channel boundary, the electron and ion gyroradii are equal to the collisionless skin depth, $p_e c(eH_0)^{-1} = p_i c(q_i H_0)^{-1} = \Delta$. In the nonrelativistic case, the magnetic energy density at the channel boundary is equal to the net density of the particle kinetic energies, which is governed mainly by the electron energy. In a channel with a thin skin layer, the electrons move predominantly across the channel axis and are slightly displaced in the axial direction every time they occur in the layer. The mean axial electron velocity V_z, which governs the electron current ($I_e = -en_e\pi R^2 V_z$), is low in comparison with the instantaneous velocity V_e, $V_z = 2\Delta R^{-1} V_e \ll V_e$. We illustrate these results quantitatively using as an example a channel filled with a fully ionized hydrogen ($e = q_i$) plasma with the current $I = 10^6$ A = 3×10^{15} esu/s, radius $R = 0.1$ cm, and density $n_e = 10^{19}$ cm^{-3}. In such a channel, we have $H_0 = 2 \times 10^6$ Oe and $R(2\Delta)^{-1} = 300$. The energy of the electrons is 1.6×10^{-8} erg = 10 keV and their instantaneous velocity is $V_e = 6 \times 10^9$ cm/s. The Alfvén current is $I_A = 3.4 \times 10^3$ A = 10^{13} esu/s and the mean axial electron velocity is $V_z = 2 \times 10^7$ cm/s.

For $F = 0$, the picture of currents is completely consistent with the results obtained by Hammer and Rostoker [4] and provides an understanding of how electrons with comparatively low energies can carry essentially unlimited currents in a plasma with no binary collisions. A similar picture can be observed, e.g., when the current rises rapidly in a narrow gas channel in vacuum[1]. In plasma channels with sufficiently small diameters, the force balance may be achieved almost without ions, because the electrons are rapidly heated over the entire cross section of the channel via high electron heat conduction, in which case the magnetic pressure of the current flowing in the channel is neutralized by the gas-kinetic electron pressure. If the plasma particles do not move in the radial direction, the ions remain immobile and cold until they are heated by ion–electron binary collisions or are involved in the current flows under the action of the fields. Let us consider a situation in which binary collisions are unimportant and the accelerating electric field in a plasma is driven by the current growing in the channel. The way in which the overall picture of currents changes depends on the rates at which the electric field accelerates electrons and ions. When the electrons are accelerated at a sufficiently high rate, the picture of currents remains essentially unchanged if the electron energy density increases synchronously with the magnetic energy density and the ion energy changes insignificantly, in which case, according to (22), the parameter F should be close to zero. In the opposite case, when the rate at which the electron energy density rises is low in comparison with $\partial/\partial t(H_0^2/8\pi)$, the ion energy content inevitably increases, because the current in the channel can grow only at the expense of the ions. The rate at which the electrons are accelerated can be estimated from the one-dimensional energy balance equation, which implies that

$$\pi R^2 n_e \frac{\partial}{\partial t}\frac{p_e^2}{2m_e} \le 2\pi R\frac{c}{4\pi} E H_0 \simeq 2\pi R\Delta\frac{\partial}{\partial t}\left(\frac{H_0^2}{8\pi}\right), \quad (24)$$

where the electric field is governed by the change in the magnetic flux in a current-carrying layer, $E \simeq \frac{\Delta}{c}\frac{\partial H_0}{\partial t}$. In this case, the accelerating field typical of high-temperature pinchlike plasma formations [1], which is usually generated in plasma constrictions and amounts to approximately $\dot{R} H_0/c$, is absent, because the channel boundary in the initial state is immobile. Equation (24) can now be recast into the form

$$\frac{\partial}{\partial t}\frac{p_e^2}{2m_e} \le \frac{2\Delta}{R}\frac{1}{n_e}\frac{\partial}{\partial t}\left(\frac{H_0^2}{8\pi}\right), \quad (25)$$

which implies that, for $2\Delta \ll R$, the electron energy in a channel with a growing current increases only very slightly. This is valid for a weak polarization charge separation such that the kinetic energy density of the electrons can be assumed to be uniform over the entire cross section of the channel. In the opposite case, when the polarization charge separation is strong, the kinetic energy density of the electrons is extremely nonuniform over the cross section of the channel, reaching a maximum at its boundary. Such a nonuniform energy distribution is attributed to a jump in the potential in the

[1] The method for creating dense gas channels several mm in diameter and plasma experiments with them will be described in a separate paper.

polarization layer: the electrons that cross this layer and move toward the channel boundary acquire additional energy. The potential of the polarization layer depends on $H_0^2/8\pi$, thereby ensuring that the kinetic energy density of the electrons increases synchronously with $H_0^2/8\pi$ as they approach the channel boundary. This situation is typical of plasma channels in which the ion pressure counterbalances a significant fraction of the magnetic pressure. Such a balance is possible either when the ion energy density is sufficiently high or when the ions are so massive that their inertia becomes important. In the cited experiments with narrow gas channels, the self-compression of a current-carrying plasma was achieved without the stage of plasma expansion in the radial direction, during which the ions might acquire significant energy. That is why, in those experiments, the ion energy in a self-compressed current-carrying plasma remained low in comparison with the electron energy over a certain time interval. Moreover, the ion energy content may, in principle, be made as low as possible by setting the diameter of the initial plasma channel almost to zero. These considerations are aimed at justifying the use of a zero ion energy approximation, under which formulas (24) and (25) were derived. Equation (25) implies that, for $2\Delta \ll R$, the kinetic energy density of the electrons cannot increase synchronously with $H_0^2/8\pi$. Consequently, the electron species alone clearly cannot ensure the rate at which the current should grow. This indicates that the ion contribution to the resulting current should also be taken into account; moreover, if the energy content in a circuit with a plasma channel is sufficiently high, the transition to a new current regime will have an insignificant impact on the rate at which the current grows. The ions can be accelerated near the anode by the electric field of the space charge in the form of a thin layer in which the electron density is reduced and which arises from insufficient electron mobility. Since the electrons move predominantly in the radial direction, the radial profile of the space charge across the layer is comparatively uniform: the radial scale characteristic of the space charge profile coincides with that of the radial current profile. The latter scale, in turn, can be on the order of the channel radius if the electron density n_e near the anode is sufficiently low. In order for the net current to be carried by the ions, the energy they acquire can be very low. Under the assumption that, e.g., the magnetic pressure $H_0^2/8\pi$ in a channel filled with a hydrogen plasma becomes higher than the kinetic energy density of the electrons by 1%, relationships (22) yield $F = 0.2$, in which case the ion energy is lower than the electron energy by a factor of 20. For the above parameters of the channel, for which we have $R(2\Delta)^{-1} = 300$, the ion current component, according to (18), exceeds the resulting current by a factor of 1.4 ($I_i = 1.4I$), and the electron contribution to the current is

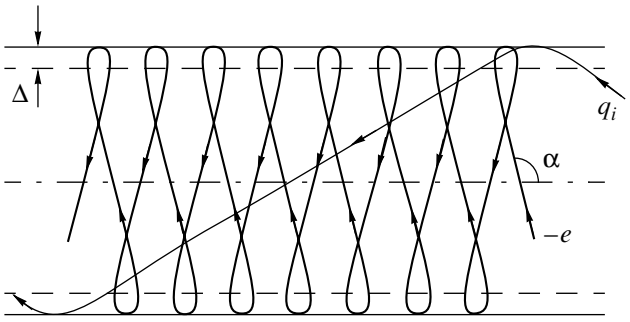

Electron and ion trajectories corresponding to a negative contribution of the electrons to the resulting current in the channel.

negative ($I_e = -0.4I$). Note that this is valid for ion energies as low as 500 eV. The figure shows electron and ion trajectories corresponding to a negative electron contribution to the resulting current in the channel. For small F, the change in the electron current component is attributed primarily to an increase in the angle α at which the electron trajectories cross the channel axis. If $\alpha = \pi/2$ at $F = 0$, then, at $F > 0$, we have $\alpha > \pi/2$. In a channel filled with a high-density plasma, even a slight increase in α from $\pi/2$ to $\alpha_1 > (\pi/2 + 2\Delta/R)$ is sufficient to cause the mean axial electron velocity to fall below zero and change sign. A negative contribution to the current comes from the electrons that are, on average, displaced along the channel in the direction opposite to that in the case $F = 0$ (see figure). In the intermediate case of closed electron trajectories, we have $I_e = 0$, which is achieved at $F = 2\Delta R^{-1}(m_i m_e^{-1})^{1/2}$. The larger the difference between the magnetic energy density and the electron kinetic energy density, the more significant the increase in the absolute values of the electron and ion contributions I_e and I_i. For example, if $H_0^2/8\pi$ becomes higher than the electron energy density by 5%, we obtain $F \approx 1$, which corresponds to $I_e = -6I$ and $I_i = 7I$. In this case, the ion kinetic energy density is approximately equal to the magnetic energy density.

Hence, taking into account the self-consistent motion of charged particles, the existence of collisionless plasma channels with overcritical currents can be attributed to the formation of thin current skin layers at their surfaces. In such channels, the electron species can easily change the direction of the mean axial velocity, making a negative contribution to the resulting current. This is clearly illustrated with the example of a growing current in a channel created without radial plasma implosion. The ion species ensures that the current grows, thereby neutralizing the negative contribution of the electrons. The resulting current flows in a thin surface layer; in the central region with zero current, the electrons and ions have the same axial velocity and form an electrically neutral axial stream whose direction coincides with the direction of the current in

the channel. This picture agrees with the known experimental data. The first experiments with a cylindrical Z-pinch [5] have already demonstrated the effect of the generation of accelerated deuterons, which was inferred from the anisotropy of neutron emission. In cylindrically asymmetric Z-pinches [1], a similar feature of high-current channels manifests itself in the axial motion of a plasma neutron source from the anode at a speed of 10^8 cm/s. The only disagreement between the results of magnetohydrodynamic calculations [6] and the experimental data is associated with this effect. It is natural to suppose that the current processes will possess the property under discussion regardless of the way in which the channels are created; however, under conditions typical of an imploding plasma, the dynamics of a transition to the regime in which the net current begins to be carried by the ions can have distinguishing features. Since the mechanism for the excitation of an axial plasma stream is kinetic in nature, the energy density of the directed plasma motion can be much higher than the magnetic field energy density in a high-current channel. A high-speed plasma stream can be generated without forming a structure typical of a plasma constriction.

4. CONCLUSION

We have studied self-consistent electron and ion motions in a high-current plasma channel using a steady-state kinetic plasma model in which the electrons and ions are regarded as particle beams moving in crossed fields, specifically, in an azimuthal magnetic field of the resulting current and a radial charge-separation electric field. We have shown that, in a channel filled with a high-density plasma, the electron and ion current components may have opposite signs and each of them may substantially exceed the resulting current. The ion species neutralizes the negative electron contribution to the current and, thus, carries the net current in the channel. The resulting current flows predominantly in a thin surface layer. In the central region, the electrons and ions move with the same axial velocities, forming an electrically neutral intense axial plasma stream, whose direction coincides with the direction of the resulting current in the channel. This picture is consistent with the high-speed axial plasma motion, which is observed in experiments with high-current plasmas and cannot be explained in the context of magnetohydrodynamics.

ACKNOWLEDGMENTS

I am grateful to L.P. Babich for supporting this work and to the participants of the Rukhadze seminar for discussing the results.

REFERENCES

1. V. A. Burtsev, V. A. Gribkov, and T. I. Filippova, Itogi Nauki Tekh., Ser.: Fiz. Plazmy **2**, 80 (1981).
2. G. Benford and D. L. Book, in *Advances in Plasma Physics*, Ed. by A. Simon and W. B. Thompson (Wiley, New York, 1969), Vol. 3.
3. R. C. Mjolsness, Phys. Fluids **6**, 1730 (1963).
4. D. A. Hammer and N. Rostoker, Phys. Fluids **13**, 1831 (1970).
5. L. A. Artsimovich, *Controlled Thermonuclear Reactions* (Fizmatgiz, Moscow, 1961; Gordon & Breach, New York, 1964).
6. D. E. Potter, Phys. Fluids **14**, 1911 (1971).

Translated by G. V. Shepekina

Plasma Physics Reports, Vol. 26, No. 2, 2000, pp. 139–146. Translated from Fizika Plazmy, Vol. 26, No. 2, 2000, pp. 153–160.

PLASMA INSTABILITY

Decay Instability of a Lower Hybrid Wave

D. I. Maslennikov*, V. S. Mikhaĭlenko*, and K. N. Stepanov**

**Kharkov State University, pl. Svobody 4, Kharkov, 310077 Ukraine*

***Kharkov Institute of Physics and Technology, National Science Center, Akademicheskaya ul. 1, Kharkov, 310108 Ukraine*

Received March 12, 1999; in final form, May 17, 1999

Abstract—A study is made of the decay instability of a lower hybrid wave with a finite wave vector ($\mathbf{k}_0 \neq 0$) and a large amplitude such that the oscillatory velocity of the electrons with respect to the ions cannot be neglected. It is shown that, depending on the angle between the propagation direction of the lower hybrid wave and the external magnetic field and the angle through which the wave is scattered, the decay instability is primarily governed either by the oscillatory electron motion with respect to the ions or by the nonlinear response of the plasma to the lower hybrid wave propagating in it. The role of the nonlinear frequency shift in the saturation of the lower hybrid decay instability is clarified. *© 2000 MAIK "Nauka/Interperiodica".*

1. INTRODUCTION

Parametric instabilities of plasma in the presence of lower hybrid waves have been studied for many years both experimentally and theoretically (see, e.g., [1–6]). Such processes as anomalous absorption of a lower hybrid pump wave in a plasma and anomalous plasma heating are attributed to the onset of parametric instabilities [7–9].

Lower hybrid parametric instabilities are studied theoretically by the following two approaches. The first approach (see, e.g., [10]), in which the nonlinear interaction of waves is assumed to be weak, applies to pump fields weak enough so that the velocity of the relative oscillations of the plasma components is negligible in comparison with their thermal velocities. In this case, the nonlinear response of the plasma to the lower hybrid wave propagating in it serves as a mechanism for the excitation of parametric instabilities. This approach was used to investigate the decay of a lower hybrid wave into two lower hybrid waves [11, 12], a lower hybrid wave and a quasi-mode [13, 14], etc.

In strong pump fields, there is an additional source of parametric instabilities—the relative oscillatory motion of the plasma components. In the case of weak pump fields, this source is neglected. Parametric instabilities that occur as a result of the relative oscillatory motion of the plasma components in strong pump fields are usually studied in the uniform pump field approximation ($\mathbf{k}_0 = 0$, where $\mathbf{k}_0$ is the wave vector of the pump wave). This approximation applies to kinetic parametric instabilities [15], decay instabilities involving quasi-modes [14], and the decay of a long-wavelength pump wave into two short-wavelength waves ($\mathbf{k}_1 + \mathbf{k}_2 = \mathbf{k}_0 \approx 0$) [16]. However, this approach cannot be used to study the decay of pump waves such that $|\mathbf{k}_1| \sim |\mathbf{k}_2| \sim |\mathbf{k}_0|$. The finite wavelength of a pump wave should be taken into account in investigating the decay processes that involve waves belonging to the same oscillation branch (e.g., the decay of a lower hybrid wave into two lower hybrid waves, the decay of an ion–ion hybrid wave into two ion–ion hybrid waves, etc.), because, in this case, the decay rate is proportional to k_0 and equals zero at $k_0 = 0$.

Here, the approach developed in our previous papers [17, 18], which generalizes the uniform pump wave approximation to the case of weakly nonuniform strong pump fields of finite wavelength ($\mathbf{k}_0 \neq 0$, but $k_0\xi \ll 1$, where ξ is the displacement of particles in the pump field), is used to investigate the decay of a lower hybrid wave into two lower hybrid waves. Section 2 is devoted to a comparative analysis of the following two mechanisms for the onset of instability: the oscillatory electron motion against the ion background and the nonlinear plasma response to the lower hybrid pump wave. In Section 3, the nonlinear frequency shift is investigated as a possible mechanism for the saturation of this decay instability.

2. BASIC EQUATIONS

Previously, we have shown [17] that, in the limit $\mathbf{k}_0\mathbf{R}_\alpha \ll 1$ of small displacements $\mathbf{R}_\alpha$ of particles of species α in a pump field $\mathbf{E}_0(\mathbf{r}, t) = \mathbf{E}_0\sin(\omega_0 t - \mathbf{k}_0\mathbf{r})$ and a constant magnetic field $\mathbf{B}_0$, the amplitudes $\varphi_1(\mathbf{k}, t)$ and $\varphi_2(\mathbf{k}_-)$ of the potential of the waves with frequencies $\omega_1(\mathbf{k})$ and $\omega_2(\mathbf{k}_\mp)$ ($\mathbf{k}_\mp = \mathbf{k} \mp \mathbf{k}_0$) into which the pump

1063-780X/00/2602-0139$20.00 © 2000 MAIK "Nauka/Interperiodica"

wave decays satisfy the set of equations

$$\begin{aligned} i\frac{\partial\varphi_1(\mathbf{k}, t)}{\partial t} + \beta_1\left(\frac{\partial\varepsilon(\mathbf{k}, \omega_1(\mathbf{k}))}{\partial\omega_1(\mathbf{k})}\right)^{-1}\varphi_2(\mathbf{k}_-, t) \\ = (\nu_1 + \nu_2)\varphi_1(\mathbf{k}, t), \\ i\frac{\partial\varphi_2(\mathbf{k}_-, t)}{\partial t} + \beta_2\left(\frac{\partial\varepsilon(\mathbf{k}_-, \omega_2(\mathbf{k}_-))}{\partial\omega_2(\mathbf{k}_-)}\right)^{-1}\varphi_1(\mathbf{k}, t) \\ = (\nu_3 + \nu_4)\varphi_2(\mathbf{k}_-, t). \end{aligned} \tag{1}$$

The frequencies $\omega_1(\mathbf{k})$ and $\omega_2(\mathbf{k}_-)$ of the waves into which the pump wave with $\omega_0(\mathbf{k}_0)$ decays obey the equation $\varepsilon(\mathbf{k}, \omega) = 1 + \delta\varepsilon_i(\mathbf{k}, \omega) + \delta\varepsilon_e(\mathbf{k}, \omega) = 0$, where $\delta\varepsilon_i$ and $\delta\varepsilon_e$ are the ion and electron contributions to the plasma permittivity $\varepsilon(\mathbf{k}, \omega)$. For long-wavelength ($k_\perp\rho_e \sim k_{0\perp}\rho_e \ll 1$, where ρ_e is the electron Larmor radius) oscillations with a phase velocity above the electron and ion thermal speeds, $\delta\varepsilon_i$ and $\delta\varepsilon_e$ have the form

$$\begin{aligned} \delta\varepsilon_e(\mathbf{k}, \omega) \approx \frac{k_\perp^2}{k^2}\frac{\omega_{pe}^2}{\omega_{ce}^2} - \frac{k_\parallel^2}{k^2}\frac{\omega_{pe}^2}{\omega^2}, \\ \delta\varepsilon_i(\mathbf{k}, \omega) \approx -\frac{\omega_{pi}^2}{\omega^2}, \end{aligned} \tag{2}$$

where $\omega_{pi(e)}$ is the ion (electron) plasma frequency, ω_{ce} is the electron cyclotron frequency, and $k_\parallel$ and $k_\perp$ are the components of the wave vector $\mathbf{k}$ along and across the magnetic field $\mathbf{B}_0$. For $k_\parallel^2 \ll k^2$, the equation $\varepsilon(\mathbf{k}, \omega) = 0$ yields

$$\omega^2(\mathbf{k}) = \omega_{lh}^2\left[1 + \frac{m_i}{m_e}\left(\frac{k_\parallel}{k}\right)^2\right], \tag{3}$$

where $\omega_{lh}^2 = \omega_{pi}^2/(1 + \omega_{pe}^2/\omega_{ce}^2)$.

In order for the lower hybrid pump wave with $\omega_0(\mathbf{k}_0)$ to decay into two lower hybrid waves, it is necessary that the condition $\omega_1(\mathbf{k}) = \omega_0(\mathbf{k}_0) + \omega_2(\mathbf{k}_-)$ be satisfied. With allowance for (3), this condition becomes

$$\begin{aligned} \left[1 + \frac{m_i}{m_e}\left(\frac{k_{\parallel 1}}{k_1}\right)^2\right]^{1/2} = \pm\left[1 + \frac{m_i}{m_e}\left(\frac{k_{\parallel 0}}{k_0}\right)^2\right]^{1/2} \\ \pm\left[1 + \frac{m_i}{m_e}\left(\frac{k_{\parallel -}}{k_-}\right)^2\right]^{1/2}. \end{aligned} \tag{4}$$

In order to satisfy (4), it is necessary that $(k_\parallel/k)^2(m_i/m_e) > 3$ [11]. We can see that, in the uniform pump field approximation ($k_0 = 0$), the decay condition (4) does not hold.

In (1), the parametric coupling coefficients β_1 and β_2 are expressed as

$$\begin{aligned} \beta_1 = \frac{1}{2}a_{ie}(\mathbf{k})e^{-i\delta_{ie}(\mathbf{k})}(\delta\varepsilon_i(\mathbf{k}_-, \omega_2(\mathbf{k}_-)) - \delta\varepsilon_i(\mathbf{k}, \omega_1(\mathbf{k}))) \\ - \sum_{\alpha = i, e} A_\alpha(\mathbf{k}_-, \omega_1(\mathbf{k}) - \omega_0(\mathbf{k}_0)), \\ \beta_2 = \frac{1}{2}a_{ie}(\mathbf{k}_-)e^{-i\delta_{ie}(\mathbf{k}_-)}(\delta\varepsilon_i(\mathbf{k}_-, \omega_2(\mathbf{k}_-)) \\ - \delta\varepsilon_i(\mathbf{k}, \omega_1(\mathbf{k}))) - \sum_{\alpha = i, e} A_\alpha(\mathbf{k}, \omega_1(\mathbf{k})), \end{aligned} \tag{5}$$

where the quantities δ_{ie} and $a_{ie} \sim kR_{ie}$ (with R_{ie} the displacement of the electrons with respect to the ions in the pump field) are described by the familiar expressions (see, e.g., [17, 18]). For a lower hybrid pump wave with a frequency $\omega_0 \ll \omega_{ce}$, they have the form

$$a_{ie} \sim \frac{k_\perp u}{\omega_0}, \quad \delta_{ie} \sim \frac{\omega_0}{\omega_{ce}} \ll 1, \tag{6}$$

where $u \sim cE_{0\perp}/B_0$. The terms that are proportional to the difference $\delta\varepsilon_i$ describe the onset of a decay instability due to the oscillatory motion of the electrons with respect to the ions in the pump-wave field. The lengthy expressions for the quantities A_α, which describe the excitation of a decay instability as a result of the nonlinear response of the plasma to the lower hybrid wave propagating in it, are presented in Appendix 1.

The nonlinear shifts of the oscillation frequencies due to weakly nonlinear interactions between the waves $(\mathbf{k}, \omega_1(\mathbf{k}))$ and $(\mathbf{k}_-, \omega_2(\mathbf{k}_-))$ and the other lower hybrid waves $(\mathbf{k}_1, \omega_1(\mathbf{k}_1))$ and $(\mathbf{k}_{1-}, \omega_2(\mathbf{k}_{1-}))$ into which the pump wave decays and due to the self-action of the waves are described by the coefficients ν_1, ν_2, ν_3, and ν_4 (see, e.g., [18]):

$$\begin{aligned} \nu_1 = \left(\frac{\partial\varepsilon(\mathbf{k}, \omega_1(\mathbf{k}))}{\partial\omega_1(\mathbf{k})}\right)^{-1} \\ \times \sum_{\alpha = i, e} U_\alpha(\mathbf{k}, \omega_1(\mathbf{k})|\mathbf{k} - \mathbf{k}_1, \omega_1(\mathbf{k}) - \omega_1(\mathbf{k}_1)| \\ - \mathbf{k}_1, -\omega_1(\mathbf{k}_1))|\varphi_1(\mathbf{k}_1)|^2, \\ \nu_2 = \left(\frac{\partial\varepsilon(\mathbf{k}, \omega_1(\mathbf{k}))}{\partial\omega_1(\mathbf{k})}\right)^{-1} \\ \times \sum_{\alpha = i, e} U_\alpha(\mathbf{k}, \omega_1(\mathbf{k})|\mathbf{k} - \mathbf{k}_{1-}, \omega_1(\mathbf{k}) - \omega_2(\mathbf{k}_{1-})| \\ - \mathbf{k}_{1-}, -\omega_2(\mathbf{k}_{1-}))|\varphi_2(\mathbf{k}_1 - \mathbf{k}_0)|^2, \\ \nu_3 = \left(\frac{\partial\varepsilon(\mathbf{k}_-, \omega_2(\mathbf{k}_-))}{\partial\omega_2(\mathbf{k}_-)}\right)^{-1} \\ \times \sum_{\alpha = i, e} U_\alpha(\mathbf{k}_-, \omega_2(\mathbf{k}_-)|\mathbf{k}_- - \mathbf{k}_1, \omega_2(\mathbf{k}_-) - \omega_1(\mathbf{k}_1)| \end{aligned} \tag{7}$$

$$-\mathbf{k}_1, -\omega_1(\mathbf{k}_1))|\varphi_1(\mathbf{k}_1)|^2,$$

$$\nu_4 = \left(\frac{\partial\varepsilon(\mathbf{k}_-, \omega_2(\mathbf{k}_-))}{\partial\omega_2(\mathbf{k}_-)}\right)^{-1}$$

$$\times \sum_{\alpha = i, e} U_\alpha(\mathbf{k}_-, \omega_2(\mathbf{k}_-)|\mathbf{k}_- - \mathbf{k}_{1-}, \omega_2(\mathbf{k}_-) - \omega_2(\mathbf{k}_{1-})|$$

$$-\mathbf{k}_{1-}, -\omega_2(\mathbf{k}_{1-}))|\varphi_2(\mathbf{k}_1 - \mathbf{k}_0)|^2.$$

The lengthy expressions for the matrix elements U_α and their long-wavelength ($k_\perp\rho_\alpha \ll 1$) asymptotics are presented in Appendix 2.

In the nonlinear stage, we can set $\nu_i = 0$ ($i = 1, 2, 3, 4$), in which case equations (1) yield the growth rate of the decay instability (see also [17, 18]):

$$\gamma \approx \gamma_0 \equiv \left[-\beta_1\beta_2\left(\frac{\partial\varepsilon(\mathbf{k}, \omega_1(\mathbf{k}))}{\partial\omega_1(\mathbf{k})}\frac{\partial\varepsilon(\mathbf{k}_-, \omega_2(\mathbf{k}_-))}{\partial\omega_2(\mathbf{k}_-)}\right)^{-1}\right]^{1/2}. \quad (8)$$

The nonlinear frequency shift can be regarded as a possible mechanism for the saturation of the decay instability. The relevant saturation level is [17, 18]

$$|\nu_1 + \nu_2 - \nu_3 - \nu_4| = 2\gamma_0. \quad (9)$$

3. LINEAR THEORY OF THE DECAY OF A LOWER HYBRID PUMP WAVE OF FINITE WAVELENGTH INTO TWO LOWER HYBRID WAVES

Since the entire analysis of the problem is rather involved, we restrict ourselves to investigating the mechanism underlying the resonant decay of a lower hybrid wave into two lower hybrid waves with $k \sim k_0 \sim k_-$ only in the important case of a dense plasma ($\omega_{pe} \gg \omega_{ce}$). Since the case of a rarefied plasma ($\omega_{pe} \ll \omega_{ce}$) can be examined in a similar manner, we will not analyze it here. Let us estimate the terms in the parametric coupling coefficients β_1 and β_2 using the asymptotic expressions (A1.7)–(A1.9). The relationship

$$a_{ie}[\delta_i\varepsilon(\mathbf{k}_-, \omega_2(\mathbf{k}_-)) - \delta_i\varepsilon(\mathbf{k}, \omega_1(\mathbf{k}))]$$

$$\approx \frac{e}{m_e}\frac{k_\perp E_{0\perp}}{\omega_0^2}\frac{\omega_0}{\omega_{ce}}\frac{\omega_{pi}^2}{\omega_{ce}^2}\left(\frac{k^2}{k_\parallel^2} - \frac{k_-^2}{k_{\parallel-}^2}\right), \quad (10)$$

and formulas (10) and (A1.9) give

$$\frac{a_{ie}\delta\varepsilon_i}{A_i} \sim \frac{k}{k_\parallel} \gg 1,$$

i.e., the ion contribution A_i to β_1 and β_2 is negligibly small.

Now, we estimate the relative contributions of A_e and $a_{ie}\delta\varepsilon_i$ to β_1 and β_2. For the wave vectors $\mathbf{k}$, $\mathbf{k}_0$, and $\mathbf{k}_-$ satisfying the condition

$$|\sin(\theta - \theta_0)| \sim |\sin(\theta - \theta_-)| \gg \frac{\omega}{\omega_{ce}} \sim \frac{k_\parallel}{k} \sim \frac{k_{\parallel 0}}{k_0}, \quad (11)$$

we obtain from (10), (A1.5), and (A1.6)

$$\frac{A_e}{a_{ie}\delta\varepsilon_i} \sim \frac{m_i}{m_e}\frac{k_\parallel}{k}\sin^2(\theta - \theta_0). \quad (12)$$

This expression implies that, in the range of angles $\theta - \theta_0$ and $\theta - \theta_-$ such that

$$\frac{\omega}{\omega_{ce}} \sim \frac{k_\parallel}{k} < |\sin(\theta - \theta_-)| \sim |\sin(\theta - \theta_0)| < \left(\frac{m_e}{m_i}\frac{k}{k_\parallel}\right)^{1/2}, \quad (13)$$

lower hybrid waves are excited mainly due to the oscillatory electron motion against the background of essentially immobile ions. In this case, we have

$$\beta_1 \sim \beta_2 \sim a_{ie}[\delta\varepsilon_i(\mathbf{k}_-, \omega_2(\mathbf{k}_-)) - \delta\varepsilon_i(\mathbf{k}, \omega_1(\mathbf{k}))], \quad (14)$$

so that, according to (8), the decay instability can occur only for waves that propagate in opposite directions. The instability growth rate $\gamma(k)$ is equal in order of magnitude to

$$\gamma \sim a_{ie}\frac{m_e}{m_i}\frac{k}{k_\parallel}\omega_{ce} \sim ku\frac{m_e}{m_i}\left(\frac{k}{k_\parallel}\right)^2. \quad (15)$$

Note that the condition $\omega_{ci} \ll \gamma \ll \omega_1 \sim \omega_0$ holds when

$$\frac{k_\parallel}{k} \ll a_{ie} \ll \frac{m_i}{m_e}\left(\frac{k_\parallel}{k}\right)^2. \quad (16)$$

In the range of angles $(\theta - \theta_0)$ satisfying (11) and the inequality

$$|\sin(\theta - \theta_0)| \sim |\sin(\theta - \theta_-)| > \left(\frac{m_e}{m_i}\frac{k}{k_\parallel}\right)^{1/2}, \quad (17)$$

the primary mechanism for the onset of the decay instability is the nonlinear response of the plasma to the lower hybrid pump wave propagating in it. In this case, we have

$$\beta_1 \sim A_e(\mathbf{k}_-, \omega_1(\mathbf{k}) - \omega_0), \quad \beta_2 \sim A_e(\mathbf{k}, \omega_1(\mathbf{k})), \quad (18)$$

and the instability growth rate is equal in order of magnitude to

$$\gamma \sim a_{ie}\omega_{ce}\sin^2(\theta - \theta_0). \quad (19)$$

According to estimates (A1.5) and (A1.6), lower hybrid waves with $\omega_1(\mathbf{k})$ and $\omega_2(\mathbf{k}_-)$ propagating in opposite directions are unstable, so that we have $k_\parallel k_{\parallel-} < 0$. In this case, the condition $\omega_{ci} \ll \gamma \ll \omega_1 \sim \omega_0$ is satisfied when

$$\frac{m_e}{m_i} \ll a_{ie}\sin^2(\theta - \theta_-) \ll \frac{k_\parallel}{k}. \quad (20)$$

In the range of scattering angles for a lower hybrid pump wave such that

$$|\sin(\theta-\theta_-)| \sim |\sin(\theta-\theta_0)| \ll \frac{\omega}{\omega_{ce}} \sim \frac{k_\parallel}{k}, \qquad (21)$$

relationships (10), (A1.7), and (A1.8) yield the estimate

$$\frac{A_e}{a_{ie}\delta\varepsilon_i} \sim \frac{m_i}{m_e}\left(\frac{k_\parallel}{k}\right)^3, \qquad (22)$$

which implies that, for $(k_\parallel/k) > (m_e/m_i)^{1/3}$, the primary mechanism for the onset of a decay instability is the nonlinear electron response to the lower hybrid wave propagating in the plasma. In this case, we have

$$\beta_1 \sim A_e(\mathbf{k}_-, \omega_1(\mathbf{k})-\omega_0), \quad \beta_2 \sim A_e(\mathbf{k}, \omega_1(\mathbf{k})), \quad (23)$$

and the instability growth rate is estimated as

$$\gamma \sim a_{ie}\frac{\omega_1(\mathbf{k})}{\omega_{ce}}\omega_1(\mathbf{k}) \ll \omega_1(\mathbf{k}). \qquad (24)$$

For $(k_\parallel/k) < (m_e/m_i)^{1/3}$, the main mechanism for the decay instability is the oscillatory electron motion against the ion background in the field of the lower hybrid pump wave, in which case the coefficients β_1 and β_2 are described by (14) and the growth rate $\gamma(k)$ is described by (15).

4. EFFECT OF THE NONLINEAR FREQUENCY SHIFT ON THE NONLINEAR EVOLUTION OF THE DECAY INSTABILITY OF A LOWER HYBRID WAVE

Now, we analyze whether the nonlinear frequency shift of the waves involved in the decay process can serve as a mechanisms for saturating the decay of a lower hybrid pump wave into two lower hybrid waves. From (9), we obtain the following condition, which should be valid in the saturation stage of the decay instability:

$$\gamma \sim \frac{1}{k^2\lambda_{De}^2}\frac{e^2}{T_e^2}(k_\perp\rho_e)^6\left(\frac{\omega_{ce}}{\omega}\right)^2\frac{k^2}{k_\parallel^2}\frac{\omega^3}{\omega_{pe}^2}|\varphi^2|, \qquad (25)$$

where φ is the larger of the amplitudes φ_1 and φ_2 of the lower hybrid decay waves. This allows us to obtain the wave energy density $W = (1/4\pi)k^2|\varphi|^2\omega(\partial\varepsilon/\partial\omega)$ at the saturation stage:

$$W \sim \frac{\gamma}{\omega}\left(\frac{k_\parallel}{k}\right)^2\frac{1}{(k_\perp\rho_e)^2}n_{0e}T_e. \qquad (26)$$

Let us consider relationship (26) for the decay mechanisms examined in Section 2. When the decay instability is driven by the oscillatory motion of the electrons with respect to the ions, the instability growth rate is estimated as (15) and the instability due to the nonlinear frequency shift is likely to be saturated at a level close to

$$\frac{W}{n_{0e}T_e} \sim \frac{m_e}{m_i}\frac{a_{ie}}{(k_\perp\rho_e)^2} \sim \frac{m_e}{m_i}\frac{k}{k_\parallel}\frac{u}{v_{Te}}\frac{1}{k_\perp\rho_e}, \qquad (27)$$

where v_{Te} is the electron thermal velocity.

The energy density W_0 of the electron oscillations in the pump-wave field is equal in order of magnitude to

$$W_0 \sim \frac{n_{0e}m_e u^2}{2} \sim \frac{n_{0e}m_e(cE_{0\perp})^2}{B_0^2}. \qquad (28)$$

If the energy density (26) of the unstable waves is low in comparison with W_0, then the pump wave amplitude can be assumed to be constant throughout the nonlinear stage and the inverse action of unstable oscillations on the pump field may be neglected. For the saturation level (27), this condition is satisfied when

$$\frac{u}{v_{Te}} \gg \frac{m_e}{m_i}\frac{k}{k_\parallel}\frac{1}{k_\perp\rho_e}. \qquad (29)$$

Under conditions (11) and (17), the decay instability with the growth rate (19) is driven primarily by the nonlinear response of the electron component to the lower hybrid pump wave propagating in the plasma. In this case, the nonlinear frequency shift causes the decay instability to saturate at the level

$$\frac{W}{n_{0e}T_e} \sim \frac{k_\parallel}{k}\frac{a_{ie}}{(k_\perp\rho_e)^2}\sin^2(\theta-\theta_0) > \frac{m_e}{m_i}\frac{a_{ie}}{(k_\perp\rho_e)^2}. \qquad (30)$$

For the saturation level (30), the condition $W \ll W_0$ is satisfied when

$$\frac{m_e}{m_i}\frac{k}{k_\parallel}\frac{1}{k_\perp\rho_e} \ll \frac{1}{k_\perp\rho_e}\sin^2(\theta-\theta_0) \ll \frac{u}{v_{Te}}. \qquad (31)$$

Under the conditions $(k_\parallel/k) > (m_e/m_i)^{1/3}$ and (21), the nonlinear electron response to the pump wave serves as the main mechanism for the onset of the decay instability with the growth rate (24). The instability is saturated at the level

$$\frac{W}{n_{0e}T_e} \sim \left(\frac{k_\parallel}{k}\right)^3\frac{a_{ie}}{(k_\perp\rho_e)^2}. \qquad (32)$$

For this level, the condition $W \ll W_0$ is satisfied when

$$\frac{m_e}{m_i}\frac{k}{k_\parallel}\frac{1}{k_\perp\rho_e} \ll \left(\frac{k_\parallel}{k}\right)^2\frac{1}{k_\perp\rho_e} < \frac{u}{v_{Te}}, \qquad (33)$$

i.e., when

$$u > 3v_{Te}\frac{m_e}{m_i}\frac{1}{k_\perp\rho_e}. \qquad (34)$$

5. CONCLUSION

We have constructed a linear theory of the decay of a lower hybrid pump wave into two lower hybrid waves with comparable wavelengths $|\mathbf{k}_0| \sim |\mathbf{k}| \sim |\mathbf{k} - \mathbf{k}_0|$. We have shown that, in addition to the nonlinear collective plasma response to the lower hybrid pump wave, there is another important mechanism for the onset of a decay instability—the oscillatory electron motion against the ion background in the field of a lower hybrid pump wave with finite wavelength ($\mathbf{k}_0 \neq 0$). We have obtained the parametric coupling coefficients and the instability growth rates for $|\mathbf{k}_0| \sim |\mathbf{k}|$ and have determined the parameter ranges in which a particular mechanism for the onset of a decay instability dominates.

We have clarified the role of the nonlinear frequency shift in the saturation of the lower hybrid decay instability. We have shown that the decay instability can be saturated by the nonlinear frequency shift if the oscillatory electron velocity satisfies condition (34).

In addition to the lower hybrid decay instability, another instability may arise in the plasma—the decay of a lower hybrid wave into a lower hybrid wave and a kinetic electron quasi-mode [14]. The growth rate of this instability is [14]

$$\gamma_{qm} \sim \omega_0 \frac{u^2}{v_s^2} \frac{m_e}{8m_i} \left(\frac{k}{k_\parallel}\right)^2, \tag{35}$$

where v_s is the speed of sound.

From (15) and (35), we obtain

$$\frac{\gamma_{decay}}{\gamma_{qm}} \sim \frac{ku}{8\omega_0} \left(\frac{v_s}{u}\right)^2 \sim a_{ie} \left(\frac{v_s}{u}\right)^2, \tag{36}$$

i.e., which of the instabilities (the decay of the pump wave into two lower hybrid waves or its decay into a lower hybrid wave and an electron quasi-mode) develops more rapidly depends on the particular experimental conditions. However, the effect of these decay instabilities on one another is insignificant, because they develop in different ranges of wave vectors of unstable oscillations: $|\omega(\mathbf{k}) - \omega_0| \gg k_\parallel v_{Te}$ corresponds to the resonant decay under discussion, and $|\omega(\mathbf{k}) - \omega_0| \sim k_\parallel v_{Te}$ corresponds to the decay involving a quasi-mode. In particular, the growth rate and the saturation level (26) of the decay instability involving two lower hybrid decay waves are insensitive to electron heating. Hence, in real experiments, these two decay instabilities may occur simultaneously.

ACKNOWLEDGMENTS

This work was supported in part by the Center for Science and Technology in Ukraine, project no. 253.

APPENDIX 1

PARAMETRIC COUPLING COEFFICIENTS A_α

The coefficients A_α are defined as

$$\begin{aligned} &\frac{4\pi e_\alpha}{k^2} \int d^3\mathbf{v}_\alpha g_\alpha^{(1)}(\mathbf{k}, \omega, \mathbf{v}_\alpha) \\ &= A_\alpha(\mathbf{k}_-, \omega - \omega_0)\varphi_\alpha(\mathbf{k}_-, \omega - \omega_0) \\ &+ A_\alpha(\mathbf{k}_+, \omega + \omega_0)\varphi_\alpha(\mathbf{k}_+, \omega + \omega_0), \end{aligned} \tag{A1.1}$$

where $g_\alpha^{(1)}$ is the particle velocity in the frame of reference associated with the particles of species α. The quantity $\mathbf{v}_\alpha$, which is proportional to the small parameter $k_0 R_\alpha \ll 1$, represents the correction to the Fourier transform of the perturbation $g_\alpha^{(0)}(\mathbf{k}, \omega, \mathbf{v}_\alpha)$ of the velocity distribution function $F_{0\alpha}$ caused by natural plasma waves (the Fourier transformation is carried out in the accompanying frame).

In the case of a Maxwellian electron velocity distribution, the coefficient $A_e(\mathbf{k}_-, \omega - \omega_0)$ for waves with frequencies $\omega(\mathbf{k}) \sim \omega_0 \gg k_\parallel v_{Te}$ is

$$\begin{aligned} A_e(\mathbf{k}_-, \omega - \omega_0) &= \frac{4\pi}{k^2} \frac{e^3}{m_e^2} \sum_{p=-\infty}^{\infty} \sum_{s=-\infty}^{\infty} \int_0^\infty dv_{e\perp} \int_{-\infty}^{\infty} dv_{ez} \\ &\times \frac{F_{0e}(v_{e\perp}, v_{ez})}{v_{Te}^2} \frac{e^{ip(\theta_- - \theta) + is(\theta_0 - \theta)}}{\omega - (p+s)\omega_{ce}} \left\{ \frac{k_{\parallel -} v_{ez} + p\omega_{ce}}{\omega - \omega_0 - p\omega_{ce}} \right. \\ &\times J_p\left(\frac{k_{-\perp} v_{e\perp}}{\omega_{ce}}\right) \left[-\frac{1}{2}\left(\frac{k_{\parallel 0} E_{\parallel 0}}{\omega_0} + \frac{\omega_0 k_{0\perp} E_{0\perp}}{\omega_0^2 - \omega_{ce}^2}\right) J_{p+s}\left(\frac{k_\perp v_{e\perp}}{\omega_{ce}}\right) \right. \\ &\times J_s\left(\frac{k_{0\perp} v_{e\perp}}{\omega_{ce}}\right) - \frac{1}{2}(k_{\parallel 0} v_{e\parallel} + s\omega_{ce}) \\ &\times \left(\frac{k_{\parallel -} E_{0\parallel}}{\omega_0^2} + \frac{k_{\parallel} E_{0\parallel}}{\omega_0(\omega - (p+s)\omega_{ce})} - \frac{k_{0\perp} E_{0\perp}}{\omega_0^2 - \omega_{ce}^2} \right. \\ &+ i\frac{k_\perp E_{0\perp}}{\omega_0 \omega_{ce}} \sin(\theta - \theta_0) \Big) J_{p+s}\left(\frac{k_\perp v_{e\perp}}{\omega_{ce}}\right) J_s\left(\frac{k_{0\perp} v_{e\perp}}{\omega_{ce}}\right) \\ &+ \frac{1}{4} \frac{(k_{\parallel 0} v_{e\parallel} + (s+1)\omega_{ce}) k_\perp E_{0\perp}}{\omega_{ce}(\omega_0 + \omega_{ce})} J_{s+1}\left(\frac{k_{0\perp} v_{e\perp}}{\omega_{ce}}\right) \\ &\times J_{p+s+1}\left(\frac{k_\perp v_{e\perp}}{\omega_{ce}}\right) - \frac{1}{4} \frac{(k_{\parallel 0} v_{e\parallel} + (s-1)\omega_{ce}) k_\perp E_{0\perp}}{\omega_{ce}(\omega_0 - \omega_{ce})} \\ &\times \left. J_{s-1}\left(\frac{k_{0\perp} v_{e\perp}}{\omega_{ce}}\right) J_{p+s-1}\left(\frac{k_\perp v_{e\perp}}{\omega_{ce}}\right) \right] - \frac{1}{2} \frac{1}{\omega_0 - s\omega_{ce}} \\ &\times \left[\frac{k_{\parallel 0} v_{e\parallel} + s\omega_{ce}}{\omega_0} E_{0\parallel} v_{e\parallel} J_s\left(\frac{k_{0\perp} v_{e\perp}}{\omega_{ce}}\right) \right. \end{aligned} \tag{A1.2}$$

$$+\frac{1}{2}\frac{k_{0\|}v_{e\|}+(s-1)\omega_{ce}}{\omega_0-\omega_{ce}}E_{0\perp}v_{e\perp}J_{s-1}\left(\frac{k_{0\perp}v_{e\perp}}{\omega_{ce}}\right)$$

$$+\frac{1}{2}\frac{k_{\|0}v_{e\|}+(s+1)\omega_{ce}}{\omega_0+\omega_{ce}}E_{0\perp}v_{e\perp}J_{s+1}\left(\frac{k_{0\perp}v_{e\perp}}{\omega_{ce}}\right)\Bigg]$$

$$\times\Bigg[-\frac{k_\|k_{\|-}}{\omega-(p+s)\omega_{ce}}J_{p+s}\left(\frac{k_\perp v_{e\perp}}{\omega_{ce}}\right)J_p\left(\frac{k_{-\perp}v_{e\perp}}{\omega_{ce}}\right)$$

$$+\frac{k_\perp k_{-\perp}}{2\omega_{ce}}\Bigg(2i\sin(\theta-\theta_-)J_{p+s}\left(\frac{k_\perp v_{e\perp}}{\omega_{ce}}\right)J_p\left(\frac{k_{-\perp}v_{e\perp}}{\omega_{ce}}\right)$$

$$-J_{p+s+1}\left(\frac{k_\perp v_{e\perp}}{\omega_{ce}}\right)J_{p+1}\left(\frac{k_{-\perp}v_{e\perp}}{\omega_{ce}}\right)$$

$$+J_{p+s-1}\left(\frac{k_\perp v_{e\perp}}{\omega_{ce}}\right)J_{p-1}\left(\frac{k_{-\perp}v_{e\perp}}{\omega_{ce}}\right)\Bigg)\Bigg]\Bigg\}.$$

For the decay of lower hybrid waves under consideration, the frequencies ω_0, $\omega_1(\mathbf{k})$, and $\omega_2(\mathbf{k}_-)$ and the growth rate $\gamma(\mathbf{k})$ (8) of the decay instability are all higher than the ion cyclotron frequency. Consequently, the ions are unmagnetized and, in the case of a Maxwellian ion velocity distribution function F_{0i}, the coefficient $A_i(\mathbf{k}_-, \omega-\omega_0)$ for waves with frequencies $\omega_0 \sim \omega \gg kv_{Ti}$ is

$$A_i(\mathbf{k}_-,\omega-\omega_0)\approx-\frac{2\pi}{k^2}\frac{e^3}{m_i^2}\int d^3\mathbf{v}_i\frac{F_{0i}(\mathbf{v}_i)}{v_{Ti}^2}\frac{(\mathbf{k}_0\cdot\mathbf{v}_i)}{\omega\omega_0} \tag{A1.3}$$
$$\times\left\{\frac{(\mathbf{E}_0\cdot\mathbf{v}_i)}{2\omega_0}\frac{(\mathbf{k}\cdot\mathbf{k}_-)}{\omega}+\frac{(\mathbf{k}_-\cdot\mathbf{v}_i)}{\omega-\omega_0}\left[\frac{(\mathbf{k}_-\cdot\mathbf{E}_0)}{\omega_0}+\frac{(\mathbf{k}\cdot\mathbf{E}_0)}{\omega}\right]\right\}.$$

The coefficients $A_\alpha(\mathbf{k}_+, \omega+\omega_0)$ can be obtained from (A1.2) and (A1.3) through the changes $k_{-\perp} \longrightarrow k_{+\perp}$, $k_{-\|} \longrightarrow k_{+\|}$, $\theta_- \longrightarrow \theta_+$, $\omega-\omega_0 \longrightarrow \omega+\omega_0$. The coefficients $A_\alpha(\mathbf{k}, \omega)$ can be found from $A_\alpha(\mathbf{k}_+, \omega+\omega_0)$ through the changes $\mathbf{k}_+ \longrightarrow \mathbf{k}$, $\mathbf{k} \longrightarrow \mathbf{k}_-$, $\omega+\omega_0 \longrightarrow \omega$, and $\omega \longrightarrow \omega-\omega_0$.

We consider the limiting case of long-wavelength ($k_\perp\rho_e \ll 1$, $k_{0\perp}\rho_e \ll 1$) low-frequency lower hybrid waves with

$$\omega_1(\mathbf{k})\approx\omega_{ce}\frac{k_\|}{k},\quad \omega_0(\mathbf{k}_0)\approx\omega_{ce}\frac{k_{\|0}}{k_0},$$
$$\omega_2(\mathbf{k}_-)\approx\omega_{ce}\frac{k_{\|-}}{k_-}, \tag{A1.4}$$

in a dense plasma ($\omega_{pe} \gg \omega_{ce}$). In this case, under conditions $1 \gg k_\|/k \gg (m_e/m_i)^{1/2}$ and (11), relationship (A1.2) yields the asymptotics

$$A_e(\mathbf{k}_-,\omega-\omega_0)$$
$$\approx-\frac{e}{2m_e}\frac{\omega_{pe}^2}{\omega_{ce}^2}\frac{k_{0\perp}^2k_{-\perp}E_{0\perp}}{k^2\omega_1(\mathbf{k})\omega_0(\mathbf{k}_0)}\sin^2(\theta_--\theta), \tag{A1.5}$$

$$A_e(\mathbf{k},\omega)$$
$$\approx\frac{e}{2m_e}\frac{\omega_{pe}^2}{\omega_{ce}^2}\frac{k_\perp^2k_{0\perp}E_{0\perp}}{k_-^2(\omega-\omega_0)\omega_0(\mathbf{k}_0)}\sin^2(\theta_0-\theta). \tag{A1.6}$$

If the propagation angles of the waves with $\omega_1(\mathbf{k})$ and $\omega_2(\mathbf{k}_-)$ satisfy the condition $|\sin(\theta-\theta_-)| \sim |\sin(\theta-\theta_0)| \ll \omega/\omega_{ce}$, then we have

$$A_e(\mathbf{k}_-,\omega-\omega_0)\approx\frac{e}{2m_e}\frac{\omega_{pe}^2}{k^2}\Bigg\{\frac{k_{0\perp}k_{-\perp}}{\omega_{ce}^2}\Bigg[-\frac{k_{\|0}E_{0\|}}{\omega\omega_0}$$
$$\times\cos(\theta_--\theta_0)-\frac{k_{\|-}}{k_{-\perp}}\frac{k_\|E_{0\perp}}{\omega^2}$$
$$+\frac{\omega-\omega_0}{\omega}\left(\frac{k_{\|-}E_{0\|}}{\omega_0^2}+\frac{k_\|E_{0\|}}{\omega\omega_0}\right)\cos(\theta_--\theta_0)\Bigg]+\frac{k_{0\perp}k_{-\perp}}{\omega_{ce}^4}$$
$$\times E_{0\perp}\Bigg(k_{0\perp}\cos(\theta_--\theta_0)-\frac{1}{2}k_\perp(\cos(\theta+\theta_- \tag{A1.7}$$
$$-2\theta_0)+\cos(\theta-\theta_-))\Bigg)-\frac{k_{\|0}k_{\|-}}{\omega(\omega-\omega_0)}$$
$$\times\left(\frac{k_{\|-}E_{0\|}}{\omega_0^2}+\frac{k_\|E_{0\|}}{\omega\omega_0}+\frac{k_{0\perp}E_{0\perp}}{\omega_{ce}^2}\right)$$
$$+\frac{k_{\|0}E_{0\|}}{\omega_0^2}\left(\frac{k_\|k_{\|-}}{\omega^2}+\frac{k_\perp k_{-\perp}}{\omega_{ce}^2}\cos(\theta-\theta_-)\right)\Bigg\},$$

$$A_e(\mathbf{k},\omega)\approx\frac{e}{2m_e}\frac{\omega_{pe}^2}{k_-^2}\Bigg\{\frac{k_\perp k_{0\perp}E_{0\perp}}{\omega_{ce}^4}\Bigg(-k_{0\perp}\cos(\theta_0-\theta)$$
$$-\frac{1}{2}k_{-\perp}(\cos(\theta-\theta_-)+\cos(\theta+\theta_--2\theta_0))\Bigg)$$
$$-\frac{k_{0\perp}k_\perp}{\omega_{ce}^2}\Bigg[\left(\frac{k_{\|0}E_{0\|}}{\omega_0(\omega-\omega_0)}+\frac{k_{\|-}\omega E_{0\|}}{\omega_0(\omega-\omega_0)^2}-\frac{k_\|E_{0\|}}{\omega_0^2}\frac{\omega}{\omega-\omega_0}\right)$$
$$\times\cos(\theta_0-\theta)+\frac{k_\|}{k_\perp}\frac{k_{\|-}E_{0\perp}}{(\omega-\omega_0)^2}\Bigg] \tag{A1.8}$$
$$-\frac{k_{\|0}k_{\|-}}{\omega(\omega-\omega_0)}\left(\frac{k_{\|-}E_{0\|}}{\omega_0^2}+\frac{k_\|E_{0\|}}{\omega\omega_0}+\frac{k_{0\perp}E_{0\perp}}{\omega_{ce}^2}\right)$$

$$+\frac{k_{\|0}E_{0\|}}{\omega_0^2}\left(\frac{k_\| k_{\|-}}{\omega^2}+\frac{k_\perp k_{-\perp}}{\omega_{ce}^2}\cos(\theta-\theta_-)\right)\Bigg\}.$$

For $(k_\|/k)^2 \sim (\omega/\omega_{ce})^2$, all terms in (A1.7) and (A1.8) are of the same order. From (A1.3), we obtain the estimate

$$A_i(\mathbf{k},\omega)\sim A_i(\mathbf{k}_-,\omega-\omega_0)$$
$$\approx \frac{e_i}{m_i}\frac{k_{-\perp}E_{0\perp}}{\omega_0^2}\frac{\omega_{pi}^2}{\omega(\omega-\omega_0)}\frac{k_{0\perp}k_{-\perp}}{k^2}. \quad \text{(A1.9)}$$

APPENDIX 2

MATRIX ELEMENTS U_α AND THEIR LONG-WAVELENGTH ASYMPTOTICS

The matrix elements U_α are defined as

$$U_\alpha(\mathbf{k},\omega|\mathbf{k}_3+\mathbf{k}_4,\omega_3+\omega_4|\mathbf{k}_4,\omega_4)$$
$$=\frac{1}{3}w_\alpha(\mathbf{k},\omega|\mathbf{k}_3+\mathbf{k}_4,\omega_3+\omega_4|\mathbf{k}_4,\omega_4)$$
$$+\frac{1}{3}w_\alpha(\mathbf{k},\omega|\mathbf{k}_1+\mathbf{k}_3,\omega_1+\omega_3|\mathbf{k}_1,\omega_1) \quad \text{(A2.1)}$$
$$+\frac{1}{3}w_\alpha(\mathbf{k},\omega|\mathbf{k}_1+\mathbf{k}_4,\omega_1+\omega_4|\mathbf{k}_4,\omega_4),$$

where the terms w_α have the form

$$w_\alpha(\mathbf{k},\omega|\mathbf{k}_3+\mathbf{k}_4,\omega_3+\omega_4|\mathbf{k}_4,\omega_4)$$
$$=\frac{1}{2}W_\alpha(\mathbf{k},\omega|\mathbf{k}_3+\mathbf{k}_4,\omega_3+\omega_4|\mathbf{k}_4,\omega_4)$$
$$+\frac{1}{2}W_\alpha(\mathbf{k},\omega|\mathbf{k}_3+\mathbf{k}_4,\omega_3+\omega_4|\mathbf{k}_3,\omega_3),$$
$$w_\alpha(\mathbf{k},\omega|\mathbf{k}_3+\mathbf{k}_1,\omega_3+\omega_1|\mathbf{k}_1,\omega_1)$$
$$=\frac{1}{2}W_\alpha(\mathbf{k},\omega|\mathbf{k}_3+\mathbf{k}_1,\omega_3+\omega_1|\mathbf{k}_1,\omega_1)$$
$$+\frac{1}{2}W_\alpha(\mathbf{k},\omega|\mathbf{k}_3+\mathbf{k}_1,\omega_3+\omega_1|\mathbf{k}_3,\omega_3),$$
$$w_\alpha(\mathbf{k},\omega|\mathbf{k}_1+\mathbf{k}_4,\omega_1+\omega_4|\mathbf{k}_4,\omega_4)$$
$$=\frac{1}{2}W_\alpha(\mathbf{k},\omega|\mathbf{k}_1+\mathbf{k}_4,\omega_1+\omega_4|\mathbf{k}_4,\omega_4)$$
$$+\frac{1}{2}W_\alpha(\mathbf{k},\omega|\mathbf{k}_1+\mathbf{k}_4,\omega_1+\omega_4|\mathbf{k}_1,\omega_1).$$

For a Maxwellian electron distribution, the matrix element $W_e(\mathbf{k},\omega|\mathbf{k}_2,\omega_2|\mathbf{k}_4,\omega_4)$ with $\mathbf{k}_2=\mathbf{k}_3+\mathbf{k}_4$ and $\omega_2=\omega_3+\omega_4$ is

$$W_e(\mathbf{k},\omega|\mathbf{k}_2,\omega_2|\mathbf{k}_4,\omega_4)=-\frac{4\pi}{k^2v_{Te}^2}\frac{e^4}{m_e^3}$$
$$\sum_{m=-\infty}^{\infty}\sum_{p=-\infty}^{\infty}\sum_{l=-\infty}^{\infty}\int_{-\infty}^{\infty}dv_{e\|}\int_0^\infty dv_{e\perp}v_{e\perp}$$
$$\times\frac{F_{0e}(v_{e\perp},v_{e\|})}{\omega_2-k_{\|2}v_{e\|}-(m+p)\omega_{ce}}$$
$$\times\Bigg\{-\frac{k_\| k_{\|1}J_l\left(\frac{k_{1\perp}v_{e\perp}}{\omega_{ce}}\right)J_{m+p+l}\left(\frac{k_\perp v_{e\perp}}{\omega_{ce}}\right)}{(\omega-k_\| v_{e\|}-(m+p+l)\omega_{ce})^2}+\frac{k_\perp k_{1\perp}}{2\omega_{ce}}$$
$$\times\frac{1}{\omega-k_\| v_{e\|}-(m+p+l)\omega_{ce}}\Bigg[J_{m+p+l+1}\left(\frac{k_\perp v_{e\perp}}{\omega_{ce}}\right)$$
$$\times J_{l+1}\left(\frac{k_{1\perp}v_{e\perp}}{\omega_{ce}}\right)-J_{m+p+l-1}\left(\frac{k_\perp v_{e\perp}}{\omega_{ce}}\right)J_{l-1}\left(\frac{k_{1\perp}v_{e\perp}}{\omega_{ce}}\right)$$
$$+2i\sin(\theta_1-\theta)J_l\left(\frac{k_{1\perp}v_{e\perp}}{\omega_{ce}}\right)J_{m+p+l}\left(\frac{k_\perp v_{e\perp}}{\omega_{ce}}\right)\Bigg]\Bigg\} \quad \text{(A2.2)}$$
$$\times\Bigg\{-\frac{k_{\|4}k_{\|3}\omega_4J_m\left(\frac{k_{3\perp}v_{e\perp}}{\omega_{ce}}\right)J_p\left(\frac{k_{4\perp}v_{e\perp}}{\omega_{ce}}\right)}{(\omega_4-k_{\|4}v_{e\|}-p\omega_{ce})^2}$$
$$+\frac{k_{\|4}v_{e\|}+p\omega_{ce}}{\omega_4-k_{\|4}v_{e\|}-p\omega_{ce}}\Bigg[\frac{k_{\|3}v_{e\|}+m\omega_{ce}}{v_{Te}^2}J_m\left(\frac{k_{3\perp}v_{e\perp}}{\omega_{ce}}\right)$$
$$\times J_p\left(\frac{k_{4\perp}v_{e\perp}}{\omega_{ce}}\right)+\frac{k_{3\perp}k_{4\perp}}{2\omega_{ce}}\left(J_{m-1}\left(\frac{k_{3\perp}v_{e\perp}}{\omega_{ce}}\right)J_{p+1}\left(\frac{k_{4\perp}v_{e\perp}}{\omega_{ce}}\right)\right.$$
$$\left.-J_{m+1}\left(\frac{k_{3\perp}v_{e\perp}}{\omega_{ce}}\right)J_{p-1}\left(\frac{k_{4\perp}v_{e\perp}}{\omega_{ce}}\right)-2i\sin(\theta_3-\theta_4)\right)$$
$$\times J_m\left(\frac{k_{3\perp}v_{e\perp}}{\omega_{ce}}\right)J_p\left(\frac{k_{4\perp}v_{e\perp}}{\omega_{ce}}\right)\Bigg)\Bigg]\Bigg\}e^{im(\theta_3-\theta)}e^{ip(\theta_4-\theta)}e^{il(\theta_1-\theta)}.$$

For low-frequency ($\omega \ll \omega_{ce}$) long-wavelength ($k_\perp\rho_e \ll 1$) waves, relationship (A2.2) yields the asymptotic

$$W_e(\mathbf{k},\omega|\mathbf{k}_2,\omega_2|\mathbf{k}_4,\omega_4)$$
$$\approx\frac{1}{k^2\lambda_{De}^2}\frac{e^2}{T_e^2}k_\perp\rho_e k_{1\perp}\rho_e k_{3\perp}\rho_e k_{4\perp}\rho_e\frac{\omega_{ce}^2}{\omega\omega_2} \quad \text{(A2.3)}$$
$$\times\sin(\theta-\theta_1)\sin(\theta_3-\theta_4)\frac{k_{\|4}v_{Te}^2}{\omega_4}\left(\frac{k_{\|2}}{\omega_2}+\frac{k_\|}{\omega}+\frac{k_{\|4}}{\omega_4}\right).$$

Note that, for the decay under consideration, the contribution of the ions,

$$W_i(\mathbf{k}, \omega|\mathbf{k}_2, \omega_2|\mathbf{k}_4, \omega_4) \approx \frac{1}{k^2\lambda_{Di}^2}\frac{e_i^2}{m_i^2}\frac{v_{Ti}^2(\mathbf{k}\cdot\mathbf{k}_2)}{\omega_2\omega_4\omega^2}$$

$$\times\left\{2k^4\frac{(\mathbf{k}\cdot\mathbf{k}_3)}{\omega\omega_4} + k_4^2\frac{(\mathbf{k}_2\cdot\mathbf{k}_3)}{\omega_2\omega_4} + 6\frac{(\mathbf{k}\cdot\mathbf{k}_3)(\mathbf{k}\cdot\mathbf{k}_4)}{\omega^2}\right.$$

$$\left. + 2\frac{(\mathbf{k}\cdot\mathbf{k}_3)(\mathbf{k}_2\cdot\mathbf{k}_4)}{\omega\omega_2} + 2\frac{(\mathbf{k}\cdot\mathbf{k}_4)(\mathbf{k}_2\cdot\mathbf{k}_3)}{\omega\omega_2}\right\},$$

turns out to be small, $\frac{W_i}{W_e} \sim \frac{m_e}{m_i} \ll 1$.

REFERENCES

1. M. Porkolab and R. P. H. Chang, Rev. Mod. Phys. **50**, 745 (1978).
2. M. Porkolab, Nucl. Fusion **18**, 367 (1978).
3. V. E. Golant and V. I. Fedorov, *High-Frequency Methods of Plasma Heating in Toroidal Devices* (Énergoatomizdat, Moscow, 1986).
4. V. A. Budnikov, Nucl. Fusion **31**, 611 (1991).
5. V. A. Budnikov and M. A. Irzak, Plasma Phys. Controlled Fusion **38**, 135 (1996).
6. E. Z. Gusakov, N. M. Kaganskaya, M. V. L'vov, *et al.*, Fiz. Plazmy **24**, 266 (1998) [Plasma Phys. Rep. **24**, 237 (1998)].
7. V. F. Tarasenko, A. B. Kitsenko, V. I. Panchenko, *et al.*, Zh. Tekh. Fiz. **42**, 1996 (1972) [Sov. Phys. Tech. Phys. **17**, 1599 (1972)].
8. A. B. Kitsenko, V. I. Panchenko, K. N. Stepanov, *et al.*, Nucl. Fusion **13**, 557 (1973).
9. M. Porkolab, S. Bernabei, W. M. Hooke, *et al.*, Phys. Rev. Lett. **38**, 230 (1977).
10. R. Z. Sagdeev and A. A. Galeev, in *Reviews of Plasma Physics*, Ed. by M. A. Leontovich (Atomizdat, Moscow, 1973; Consultants Bureau, New York, 1979), Vol. 7.
11. E. Ott, Phys. Fluids **18**, 566 (1975).
12. A. Reiman, Phys. Fluids **23**, 1254 (1980).
13. A. B. Kitsenko, V. I. Panchenko, and K. N. Stepanov, Plasma Phys. **16**, 1109 (1974).
14. M. Porkolab, Phys. Fluids **17**, 1432 (1974).
15. A. B. Kitsenko, V. I. Panchenko, and K. N. Stepanov, Zh. Tekh. Fiz. **43**, 1426 (1973) [Sov. Phys. Tech. Phys. **18**, 905 (1973)].
16. A. B. Kitsenko, V. I. Panchenko, and K. N. Stepanov, Zh. Tekh. Fiz. **43**, 1437 (1973) [Sov. Phys. Tech. Phys. **18**, 911 (1973)].
17. D. I. Maslennikov, V. S. Mikhaĭlenko, and K. N. Stepanov, Fiz. Plazmy **21**, 791 (1995) [Plasma Phys. Rep. **21**, 749 (1995)].
18. D. I. Maslennikov, V. S. Mikhaĭlenko, and K. N. Stepanov, Fiz. Plazmy **23**, 1088 (1997) [Plasma Phys. Rep. **23**, 1007 (1997)].

Translated by I. A. Kalabalyk

Plasma Physics Reports, Vol. 26, No. 2, 2000, pp. 147–151. Translated from Fizika Plazmy, Vol. 26, No. 2, 2000, pp. 161–165.

PLASMA TURBULENCE

Polarization of Electromagnetic Radiation at the Second Harmonic of the Electron Gyrofrequency in a Turbulent Plasma

V. V. Tirskiĭ*, V. G. Ledenev, and V. M. Tomozov****

**Institute of Laser Physics, Irkutsk Branch, Siberian Division, Russian Academy of Sciences, Irkutsk, Russia*
***Institute of Solar and Terrestrial Physics, Siberian Division, Russian Academy of Sciences, Irkutsk, 664033 Russia*
Received April 30, 1999

Abstract—A study is made of the polarization of electromagnetic radiation at the second harmonic of the electron gyrofrequency. The radiation is emitted by a highly ionized collisionless plasma in which the turbulence is excited at electron gyrofrequencies in a strong magnetic field. The mechanism for the generation of electromagnetic waves during mergings of the gyrofrequency plasmons is analyzed. It is shown that, even in a strong magnetic field, the degree of circular polarization of electromagnetic radiation at the second harmonic of the electron gyrofrequency may be moderate or weak. © *2000 MAIK "Nauka/Interperiodica".*

1. INTRODUCTION

A highly ionized collisionless plasma in a strong magnetic field ($\omega_{He} \gg \omega_{pe}$, where ω_{He} is the electron gyrofrequency and ω_{pe} is the electron Langmuir frequency) is encountered in laboratory experiments (in beam–plasma devices, magnetic confinement systems, etc. [1]) and in space (e.g., in the solar corona [2]). It is well known that an electron beam propagating in such a plasma generates electromagnetic radiation at the harmonics of the electron gyrofrequency ω_{He} [3].

The data from measurements of the intensity and polarization of electromagnetic radiation at the second harmonic of the electron gyrofrequency are often used to determine the plasma parameters and the magnitude of the magnetic field. Tsytovich and Kaplan [4] showed that electromagnetic radiation at the second harmonic of the gyrofrequency can also be driven by the mechanisms associated exclusively with plasma processes.

For example, an electron beam propagating in a highly ionized collisionless plasma in a strong magnetic field (along the magnetic field lines) can efficiently excite gyrofrequency plasmons (h). Two plasmons can merge into one ($h + h \longrightarrow t$), thereby generating electromagnetic radiation at the second harmonic of ω_{He} [5].

This merging process can compete with the generation of electromagnetic radiation at the second harmonic of ω_{He} directly by an electron beam [3]. It is also well known that the degree of circular polarization of electromagnetic radiation generated directly by an electron beam at the second harmonic of ω_{He} is close to 100% [6]. In this connection, it is of interest to investigate the polarization of electromagnetic radiation generated via the merging process $h + h \longrightarrow t$. This question is the subject of our paper.

2. GENERATION OF POLARIZED ELECTROMAGNETIC RADIATION VIA THE MERGING OF GYROFREQUENCY PLASMONS

The method for deriving equations that describe the merging of plasmons, $h + h \longrightarrow t$, was presented by Tsytovich [5]. However, he did not obtain equations for the polarization characteristics (the Stokes parameters) of electromagnetic radiation generated during the merging process. Below, we will derive these equations.

We will investigate the problem using the following assumptions: the plasma ions are unmagnetized, $(\omega_{pe}/\omega_{He})^2 \ll 1$, the spectral function $W_{\mathbf{k}_1}$ of the gyrofrequency turbulence is isotropic (this assumption was justified in [5]), and the phase velocities v_{ph} of the gyrofrequency plasmons are much lower than the speed of light c in vacuum (i.e., $(v_{ph}/c)^3 \ll 1$).

The assumption $(\omega_{pe}/\omega_{He})^2 \ll 1$ allows us to describe the process $h + h \longrightarrow t$ by the equation [5]

$$\frac{d}{dt}I_{\mathbf{k},ij} = \frac{\partial}{\partial t}I_{\mathbf{k},ij} + \left(\mathbf{v}_g\frac{\partial}{\partial \mathbf{r}}\right)I_{\mathbf{k},ij} = \left.\frac{4(2\pi)^3\omega^2 R_{\kappa,ij}}{\left(\frac{\partial}{\partial\omega}(\omega^2\varepsilon^t_\kappa)\right)^2}\right|_{\omega=\omega_{\mathbf{k}}}, \quad (1)$$

where $\mathbf{v}_g$ is the group velocity of electromagnetic radiation at the frequency $2\omega_{He}$, $\omega_{\mathbf{k}} = kc$, k is the wavenumber, ω is the angular frequency of the radiation, and $\kappa = \{\mathbf{k}, \omega\}$. In equation (1), the vector and tensor components are written in the laboratory frame X^h, Y^h, and

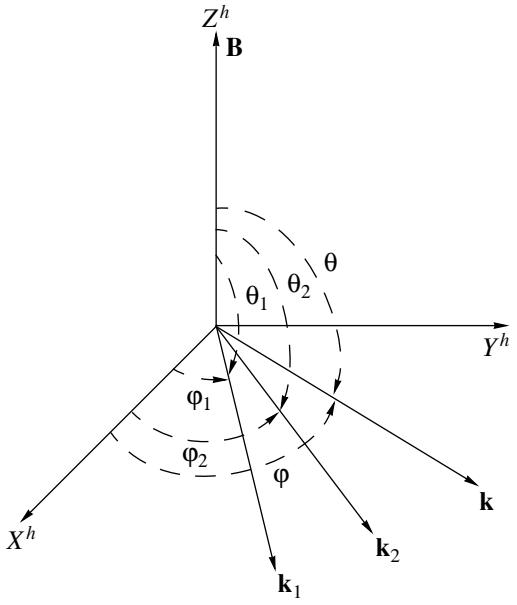

Fig. 1. Working coordinate system.

Z^h (Fig. 1). To simplify the analysis of the matrices $I_{\mathbf{k},ij}$ describing electromagnetic radiation, it is convenient to pass over to the so-called intrinsic frame of reference [7] with the help of the transition matrix $M_{ij}\{\mathbf{h}, \mathbf{n}\}$, where **h** and **n** are unit vectors (Fig. 1). Taking the product of the left- and right-hand sides of (1) with $M_{i\alpha}$ and $M_{j\beta}$, we obtain the equation

$$\frac{d}{dt}I_{\mathbf{k},\alpha\beta} = \left.\frac{4(2\pi)^3\omega^2 M_{i\alpha}R_{\kappa,ij}M_{j\beta}}{\left(\frac{\partial}{\partial\omega}(\omega^2\varepsilon^t_\kappa)\right)^2}\right|_{\omega=\omega_{\mathbf{k}}}. \quad (2)$$

Now, we switch from the matrices $I_{\mathbf{k},\alpha\beta}$ to the Stokes parameters using the standard relationships

$$I_{\mathbf{k}} = I_{\mathbf{k},xx} + I_{\mathbf{k},yy}, \quad Q_{\mathbf{k}} = I_{\mathbf{k},xx} - I_{\mathbf{k},yy},$$
$$U_{\mathbf{k}} = I_{\mathbf{k},xy} + I_{\mathbf{k},yx}, \quad V_{\mathbf{k}} = -i(I_{\mathbf{k},xy} - I_{\mathbf{k},yx}), \quad (3)$$

where $I_{\mathbf{k}}$ is the radiation intensity in units of J/m^2 s and $Q_{\mathbf{k}}$, $U_{\mathbf{k}}$, and $V_{\mathbf{k}}$ are the Stokes parameters expressed in the corresponding units. From here, we obtain

$$\frac{d}{dt}I_{\mathbf{k}} = \frac{4(2\pi)^3\omega^2}{\left(\frac{\partial}{\partial\omega}(\omega^2\varepsilon^t_\kappa)\right)^2}[M_{ix}R_{\kappa,ij}M_{jx} + M_{iy}R_{\kappa,ij}M_{jy}]|_{\omega=\omega_{\mathbf{k}}}, \quad (4)$$

$$\frac{d}{dt}Q_{\mathbf{k}} = \frac{4(2\pi)^3\omega^2}{\left(\frac{\partial}{\partial\omega}(\omega^2\varepsilon^t_\kappa)\right)^2}[M_{ix}R_{\kappa,ij}M_{jx} - M_{iy}R_{\kappa,ij}M_{jy}]|_{\omega=\omega_{\mathbf{k}}}, \quad (5)$$

$$\frac{d}{dt}U_{\mathbf{k}} = \frac{4(2\pi)^3\omega^2}{\left(\frac{\partial}{\partial\omega}(\omega^2\varepsilon^t_\kappa)\right)^2}[M_{ix}R_{\kappa,ij}M_{jy} + M_{iy}R_{\kappa,ij}M_{jx}]|_{\omega=\omega_{\mathbf{k}}}, \quad (6)$$

$$\frac{d}{dt}V_{\mathbf{k}} = \frac{4(2\pi)^3\omega^2 i}{\left(\frac{\partial}{\partial\omega}(\omega^2\varepsilon^t_\kappa)\right)^2}[M_{iy}R_{\kappa,ij}M_{jx} - M_{ix}R_{\kappa,ij}M_{jy}]|_{\omega=\omega_{\mathbf{k}}}. \quad (7)$$

To evaluate the right-hand sides of (4)–(7), we need to know explicit expressions for both the matrices $R_{\kappa,ij}$ and the dielectric function ε^t_κ for electromagnetic waves. For radiation emitted at the frequency $\omega = 2\omega_{He}$, we have $\varepsilon^t_\kappa \approx 1 - (\omega_{He}/\omega)^2$. According to [5], the matrix $R_{\kappa,ij}$ for the process $h + h \longrightarrow t$ has the form

$$R_{\kappa,ij} = \int d\kappa_1 d\kappa_2 \delta(\kappa - \kappa_1 - \kappa_2)\lambda_i(\kappa, \kappa_1, \kappa_2) \times \lambda_j^*(\kappa, \kappa_1, \kappa_2) I^{\sigma_1}_{\kappa_1} I^{\sigma_2}_{\kappa_2}. \quad (8)$$

Here, $\kappa\{\mathbf{k}, \omega\}$, $\kappa_1\{\mathbf{k}_1, \omega_1\}$, and $\kappa_2\{\mathbf{k}_2, \omega_2\}$ are the four-dimensional wave vectors characterizing electromagnetic radiation and the first and second gyrofrequency plasmons, respectively; $\mathbf{k}_1$ and $\mathbf{k}_2$ are the wave vectors of the gyrofrequency plasmons; and ω_1 and ω_2 are their angular frequencies. The function $I^{\sigma_1}_{\kappa_1}$, which characterizes gyrofrequency plasmons, can be written as

$$I^{\sigma_1}_{\kappa_1} = \frac{\left|\omega^{\sigma_1}_{\mathbf{k}_1}\right| W^{\sigma_1}_{\mathbf{k}_1}\delta(\omega_1 - \left|\omega^{\sigma_1}_{\mathbf{k}_1}\right|)}{2\pi^2\frac{\partial}{\partial\omega_1}(\omega_1^2\varepsilon^{\sigma_1}_{\mathrm{Re},\kappa_1})\Big|_{\omega_1=\left|\omega^{\sigma_2}_{\mathbf{k}_1}\right|}}. \quad (9)$$

Here, the spectral function of the gyrofrequency plasmons, $W^{\sigma_1}_{\mathbf{k}_1}$, is related to their energy density W^σ by

$$\int W^{\sigma_1}_{\mathbf{k}_1}\frac{d\mathbf{k}_1}{(2\pi)^3} = W^\sigma, \quad (10)$$

and $\varepsilon^{\sigma_1}_{\mathrm{Re},\kappa_1}$ is the real part of the dielectric function for the gyrofrequency plasmons [5],

$$\varepsilon^\sigma_{\mathrm{Re},\kappa_1} = \varepsilon_{ij,\kappa_1}e^\sigma_{\mathbf{k}_1,i}e^{\sigma*}_{\mathbf{k}_1,j} + \frac{c^2}{\omega_1^2}(\mathbf{k}_1\mathbf{e}^\sigma_{\mathbf{k}_1})(\mathbf{k}_1\mathbf{e}^{\sigma*}_{\mathbf{k}_1}), \quad (11)$$

where $\varepsilon_{ij,\kappa_1}$ is the plasma dielectric tensor and $e^\sigma_{\mathbf{k}_1,i}$ are the components of the unit polarization vector of the electric field of a gyrofrequency plasmon. For

$(\omega_{pe}/\omega_{He})^2 \ll 1$, the real part of the dielectric function for a gyrofrequency plasmon has the form [5]

$$\varepsilon^{\sigma}_{\mathrm{Re},\,\kappa_1} \approx 1 - \frac{\omega_{pe}^2 \sin^2\theta_1}{\omega_1^2 - \omega_{He}^2} + \frac{k_1^2 c^2}{\omega_1^2}, \tag{12}$$

where θ_1 is the angle between the magnetic induction vector and the unit polarization vector of the electric field of a gyrofrequency plasmon. An expression for $\omega^{\sigma_1}_{\mathbf{k}_1}$ can be obtained from the equation [5]

$$\varepsilon^{\sigma_1}_{\mathrm{Re},\,\kappa_1} - \frac{k_1^2 c^2}{\omega_1^2} = 0. \tag{13}$$

Substituting $\varepsilon^{\sigma_1}_{\mathrm{Re},\,\kappa_1}$ from (12) into (13) yields the following expression for $\left|\omega^{\sigma_1}_{\mathbf{k}_1}\right|^2$:

$$\omega_1^2 = \left|\omega^{\sigma_1}_{\mathbf{k}_1}\right|^2 = \omega_{He}^2 + \omega_{pe}^2 \sin^2\theta_1. \tag{14}$$

The quantities $\lambda_i(\kappa, \kappa_1, \kappa_2)$ have the form [5]

$$\lambda(\kappa, \kappa_1, \kappa_2) = 2\tilde{S}_{mjl}(\kappa, \kappa_1, \kappa_2) e^{\sigma_1}_{\mathbf{k}_1,\,j} e^{\sigma_2}_{\mathbf{k}_2,\,l} \left(\delta_{im} - \frac{k_i k_m}{k^2}\right), \tag{15}$$

where

$$\tilde{S}_{mjl}(\kappa, \kappa_1, \kappa_2) = \frac{1}{2}\{S_{mjl}(\kappa, \kappa_1, \kappa_2) + S_{mlj}(\kappa, \kappa_2, \kappa_1)\}. \tag{16}$$

The components of the nonlinear conductivity tensor S_{mjl} of a plasma in a magnetic field are [5]

$$S_{xnm}(\kappa, \kappa_1, \kappa_2) = \frac{e}{4\pi m_e \omega} \frac{[\delta_{xn} + i(\omega_{He}/\omega)\delta_{yn}]}{1 - (\omega_{He}/\omega)^2} \times \{k_{2s}[\varepsilon^{\sigma}_{sm}(\mathbf{k}_2, \omega_2) - \delta_{sm}]\}, \tag{17}$$

$$S_{ynm}(\kappa, \kappa_1, \kappa_2) = \frac{e}{4\pi m_e \omega} \frac{[\delta_{yn} - i(\omega_{He}/\omega)\delta_{xn}]}{1 - (\omega_{He}/\omega)^2} \times \{k_{2s}[\varepsilon^{\sigma}_{sm}(\mathbf{k}_2, \omega_2) - \delta_{sm}]\}, \tag{18}$$

$$S_{znm}(\kappa, \kappa_1, \kappa_2) = \frac{e}{4\pi m_e \omega} \times \delta_{zn}\{k_{2s}[\varepsilon^{\sigma}_{sm}(\mathbf{k}_2, \omega_2) - \delta_{sm}]\}, \tag{19}$$

where m_e is the mass of an electron. The integrand in expression (8) for $R_{\kappa,\,ij}$ is a complicated function of the wave vectors $\mathbf{k}$, $\mathbf{k}_1$, and $\mathbf{k}_2$ and the frequencies ω, ω_1, and ω_2 (the indices s, n, and m run through the coordinates x, y, and z).

The momentum and energy conservation laws for the waves in the merging process $h + h \longrightarrow t$ give

$$\mathbf{k} = k\mathbf{n} = 2\frac{\omega_{He}}{c}\mathbf{n} = \mathbf{k}_1 + \mathbf{k}_2 = k_1\mathbf{n}_1 + k_2\mathbf{n}_2 = \frac{\omega_{He}}{v_{ph1}}\mathbf{n}_1 + \frac{\omega_{He}}{v_{ph2}}\mathbf{n}_2, \tag{20}$$

where v_{ph1} and v_{ph2} are the phase velocities of gyrofrequency plasmons. Assuming that $k < k_1$ and $k < k_2$ yields $v_{ph1} < c$ and $v_{ph2} < c$ in accordance with (20). We expand the integrand in expression (8) for the matrix $R_{\kappa,\,ij}$ in powers of the small parameters k/k_1 and k/k_2, neglect terms proportional to $(k/k_1)^3$ and $(k/k_2)^3$, and integrate the resulting expression over $d\mathbf{k}_1$, $d\mathbf{k}_2$, $d\omega_1$ and $d\omega_2$ to arrive at a simpler representation for the matrix $R_{\kappa,\,ij}$. We assume that the spectral function $W_{\mathbf{k}_1}$ is isotropic and substitute this representation for $R_{\kappa,\,ij}$, the explicit expression for the matrix M_{ij} taken from [7], and expression (12) for the function $\varepsilon^{t}_{\mathrm{Re},\,\kappa}$ into equations (4)–(7). As a result, we obtain the following equations for the Stokes parameters:

$$\frac{d}{dt}I_{\mathbf{k}} = \frac{\omega_{pe}^6}{18\pi\omega_{He}^4 m_e c^2 n_e}\left\{\frac{16}{63}\sin^2\theta + \frac{38}{105}\sin^2\theta\cos^2\theta + \frac{64}{63}\right\}\int W^2_{\mathbf{k}_1} k_1^2 dk_1 \delta(\omega_{\mathbf{k}} - 2\omega_{He}), \tag{21}$$

$$\frac{d}{dt}Q_{\mathbf{k}} = \frac{\omega_{pe}^2}{18\pi\omega_{He}^4 m_e c^2 n_e}\left\{\frac{256}{315}\sin^2\theta - \frac{38}{105}\sin\theta\cos^2\theta\right\}\int W^2_{\mathbf{k}_1} k_1^2 dk_1 \delta(\omega_{\mathbf{k}} - 2\omega_{He}), \tag{22}$$

$$\frac{d}{dt}V_{\mathbf{k}} = \frac{\omega_{pe}^6}{18\pi\omega_{He}^4 m_e c^2 n_e}\left\{\frac{56}{105}\cos\theta\sin^2\theta + \frac{256}{315}\cos\theta\right\}\int W^2_{\mathbf{k}_1} k_1^2 dk_1 \delta(\omega_{\mathbf{k}} - 2\omega_{He}), \tag{23}$$

$$\frac{d}{dt}U_{\mathbf{k}} = 0. \tag{24}$$

Here, $dI_{\mathbf{k}}/dt$ is the power of the emitted electromagnetic radiation; $I_{\mathbf{k}}$, $Q_{\mathbf{k}}$, and $V_{\mathbf{k}}$ are expressed in J; and n_e is the electron plasma density. Multiplying the left- and right-hand sides of (21)–(24) by $4\pi\omega^2/c^2$ and integrating the resulting equations over $d\omega$ from 0 to ∞ yields the following equations for the radiation intensity I (in units of J/m^2 s) and for the Stokes parameters Q, U, and

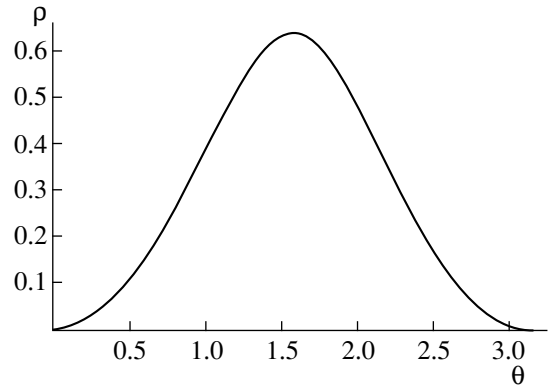

Fig. 2. Dependence of the degree of linear polarization on the angle between the direction of the electromagnetic wave propagation and the magnetic induction vector.

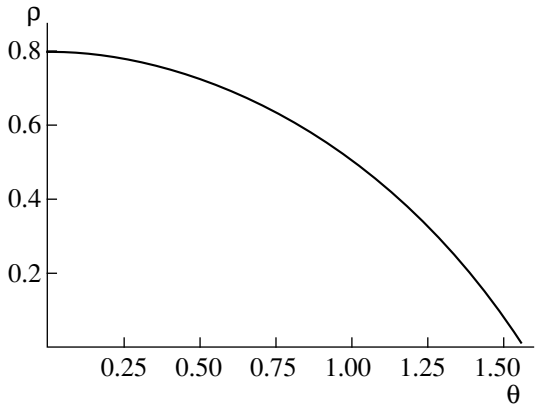

Fig. 3. The same as in Fig. 2, but for circular polarization.

V (in corresponding units):

$$\frac{d}{dt}I = \frac{8\omega_{pe}^6}{9\omega_{He}^2 m_e c^4 n_e}\left\{\frac{16}{63}\sin^2\theta + \frac{38}{105}\sin^2\theta\cos^2\theta + \frac{64}{63}\right\}\int W_{\mathbf{k}_1}^2 k_1^2 dk_1, \quad (25)$$

$$\frac{d}{dt}Q = \frac{8\omega_{pe}^6}{9\omega_{He}^2 m_e c^4 n_e}\left\{\frac{256}{315}\sin^2\theta - \frac{38}{105}\sin^2\theta\cos^2\theta\right\}\int W_{\mathbf{k}_1}^2 k_1^2 dk_1, \quad (26)$$

$$\frac{d}{dt}V = \frac{8\omega_{pe}^6}{9\omega_{He}^2 m_e c^4 n_e}\left\{\frac{56}{105}\cos\theta\sin^2\theta + \frac{256}{315}\cos\theta\right\}\int W_{\mathbf{k}_1}^2 k_1^2 dk_1, \quad (27)$$

$$\frac{d}{dt}U = 0. \quad (28)$$

Now, we divide the left- and right-hand sides of (25)–(28) by the width $\Delta\omega$ of the electromagnetic radiation spectrum to arrive at the expressions for the radiation power $J_{I\omega} = (1/\Delta\omega)dI/dt$) emitted from a unit volume of the turbulent plasma into a unit solid angle per unit frequency interval and for the Stokes parameters $J_{Q\omega}$, $J_{V\omega}$, and $J_{U\omega}$ (expressed in corresponding units):

$$J_{I\omega}(\theta) = 2\left(\frac{2}{3}\right)^3\left(\frac{\omega_{pe}}{\omega_{He}}\right)^2\frac{\omega_{pe}^4}{m_e}\frac{1}{c^4 n_e\Delta\omega}\frac{1}{105} \times (160 + 40\sin^2\theta + 57\sin^2\theta\cos^2\theta)\int W_{\mathbf{k}_1}^2 k_1^2 dk_1, \quad (29)$$

$$\frac{J_{Q\omega}(\theta)}{J_{I\omega}(\theta)} = \sin^2\theta\frac{128 - 57\cos^2\theta}{160 + 40\sin^2\theta + 57\sin^2\theta\cos^2\theta}, \quad (30)$$

$$\frac{J_{V\omega}(\theta)}{J_{I\omega}(\theta)} = \cos\theta\frac{128 + 84\sin^2\theta}{160 + 40\sin^2\theta + 57\sin^2\theta\cos^2\theta}, \quad (31)$$

$$J_{U\omega}(\theta) = 0. \quad (32)$$

Here, θ is the angle between the direction in which electromagnetic radiation is emitted and the magnetic field vector **B**, k_1 are the wavenumbers of gyrofrequency turbulence, and $\Delta\omega$ is the radiation spectrum width.

From expressions (29)–(32), we can readily see that electromagnetic radiation generated during the merging process $h + h \longrightarrow t$ is elliptically polarized. In the angular range $0 < \theta < \pi/2$, the degree of circular polarization, $\rho = J_V/J_I$, changes from about 80% to 0, in which case extraordinary waves dominate in the radiation spectrum. The polarization of the waves emitted in the direction nearly orthogonal relative to the vector **B** is to some extent linear ($J_Q/J_I \sim$ 60–65%).

Hence, in contrast to the mechanism for generating electromagnetic radiation directly by an electron beam (when the degree of circular polarization of the emitted radiation is close to 100%), the polarization of electromagnetic waves generated during the process $h + h \longrightarrow t$ can be moderately or weakly circular. Figures 2 and 3 show how the linear and circular polarization ρ of the emitted radiation varies with the angle θ.

3. CONCLUSION

We have investigated the polarization of electromagnetic radiation generated during the merging of gyrofrequency plasmons, $h + h \longrightarrow t$, in the limit $\omega_{He} \gg \omega_{pe}$ using the assumptions that the spectrum of

gyrofrequency turbulence is isotropic and the plasma ions are unmagnetized.

We have shown that, under the conditions adopted here, the merging process $h + h \longrightarrow t$ results in the generation of elliptically polarized radiation. In the angular range $0 \le \theta \le \pi/2$, the degree of circular polarization of the excited radiation J_V/J_I changes from about 80% to about 0 and the spectrum of the emitted waves is dominated by extraordinary waves. The polarization of electromagnetic waves emitted in the direction nearly orthogonal relative to the magnetic induction vector is to some extent linear ($J_Q/J_I \sim 60$–65%). Hence, we can conclude that the polarization of electromagnetic radiation emitted during the merging process $h + h \longrightarrow t$ may be moderately or weakly circular even when $\omega_{He} \gg \omega_{pe}$.

The results obtained can be used to process data from beam–plasma experiments and to interpret observations of radio emission from the Sun and other objects in the universe. The effects we have investigated can be observed in beam–plasma experiments in which the beam electron density is 10^{-3}–10^{-4} of the background plasma density and the plasma ions are unmagnetized.

ACKNOWLEDGMENTS

This work was supported in part by the Russian Foundation for Basic Research (project no. 98-02-17727) and the Government of the Russian Federation (project no. 961596733 under the program "Leading Scientific Schools").

REFERENCES

1. A. V. Burdakov, S. G. Voropaev, V. S. Koĭdan, *et al.*, Fiz. Plazmy **20**, 223 (1994) [Plasma Phys. Rep. **20**, 206 (1994)].
2. S. A. Kaplan and V. N. Tsytovich, *Plasma Astrophysics* (Pergamon, Oxford, 1974; Nauka, Moscow, 1972).
3. A. A. Andronov, V. V. Zheleznyakov, and M. I. Petelin, Izv. Vyssh. Uchebn. Zaved., Radiofizika **7**, 251 (1964).
4. V. N. Tsytovich and S. A. Kaplan, Astron. Zh. **45**, 777 (1968) [Sov. Astron. **12**, 618 (1968)].
5. V. N. Tsytovich, *Theory of Turbulent Plasma* (Atomizdat, Moscow, 1971; Plenum Press, New York, 1974).
6. V. G. Ledenev, Solar Physics **179**, 405 (1998).
7. A. Z. Dolginov, Yu. N. Gnedin, and N. A. Silant'ev, *Propagation and Polarization of Radiation in Space Media* (Nauka, Moscow, 1979).

Translated by O. E. Khadin

Plasma Physics Reports, Vol. 26, No. 2, 2000, pp. 152–156. Translated from Fizika Plazmy, Vol. 26, No. 2, 2000, pp. 166–171.

PLASMA DIAGNOSTICS

Measurements of the Electron Distribution Function in the AMBAL-M Startup Plasma by an Electrostatic Analyzer

T. D. Akhmetov, V. I. Davydenko, and S. Yu. Taskaev

Budker Institute of Nuclear Physics, Siberian Division, Russian Academy of Sciences, pr. akademika Lavrent'eva 11, Novosibirsk, 630090 Russia

Received May 21, 1999

Abstract—The electron distribution function over longitudinal energies in the startup plasma of the end cell of the AMBAL-M device is measured with a small-size movable electrostatic analyzer. It is found that, in the region where a substantial longitudinal current flows, the electron distribution function over longitudinal energies has a plateau in the 150–350-eV energy range. © *2000 MAIK "Nauka/Interperiodica".*

1. INTRODUCTION

A hot startup plasma with a diameter of 20 cm, a density of ~10^{13} cm^{-3}, an electron temperature of 50 eV, and an ion temperature of 200 eV is obtained in the end cell of the AMBAL-M device [1]. The plasma is produced by a gas-discharge plasma source located beyond the magnetic mirror. The specific feature of the obtained plasma is a ~1-kA longitudinal electric current flowing in the axial region [2]. To determine the heating and current-drive mechanisms, it is necessary to carry out direct measurements of the electron distribution function in the mirror system. The results of reconstructing the electron distribution function from the current–voltage characteristics of a Langmuir probe [3] located in a hot plasma lead to ambiguous interpretation.

The goal of this work is to measure the electron distribution function in the end cell of the AMBAL-M device by a small-size electrostatic energy analyzer specially designed for this purpose.

Similar energy analyzers have already been used for local measurements of the longitudinal electron current in reversed-field pinches [4–6]. These measurements demonstrated the possibility of using such energy analyzers to determine the electron distribution function over longitudinal energies.

2. DESCRIPTION OF THE ANALYZER

The schematic of the end cell of the AMBAL-M device and the position of the analyzer in the mirror system are presented in Fig. 1. The analyzer is attached to a ceramic tube and is inserted into the plasma with the use of a positioner. The analyzer (Fig. 2) consists of two symmetric sections placed inside an insulating case made of boron nitride. Each of the analyzer sections consists of an input diaphragm with a small aperture, an analyzing diaphragm, and a collector. The thickness of the input diaphragm made of niobium is 1 mm, and the diameter of the input aperture is 0.3 mm. The analyzing diaphragm has a thickness of 2 mm and an aperture diameter of 1 mm. The centers of the apertures of both diaphragms lie on the axis directed along the magnetic field. The diameters of the electrode apertures were chosen taking into account the energy of ions and electrons in the measurement region.

The measurement method is based on the violation of quasineutrality in the small input aperture, whose diameter is comparable with the Debye length. The ion flux into the analyzer is attenuated due to the relatively

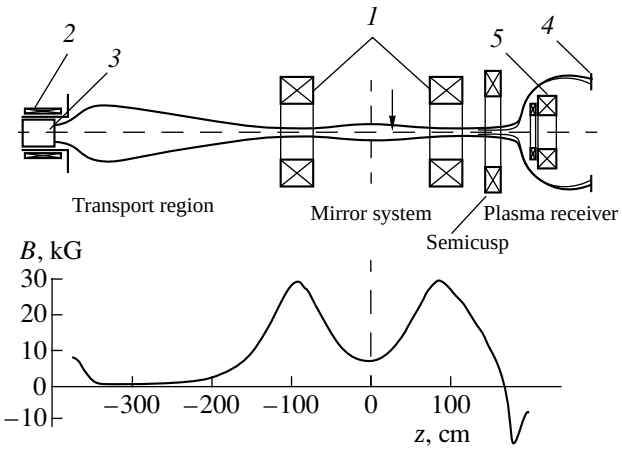

Fig. 1. Schematic of the end cell of the AMBAL-M device: (*1*) coils of the mirror system, (*2*) plasma-source solenoid, (*3*) plasma source, (*4*) plasma receiver, and (*5*) semicusp coils. The position of the analyzer is marked with an arrow. At the bottom, the profile of the magnetic field on the axis is shown.

1063-780X/00/2602-0152$20.00 © 2000 MAIK "Nauka/Interperiodica"

large thickness of the input diaphragm. Since the ion Larmor radius ($\rho_i \approx 2.5$ mm) in the region where the analyzer is located is substantially larger than the diameter of the input aperture, for the chosen diaphragm thickness, most of the ions fall on the wall of the aperture and do not enter the analyzer. On the other hand, the characteristic electron Larmor radius ($\rho_e \approx 0.025$ mm) is less than the aperture size, so that the electrons pass freely into the analyzer along the magnetic field lines. When the analyzer is inserted into the plasma, the insulated input diaphragm acquires a ~ 2.5–$3T_e/e$ negative potential with respect to the space potential, so that the current to the input diaphragm is equal to zero. This potential substantially reduces the plasma electron flux through the input aperture. Therefore, the analyzer in fact measures the distribution function of superthermal electrons with energies exceeding 2.5–$3T_e$. The energy analysis of the electrons entering the analyzer is carried out by applying a negative potential to the analyzing diaphragm with respect to the input diaphragm. In order to suppress secondary electron emission from the collector and reject a small portion of ions entering the analyzer because of their small transverse energy, a positive (with respect to the input diaphragm) potential is applied to the collector. The numerical solution of the Laplace equation shows that, for the –100-V potential of the analyzing diaphragm and +90-V potential of the collector, the retarding potential on the axis is –99.6 V. Therefore, in the absence of the electron space charge in the aperture, the retarding potential is approximately equal to the potential of the analyzing diaphragm. The current to the collector is measured with the use of a resistor placed between the input diaphragm and the collector. The electron distribution function $f(U) \propto -\partial j(U)/\partial U$ over longitudinal energies can be obtained by differentiating the measured dependence $j(U)$ of the collector current on the retarding voltage.

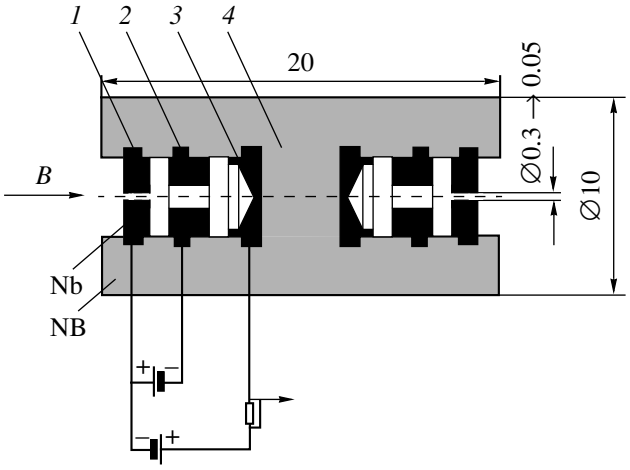

Fig. 2. Schematic of the energy analyzer: (*1*) input diaphragm, (*2*) analyzing diaphragm, (*3*) collector, and (*4*) insulating case.

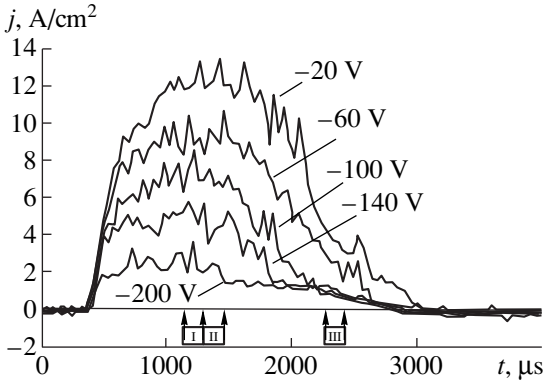

Fig. 3. Oscillograms of the collector current at different retarding potentials. The analyzer is located on the axis and faces the plasma source.

3. RESULTS OF MEASUREMENTS

The measurements were carried out in the axial plasma region in the single-shot regime. The shot-to-shot reproducibility of the plasma parameters was 5–10%. In Fig. 3, the oscillograms of the collector current of the analyzer section that faces the plasma source are shown at different values of the retarding potential. It is seen that an increase in the retarding potential results in a monotonic decrease in the collector current. To find the current as a function of the retarding potential, we averaged the current over three 160-μs time intervals, which are marked by the Roman numerals in Fig. 3. In the dependences obtained (see Fig. 4), most of the parts of the curves are well approximated by straight lines; this is evidence that there is a plateau in the electron distribution function up to energies of 180, 160, and 60 eV, respectively, with a further drop as the energy increases by 50 eV.

As was noted above, the distribution function can be found by differentiating the experimental dependence $j_{\exp}(U)$. However, in this case, the measurement errors lead to undesirable distortion of the sought-for functions. In order to eliminate these errors, the experimental curves should be carefully smoothed beforehand. Therefore, we chose another procedure that also allows evaluation of the distribution function by the measured current provided that the distribution function permits an analytical approximation with several free parameters. For simplicity, we assume that the measured current can be represented as a sum of contributions from the electrons with the Maxwellian distribution over longitudinal energies and an electron beam with a finite temperature. The thermal electrons in the mirror system are described by the Maxwellian distribution function $j_{\max w} = c_m \exp(-\varepsilon/T_m)$, and the beam is given by the Maxwellian distribution shifted by the longitudinal velocity,

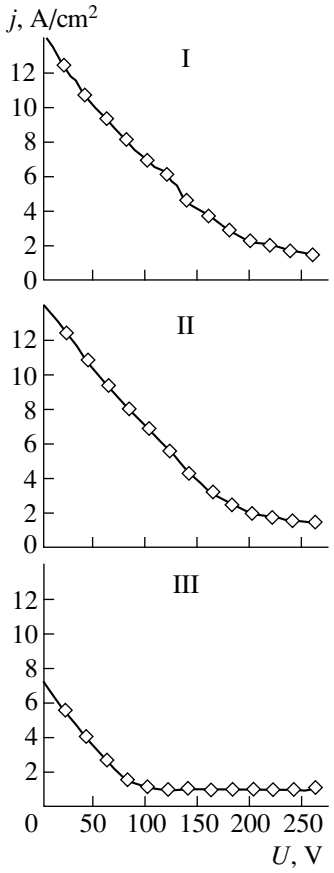

Fig. 4. The current as a function of the retarding potential for three time intervals (I, II, and III) shown in Fig. 3.

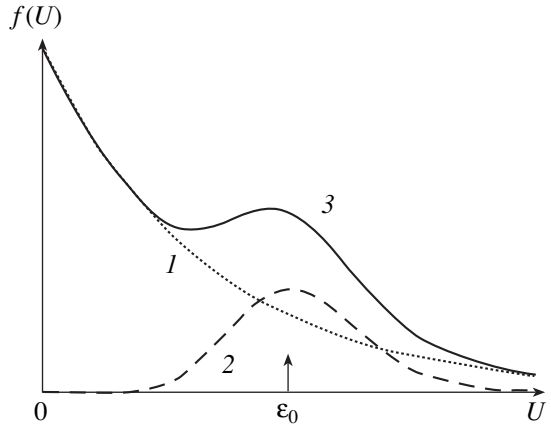

Fig. 5. Model electron distribution function: (*1*) Maxwellian distribution function $f_{\max w}(U)$, (*2*) fast-electron distribution function $f_{\text{fast}}(U)$, and (*3*) total distribution function $f(U) = f_{\max w}(U) + f_{\text{fast}}(U)$.

$f_{\text{fast}} = c_f \exp(-(\sqrt{\varepsilon} - \sqrt{\varepsilon_0})^2/T_f)$. Here, c_m and c_f are constants determining the densities of Maxwellian and fast electrons; T_m and T_f are the temperatures of these two electron species, respectively; ε is the longitudinal energy ($\varepsilon = m v_\parallel^2/2$); and ε_0 is the average longitudinal energy of the beam electrons. These functions and their sum are presented in Fig. 5. The sought-for parameters c_m, c_f, T_m, T_f, and ε_0 are found by minimizing the sums of squared deviations of the calculated current from the measured current with respect to the free parameters at different voltages. This procedure resulted in the following estimates for the electron energy characteristics: the temperature of the Maxwellian electrons is 100, 80, and 30 eV for the I, II, and III intervals in Fig. 3, respectively; the beam-electron energy is 150, 135, and 60 eV, respectively; the beam-electron temperature is ~3 eV in all cases; and the fast-electron density is at least one order lower than the density of the warm Maxwellian plasma. Note that these solutions give somewhat overestimated current values at retarding potentials below 50 eV. Presumably, the low temperature of the beam electrons is explained by the cooling effect (the decrease in the mean-square deviation of the particle velocity from the averaged directional velocity) during the particle acceleration. This effect shows up when the electrons move in the accelerating ambipolar electric field from the input magnetic mirror to the center of the device.

The retarding curve for the analyzer section facing the plasma receiver is shown in Fig. 6. In this case, at the zero retarding potential, the collector current is approximately three-and-a-half times below the current in the case considered above. As before, the electron current flowing into the analyzer is suppressed at retarding potentials up to 200 V. In this case, the electron flux into the analyzer can be related to both the partial reflection of fast electrons by the output magnetic mirror and the superthermal Maxwellian electrons.

Although the measurements show the presence of a plateau in the electron distribution function over longitudinal energies, there are two factors that affect the measurement accuracy. First, the retarding potential applied to the analyzing diaphragm leads to a proportional increase in the potential of the input diaphragm. Thus, when the retarding potential was –200 V, the potential of the input diaphragm increased by 80 V. This effect is similar to the behavior of a double probe in a plasma when the voltage is applied across the interelectrode gap. However, it is difficult to explain the increase in the potential of the input diaphragm quantitatively. Actually, the value of the retarding potential is less than the voltage between the input and analyzing diaphragms. It is found that the dependence of the retarding potential U_{repel} on the potential of the analyzing diaphragm U_d is close to linear: $U_{\text{repel}} \approx 0.6U_d$. Therefore, the retarding curve can be corrected so that its shape remains almost unchanged.

Another factor affecting the accuracy is the electron space charge. The decrease in the potential on the axis in the input aperture is associated with this space charge and is estimated as $\delta\varphi \approx \pi r^2 ne$. Assuming the

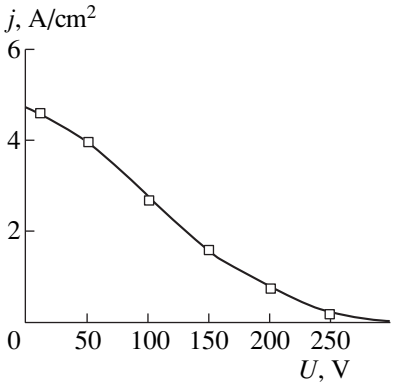

Fig. 6. Retarding curve for the analyzer section facing the plasma receiver.

average electron energy to be 60 eV, we obtain that, for the current density $j \approx 15$ A/cm^2, the density of the electron flow is $n \approx 2 \times 10^{11}$ cm^{-3} and the decrease in the potential on the axis is $\delta\varphi \approx 20$ V. A certain measurement error can also be introduced by the radial nonuniformity of the potential.

In order to carry out more accurate measurements, the aperture diameter of the input diaphragm was reduced to 0.05 mm. In this case, a –200-V retarding potential leads to only a 10-V increase in the potential of the input diaphragm. Hence, we can say that the potential of the analyzing diaphragm has no effect on the potential of the input diaphragm and that it is actually the retarding potential. At the zero potential of the analyzing diaphragm, a decrease in the input aperture area by a factor of 36 resulted in a decrease in the collector current by a factor of 100. This extra decrease in the current is associated with the fact that the radius of the input aperture in this case is equal to the Larmor radius of electrons with a 50-eV transverse energy, so that not all of the electrons enter the analyzer. Such a small input aperture of the analyzer cuts off not only the ions but also the electrons with high transverse velocities. This selection emphasizes the contribution from beam electrons with a small transverse temperature. Since the recorded current decreases 100-fold, the space-charge potential also decreases 100-fold, and its influence on the measurement accuracy becomes negligible.

Figure 7a shows the dependence of the collector current on the retarding potential, which was measured by the analyzer with the reduced input aperture. Although the dispersion of the experimental points increased because of the decrease in the collector current, it is seen that the electron distribution function is fairly broad and non-Maxwellian. The dispersion of the experimental points introduces some uncertainty in drawing the smooth curve through these points (this curve should be differentiated with respect to the retarding potential in order to obtain the distribution function). As an example, we drew two curves through the experimental points. Figure 7b shows two electron distribution functions over longitudinal energies for two curves drawn through the experimental points. It is seen that, in both cases, the electron distribution function has a plateau in the energy range from $e\varphi_{fl}$ to $e\varphi_{fl}$ + 200 eV. Assuming that $e\varphi_{fl} \approx 3T_e \approx 150$ eV, we can state that the plateau is located in the 150–350-eV range of the electron longitudinal energy.

To understand the influence of superthermal plasma electrons, we carried out measurements at a radius of 6 cm (outside the region ~4 cm, where the longitudinal current flows) using the analyzer with the reduced aperture. The results are presented in Fig. 8. At this radius, the bulk-plasma parameters are almost the same as on the axis, but the longitudinal current is absent. The data

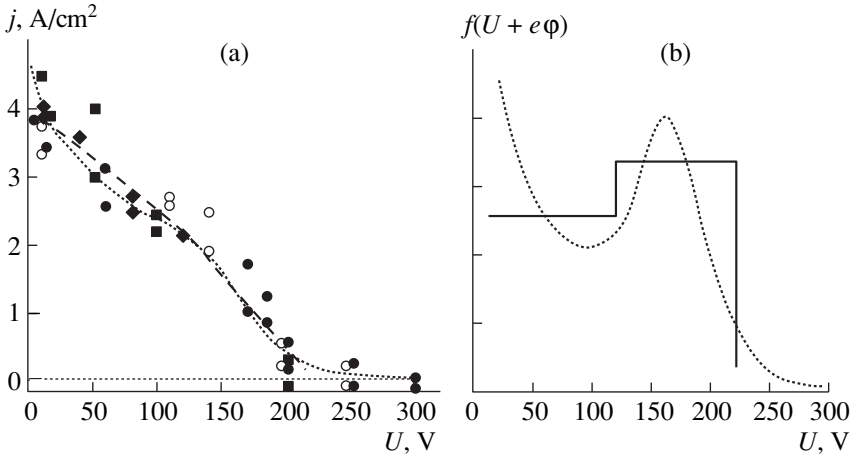

Fig. 7. (a) The retarding curve for the analyzer with a reduced input aperture and (b) the electron distribution functions over longitudinal energies obtained from dashed and dotted curves in plot (a). Averaging is performed over the 1–1.5-ms time interval. The results of different series of measurements are shown by different symbols.

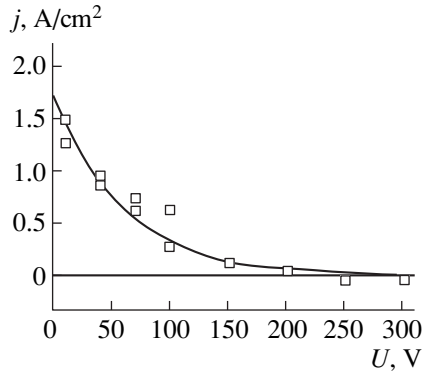

Fig. 8. The retarding curve for the analyzer positioned at a 6-cm radius. The solid line shows the retarding curve for the Maxwellian electron distribution with a 60-eV temperature.

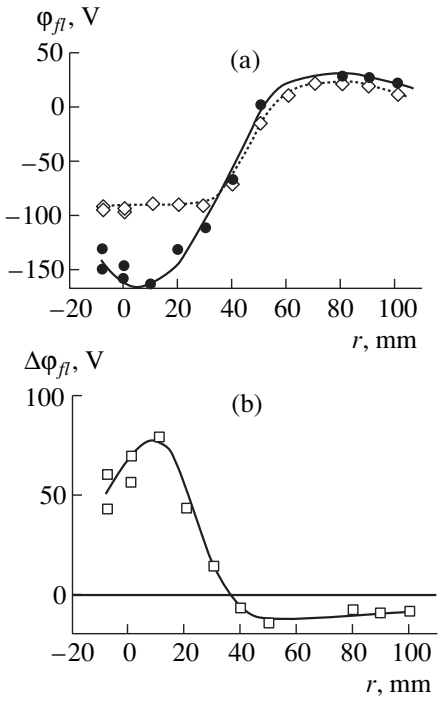

Fig. 9. (a) Radial profiles of the floating potential of the analyzer input diaphragms facing (◇) the plasma source and (●) plasma receiver and (b) their difference.

presented in Fig. 8 are well approximated by the Maxwellian distribution with a 60-eV temperature. For the zero retarding potential, the collector current dropped 2.5 times compared to that measured on the axis, which is explained by the absence of fast electrons. Thus, we can conclude that the previous measurements showed approximately the same contribution to the current from the Maxwellian and beam electrons.

In addition, we measured the radial profiles of the floating potentials of both input diaphragms, one of which faced the plasma source and the other one faced the plasma receiver. The results are presented in Fig. 9. The profile of the potential difference between the diaphragms shows that the electron distribution function in the axial region is anisotropic. As would be expected, this region coincides with the region where the current flows that was previously detected by a magnetic probe [2].

4. CONCLUSION

A small-size electrostatic electron-energy analyzer is designed and used to measure the electron distribution function over longitudinal energies in the end cell of the AMBAL-M device. It is found that the distribution function has a plateau in the 150–350-eV range in the current-carrying channel of the mirror system and is Maxwellian (with a temperature of 60 eV) outside this channel. The data obtained can be used to carry out numerical simulations of the generation of electrons carrying the current in the transport region between the plasma source and the mirror system.

ACKNOWLEDGMENTS

We thank V.A. Novikov for fabricating the analyzer and P.D. Rybakov for assistance in measurements. This work was supported by the Russian Foundation for Basic Research, project no. 98-02-17801.

REFERENCES

1. T. D. Akhmetov, V. S. Belkin, E. D. Bender, *et al.*, Fiz. Plazmy **23**, 988 (1997) [Plasma Phys. Rep. **23**, 911 (1997)].
2. T. D. Akhmetov, V. I. Davydenko, A. A. Kabantsev, *et al.*, Fiz. Plazmy **24**, 1065 (1998) [Plasma Phys. Rep. **24**, 995 (1998)].
3. S. Yu. Taskaev, Preprint no. 95-92, IYaF SO RAN (Institute of Nuclear Physics, Siberian Division, Russian Academy of Sciences, Novosibirsk, 1995).
4. J. C. Ingraham, R. F. Ellis, J. N. Downing, *et al.*, Phys. Fluids B **2**, 143 (1990).
5. M. R. Stoneking, S. A. Hokin, S. C. Prager, *et al.*, Phys. Rev. Lett. **73**, 549 (1994).
6. Y. Yagi, V. Antoni, M. Bagatin, *et al.*, Plasma Phys. Controlled Fusion **39**, 1915 (1997).

Translated by A. D. Smirnova

Plasma Physics Reports, Vol. 26, No. 2, 2000, pp. 157–163. Translated from Fizika Plazmy, Vol. 26, No. 2, 2000, pp. 172–178.

LOW-TEMPERATURE PLASMAS

Transition of a Multipin Negative Corona in Atmospheric Air to a Glow Discharge

Yu. S. Akishev, M. E. Grushin, I. V. Kochetov, A. P. Napartovich, M. V. Pan'kin, and N. I. Trushkin

Troitsk Innovation and Fusion Research Institute, Russian State Science Center, Troitsk, Moscow oblast, 142092 Russia

Received April 22, 1999

Abstract—It is commonly accepted that, as the current increases, a diffuse negative corona inevitably goes over to a strongly nonuniform and nonsteady spark discharge. In this paper, a new effect—the transition of a negative corona to a diffuse glow discharge at atmospheric pressure—is studied experimentally and numerically. The evolution of the corona parameters during the transition to the regime of a glow discharge is traced.

1. INTRODUCTION

According to the classification of gas discharges proposed in [1], a negative corona and a glow discharge refer to the same type of discharge, because, in both of them, the current in the cathode sheath is maintained by the same processes, specifically, photoemission and avalanche multiplication of the electrons emitted from the cathode due to electrostatic extraction by metastables and positive ions.

Historically, these two kinds of the same discharge were studied separately: classical glow discharges were observed in low-pressure gases in sealed glass tubes, whereas corona discharges were observed in high-pressure gases (in particular, at atmospheric pressure).

The glow discharge is characterized by a high value of the reduced electric field E/N (where E is the electric field and N is the gas number density) in the interelectrode gap. This field is sufficiently high for producing intense ionization of a gas; a result, the gap is filled with a plasma. In the case of a negative corona, the reduced field in the gap is much less and there is an uncompensated negative space charge in the gap.

As the corona current increases, the density of the negative space charge and the electric field in the gap both increase. Hence, when the electric field becomes sufficiently high to produce intense gas ionization, a plasma will arise between the electrodes of the corona discharge; i.e., the negative corona will go over to the regime of a glow discharge.

A pin–plane electrode configuration is the most typical for producing a corona discharge. Note that such an electrode system is not convenient for realizing a transition from a negative corona to a glow discharge. The reason is that, in this configuration, the current-carrying channel significantly broadens with distance from the pin; thus, the space-charge density between the electrodes is low. Rather high currents are needed to obtain a sufficient space-charge density and, accordingly, a strong electric field in the discharge gap. However, under normal conditions (at atmospheric air), it is difficult to produce high currents with this geometry of the corona, because, even at relatively low currents, a single-pin corona goes over to the spark discharge.

2. DESCRIPTION OF THE EXPERIMENT

To investigate the transition from a negative corona to a glow discharge in air at atmospheric pressure, we used a special electrode system with a multipin cathode and a flat metal anode (Fig. 1). The pins were stainless-steel needles 0.5 mm in diameter tapered to a cone with a vertex curvature radius of R_C = 0.06 mm. Fifty-two needles were uniformly distributed over an area of 10×40 mm^2 in four rows of 13 needles each.

The distance d between needles (i.e., the spatial period of the cathode structure) was equal to 3.5 mm and was small compared to the distance between their vertexes and the anode, h = 5–20 mm. In this case, the current density in the negative-corona gap increases substantially (by nearly a factor of $3(h/d)^2$) in comparison with the pin–plane configuration and the transition

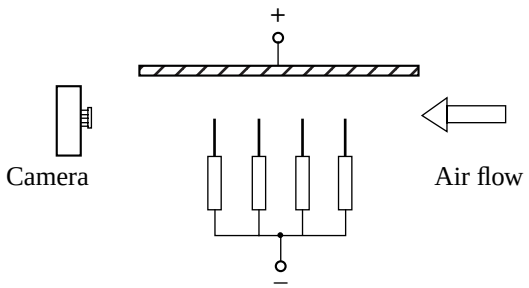

Fig. 1. Experimental setup.

1063-780X/00/2602-0157$20.00 © 2000 MAIK "Nauka/Interperiodica"

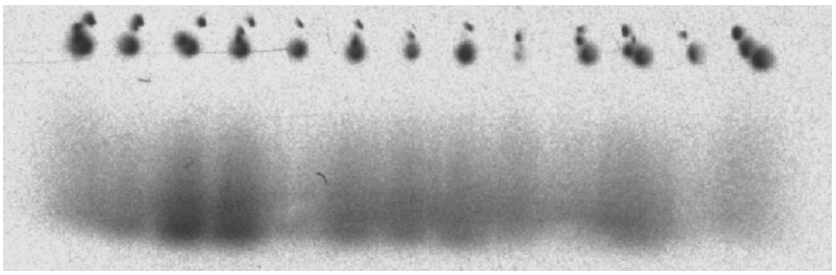

Fig. 2. Photograph (negative) of the discharge in room air; the discharge current per pin is 39 μA.

from the corona to a glow discharge occurs at a relatively low current through each pin.

In order to ensure a stable diffuse regime of the negative corona, each needle was supplied through a high-resistance load: $R \simeq 2$ MΩ. In addition, the anode plate was connected to a high-voltage supply through a 0.2 MΩ resistor. The stability of the corona against its transition to a spark was also ensured by air flowing through the discharge; the cathode unit was oriented so that its longest side was perpendicular to the air flow. A typical flow velocity was on the order of several tens of meters per second.

Along with the recording of I–V characteristics, we photographed the discharge in the direction opposite to the air-flow velocity.

3. EXPERIMENTAL RESULTS

If the discharge is in the corona regime, only the needle ends are luminous, whereas the interelectrode gap is hardly visible and the anode is dark. The photograph (negative) of the discharge in the steady-state glow regime is shown in Fig. 2. It is seen that the glow discharge is diffuse and rather uniform, although the discrete structure of the plasma column caused by the discrete structure of the multipin cathode is also clearly seen.

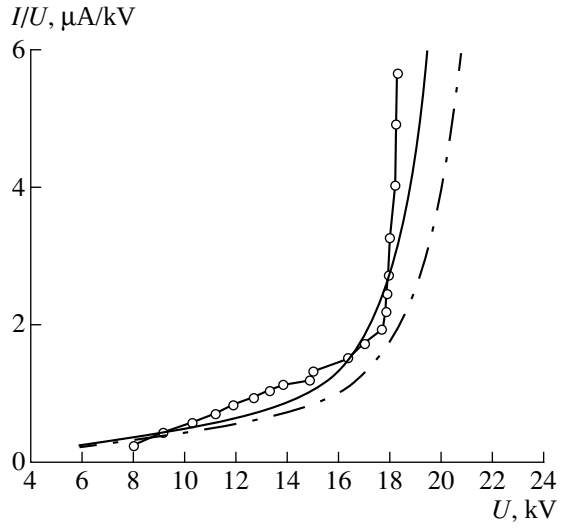

Fig. 3. Reduced I–V characteristic of the discharge in room air (I is the current per pin). The points correspond to the experiment; the solid and dashed-and-dotted lines correspond to the calculation for relative humidity of 30 and 65%, respectively. The needle point radius is $R_C = 0.06$ mm; $h = 10.5$ mm.

Figure 3 shows a typical reduced I–V characteristic of the discharge under study. Here, the ratio I/U (instead of the total discharge current) is plotted versus the discharge voltage U, I being the discharge current per pin.

In the reduced I–V characteristic, we can distinguish two segments (the first in the range of initial corona currents and the second in the range of high currents corresponding to the regime of a developed glow discharge) in which the reduced current is a nearly linear function of the voltage. It is seen that, in the glow discharge, the current increases with voltage more sharply in comparison with the corona regime. This is explained by the increasing role of ionization (which depends strongly on the field) in creating the conductivity in the interelectrode gap of the glow discharge.

The kink point of the reduced I–V characteristic (i.e., the point of intersection of two extrapolated straight lines corresponding to the linear dependences) can be considered a critical voltage corresponding to the transition of the corona to a glow discharge. Near this point of the I–V characteristic, a luminous thin sheath appears on the anode. This is evidence that the anode sheath is formed, which is characteristic of a glow discharge. At voltages higher than the critical one, the gap luminosity increases sharply with the current and the discharge exhibits more and more features typical of glow discharges.

It was noted above that the luminous anode sheath becomes visible when the current reaches the threshold I_1 corresponding to the beginning of the transition from the corona to a glow discharge. Figure 4 shows the dependence of the threshold current on the interelectrode distance h. A similar dependence of the threshold current I_2 corresponding to the transition from the glow discharge to a spark is also shown. Hence, the current range in which a uniform glow discharge at atmo-

spheric pressure can exist is bounded by two curves $I_1(h)$ and $I_2(h)$. Note that this range may be extended substantially by using gasdynamic effects and anodes of a special design.

4. DESCRIPTION OF THE NUMERICAL MODEL OF THE DISCHARGE

The numerical model of a corona in humid air is based on the well-known continuity equations for electrons and positive and negative ions, Poisson's equation, and an equation for the simplest electric circuit with parameters corresponding to the experiment. The discharge kinetics in air plasma is very involved. For its complete description, it is necessary to consider the evolution of a great number of components. However, in our previous paper, we already formulated a simplified model based on the full kinetic model. This model was used to predict average characteristics of a corona on a thin wire in air at atmospheric pressure [2].

Here, we use the same model with one species of positive ions and one species of negative ions. The model includes the ionization, three-body attachment of electrons to an oxygen molecule, detachment, and ion–ion recombination. The presence of water vapor in air was taken into account by introducing an additional attachment rate caused by three-body attachment to oxygen with the participation of water molecules acting as a third body. The frequencies of relevant processes for P = 740 torr, T = 294 K, and a relative air humidity of 30% are shown in Fig. 5.

The key point of our approach to the problem that previously allowed us to describe the periodical generation of Trichel pulses [3–5] is the use of a one-and-a-half-dimensional approximation in solving all of the equations in order to describe a strong broadening of the current channel between the cathode and the anode.

In these calculations, the equivalent radius of the discharge at the anode was determined from the discharge area per pin. The total area was calculated by the formula $S = S_0 + \alpha 2h(a + b)$, where S_0 is the area enveloped by the contour drawn through the edge pins, $2(a + b)$ is the circumference of this contour, h is the distance between the electrodes, and α is the phenomenological parameter (α = 0.5). The shape of the current channel was chosen according to visual observations: at a distance of one-third of the full distance between the electrodes, the channel rapidly broadens until its radius becomes equal to the anode radius; further, the cross-section area remains constant. Possible variations in the shape of the current channel due to variations in the current value were neglected in calculations.

In calculations, all of the parameters were reduced to the conditions referred to one pin. The equivalent resistance of the ballast resistor in the discharge circuit for each pin was R = 12.2 MΩ (the resistance of the anode circuit was taken into account). Note that a series of calculations of I–V characteristics was performed with various values of the ballast resistance (from 100 kΩ to 18 MΩ); these calculations showed that the value of the ballast resistor has little effect on the shape of the I–V characteristics (in appearance, these characteristics remain almost the same).

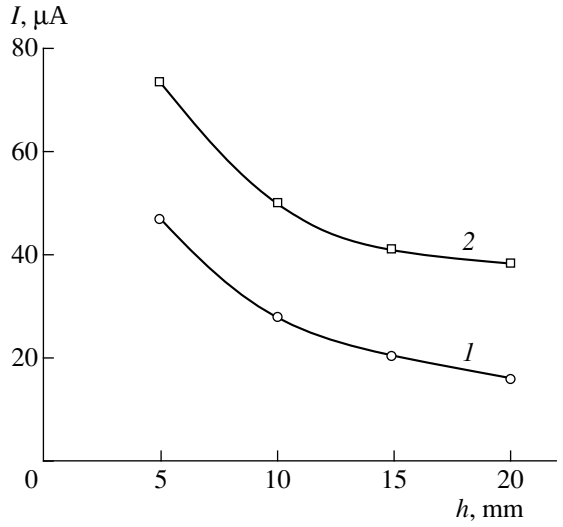

Fig. 4. Threshold currents I_1 (curve *1*) and I_2 (curve *2*) per pin for the transition from the corona to a glow discharge and from the glow discharge to a spark, respectively, as functions of the interelectrode distance h.

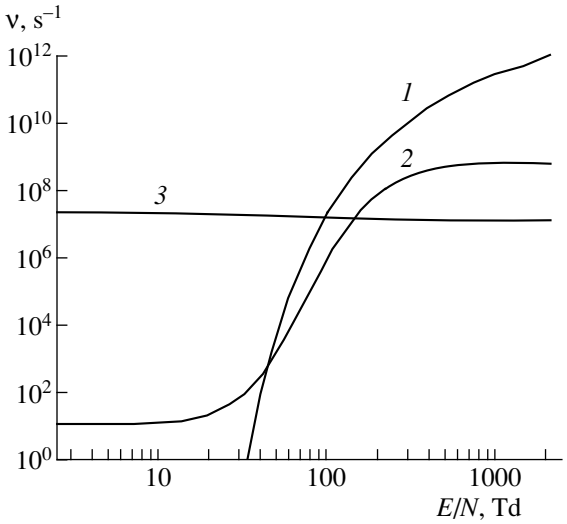

Fig. 5. Dependences of (*1*) the ionization, (*2*) electron detachment, and (*3*) three-body attachment rates on the reduced electric field for room air at relative humidity of 30%.

The set of equations describing the discharge parameters averaged over the current-channel cross section has the form [4]

$$\frac{\partial n_e}{\partial t} + \frac{1}{S}\frac{\partial}{\partial x}(Sn_e w_e) = (\nu_i - \nu_a)n_e + \nu_d n_n, \qquad (1)$$

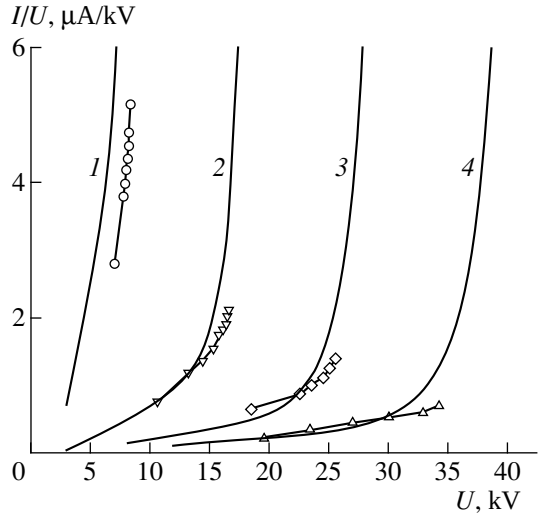

Fig. 6. Reduced I–V characteristic of the discharge in dry air (*I* is the current per pin) for R_C = 0.06 mm and *h* = (*1*) 5, (*2*) 10, (*3*) 15, and (*4*) 20 mm. The points correspond to the experiment; the solid lines correspond to the calculation.

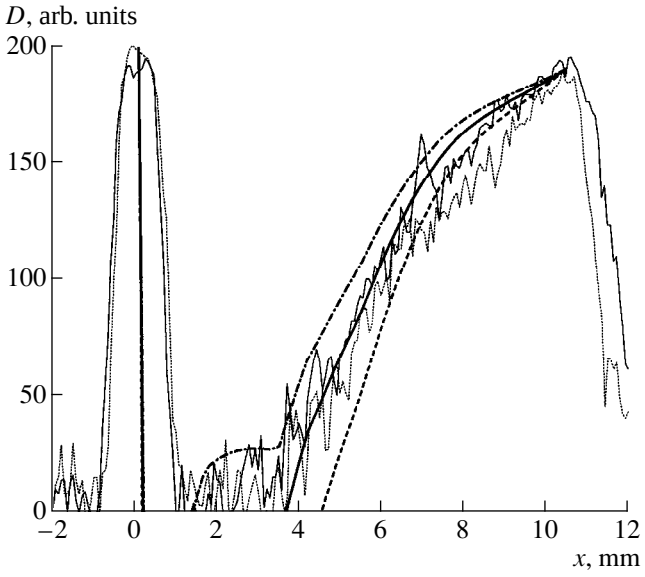

Fig. 7. Comparison of the calculated and experimental discharge radiation intensity for room air at relative humidity of 30% and a current per pin of 39 μA. The calculation is performed for different values of the contrast coefficient θ: the solid, dashed, and dashed-and-dotted lines correspond to θ = 0.5, 0.67, and 0.4, respectively. The fluctuating lines show the experimental results.

$$\frac{\partial n_p}{\partial t} - \frac{1}{S}\frac{\partial}{\partial x}(Sn_p w_p) = \nu_i n_e, \tag{2}$$

$$\frac{\partial n_n}{\partial t} + \frac{1}{S}\frac{\partial}{\partial x}(Sn_n w_n) = \nu_a n_e - \nu_d n_n, \tag{3}$$

$$\frac{1}{S}\frac{\partial}{\partial x}(SE) = -(n_p - n_e - n_n)\frac{e}{\varepsilon_0}, \tag{4}$$

where the subscripts *e*, *p*, and *n* refer to electrons and positive and negative ions, respectively; n_e, n_p, and n_n are the densities of electrons and positive and negative ions; w_e, w_p, and w_n are their drift velocities; ν_i, ν_a, and ν_d are the ionization, attachment, and detachment rates; *e* is the electron charge; ε_0 is the permittivity of vacuum; and $S(x)$ is the running area of the discharge cross section, which is a given function of the coordinate *x*.

The current *I* in the external circuit is found from the equation

$$U = U_0 - RI, \tag{5}$$

where *U* and U_0 are the voltage at the discharge gap and the supply voltage, respectively, and *R* is the ballast resistance.

The boundary conditions for positive and negative ions are evident: their densities vanish at the anode and cathode surfaces, respectively.

The boundary conditions for electrons at the cathode ($x = 0$) are formulated through the secondary emission coefficient γ:

$$j_e(0, t) = \gamma j_p(0, t), \tag{6}$$

where $j_e = n_e w_e$, $j_p = n_p w_p$, and $\gamma = 0.01$.

Equations (1)–(4) were solved by an implicit difference scheme with a nonuniform spatial mesh (the mesh size decreased near the cathode). A detailed description of the numerical scheme is presented in [6].

Upon calculating the distribution of the reduced electric field across the discharge gap, we calculated the distribution of radiation intensity in the discharge. It was assumed that the first and second positive systems of nitrogen ($B^3\Pi_g$ and $C^3\Pi_u$ levels) make the main contribution to the radiation and that the total radiation intensity is proportional to the total excitation rate for these levels. The excitation rate constants for these levels were determined by numerically solving the Boltzmann equation for the electron energy distribution function with the cross sections for these levels taken from [7].

5. COMPARISON OF THE CALCULATION WITH THE EXPERIMENT

Based on the numerical model described above, we computed the I–V characteristic of the discharge under study, the distribution of the intensity of the radiation along the current channel of an individual pin, and the change of the longitudinal structures of the electric field, the components of the total current, and the charged-particle (electron, ion, and negative ion) densities in the interelectrode gap with increasing the discharge current.

A comparison of the computed reduced I–V characteristics with the experiment is shown in Figs. 3 and 6. It is seen that, for the parameters chosen, the calculation is in good qualitative and quantitative agreement

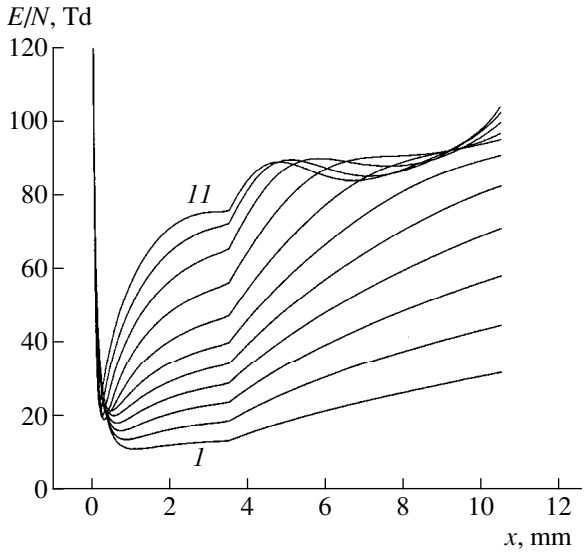

Fig. 8. Longitudinal profile of the reduced electric field across the discharge gap for different values of the discharge current. The numerals correspond to the current values as given in the table.

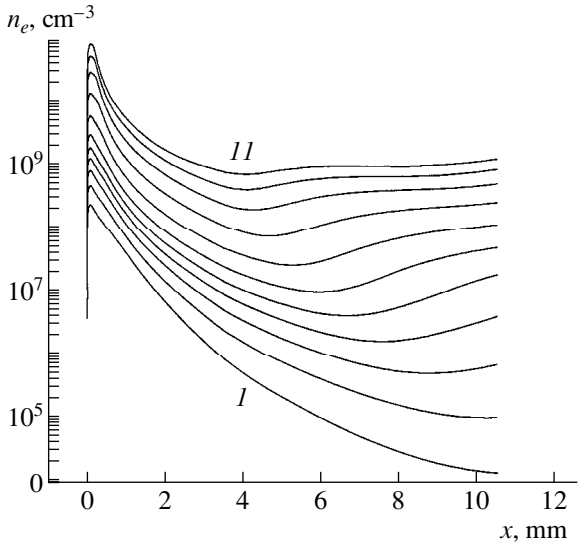

Fig. 9. Longitudinal profile of the electron density across the discharge gap for different values of the discharge current. The numerals correspond to the current values as given in the table.

with the experimentally observed dependence of the current on the discharge voltage.

The calculated distribution of the radiation intensity across the gap is also in good agreement with the experiment. In the experiment, we measured the normalized distribution of the blackening of the film on which the negative image of the discharge was produced (see, e.g., Fig. 2). The degree of blackening D is related to the radiation intensity K by the relationship (see [8])

$$D = 200\theta(\log K - \log K_{h=1.05} + 1/\theta), \qquad (7)$$

where θ is the film contrast factor and $K_{h=1.05}$ is the normalizing intensity.

A comparison of the calculated radiation intensity with the experiment is shown in Fig. 7. We recall that it was assumed in calculations that the intensity of visible radiation of the glow discharge is determined by the total radiation intensity from the first and second positive nitrogen systems. A narrow peak near the coordinate origin corresponds to the radiation from the cathode sheath located near the vertex of the needle.

6. CALCULATED LONGITUDINAL DISCHARGE STRUCTURE

Poisson's equation, together with the charge and transport processes, determines the longitudinal profiles of the electric field and charged-particle density across the gap. Comparing Figs. 8–12 to each other, we can trace self-consistent variations in the electric field and charge density in the interelectrode gap as the discharge current varies. The computation was performed for room air (the relative humidity was 30%) and an interelectrode distance of 10.5 mm. The calculated values of the discharge current I and voltage U are presented in the table for different values of the supply voltage (U_0).

It is seen in Fig. 8 that the electric field within the gap (outside of the cathode sheath) is maximum near the anode. The ionization rate is also maximum near the anode. Note that the kink in the electric-field profile at $x = 0.35$ cm, which is seen in the figure, is not physical in nature but is due to the particular shape of the current channel used in the model.

The minimum of the electric field near the boundary of the positively charged cathode sheath is caused by

Calculated values of the discharge current I and discharge voltage U for different values of the supply voltage U_0 in room at relative humidity of 30%

no.	1	2	3	4	5	6	7	8	9	10	11
U_0, kV	6	8	10	12	14	16	18	20	22	24	26
U, kV	5.93	7.90	9.86	11.81	13.75	15.66	17.43	18.92	19.97	20.62	21.08
I, μA	1.4	2.79	4.76	7.34	10.8	17.5	34.3	75.2	152	261	386

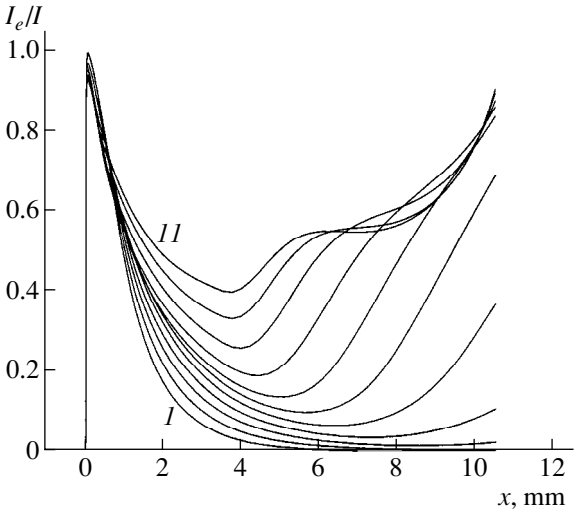

Fig. 10. Longitudinal profile of the contribution from the electron current to the total current for different values of the discharge current. The numerals correspond to the current values as given in the table.

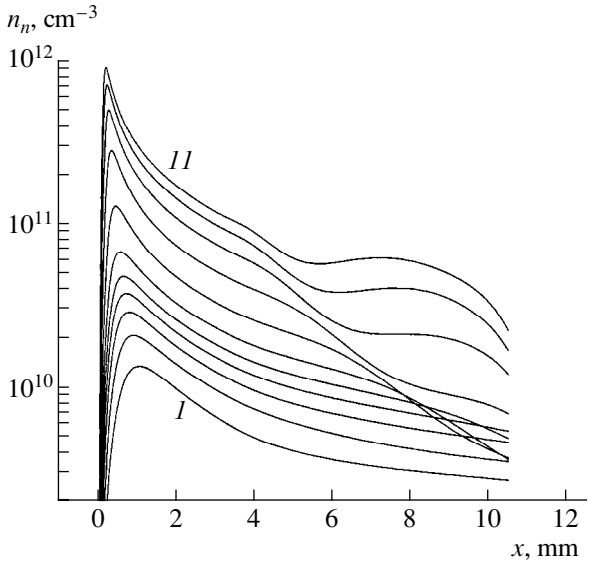

Fig. 11. Longitudinal profile of the negative-ion density across the discharge gap for different values of the discharge current. The numerals correspond to the current values as given in the table.

the high density of the electrons leaving the cathode sheath (Fig. 9). The discharge current in this region is carried predominantly by the electrons (Fig. 10). The increase in the field with distance from the cathode is explained by the attachment of electrons and the decrease in their contribution to the total current (Figs. 8–11).

As the discharge voltage increases, the profile of the electron component of the current along the discharge gap becomes nonmonotonic: after a decrease in the region of low fields near the cathode, the electron flow increases again in the region of high fields far from the cathode. As the voltage increases, the electric-current minimum shifts outward from the anode and the contribution of the electron current to the total current increases.

We note that the electron flow in the gap starts to increase at field values at which the ionization rate is still low compared to the attachment rate. This fact indicates that the processes of destruction of negative ions play an important role in the growth of the electron flow and the formation of the anode sheath.

It is clearly seen in Fig. 11 that the negative-ion density near the anode sharply decreases as the electric field approaches the critical value corresponding to the kink point of the I–V characteristics. Since the negative-ion density near the anode well exceeds the electron density ($n_n/n_e \gg 1$), even a weak detachment ($\nu_d \ll \nu_i, \nu_a$) significantly contributes to the electron-current growth in this region and thus reduces the electric field (and, correspondingly, the corona current) at which the anode sheath arises.

Let us consider in more detail the conditions under which the anode sheath is formed. Two processes occur in the anode sheath: the generation of the positive-ion current j_p via gas ionization and the almost complete disappearance of the current j_n of negative ions entering the sheath from the anode region (i.e., from a ~1-mm-wide region near the anode). Under conditions close to the establishment of the anode sheath, the j_p and j_n currents near the anode become comparable. In this case, the divergences of these flows in the anode sheath also become comparable. In other words, near the threshold

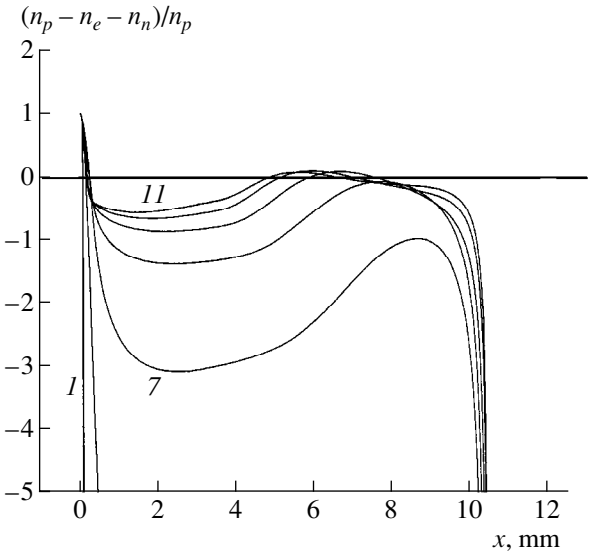

Fig. 12. Longitudinal profile of the space charge across the discharge gap for different values of the discharge current. The numerals correspond to the current values as given in the table.

current I_1, the following equality must hold (see equations (2) and (3))

$$\nu_i \simeq \nu_d(n_n/n_e) - \nu_a. \quad (8)$$

The numerical calculations show that equality (8) holds near the kink point of inclination of the I–V characteristics, i.e., in the initial stage of the transition from the corona to a glow discharge. This fact also indicates that the collisional detachment plays an important role in the transition from the corona to a glow discharge.

Thus, the calculations show that, in a multipin electrode system (i.e., under the conditions when the discharge has a fixed cross section at the anode), the plasma column in the glow discharge does not form simultaneously along the entire interelectrode gap. After the anode sheath has formed, the quasineutrality conditions are first created near the anode. As the discharge current increases, the region of quasineutral plasma extends toward the cathode progressively covering the interelectrode gap (Fig. 12).

The parameters of the plasma column produced in the gap are close to the parameters of a glow discharge that we computed previously with the zero-dimensional model [9].

7. CONCLUSION

Based on the results of experimental studies and numerical calculations, we have traced the evolution of the parameters of a multipin negative corona during the transition to the regime of a glow discharge at atmospheric pressure.

The current range in which the glow discharge can exist is experimentally determined.

ACKNOWLEDGMENTS

We thank A.G. Sukharev for providing us with the program for processing the discharge images. This work was supported in part by the International Science and Technology Center (project no. 439) and the Russian Foundation for Basic Research (project no. 97-02-17888).

REFERENCES

1. V. L. Granovskiĭ, *Electric Current in a Gas: Steady-State Current*, Ed. by L. A. Sena and V. L. Golant (Nauka, Moscow, 1971), p. 543.
2. Yu. S. Akishev, A. A. Deryugin, A. P. Napartovich, *et al.*, in *Proceedings of XXII International Conference on Phenomena in Ionized Gases, Hoboken, NJ, 1995*, Part 2, p. 147.
3. Yu. S. Akishev, A. A. Deryugin, I. V. Kochetov, *et al.*, Pis'ma Zh. Tekh. Fiz. **22**, 1 (1996) [Tech. Phys. Lett. **22**, 819 (1996)].
4. A. P. Napartovich, Yu. S. Akishev, A. A. Deryugin, *et al.*, J. Phys. D: Appl. Phys. **30**, 2726 (1997).
5. Yu. S. Akishev, M. E. Grushin, I. V. Kochetov, *et al.*, Fiz. Plazmy **25**, 998 (1999) [Plasma Phys. Rep. **25**, 922 (1999)].
6. Yu. S. Akishev, N. N. Elkin, and A. P. Napartovich, Fiz. Plazmy **12**, 1225 (1986) [Sov. J. Plasma Phys. **12**, 706 (1986)].
7. A. V. Phelps and L. C. Pitchford, Preprint No. 26 (JILA Information Center, University of Colorado, Boulder, CO, 1985).
8. Yu. I. Zhurba, *Handbook of Photographic Processes and Materials* (Iskusstvo, Moscow, 1990), p. 352.
9. Yu. S. Akishev, A. A. Deryugin, V. B. Karal'nik, *et al.*, Fiz. Plazmy **20**, 571 (1994) [Plasma Phys. Rep. **20**, 511 (1994)].

Translated by N. F. Larionova

Plasma Physics Reports, Vol. 26, No. 2, 2000, pp. 164–173. Translated from Fizika Plazmy, Vol. 26, No. 2, 2000, pp. 179–189.

LOW-TEMPERATURE PLASMAS

Kinetic Theory of a Gas-Discharge Positive Column and Wall Sheath

S. A. Dvinin, V. A. Dovzhenko, and A. A. Kuzovnikov

Moscow State University, Vorob'evy gory, Moscow, 119899 Russia

Received February 9, 1999; in final form, April 16, 1999

Abstract—The positive column and wall sheath in a gas discharge are studied with allowance for ion collisions in a plasma and ion reflection from a solid surface under conditions of incomplete ion neutralization. The kinetic equation for ions in a positive column is reduced to a Fredholm equation of the second kind. This makes it possible to solve the kinetic equation using a resolvent and thereby derive a single integrodifferential equation for the potential, which is referred to as a generalized plasma–sheath equation. Specific versions of the plasma–sheath equation are obtained that take into account charge exchange of the ions in a plasma and the thermal spread in velocities of the ionization-produced ions. *© 2000 MAIK "Nauka/Interperiodica".*

INTRODUCTION

One of the problems in classical physics of a gas discharge that has remained unresolved is the problem of calculating the parameters of the positive plasma column in the range of intermediate pressures at which the ion motion toward the plasma boundary ceases to be collisionless and classical ambipolar diffusion has not yet come into play. The Langmuir–Tonks theory [1], which implies that the ion mean free path λ_i is much longer than the characteristic dimension R of the discharge, yields correct results only for $\lambda_i > 10R$. The Schottky theory [2] applies to the range $\lambda_i < 0.03R$. Taking into account the so-called "anomalous drift" of the ions and assuming that the ion mean free path is constant makes it possible to construct an analogue of the Schottky theory but for $\lambda_i < 0.3R$. Further refinements aimed at incorporating ion inertia into the hydrodynamic approximation did not substantially extend the theory to the range of lower pressures, nor did they make it possible to pass over to the limit $\lambda_i \longrightarrow \infty$ correctly. In [3], we derived a collisionless plasma–sheath equation appropriate for describing the range of intermediate pressures under the assumptions that the only collisional mechanism for the ions is charge exchange and the initial energy of both charge-exchange and ionization-produced ions is zero. Although we succeeded in filling the gap in the range $0.03R < \lambda_i < 10R$, some questions remain unresolved. First, using the method proposed in [3], we can in principle generalize the collisional plasma–sheath equation to the case in which the ion mean free path depends on energy, but doing so is complex and laborious. Also, it becomes more difficult to pass over to the classical Schottky theory, which assumes that the ion drift proceeds in the normal regime, i.e., the ion–atom collision frequency (rather than the ion mean free path) is constant.[1] Second, we are justified in exclusively taking into account charge exchange processes (neglecting ion–ion elastic collisions) only in the case of monatomic gases, while, in gas mixtures, elastic collision cross sections are usually larger than the charge-exchange cross sections, because the electron structures of the colliding particles are different. Third, since this method fails to construct perturbation theory for the collisional plasma–sheath equation, it is inappropriate for studying unsteady processes and incorporating ion–neutral and ion–ion elastic collisions. The collisional plasma–sheath equation cannot be used to allow for incomplete ion recombination on the walls and its influence on the properties of a positive column (PC). An alternative to the approach proposed in [3] is the method for simulating particle dynamics in a discharge plasma by modeling chemical transformations with Monte Carlo calculations [4]. However, this method also fails to construct perturbation theory (e.g., to study the waves propagating in a discharge plasma); moreover, it involves a considerable expenditure of computational effort (in comparison with the plasma–sheath equation).

Incorporating the above-mentioned processes will require further refinement of the theory by way of solving the ion kinetic equation. This makes it possible not only to determine the spatial distributions of the poten-

[1] The ion mobilities in normal and anomalous regimes are different because, in the first case, the stochastic velocity V_{Ti} of the ions is higher than their directed velocity V. Consequently, it is stochastic velocity that governs the collision frequency ν and ion mobility μ, which are both independent of the ambipolar electric field E_a in a plasma. In the case of anomalous drift, the ion stochastic velocity is on the order of the ion directed velocity, so that we have $\nu \approx \lambda_i/V$ and $\mu \sim \sqrt{E_a}$.

1063-780X/00/2602-0164$20.00

tial and particles but also to evaluate the ion velocity distribution function (IVDF) at an arbitrary point in space (in particular, at the wall, which is especially important from the standpoint of applications). In this paper, we will show that solving the time-independent kinetic equation systematically together with Poisson's equation and the equilibrium equation for the electrons results in a hierarchy of integrodifferential equations, which are similar in structure to the plasma–sheath equation (they even go over to this equation in a certain limit) and can be used to examine the above processes. Time-dependent equations of the perturbation theory for this hierarchy are also integrodifferential equations. The problem in question is of interest not only from a methodological standpoint but also from the standpoint of practical applications, because the parameter values under consideration here are characteristic of plasmochemical devices used in microelectronics [5].

1. MAIN MODEL ASSUMPTIONS AND BASIC EQUATIONS

The main assumptions underlying our model are as follows.

(i) The plasma column is nonuniform in one direction and occupies the region $-L < x < L$.

(ii) The plasma in the PC consists of electrons, neutrals, and singly charged ions of one species.

(iii) The discharge has no impact on the spatial distribution of neutrals or on their temperature T_g.

(iv) The electron velocity distribution over the PC is Maxwellian with a coordinate-independent temperature T_e.

(v) The main ionization mechanism is direct ionization by electron impact from the ground state, and the main recombination mechanism is recombination on the walls. The ionization-produced ions obey the velocity distribution function $f_i^0(\mathbf{V})$. For the plasma–sheath equation from [1], we have $f_i^0(\mathbf{V}) = \delta(\mathbf{V})$, where $\delta(V)$ is the Dirac delta function. Along with $\delta(x)$, we will also use the Heaviside step function $\theta(x)$ defined by $\theta(x) = 1$ for $x \geq 0$ and $\theta(x) = 0$ for $x < 0$.

(vi) The ions moving in a PC collide with neutrals; each collision event can be regarded as either an elastic collision or charge exchange between an ion and a neutral.

(vii) Ion–ion collisions are neglected; otherwise, the collision integral would be nonlinear in the IVDF and the problem becomes far more difficult to solve in general form. This assumption is not very strict, because, in most regimes of the PC in a gas discharge, the degree of ionization is not too high and can be taken into account using perturbation theory.

(viii) The electric field potential in a PC is monotonic.

(ix) Correlations between the ions that are reflected from the wall and neighboring ions are neglected.

Note that these assumptions, except for (vi) and (ix), coincide with those made in [1, 2]. Which discharge regime occurs depends on the details of condition (vi). Condition (ix) differs from an analogous condition that was used in [1, 2] and implies 100% ion recombination on the wall. Also, condition (ix) makes it possible to take into account ion emission, i.e., such ion reflections from the wall as a result of which not all of the ions recombine into neutrals.

We describe the ions using the kinetic equation

$$\frac{\partial f}{\partial t} + (\mathbf{V}\nabla) f - \frac{e}{M}\left(\nabla\varphi\frac{\partial f}{\partial \mathbf{V}}\right) = I, \qquad (1.1)$$

where M is the mass of an ion, $f(\mathbf{V}, x)$ is the IVDF, I is the ion–ion collision integral, φ is the electric field potential, and $e > 0$ is an elementary electric charge.

Under the above assumptions, the collision integral in (1.1) can be written as

$$I = I_e + I_N, \quad I_e = n_e \nu_i(T_e) f_i^0(\mathbf{V}),$$
$$I_N = -\int_{-\infty}^{\infty} (K(\mathbf{V}, \mathbf{V}') f(\mathbf{V}) - K(\mathbf{V}', \mathbf{V}) f(\mathbf{V}')) d\mathbf{V}'. \qquad (1.2)$$

The first term in (1.2) describes the ionization-produced ions and the second term describes the loss of fast ions due to charge exchange, the appearance of new ions via the same process, and elastic scattering of ions by neutrals.[2] The number of ion–ion collision events is proportional to the squared distribution function, and ion–ion collisions cannot be described by formula (1.2). Assumption (ix) allows us to write the boundary

[2] Expression (1.2) is a reduced Boltzmann collision integral describing collisions between ions and particles of species j, which are either electrons or neutral particles (see, e.g., [6]):

$$I_j(\mathbf{V}, \mathbf{V}') = -\int d\Omega d\mathbf{V}_j (|\mathbf{V} - \mathbf{V}_j|)\sigma(|\mathbf{V} - \mathbf{V}_j|, \tilde{\theta}) f(\mathbf{V}) f_j(\mathbf{V}_j) + \int d\Omega d\mathbf{V}_j (|\mathbf{V} - \mathbf{V}_j|)\sigma(|\mathbf{V} - \mathbf{V}_j|, \tilde{\theta}) f(\mathbf{V}') f_j(\mathbf{V}_j'), \qquad (1.2a)$$

where f_j is the distribution function of the particles of species j, $\tilde{\theta}$ is the scattering angle, and $d\Omega = \sin\tilde{\theta}\, d\tilde{\theta}\, d\varphi$ is a solid angle in velocity space. The velocities $\mathbf{V}'$ and $\mathbf{V}_j'$ of the particles after they have experienced a collision are governed by their velocities $\mathbf{V}$ and $\mathbf{V}_j$ before the collision event and by the angle $\tilde{\theta}$ between the vectors $\mathbf{V} - \mathbf{V}_j$ and $\mathbf{V}' - \mathbf{V}_j'$. The first term in (1.2) describes the loss of ions with velocity $\mathbf{V}$ due to their scattering by neutrals, and the second term describes the appearance of new ions with the same velocity due to the reverse process.

condition for the ions at the wall as

$$f(-V_x, V_y, V_z, L)\big|_{V_x>0} = \int_0^\infty dV_x' \int_{-\infty}^\infty dV_y' \int_{-\infty}^\infty dV_z' \Gamma(V_x, V_y, V_z, V_x', V_y', V_z') \times f(V_x', V_y', V_z', L)\Big|_{V_x'>0} + Q(V_x, V_y, V_z). \quad (1.3)$$

The function Γ is governed by the physical processes on the wall. In the simplest case of 100% ion recombination (which was treated in the classical models of the PC of a gas discharge, in particular, in the Schottky model and the plasma–sheath equation), we have $\Gamma = 0$.[3] The last term $Q(V_x, V_y, V_z)$ describes ion emission from the electrode surface as a result of, e.g., the ionization of neutral atoms hitting an electrode. This emission, which is unimportant under conditions typical of the PC in a conventional gas discharge, can play a decisive role in the processes near the cathode in thermal-emissive converters, in which the discharges are ignited in alkali-metal vapors [7]. For convenience of further analysis, we do not specify here the function Γ.

We describe the electron behavior using the following equilibrium equation, which is a consequence of the relevant dynamic equation without allowance for electron inertia:

$$n_e = n_0 \exp(e\varphi/kT_e), \quad (1.4)$$

where k is the Boltzmann constant, n_e is the electron density, T_e is the electron temperature, m is the mass of an electron, and n_0 is the electron density at zero potential. The conditions under which formula (1.4) is valid were discussed in our earlier paper [8]. The ambipolar electric field in a plasma satisfies Poisson's equation:

$$\frac{d^2\varphi}{dx^2} = 4\pi e\left\{n_0 \exp\left(\frac{e\varphi}{kT_e}\right) - \int_{-\infty}^\infty dV_x' \int_{-\infty}^\infty dV_y' \int_{-\infty}^\infty dV_z' f(V_x', V_y', V_z')\right\}. \quad (1.5)$$

Equations (1.2)–(1.5) should be supplemented with the boundary conditions for Poisson's equation,

$$\left.\frac{d\varphi}{dx}\right|_{x=L} = 4\pi\sigma, \quad \frac{d\sigma}{dt} = -\frac{1}{4}n_e e V_T + ne(\boldsymbol{\xi}\mathbf{V}), \quad (1.6)$$

where $V_T = \sqrt{8kT_e/\pi m}$ is the most probable electron velocity, σ is the surface charge density, and $\boldsymbol{\xi}$ is a vector normal to the boundary. Since the potential is specified to within an arbitrary constant, we can assume that it is equal to zero ($\varphi|_{x=0} = 0$) at the plasma center. The effect of a deviation of the electron energy distribution function (EEDF) from a Maxwellian in the range of high energies was studied by Baksht *et al.* [9]. This deviation, which may substantially affect the magnitude of the electron current, can be incorporated into our model by introducing the kinetic reflection coefficient γ such that $j_e = j_0 \times \gamma$. We also assume that the charged-particle density distribution in a plasma is symmetric and switch from the boundary conditions at the wall $x = -L$ to the conditions at the coordinate origin,

$$\left.\frac{d\varphi}{dx}\right|_{x=0} = 0, \quad (1.6a)$$

$$\left.\frac{df(\mathbf{V})}{dx}\right|_{x=0} = 0 \quad \text{or} \quad f(V_x, V_y, V_z) = f(-V_x, V_y, V_z)\big|_{x=0}. \quad (1.3a)$$

We denote the potential at the wall (which should be determined from solving the basic equations) with respect to the potential at the plasma center by φ_0.

2. SOLUTION TO THE ION KINETIC EQUATION AND DERIVATION OF ANALOGUES OF THE PLASMA–SHEATH EQUATION

The time-independent ion kinetic equation (1.1) with the collision integral (1.2) can be solved by the method of characteristics. Since the ions are accelerated when they move toward the wall, we assign the relevant ion velocity at the wall to each of the characteristics. It is convenient to solve the kinetic equation by dividing the IVDF into two parts describing the ions with oppositely directed velocities,

$$f^+(x, V_x, V_y, V_z) = \begin{cases} f(x, V_x, V_y, V_z), & V_x \ge 0 \\ 0, & V_x < 0 \end{cases}$$
$$f^-(x, V_x, V_y, V_z) = \begin{cases} 0, & V_x \ge 0 \\ f(x, V_x, V_y, V_z), & V_x < 0. \end{cases} \quad (2.1)$$

Since we do not need f^+ in the region $V_x < 0$ or f^- in the region $V_x > 0$, we set these functions to zero in (2.1); however, they can also be predefined in a different manner. The function f^+ describes the particles that move toward the wall, and the function f^- refers to the particles moving away from the wall. Under the assumptions made, the kinetic equation (1.1) is equivalent to a set of ordinary differential equations. In terms of the functions f^+ and f^- just introduced, the ion kinetic equation takes the form

$$\frac{\partial f^\pm}{\partial t} + (\mathbf{V}\nabla) f^\pm - \frac{e}{M}\left(\nabla\varphi \frac{\partial f^\pm}{\partial \mathbf{V}}\right) = I^\pm, \quad (2.2)$$
$$I^+ = I_e^+ + I_N^+, \quad I_e^+ = n_e \nu_i(T_e) f_i^{0+}(\mathbf{V}),$$

[3] Note that $\Gamma(\mathbf{V}, \mathbf{V}')$ in (1.3) is related to the probability $\gamma(\mathbf{V}, \mathbf{V}')$ that the reflection of an ion from the wall is not accompanied by its recombination into a neutral atom through the relationship $\Gamma(\mathbf{V}, \mathbf{V}') = \gamma(\mathbf{V}, \mathbf{V}')[V_x'/V_x]$.

$$I_N^+ = -\int_0^\infty dV_x' \int_{-\infty}^\infty (K^+(\mathbf{V}, \mathbf{V}') f^+(\mathbf{V}) - K^+(\mathbf{V}', \mathbf{V}) f^+(\mathbf{V}')) dV_y' dV_z' \quad (2.3a)$$

$$- \int_0^\infty dV_x' \int_{-\infty}^\infty (K^-(\mathbf{V}, \mathbf{V}') f^-(\mathbf{V}) - K^-(\mathbf{V}', \mathbf{V}) f^+(\mathbf{V}')) dV_y' dV_z',$$

$$I^- = I_e^- + I_N^-, \quad I_e^- = n_e \nu_i(T_e) f_i^{0-}(\mathbf{V}),$$

$$I_N^- = -\int_0^\infty dV_x' \int_{-\infty}^\infty (K^+(\mathbf{V}, \mathbf{V}') f^-(\mathbf{V}) - K^+(\mathbf{V}', \mathbf{V}) f^-(\mathbf{V}')) dV_y' dV_z' \quad (2.3b)$$

$$- \int_0^\infty dV_x' \int_{-\infty}^\infty (K^-(\mathbf{V}, \mathbf{V}') f^+(\mathbf{V}) - K^-(\mathbf{V}', \mathbf{V}) f^-(\mathbf{V}')) dV_y' dV_z'.$$

The first integral term in (2.3a) [or in (2.3b)] describes the scattering (or charge-exchange) events during which the projection of the velocity of the ions moving either toward the wall or away from it onto the x-axis does not reverse direction. The first part of this term describes losses of the ions that have experienced a scattering event, and the second part describes the appearance of ions with new velocities as a result of scattering. The second integral term describes ion losses resulting from the scattering events during which the projection of the ion velocity onto the x-axis reverses direction. Consequently, the first integral term in (2.3a), which describes the losses of ions with a given velocity due to scattering, corresponds to the second integral term in (2.3b) and vice versa.

The functions $f^\pm$ should also satisfy the boundary condition

$$f^-(L, V_x, V_y, V_z) = \int_0^\infty dV_x' \int_{-\infty}^\infty dV_y' \int_{-\infty}^\infty dV_z' \Gamma(V_x, V_y, V_z, V_x', V_y', V_z') \times f^+(L, V_x', V_y', V_z') + Q(V_x, V_y, V_z). \quad (2.4)$$

The partial differential equation is equivalent to the following set of ordinary differential equations (see, e.g., [10]):[4]

$$\pm \frac{dx}{V_x} = \frac{dV_x}{-\frac{e}{M}\frac{d\varphi}{dx}} = \frac{df^\pm}{I^\pm} = ds. \quad (2.5)$$

[4] Although equations (2.5) are equivalent to a time-dependent kinetic equation (ds is the time differential), below, we will be interested only in steady-state processes.

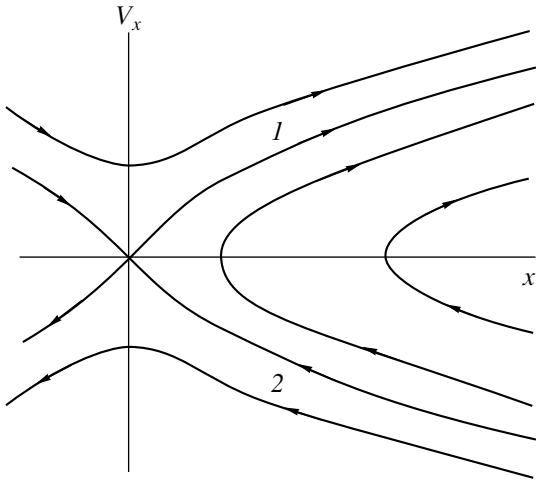

Characteristics of the kinetic equation on the plane of the independent variables x and V_x.

The characteristics of equation (2.2) satisfy the equation

$$\pm V_x dV_x = \frac{e}{M}\frac{d\varphi}{dx} dx = \frac{e}{M} d\varphi, \quad (2.6)$$

and the distribution function obeys the equation

$$df^\pm = \pm \frac{I^\pm dx}{V_x}. \quad (2.7)$$

Relationship (2.6) reflects energy conservation along the characteristics. According to assumption (vii), the PC contains no trapped particles (i.e., particles that do not collide with the wall) and the characteristics on the plane of the independent variables V_x and x are as shown in the figure. Characteristics *1* and *2*, which pass through the origin of the coordinates ($x = 0$, $V_x = 0$), are separatrices. We outline some features of formula (2.5) that are important for practical applications. Formula (2.5) implies that, in the absence of sources, the IVDF is constant along the characteristics. Collisions between the particles cause the ions to pass over from one characteristic to another (as a result of scattering or charge exchange) and lead to the appearance of ionization-produced ions on the characteristics. On the other hand, it is well known that, during the acceleration of a charged-particle beam in the absence of particle sources, the beam density in space decreases. This illusory contradiction stems from the fact that the distribution functions are normalized in a different manner. The constancy of the IVDF along the characteristics indicates that the phase volume is conserved: the particle acceleration is accompanied by stretching the elementary volume in phase space along the coordinate axes (so that the density decreases) and squeezing this volume along the velocity axes.

Since all of the characteristics originate or terminate at the wall, we will describe them by the relevant ion velocities V_{x0} on the wall.

Now, we are going to derive an integral equation that is equivalent to equations (2.5) and refers to an arbitrary monotonic potential distribution, which is assumed to be known. We integrate the equation for f^- from the point x to the point at which the ions are reflected (and their velocities vanish). Since the condition $f^-(x, 0) = f^+(x, 0)$ holds at the reflection point, we integrate f^+ from this point to the point $\tilde{x}$. As a result, we obtain the desired integral relationship. Note that, for ions with energies high enough to overcome the potential barrier, the functions f^+ and f^- are equal to one another at the center $x = 0$ of a PC by virtue of the symmetry relation $f^-(0, -|V_x|) = f^+(0, |V_x|)$. The IVDFs in both energy ranges can be related through a single integral in terms of the Heaviside step function $\theta(V_x^2)$:

$$\begin{aligned} &f^+(\tilde{x}, V_x(\tilde{x}, |V_{x0}|), V_y, V_z) \\ &= f^-(x, V_x(x, -|V_{x0}|), V_y, V_z) \\ &+ \left\{ \int_0^x dx' \theta(MV_{x0}^2 - 2e(\varphi(x) - \varphi_0)) I^-(x', V_x, f^\pm) \right. \\ &\left. + \int_0^{\tilde{x}} dx' \theta(MV_{x0}^2 - 2e(\varphi(x) - \varphi_0)) I^+(x', V_x, f^\pm) \right\} / |V_{x0}|. \end{aligned} \tag{2.8}$$

Analogously, integrating equation (2.7) for f^+ from x to L and then integrating the equation for f^- from L to x with allowance for the boundary condition (1.3) yields the following relationship:[5]

$$\begin{aligned} &f^-(\tilde{x}, V_x(\tilde{x}, V_{x0}), V_y, V_z) \\ &= \int_0^\infty dV_x' \int_{-\infty}^\infty dV_y' \int_{-\infty}^\infty dV_z' \Gamma(V_{x0}, V_y, V_z, V_{x0}', V_y', V_z') \\ &\times [f^+(x, V_x'(x, V_{x0}), V_y', V_z') \\ &+ \left\{ \int_x^L dx \theta(MV_0^2 - 2e(\varphi(x) - \varphi_0)) \right. \\ &\left. \times I^+(x, V_x'(x, V_{x0}), f^\pm(x, V_{x0})) \right\} / |V_{x0}|] \\ &+ \left\{ \int_{\tilde{x}}^L dx \theta(MV_0^2 - 2e(\varphi(x) - \varphi_0)) \right. \\ &\left. \times I^-(x, V_x(x, V_{x0}), f^\pm(x, V_{x0})) \right\} / |V_{x0}|. \end{aligned} \tag{2.9}$$

[5] Without loss of generality, ion emission from the wall, described by the term with $Q(V_x, V_y, V_z)$, can be regarded as an additional internal source that produces ions with velocities $V_x < 0$ at $x = L$:

$$I^{add+}(x, \mathbf{V}) = 0,$$
$$I^{add-}(x, V_x, V_y, V_z) = \delta(x - L) V_x Q(V_x, V_y, V_z).$$

Equations (2.8) and (2.9) can be reduced to the following equation for the IVDF:

$$\begin{aligned} &f(\tilde{x}, V_x(\tilde{x}, V_{x0}), V_y, V_z) \\ &= \int_{-\infty}^\infty dV_x' \int_{-\infty}^\infty dV_y' \int_{-\infty}^\infty dV_z' \tilde{Z}(V_x, V_y, V_z, V_x', V_y', V_z', x, \tilde{x}) \\ &\times f(x, V_x', V_y', V_z') \\ &+ \int_{-\infty}^\infty dV_x' \int_{-\infty}^\infty dV_y' \int_{-\infty}^\infty dV_z' \int_0^L dx Z(\tilde{x}, x, V_x, V_y, V_z, V_x', V_y', V_z') \\ &\times [\theta(MV_0^2 - 2e(\varphi(x) - \varphi_0)) I(x)] / |V_{x0}|. \end{aligned} \tag{2.10}$$

Since the functions $Z(\tilde{x}, x, V_x, V_y, V_z, V_x', V_y', V_z')$ and $\tilde{Z}(V_x, V_y, V_z, V_x', V_y', V_z', x, \tilde{x})$ are very cumbersome, we will omit them to save space. Assumptions (ii)–(vii) enable us to simplify (2.10) by dividing the ion sources into two groups: the sources associated with ionization, which are independent of the IVDF, and the sources associated with elastic collisions and charge exchange, which produce ions at a rate linearly dependent on the IVDF. Simple but fairly involved transformations show that equation (2.10) is equivalent to a Fredholm equation of the second kind for the IVDF:

$$\begin{aligned} &f(\tilde{x}, V_x(\tilde{x}, V_{x0}), V_y, V_z) \\ &= \int_0^\infty dV_x' \int_{-\infty}^\infty dV_y' \int_{-\infty}^\infty dV_z' \int_0^L dx G^E(\tilde{x}, x, V_x, V_y, V_z, V_x', V_y', V_z') \\ &\times n_e \nu_i(T_e) f_i^0(\mathbf{V}) + \lambda \int_0^\infty dV_x' \int_{-\infty}^\infty dV_y' \int_{-\infty}^\infty dV_z' \\ &\times \int_0^L dx G^I(\tilde{x}, x, V_x, V_y, V_z, V_x', V_y', V_z') \\ &\times f(x, V_x'(x, V_{x0}), V_y', V_z'), \end{aligned} \tag{2.11}$$

where the factor λ is equal to unity.[6] This indicates that the solution to equation (2.11) necessarily exists and can be expressed in terms of a Fredholm resolvent:

$$\begin{aligned} &f(x, \mathbf{V}) \\ &= \int_0^L dx' \int_{-\infty}^\infty \int_{-\infty}^\infty \int_{-\infty}^\infty d^3\mathbf{V}' \tilde{R}_\lambda(x, x', \mathbf{V}, \mathbf{V}', \varphi) J(x', \mathbf{V}')|_{\lambda = 1}. \end{aligned} \tag{2.12}$$

The tilde indicates that the resolvent is generally an operator with respect to the potential; i.e., the resolvent

[6] We will not write out explicit expressions for the functions G^E and G^I, because they are very cumbersome.

depends not only on $\varphi(x)$ but also on all the derivatives of the potential with respect to the coordinate. The resolvent can be most easily evaluated iteratively, in which case we arrive at the Neumann series

$$\tilde{R}_\lambda(x, x', \mathbf{V}, \mathbf{V}') = \sum_{n=0}^{\infty} G^I_{n+1}(x, x', \mathbf{V}, \mathbf{V}')\lambda^n, \quad (2.13)$$

where

$$G^I_1(x, x', \mathbf{V}, \mathbf{V}') = G^I(x, x', \mathbf{V}, \mathbf{V}'),$$
$$G^I_{n+1}(x, x', \mathbf{V}, \mathbf{V}') = \int d^3\mathbf{V}_1 dx_1 G^I_n(x, x_1, \mathbf{V}, \mathbf{V}_1) \quad (2.14)$$
$$\times G^I_1(x_1, x', \mathbf{V}_1, \mathbf{V}').$$

The construction of the operator G^I implies that it transforms the IVDF to a distribution function that is established after the ions have completed their motion along the characteristics.[7] Since some of the ions moving along the characteristics recombine on the wall, the series in (2.13) appears to be an expansion in powers of a small parameter equal to the probability (or, more precisely, to the square root of the probability) for an ion to return to its starting point (possibly, with a different velocity). When both elastic scattering in the plasma and ion reflection from the wall are absent, only the first term in the series in (2.13) is nonzero (see Section 3.1). Generally, at $\lambda = 1$, the series may converge fairly slowly. However, for most of the physically interesting cases we will analyze below (e.g., for the plasma–sheath equation [1, 12] or for the collisional plasma–sheath equation [3, 8]), we can evaluate the resolvent exactly.[8] The plasma states described by the corresponding solutions to the integral equation can be regarded as the initial states to which perturbation theory has to be applied (possibly, with another small parameter, e.g., the ion-to-electron temperature ratio). For further analysis, convergence of the series in (2.13) is an important issue, because it ensures the desired analytic properties of the resolvent and provides the possibility of representing the IVDF through the source terms for a prescribed potential with the help of relationship (2.12).[9] Representation (2.13) illustrates how the resolvent depends on the potential,

$$\tilde{R}(\varphi) = \sum_{n=1}^{\infty} \int dx_1 dx_2 \ldots dx_{n-1} F_n(\varphi(x), \varphi(x_1), \ldots, \varphi(x_n)). \quad (2.13a)$$

Knowing solutions to equation (2.11), we can use the relationships discussed above to calculate the IVDF (2.12) at an arbitrary point in space and then reduce the basic equations to the following integrodifferential equation for the potential:

$$\frac{d^2\varphi}{dx^2} = 4\pi e n_0 \left\{ \exp\left(\frac{e\varphi(x)}{kT_e}\right) \right.$$
$$\left. - \int_{-\infty}^{\infty} dV_x \int_{-\infty}^{\infty} dV_y \int_{-\infty}^{\infty} dV_z \int_0^L dx' \int_0^{\infty} d\mathbf{V}' \tilde{R}(x, x', \mathbf{V}, \mathbf{V}', \varphi) \right. \quad (2.15)$$
$$\left. \times f_i^0(\mathbf{V}')\nu_i \exp\left(\frac{e\varphi(x')}{kT_e}\right) \right\},$$

which will be referred to as a generalized plasma–sheath equation.

We supplement equation (2.15) with the boundary conditions

$$\varphi(0) = 0, \quad \left.\frac{d\varphi}{dx}\right|_{x=0} = 0,$$
$$\frac{1}{4} e V_T n_0 \exp\left(\frac{e\varphi(L)}{kT_e}\right) - ne V_x\big|_{x=L} = 0. \quad (2.16)$$

The first condition reflects the fact that the potential is specified to within an arbitrary constant, the second condition implies the symmetry of the plasma column, and the third condition indicates charge conversion at the wall. It is convenient to obtain an expression for the hydrodynamic ion velocity from the ion continuity equation. As a result, the last boundary condition in (2.16) becomes

$$\left\{ \int_0^x \nu_i(x') \exp\left(\frac{e\varphi(x')}{kT_e}\right) dx' \right.$$
$$\left. - \frac{1}{4} V_T \exp\left(\frac{e\varphi(x)}{kT_e}\right) \right\}\Bigg|_{x=L} = 0. \quad (2.16a)$$

Hence, we have formulated the eigenvalue problem for determining the potential distribution in the PC of a gas discharge. The problem appears to be nonlinear and nonlocal with respect to the potential. The eigenvalue of the problem is the ionization rate in a plasma.

Equation (2.15) is a version of the complete plasma–sheath equation, which was derived by Lang-

[7] Strictly speaking, the operator should be applied to the IVDF twice.

[8] In the absence of ion collisions in a plasma, integration over the coordinate is independent of integration over velocities, so that equation (2.11) can be treated in velocity space $\mathbf{V}$ rather than in phase space $(x, \mathbf{V})$ (see Section 3.1 for details). In other words, the order of equation (2.11) can be lowered by unity.

[9] To save space, we will omit a rigorous mathematical proof that the series in (2.13) converges.

muir and Tonks [1] in the form

$$\frac{d^2\varphi}{dx^2} = 4\pi e\left\{n_0\exp\left(\frac{e\varphi(x)}{kT_e}\right) - \int_0^x \frac{dx'}{V_x(x')}\nu_i n_0\exp\left(\frac{e\varphi(x')}{kT_e}\right)\right\}. \quad (2.17)$$

Expression $V_x(x, x') = \sqrt{(2e/M)(\varphi(x') - \varphi(x))}$ converts equation (2.17) to the familiar plasma–sheath equation. Langmuir and Tonks [1] showed that neglecting the second-order derivative of the potential and using the expression $V_x(x) = \mu_i E(x)$ transforms equation (2.17) into the ambipolar diffusion equation. Below, we will analyze some models that make it possible to consider the intermediate range $\lambda_i \sim 1$. Note that Langmuir and Tonks excluded ion emission and incomplete ion recombination on the wall from the analysis. We emphasize that, in many cases of practical importance, the kernel of equation (2.15) is degenerate, so that this equation is easier to solve (its solutions can also be used as initial states in implementing the algorithms based on perturbation theory).

The above analysis may be generalized to the case of discharges maintained externally by an ionizer or by ion emission from the wall [12]. Let the density of the ions that have velocity $\mathbf{V}$ and are produced by an external ionizer at the point x be $N(x, \mathbf{V})$ and let the distribution function of the ions emitted from the wall be $Q(\mathbf{V})$. Then, by virtue of charge conservation, the density of the electrons that originate at the same point is equal to the integral of N over velocities. In this case, equation (2.15) has the form

$$\frac{d^2\varphi}{dx^2} = 4\pi e\left\{n_0\exp\left(\frac{e\varphi(x)}{kT_e}\right) - \int_{-\infty}^{\infty}dV_x\int_{-\infty}^{\infty}dV_y\int_{-\infty}^{\infty}dV_z \times \int_0^{\infty}d\mathbf{V}'\left\{\tilde{R}^Q(x, \mathbf{V}, \mathbf{V}', \varphi)Q(\mathbf{V}') + \int_0^L dx'\tilde{R}(x, x', \mathbf{V}, \mathbf{V}', \varphi) \times \left\{\nu_i n_0 f_i^0(\mathbf{V}')\exp\left(\frac{e\varphi(x')}{kT_e}\right) + N(x', \mathbf{V}')\right\}\right\}\right\}, \quad (2.18)$$

and the boundary condition (2.16a) becomes

$$\left\{\int_0^x\left\{\nu_i(x')e^{\left(-\frac{e\varphi(x')}{kT_e}\right)} + \int_{-\infty}^{\infty}d^3\mathbf{V}'\frac{N(x', \mathbf{V}')}{n_0}\right\}dx' - \int_{-\infty}^{\infty}d^3\mathbf{V}V_x Q(\mathbf{V}) - \frac{1}{4}V_T e^{\left(-\frac{e\varphi(x)}{-kT_e}\right)}\right\}\Bigg|_{x=L} = 0. \quad (2.19)$$

In accordance with the footnote to formula (2.9), R^Q can be expressed in terms of R as

$$\tilde{R}^Q(x, \mathbf{V}, \mathbf{V}', \varphi) = \tilde{R}(x, L, \mathbf{V}, \mathbf{V}', \varphi)\theta(-V_x)V_x. \quad (2.20)$$

Below, we will consider specific versions of the boundary-value problem (2.14)–(2.19) for a PC with 100% ion recombination on the wall. The equations that refer to various models of ion emission and incomplete ion recombination on the wall and describe the influence of these processes on the properties of a PC will be considered in subsequent papers.

3. PLASMA–SHEATH EQUATION FOR A PC WITH 100% ION RECOMBINATION ON THE WALL

A version of the boundary-value problem (2.2)–(2.4) that assumes 100% ion recombination on the wall and in which the Fredholm resolvent can be obtained in an explicit form is the most important and was studied first. The simplest version of the model problem is the one described by the plasma–sheath equation derived by Langmuir and Tonks as early as 1929 [1].

3.1. Plasma–Sheath Equation

We work from assumptions (i)–(v) and (viii) and, following Langmuir and Tonks, assume that, first, the neutral pressure is low enough (the mean free path is shorter than the transverse dimensions of the plasma column) to ignore ion–ion collisions (mathematically, this indicates that $I_N \equiv 0$) and, second, the ions do not recombine into neutrals as they are reflected from the wall ($\Gamma \equiv 0$). In this case, the resolvent for the kinetic equation has the form

$$R(x, x', V_x, V_x') = \theta(x' - x)\theta(MV_x'^2 - 2e(\varphi(x) - \varphi(x')))/\sqrt{V_x'^2 - (2e/M)(\varphi(x) - \varphi(x'))}\,\theta(-V_x') \times \left\{\delta\left(V_x - \sqrt{V_x'^2 - (2e/M)(\varphi(x) - \varphi(x'))}\right) + \delta\left(V_x + \sqrt{V_x'^2 - (2e/M)(\varphi(x) - \varphi(x'))}\right)\right\} + \theta(x - x')\theta(V_x')\delta\left(V_x - \sqrt{V_x'^2 - (2e/M)(\varphi(x) - \varphi(x'))}\right)/\sqrt{V_x'^2 - (2e/M)(\varphi(x) - \varphi(x'))},$$

and

$$R^Q(x, V_x, V_x') = \theta(x' - x)\theta(MV_x'^2 - 2e(\varphi(x) - \varphi(L)))V_x/\sqrt{V_x'^2 - (2e/M)(\varphi(x) - \varphi(L))} \times \left\{\delta\left(V_x - \sqrt{V_x'^2 - (2e/M)(\varphi(x) - \varphi(L))}\right) + \delta\left(V_x + \sqrt{V_x'^2 - (2e/M)(\varphi(x) - \varphi(L))}\right)\right\}.$$

Langmuir and Tonks also assumed that the ions originate with a zero initial velocity, $I_e = n_e\nu_i(T_e)\delta(\mathbf{V})$, so that we have

$$f^-(x, V_x(x, V_{x0}), V_y, V_z) \equiv 0, \tag{3.1}$$

$$f^+(x, V_x, V_y, V_z) = \int_0^x dx' n_e(x')\nu_i(T_e) \times \delta\left(V_x - \left(\frac{2e}{M}(\varphi(x') - \varphi(x))\right)^{1/2}\right)\delta(V_y)\delta(V_z)/|V_x|. \tag{3.2}$$

The ion density is calculated from the formula

$$n(x) = \int_0^\infty\int_0^\infty\int_0^\infty dV_x dV_y dV_z((f^-(x, V_x, V_y, V_z) + f^+(x, V_x, V_y, V_z))) = \int_0^x \{dx' n_e(x')\nu_i(T_e)/((\varphi(x') - \varphi(x))(2e/M))^{1/2}\}. \tag{3.3}$$

As is expected, the plasma–sheath equation with the potential-dependent electron density (1.4) coincides exactly with the equation derived by Langmuir and Tonks:

$$\frac{d^2\varphi}{dx^2} = 4\pi e n_0\left\{\exp\left(\frac{e\varphi(x)}{kT_e}\right) - \nu_i\int_0^x dx'\left\{\exp\left(\frac{e\varphi(x')}{kT_e}\right)/\left(\frac{2e}{M}(\varphi(x') - \varphi(x))\right)^{1/2}\right\}\right\}. \tag{3.4}$$

3.2. Plasma–Sheath Equation with Allowance for the Finite Energy of the Produced Ions

A first attempt at incorporating the finite velocity with which the ions are produced was made by Langmuir and Tonks [1]. They showed that the relevant correction is maximum at the center of the plasma column, where it is on the order of T_i/T_e. In the case at hand, we begin with reducing equations (2.8) and (2.9) to

$$f^+(x, V_x(x, |V_{x0}|), V_y, V_z) = f^-(x, -|V_x(x, |V_{x0}|)|, V_y, V_z) + \int_0^x \theta(MV_0^2 - 2e(\varphi(x) - \varphi_0))n_e\nu_i(f_i^{0+}(x', V_x) + f_i^{0-}(x', V_x))dx'/|V_x(x, |V_{x0}|)|, \tag{3.5}$$

$$f^-(x, V_x(x, |V_{x0}|), V_y, V_z) = \int_{\tilde{x}}^L \theta(MV_0^2 - 2e(\varphi(x) - \varphi(x')))n_e\nu_i f_i^{0-}(x', V_x)dx'/|V_x(x, |V_{x0}|)|. \tag{3.6}$$

Consequently, we have

$$n(x) = \left(\int_0^x n_e(x')\nu_i dx'\int_0^\infty dV'\frac{(f_i^{0+}(x', V') + f_i^{0-}(x', V'))\theta(MV'^2 - 2e(\varphi(x) - \varphi(x')))}{\sqrt{V'^2 - 2e(\varphi(x) - \varphi(x'))/M}} + \int_x^L n_e(x')\nu_i dx'\int_0^\infty dV'\frac{2f_i^{0-}(x', V')\theta(MV'^2 - 2e(\varphi(x) - \varphi(x')))}{\sqrt{V'^2 - 2e(\varphi(x) - \varphi(x'))/M}}\right), \tag{3.7}$$

so that the plasma–sheath equation becomes

$$\frac{d^2\varphi}{dx^2} = 4\pi e n_0\left\{\exp\left(\frac{e\varphi(x)}{kT_e}\right) - \nu_i\left(\int_0^x dx'\int_0^\infty dV' e^{\left(\frac{e\varphi(x')}{kT_e}\right)} \times\frac{(f_i^{0+}(x', V') + f_i^{0-}(x', V'))\theta(MV'^2 - 2e(\varphi(x) - \varphi(x')))}{\sqrt{V'^2 - 2e(\varphi(x) - \varphi(x'))/M}} + \int_x^L dx'\int_0^\infty dV' e^{\left(\frac{e\varphi(x')}{kT_e}\right)} \times\frac{2f_i^{0-}(x', V')\theta(MV'^2 - 2e(\varphi(x) - \varphi(x')))}{\sqrt{V'^2 - 2e(\varphi(x) - \varphi(x'))/M}}\right)\right\}. \tag{3.8}$$

Usually, there is no reason to assume that in a weak electric field in a plasma the distribution function of the ionization-produced ions is anisotropic and coordinate-dependent. Therefore, we can set $f_i^{0+}(x', V) = f_i^{0-}(x', V) = f_i^0(V) = f_i^0(-V)$ in order to simplify equation (3.8) to

$$\frac{d^2\varphi}{dx^2} = 4\pi e n_0 \left\{ e^{\left(\frac{e\varphi(x)}{kT_e}\right)} - \nu_i \int_0^L dx' \int_0^\infty dV' e^{\left(\frac{e\varphi(x')}{kT_e}\right)} \times \frac{2 f_i^0(V')\theta(MV'^2 - 2e(\varphi(x) - \varphi(x')))}{\sqrt{V'^2 - 2e(\varphi(x) - \varphi(x'))/M}} \right\}. \quad (3.9)$$

An analytic analysis of the solutions to equation (3.9) is nontrivial, because the ion-density decrease associated with the fact that the ions originate with nonzero velocities is partially balanced by the influx of ions having negative velocities and moving away from the wall. Consequently, we restricted ourselves to obtaining numerical estimates with the help of perturbation theory. Our estimates showed that the thermal spread in velocities of the ionization-produced ions raises the ionization rate required to maintain the discharge; moreover, in order of magnitude, we obtained $\delta\nu_i/\nu_{i0} \sim T_i/T_e$. In gas discharges, the T_e/T_i ratio usually lies between 100 and 1000, so that, for discharges in planar geometry, the correction introduced by the ion thermal motion is less than 2%.

3.3. Collisional Plasma–Sheath Equation

A collisional plasma–sheath equation was derived in our earlier paper [3]. In addition to assumptions (i)–(ix), we assume that the initial energy of the charge-exchange and ionization-produced ions is zero and all of the ions hitting the wall recombine on it. If the charge exchange rate depends on ion velocity, then we have

$$I_e = n_e \nu_i(T_e)\delta(\mathbf{V}),$$
$$I_N = \int_{-\infty}^{\infty} (\nu_r(\mathbf{V}') f(\mathbf{V}')\delta(\mathbf{V}) - \nu_r(\mathbf{V}) f(\mathbf{V})\delta(\mathbf{V}'))d\mathbf{V}', \quad (3.10)$$

where $\nu_i(T_e)$ is the ionization rate and $\nu_r(V)$ is the charge exchange rate, in which case equations (2.8) and (2.9) with zero velocity components V_y and V_z become

$$f^-(x, V_x) \equiv 0,$$
$$f^+(x, V_x) = -\int_0^x dx' \nu_r(V_x) f(x', V_x)/|V_x|$$
$$+ \int_0^x dx' \int_0^\infty dV_x' \nu_r(V_x') f(x', V_x')\delta(V_x - (2e(\varphi(x') - \varphi(x))/M)^{1/2})/|V_x| + \int_0^x dx' n_e(x')\nu_i(T_e) \times \delta(V_x - (2e(\varphi(x') - \varphi(x))/M)^{1/2})/|V_x|. \quad (3.11)$$

Equation (3.11) can be solved either numerically or by iteration,

$$f^{(0)+}(x, V_x) = \int_0^x dx' n_e(x')\nu_i(T_e) \times \exp\left(-\int_{x'}^x dx'' \frac{\nu_r((2e(\varphi(x') - \varphi(x''))/M)^{1/2})}{(2e(\varphi(x') - \varphi(x''))/M)^{1/2}}\right),$$
$$f^{(1)+}(x, V_x) = f^{(0)+}(x, V_x) + \int_0^x dx' \int_0^\infty dV_x \nu_r(V_x) f^{(0)+}(x', V_x) \times \exp\left(-\int_{x'}^x dx'' \frac{\nu_r((2e(\varphi(x') - \varphi(x''))/M)^{1/2})}{(2e(\varphi(x') - \varphi(x''))/M)^{1/2}}\right),$$
$$f^{(2)+}(x, V_x) = f^{(1)+}(x, V_x) + \int_0^x dx' \int_0^\infty dV_x \nu_r(V_x)[f^{(1)+}(x', V_x) - f^{(0)+}(x', V_x)] \times \exp\left(-\int_{x'}^x dx'' \frac{\nu_r((2e(\varphi(x') - \varphi(x''))/M)^{1/2})}{(2e(\varphi(x') - \varphi(x''))/M)^{1/2}}\right) \dots . \quad (3.12)$$

If the ion collision frequency is energy-independent, then we can substitute the series in (3.12) into Poisson's equation in order to obtain an equation that formally describes the normal regime of ion drift motion. However, since we neglected the thermal spread in velocities of the ionization-produced and charge-exchange ions, this equation does not reflect the physical essence of the normal drift regime. If the ion–neutral charge-exchange cross section is energy-independent, then we can sum up the above series to obtain an explicit expression for the resolvent,

$$f^+(x, V_x) = \int_0^x dx' \left\{ \frac{\delta(V_x - \sqrt{(2e/M)(\varphi(x') - \varphi(x))})}{\sqrt{(2e/M)(\varphi(x') - \varphi(x))}} \times e^{-(x-x')/\lambda_i} \left\{ \nu_i(x') e^{\frac{e\varphi(x')}{kT_e}} + \frac{1}{\lambda_i} \int_0^{x'} dx'' \nu_i(x'') e^{\frac{e\varphi(x'')}{kT_e}} \right\} \right\}. \quad (3.13)$$

In [3], this expression was obtained in a different way: instead of the kinetic equation, we used Newton's equation and the continuity equation and exploited the methods of probability theory.

In this case, the ion density is

$$n(x) = \int_0^x dx' \left\{ \frac{e^{-(x-x')/\lambda_i}}{\sqrt{(2e/M)(\varphi(x') - \varphi(x))}} \times \left\{ \nu_i(x') e^{\frac{e\varphi(x')}{kT_e}} + \frac{1}{\lambda_i} \int_0^{x'} dx'' \nu_i(x'') e^{\frac{e\varphi(x'')}{kT_e}} \right\} \right\}. \quad (3.14)$$

Substituting the expressions for electron and ion densities into Poisson's equation, we arrive at the desired integral equation for the potential:

$$\frac{d^2\varphi}{dx^2} = 4\pi e n_0 \left\{ \exp\left(\frac{e\varphi(x)}{kT_e}\right) - \int_0^x dx' \frac{\exp(-(x-x')/\lambda_i)}{\sqrt{(2e/M)(\varphi(x') - \varphi(x))}} \times \left\{ \nu_i(x') e^{\left(\frac{e\varphi(x')}{kT_e}\right)} + \frac{1}{\lambda_i} \int_0^{x'} dx'' \nu_i(x'') e^{\left(\frac{e\varphi(x'')}{kT_e}\right)} \right\} \right\}. \quad (3.15)$$

In [3], this equation was referred to as a collisional plasma–sheath equation. Since the ion thermal velocities are zero, this equation applies to the anomalous regime of ion drift and fails to describe the normal drift regime. The method for solving the collisional plasma–sheath equation was described in detail in [8], where we also discussed the range of PC parameters to which this equation is applicable.

CONCLUSION

We have proposed a method for solving the problem of maintaining the PC of a gas discharge. The method consists of the following. The ion motion is described by the kinetic equation, which is solved by the method of characteristics. This allows us to arrive at an integrodifferential equation for the potential, which is referred to as a generalized plasma–sheath equation, because the familiar plasma–sheath equation, which describes collisionless PCs, appears to be its specific version. With this approach, it is possible to take into account incomplete ion recombination on a solid surface, elastic ion scattering, and charge exchange and also evaluate the IVDF at an arbitrary point of the discharge (in particular, at the wall, which is especially important from the standpoint of practical applications in the area of low-temperature plasma physics). We have obtained some particular versions of the plasma–sheath equation that generalize the Langmuir–Tonks equation and take into account charge-exchange recombination between ions and neutrals in a plasma and the thermal spread in the initial velocities of the ionization-produced ions.

The integrodifferential equation derived makes it possible to calculate the spatial parameters of a gas discharge plasma over a wide range of pressures—from the regime of collisionless ion motion (the Langmuir–Tonks regime) to the regime of ambipolar diffusion in a strong electric field of the space charge—and take into account both ion emission and incomplete ion recombination on the wall.

The rigorous mathematical approach taken in deriving the plasma–sheath equation allowed us to construct a systematic perturbation theory for this equation, which had not been done before.

Since the mechanisms for conversion of the electric field energy into electron energy were discarded, the above analysis is also valid for RF and microwave discharges in the regimes in which the nonlinear processes in the sheath are unimportant.

The results obtained can be used, in particular, to analyze the processes in low-pressure plasmochemical reactors.

REFERENCES

1. I. Langmuir and L. Tonks, Phys. Rev. **34**, 876 (1929).
2. W. Schottky, Z. Phys. **25**, 342 (1924); Z. Phys. **25**, 635 (1924).
3. S. A. Dvinin, V. A. Dovzhenko, and A. A. Kuzovnikov, Vest. Mosk. Univ., Ser. 3: Fiz., Astron., No. 5, 13 (1999).
4. J. E. Lawler, Phys. Rev. A **32**, 2977 (1985); S. Hamaguchi, R. T. Farouki, and M. Dalvie, Phys. Rev. A **44**, 3804 (1991).
5. G. F. Ivanovskiĭ and V. I. Petrov, *Ion–Plasma Treatment of Materials* (Radio i Svyaz', Moscow, 1986).
6. A. V. Gurevich and A. B. Shvartsburg, *Nonlinear Theory of Radiowave Propagation in the Ionosphere* (Nauka, Moscow, 1973), Chap. 6.
7. *Thermoemission Converters and Low-Temperature Plasma*, Ed. by B. Ya. Moĭzhes and G. E. Pikus (Nauka, Moscow, 1973), p. 176.
8. S. A. Dvinin, V. A. Dovzhenko, and A. A. Kuzovnikov, Fiz. Plazmy **25**, 957 (1999) [Plasma Phys. Rep. **25**, 882 (1999)].
9. F. G. Baksht, B. Ya. Moĭzhes, and V. A Nemchinskiĭ, Zh. Tekh. Fiz. **37**, 729 (1967) [Sov. Phys. Tech. Phys. **12**, 522 (1967)].
10. V. I. Smirnov, *Course of Higher Mathematics* (Nauka, Moscow, 1981), Vol. 4, Part 2, p. 12.
11. V. I. Smirnov, *Course of Higher Mathematics* (Nauka, Moscow, 1974), Vol. 4, Part 1, Chap. 1.
12. V. L. Granovskiĭ, *Electric Current in a Gas: Steady-State Current*, Ed. by L. A. Sena and V. E. Golant (Nauka, Moscow, 1971), p. 235.

Translated by O. E. Khadin

Plasma Physics Reports, Vol. 26, No. 2, 2000, pp. 174–176. Translated from Fizika Plazmy, Vol. 26, No. 2, 2000, pp. 190–192.

LOW-TEMPERATURE PLASMAS

Optical Characteristics of the Plasma of a Transverse Volume Discharge in a Ne/Ar/SiH_4 Mixture

A. K. Shuaibov

Uzhgorod State University, Podgornaya ul. 46, Uzhgorod, 294000 Ukraine

Received December 21, 1998; in final form, April 23, 1999

Abstract—Results are presented from studies of the characteristics of a transverse volume discharge in a Ne/Ar/SiH_4 mixture at pressures of 5–35 kPa. It is shown that SiI 288.2-nm, H_β 486.1-nm, and NeI 585.3-nm lines and H_2 Lyman bands can be used to monitor the process of destruction of silane molecules. The obtained porous film, consisting of the products of SiH_4 destruction, is of interest for yielding siliceous fullerenes and for application in optoelectronics. © *2000 MAIK "Nauka/Interperiodica".*

Thin silicon films are produced by depositing silicon atoms from an Ar/SiH_4 mixture onto a heated substrate. For this purpose, either high-power excimer lasers [1] or high-frequency low-pressure (≤0.1 kPa) discharges [2] are usually used. Of particular interest is the synthesis of nanocrystalline films [2] or porous silicon, whose luminescence in the visible spectral region [3] can find application in optoelectronics. The use of a transverse volume discharge (TVD) makes it possible to substantially increase the plasma electron density (in comparison with high-frequency low-pressure discharges), the pressure of the working gas (as well as the content of SiH_4 molecules in it), and the volume of the reaction zone. In TVD plasmas, conditions can be created that are favorable for the synthesis of siliceous fullerene molecules similar to carbonic atomic structures, such as C_{60} and C_{70}. The most appropriate working media for the synthesis of such molecules are those based on helium or neon plasmas at pressures of 10–30 kPa [4]. In [5], results are presented on the synthesis of porous silicon compounds in laser sparks in mixtures of inert gases with silane molecules at high pressures ($P \geq 100$ kPa). In [6], we studied the optical characteristics of a TVD in an Ar/SiH_4 mixture in the 200–600-nm spectral region at pressures of $P \leq 10$ kPa.

In this paper, we present the results of studying the optical characteristics of a plasma produced in a TVD in a Ne/Ar/SiH_4 mixture. The emission spectra in the 130–600-nm spectral range and the resource characteristics and dynamics of the emission from excited neon atoms and the products of destruction of SiH_4 molecules are studied. SiH_4 molecules are electronegative [7]; this property is important for both obtaining TVDs in the regime of prebreakdown multiplication of electrons [8] and using these molecules as a Penning addition in emitters based on Ne(3*s*–3*p*) transitions.

A transverse discharge with spark UV preionization was ignited in a polyethylene pipe with an inner diameter of 14 cm; the plasma volume was 54 × 2.0 × 0.7 cm^3. An LC generator initiating the TVD triggered a 40-nF storage capacitor and a 34-nF sharpening capacitor. A TGII 1000/25 thyratron was used as a switch. The TVD characteristics in the 220–600-nm spectral region were measured with a diagnostic complex described in [6, 8]. VUV radiation was studied with the help of a vacuum monochromator based on the Seia–Namioki scheme. The plasma radiation was output through a CaF_2 window, which allowed measurements in the spectral region $\Delta\lambda$ = 130–350 nm, and was recorded by an FEU-142 photomultiplier with a LiF window.

In the emission spectra of the TVD plasma, we observed a broadband emission in the 170–400-nm range, which can be attributed to H_2^* and ArH* molecules. The most intense lines were SiI ($3p^2\,{}^1D_2$–$4s\,{}^1P_1^0$) 288.2-nm and H_β 486.1-nm lines. In the VUV spectral region, the most intense lines were H_2^* Lyman bands ($\Delta\lambda$ = 140–160 nm). Weak bands of Si_2^* molecules were detected at $\lambda \leq 200$ nm. In TVDs ignited in a freshly prepared mixture, the radiation from silicon atoms was dominant in the initial stage of discharge. As silane was decomposed, H_2^* and H_β line radiation became dominant.

The regime with prebreakdown multiplication of electrons, which was observed in TVDs in Ne/SF_6 mixtures [6], was not obtained in silane-containing mixtures. This is explained by both the small effective cross section of dissociative attachment ($\sigma \leq 2 \times 10^{-18}$ cm^2) and the specific character of the energy dependence of the cross section (a narrow maximum at an electron energy of 8–9 eV) [7].

Figure 1 shows the intensity of NeI 585.3-nm line radiation and emission from the products of SiH_4 destruction as functions of the number of TVD pulses (*n*) in Ne/Ar/SiH_4 mixtures with different contents of Ar

1063-780X/00/2602-0174$20.00

and SiH_4. The behavior of the brightness of Lyman bands and continuum of hydrogen molecules is similar to the dependence of the intensity of the H_β line on the number of TVD pulses. As n increases to $\geq(0.5–1.0) \times 10^3$, the intensity of the SiI 288.2-nm line falls off sharply, indicating that silicon precipitates almost completely. At the same time, the intensity of the NeI 585.3-nm line increases substantially. This is evidence of the efficient quenching of Ne($3p$) atoms by silane molecules and the main gas-phase products of silane conversion in a plasma, which proceeds until the complete destruction of these products. Hence, this neon line can be used for monitoring the destruction of SiH_4 in the plasma under study. As the silane content increases, the intensity of emission from Si and Ne atoms decreases.

Figure 2 shows the waveforms of the voltage, the TVD current, and the intensity of emission from plasma components in different stages of destruction of a silane-containing plasma. The TVD current oscillates, and its maximum amplitude (for a discharge voltage of 5–20 kV) is in the 5–15-kA range. The initial part (h) of the current time profile is associated with the charge of the sharpening capacitor, as in TVDs in He(Ne)/NF_3 mixtures [9]. The amplitude and duration of the pulses of SiI 288.2-nm line radiation are maximum at n = 1–10, which corresponds to the shape of the resource characteristic of the emission from Si* atoms (Fig. 1). The maximum of Si* emission was observed after the first half-wave of the discharge current, which can be related to the dissociative excitation of SiH_4 and the main products of its conversion in a plasma, such as Si_2H_6 and Si_2H_4 [7]. The duration of H_β and Ne* line radiation attained 300–320 ns. The maximum intensity of Ne* radiation was observed at the front of the discharge current, whereas the maximum of H_β radiation was observed in the afterglow. Such behavior of neon radiation is associated with the electronic mechanism of the excitation of NeI atoms in the initial stage of a TVD, whereas the dissociative-excitation and recombination reactions most probably are responsible for the H_β line radiation.

After 10^5 TVD pulses (10^4 pulses for each freshly prepared mixture), the inner surface of the discharge chamber was covered by a thick (d = 0.5 mm) brown porous film similar to that synthesized in laser-spark experiments. An analysis of this film [5] showed that it has a characteristic structure constant of 50–100 nm. An X-ray structural analysis of the porous silicon compounds synthesized in a TVD showed that they have a complicated structure with a structure constant of d = 100 nm. As compared to a laser spark, a TVD makes it possible to lower the cost of the synthesis and increase the yield of porous siliceous products (presumably, compounds of the Si/SiO_2 or Si/Si_mH_n type, where m, n = 1–60), among which there can be Si_{60} and $Si_{60}H_{60}$ fullerenes.

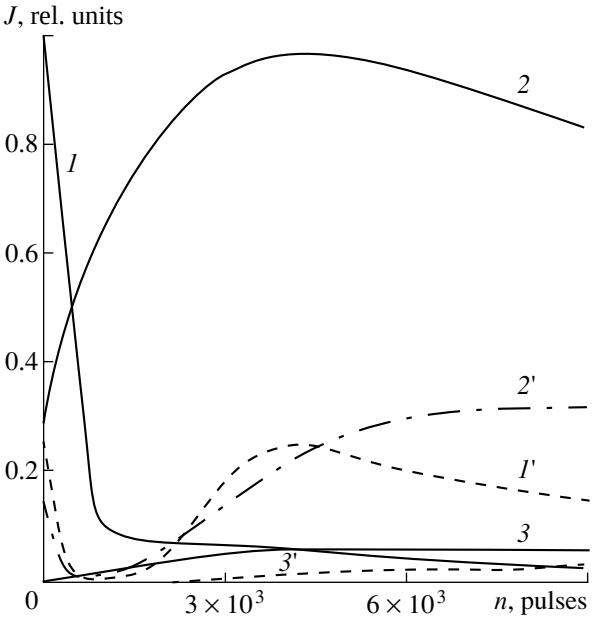

Fig. 1. Intensity of NeI 585.3-nm line radiation and emission from the products of destruction of silane molecules as functions of the number of TVD pulses in Ne : Ar : SiH_4 = (*1–3*) 32 : 1.5 : 0.06 and (*1*'–*3*') 32 : 7.7 : 0.32 kPa mixtures: (*1, 1*') SiI 288.2-nm, (*2, 2*') NeI 585.3-nm, and (*3, 3*') H_β 486.1-nm lines. The discharge voltage is U = 15 kV.

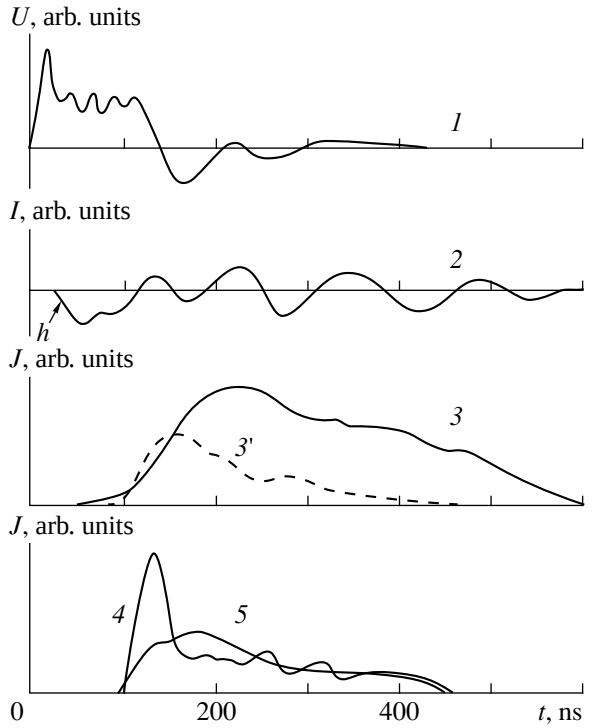

Fig. 2. Waveforms of the (*1*) discharge voltage, (*2*) discharge current, and the intensity of emission from neon atoms and the products of SiH_4 destruction in a TVD plasma in Ne : Ar : SiH_4 = (*1–5*) 32 : 1.5 : 0.06 and (*3*') 32 : 7.7 : 0.32 kPa mixtures: (*3, 3*') SiI 288.2-nm ($n \leq 10$ pulses), (*4*) NeI 585.3-nm ($n \geq 6 \times 10^2$ pulses), and (*5*) H_β 486.1-nm ($n \geq 2 \times 10^3$ pulses) lines.

Hence, we have shown that the SiI 288.2-nm, NeI 585.3-nm, and H_β 486.1-nm line radiation and the H_2 Lyman band can be used to monitor the process of destruction of silane molecules in a TVD plasma. Also demonstrated is the possibility of creating a plasmochemical reactor based on a repetitive TVD for the synthesis of porous siliceous-containing compounds that can find application in optoelectronics.

ACKNOWLEDGMENTS

I am grateful to A.I. Dashchenko for assistance in experiments.

REFERENCES

1. V. Yu. Baranov, V. Yu. Borisov, and Yu. Yu. Stepanov, *Inert-Gas Halogenide Electric-Discharge Excimer Lasers* (Énergoatomizdat, Moscow, 1988).
2. V. G. Golubev, A. V. Medvedev, A. B. Pevtsov, *et al.*, Pis'ma Zh. Tekh. Fiz. **24**, 26 (1998) [Tech. Phys. Lett. **24**, 758 (1998)].
3. E. A. Vinogradov, A. V. Zayats, D. N. Nikogosyan, *et al.*, Opt. Spektrosk. **76**, 323 (1994).
4. A. V. Eletskiĭ and B. M. Smirnov, Usp. Fiz. Nauk **163**, 33 (1993) [Phys. Usp. **36**, 202 (1993)]; **165**, 977 (1995) [Phys. Usp. **38**, 935 (1995)].
5. S. A. Batishche, A. A. Kuz'muk, and N. A. Malevich, in *Proceedings of III Conference on Laser Physics and Spectroscopy*, Minsk, Belorussia (1997), Vol. 1, p. 59.
6. A. K. Shuaibov, L. L. Shimon, A. I. Dashchenko, *et al.*, Pis'ma Zh. Tekh. Fiz. **24**, 35 (1998) [Tech. Phys. Lett. **24**, 844 (1998)].
7. M. J. Kushner, J. Appl. Phys. **63**, 2532 (1988).
8. A. K. Shuaibov, Pis'ma Zh. Tekh. Fiz. **24**, 85 (1998) [Tech. Phys. Lett. **24**, 38 (1998)].
9. M. I. Lomaev and V. F. Tarasenko, Kvantovaya Électron. (Moscow) **15**, 1978 (1988) [Sov. J. Quantum Electron. **18**, 1237 (1988)].

Translated by N. F. Larionova

Plasma Physics Reports, Vol. 26, No. 2, 2000, pp. 87–108. Translated from Fizika Plazmy, Vol. 26, No. 2, 2000, pp. 99–121.

TOKAMAKS

Numerical Analysis of the Safety Factor and Effective Ion Mass in a Tokamak Plasma with the Help of the Discrete Alfvén Wave Spectrum

A. Yu. Novikov and A. V. Dobryakov

Russian Research Centre Kurchatov Institute, pl. Kurchatova 1, Moscow, 123182 Russia

Received September 11, 1997; in final form, December 26, 1998

Abstract—Numerical aspects of the method for diagnosing a tokamak plasma with the help of the discrete Alfvén wave spectrum are considered. It is shown that this diagnostics should be supported with highly accurate computational tools. A code suitable for implementing the relevant calculation scheme is developed, which makes it possible to identify the eigenmodes numerically with the desired accuracy. The code can also provide recommendations for performing tokamak experiments and can be used to study the possibility of auxiliary plasma heating by Alfvén waves. The discrete Alfvén wave spectrum, radial profiles of the energy deposited in the plasma, and the dependence of the Alfvén mode frequencies on the damping rate and on the class of the current-density profiles chosen are calculated for the first time for the T-10 tokamak. It is also shown that the diagnostic method proposed makes it possible to obtain reliable information about the plasma parameters.

1. INTRODUCTION

It is well known that such tokamak plasma parameters as the current density profile and the central safety factor q are very difficult to measure. The diagnostic methods developed so far for determining the safety factor are based on measuring the poloidal magnetic field, which governs the central q value. In recent years, the poloidal field in some tokamaks has been measured by using the Zeeman [1] and Stark [2, 3] effects in emissions of hydrogen, lithium, and helium neutral diagnostic beams specially injected into the plasma and also by monitoring the Faraday rotation of the plane of polarization of the probing laser beam [4].

The above active particle diagnostics, being the most fundamental and universal methods, provide information not only about the safety factor but also about some other important parameters. On the other hand, in view of the universality of particle diagnostics, they provide measurements of the q profile with an insufficiently high temporal and spatial resolution and require fairly complex and expensive equipment.

The diagnostic technique for measuring the central q value with the help of the discrete Alfvén wave (DAW) spectrum was implemented for the first time in the TEXTOR tokamak in 1990. In the TEXTOR plasma, the Alfvén eigenmodes were excited by a poloidal antenna [5].

An important feature of this diagnostics is that it combines experimental methods with numerical analysis.

We have developed a simulation code aimed at identifying the eigenmodes of the DAW spectrum (measured experimentally in tokamak plasmas in order to determine the radial profiles of the current density and effective ion mass).

An important advantage of the diagnostic method proposed here is that it requires simple experimental equipment. The experimental scheme proposed for implementing this diagnostics in T-10 is shown in Fig. 1 and includes the following units.

(a) A loop antenna for exciting the Alfvén eigenmodes in a plasma. The antenna is oriented poloidally; the poloidal angle span of the antenna is 90° (which corresponds to an antenna length of 58 cm in the poloidal direction) and its toroidal angle span is 1.9° (which corresponds to an antenna width of 5 cm in the toroidal direction).

(b) Two magnetic probes installed in the same poloidal cross section at diametrically opposite positions in order to record eigenmodes with even and odd poloidal numbers m. To distinguish between eigenmodes with even and odd toroidal numbers n, it is required that this cross section be opposite to the cross section where the antenna is arranged.

(c) A generator unit capable of sweeping the frequency from the minimum value 0.8 MHz to the maximum value 8 MHz over a time interval of 20 ms. The generator is equipped with a broadband amplifier that ensures the desired level of radiation power fed into the plasma (100 W, the antenna current being 14.4 A).

(d) Two synchronized detectors.

(e) A recording and storing system based on programmable CAMAC interfaces and a personal computer.

1063-780X/00/2602-0087$20.00

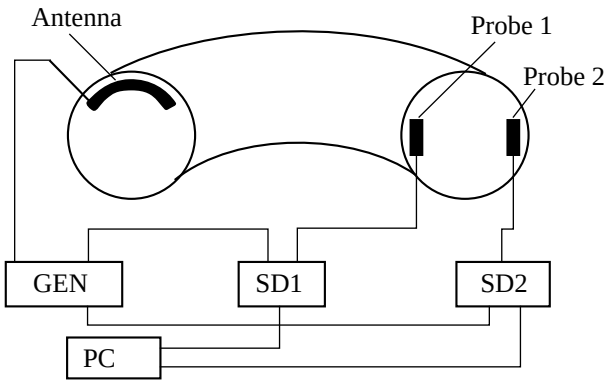

Fig. 1. Schematic of the experiment for the T-10 tokamak: GEN is a broadband amplification unit with frequency sweeping, SD1 and SD2 are synchronized detectors, and PC is a recording and storing system.

In the course of discharge, the diagnostics proposed can provide several consecutive sweeps, thereby making it possible to trace the time evolution of the radial profiles $q(r)$ and $A_{\text{eff}}(r)$.

In Section 2, we briefly review previous theoretical and experimental results. We also present the dispersion relation for the continuous part of the Alfvén wave (AW) spectrum in order to obtain a rough estimate of the eigenfrequencies of the DAW spectrum. In Section 3, we justify the technical details of the experimental diagnostic scheme proposed for use in the T-10 tokamak. We also list important new results that were obtained with our code and differ from those found previously. In Section 4, we analyze what might be the classes of current profiles for which the q profile can be reconstructed. In Section 5, we present the methods for finding the central value $q(0)$ of the safety factor and determining the radial profiles of $q(r)$ and effective ion mass $A_{\text{eff}}(r)$. In Section 6, we describe the steps taken in improving the numerical model. We control the reliability of our calculation scheme by comparing the test simulation results with experimental data from the TEXTOR tokamak. We systematically examine the cases of cold ($T_{i,e} = 0$) and real plasmas. We present numerical results obtained for the T-10 tokamak with the relevant boundary conditions. We focus on the accuracy of determining the $q(0)$ value, the AW eigenfrequencies as functions of the damping rate, and the stability of the plasma–antenna system against variations of the external parameters. An overall summary is given in Section 7. In Appendix 1, we justify the choice of the main parameters for the diagnostic method proposed and estimate their values using T-10 as an example. In Appendices 2–5, we present the details of the mathematical apparatus underlying our numerical model.

2. THEORETICAL AND EXPERIMENTAL BASIS OF THE CODE

2.1. Numerical Results Obtained in Earlier Studies

Appert and Vaclavik [5] derived the basic set of equations for radial profiles of the AW field components $E_\perp$ and $B_\parallel$ for the case of a cold, ideally conducting plasma. All of these equations were treated in local cylindrical coordinates with triply orthogonal unit vectors $\mathbf{e}_r$, $\mathbf{e}_\perp = [\mathbf{e}_\parallel \mathbf{e}_r]$, and $\mathbf{e}_\parallel = \mathbf{B}_0/B_0$, where $\mathbf{B}_0$ is the equilibrium magnetic field. The basic equations were integrated numerically using the Runge–Kutta method. Appert and Vaclavik [5] obtained

(i) the absorbed AW power and the position of the resonant layer as functions of the axial wavenumber for $m = 1$ and for different values of the ratio ω/ω_{ci} of the generator frequency to the ion cyclotron frequency,

(ii) the absorbed AW power as a function of the position of the resonant layer, and

(iii) the absorbed power as a function of the ratio ω/ω_{ci} of the generator frequency to the ion cyclotron frequency.

They also showed that the radial profile of the absorbed power is peaked at the radius $0.15a$ (where a is the plasma radius) for $\omega/\omega_{ci} = 0.075$.

Ross *et al.* [6] numerically integrated the set of differential equations for the AW field components E_r and $E_\perp$ in the same cylindrical coordinates as in [5]. They obtained the radial profiles of E_r and $E_\perp$ and the AW power deposited in a plasma for the (–2, –1) eigenmode.

In the basic paper [7], Descamps *et al.* described the methods for determining the q and A_{eff} profiles in the TEXTOR tokamak and presented the final results of numerically solving the problem of identifying the eigenmodes and determining $q(0)$.

The results obtained in most of the cited papers are difficult to reconstruct and unsuitable for comparison because of the lack of intermediate manipulations. Those papers presented only a few preliminary experimental results, which are, nonetheless, very important for checking the reliability of the numerical method developed here. For example, we will compare the eigenfrequencies of the DAW spectrum that were computed using our code for the TEXTOR parameters with those measured experimentally in the TEXTOR tokamak. Note that the initial conditions were described incompletely in the cited papers.

Unlike the previous investigations, we will present here the intermediate manipulations and the results obtained in more detail for the benefit of readers who may thus check whether the problem under discussion is formulated and solved correctly.

2.2. Wentzel–Kramers–Brillouin Method

Mahajan *et al.* [8] derived the dispersion relation for the DAW spectrum in the MHD approximation and applied the Wentzel–Kramers–Brillouin (WKB) method to solve an eigenvalue problem for the case of an inhomogeneous cylindrical plasma with the boundary conditions stated at infinity: $E(r = \infty) = 0$. They considered exclusively radially localized modes, i.e., those for which the solution outside the localization region is exponentially small. However, when applied to the modes excited near the plasma boundary, this dispersion relation yields incorrect results. To improve the accuracy to acceptable levels, the boundary conditions should be substantially modified. The dispersion relation from [8] is obviously inapplicable to the modes localized at the central plasma region.

2.3. Experiments Aimed at Choosing Antennas for the Excitation of Alfvén Eigenmodes

Appert *et al.* [9] studied toroidal coupling between purely cylindrical modes and modes with the highest poloidal numbers *m* in the TCA device.

Collins *et al.* [10] showed experimentally that the antenna structure consisting of two antenna arrays (one array above the discharge chamber, the other below) excites modes with all toroidal numbers *n* and either odd or even poloidal numbers *m*.

In the TCA experiments, the eigenmodes of the DAW spectrum were recorded from the resonance peaks in the antenna load resistance as the plasma density changed with time, in the course of RF pulses at a fixed frequency. The profiles obtained are illustrated schematically in Fig. 2. Profile *a* was obtained for antenna arrays operating in opposite phases, and profile *b* was obtained for the same phases of the currents flowing in the antenna arrays. In other words, antenna arrays were turned on in opposite phases in order to excite modes exclusively with odd poloidal numbers, while switching on the arrays in the same phase was aimed at exciting modes exclusively with even numbers *m*.

The experimental results show that the tendency to excite purely poloidal modes with either even or odd numbers *m* by two antenna arrays offers no advantages: because of the toroidal feedback coupling between two different, purely cylindrical modes, toroidally coupled modes (1, 2) and (3, 0) that were excited indirectly in case *a* turned out to be even somewhat more intense than those excited directly by the antenna arrays in case *b*.

The TEXTOR experiments on the DAW spectrum were carried out with an antenna in the form of a poloidally oriented semi-ring placed in the limiter shadow. Earlier, this antenna was used in the TEXTOR experiments on auxiliary plasma heating by magnetosonic waves.

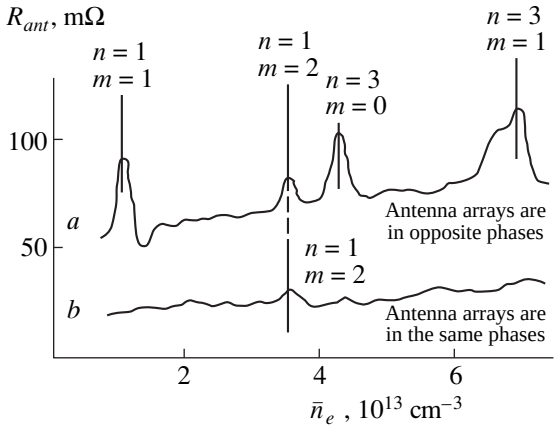

Fig. 2. Experimental profiles of the antenna impedance versus the plasma density for the TCA device: the antenna currents are *a*—in opposite phases and *b*—in the same phases ($\bar{n}_e$ is the electron plasma density per cm^{-3} averaged over the plasma-column axis and R_{ant} is the antenna resistance).

Hence, in real experiments carried out in some tokamaks with diagnostic purposes, the eigenmodes of the DAW spectrum were excited by antennas with significantly different geometries [7–10]. The antenna geometries were chosen so as to minimize technological difficulties and to make the assembly of antenna arrays adequate for experiments. Although, in each case, the antenna arrays excited only some of the Alfvén eigenmodes, the qualitative and quantitative features of the DAW spectra in real experiments with low input powers differed only slightly. This circumstance implies the possibility of energy exchange between the eigenmodes via such mechanisms as toroidal feedback mode coupling and collisions between particles. It is these mechanisms that result in the excitation of essentially all eigenmodes of the DAW spectrum.

Based on what was said above, we can conclude that the antenna geometries for practical or theoretical purposes should be properly chosen so as to minimize technological or computational difficulties, respectively. Also, the characteristic sweeping time for the frequency of the antenna current should be much longer than the characteristic collisional time of the plasma particles in order for the energy redistribution among the Alfvén eigenmodes to be "quasi-steady."

The choice of the specific antenna parameters (in particular, for the T-10 tokamak) is justified in Appendix 1, which also presents estimates of the relevant parameter values.

2.4. Some Features of the Discrete and Continuous Spectra of Alfvén Waves

In the case of a large-aspect-ratio tokamak, we can use the cylindrical approximation, in which the disper-

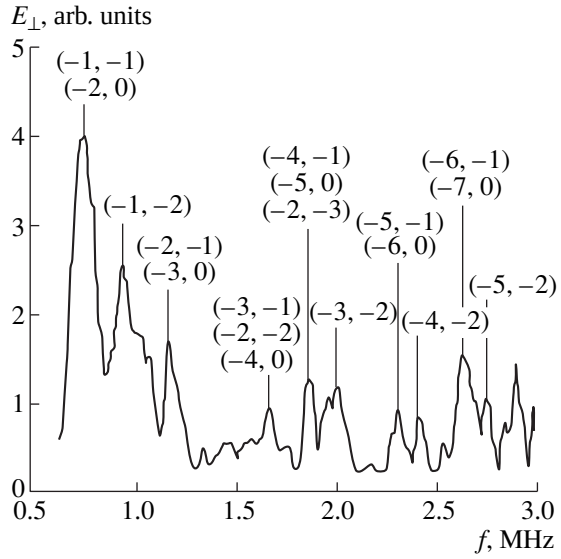

Fig. 3. Experimental DAW spectrum measured in the TEXTOR tokamak. The heights of the peaks reflect the eigenmode intensities.

sion relation for AWs is [4]

$$\omega_A^2(r) = \{[n + m/q(r)]^2 B_t^2/[\mu_0 \rho(r) R^2]\} \times [1 - (\omega/\omega_{ci})^2], \quad (1)$$

where $q(r)$ is the local safety factor, $\rho(r)$ is the local plasma density, and R is the major radius of the torus. Dispersion relation (1) implies that the function $\omega_A(r)$ increases continuously from the minimum central value to the maximum value at the plasma boundary, where the density $\rho(r)$ is lowest. Consequently, dispersion relation (1) describes the AW continuum.

The wave vector component $k_\parallel$ in (1) is a function of radius, $k_\parallel = (n + m/q(r))/R$, so that the function $\omega_A(r)$ can be either monotonic or nonmonotonic. In the latter case, the frequency of the continuum is minimum ($\omega_{min} = \omega_A(r_{min})$, at a certain radius $r_{min} > 0$, which depends on the specific profiles of the current and mass densities, $j(r)$ and $\rho(r)$. In most of the papers in which AWs were regarded as a diagnostic tool, the profile $j(r)$ was chosen to be $j(r) = j(0)[1 - (r/a)^2]^\delta$ with the parameter $\delta = q(a)/q(0) - 1$. In this case, the larger δ, the larger r_{min} [11].

According to [8, 10, 11], the eigenmodes of the discrete spectrum (with the same mode numbers) occur to the left of the minimum frequency $\omega_A(r_{min})$ of the continuum. Each eigenmode is characterized by the integer l, which is the radial mode number and takes on all values from zero to infinity. The eigenmode with the radial number $l = 0$ is the most intense and occurs closer to the minimum frequency of the continuum than the remaining eigenmodes, whose intensities decrease exponentially as l approaches infinity. Consequently, there exists a numbered (by l) infinite set of eigenmodes that "group" near the minimum frequency of the continuum. As an example, Fig. 3 illustrates the DAW spectrum obtained experimentally in TEXTOR.

Theoretical information about the structure and characteristic features of the AW spectrum served as the basis for the code.

3. PRINCIPLES OF EXPERIMENTAL DETECTION AND NUMERICAL IDENTIFICATION OF THE EIGENMODES

3.1. Three Factors Underlying the Diagnostic

The diagnostic proposed is based on (a) experimental measurements of the resonant frequencies of the DAW spectrum by two magnetic probes, (b) a comparison of experimental data with the theoretical DAW spectrum calculated with the specially developed numerical code, and (c) experimental data on the plasma density obtained by the interferometry technique.

Expanding the antenna currents in a Fourier series yields the following formula for the intensities of the eigenmodes excited in a plasma via the conversion of the antenna electromagnetic energy into the energy of plasma particles:

$$I_{n,m} = I\frac{\sin(m\theta_A)}{m}\frac{\sin(n\Phi_A)}{n}, \quad (2)$$

where I is the antenna current amplitude, $2\theta_A$ is the poloidal angle span of the antenna, and $2\Phi_A$ is its toroidal angle span [10]. In this way, only some of the eigenmodes of the DAW spectrum can be excited; the remaining eigenmodes are generated via such mechanisms for energy redistribution between the eigenmodes as toroidal feedback coupling and energy dissipation (these mechanisms are incorporated into the numerical model). The latter mechanism is implicitly taken into account through the imaginary correction $i\nu$ to the frequency.

Formula (2) yields the following two conclusions.

(i) Since the antenna width in the toroidal direction is much less than the toroidal circumference of the torus, the intensities of the eigenmodes with moderate n are essentially the same. The difference in intensities becomes more or less pronounced for eigenmodes whose toroidal numbers are sufficiently large.

(ii) Since the poloidal angle span of the antenna is sufficiently large ($2\theta_A \geq 90°$), the intensities of the eigenmodes with the largest poloidal numbers m decrease in proportion to $\sin(m\theta_A)/m$. Consequently, the intensities of the neighboring odd eigenmodes (with, e.g., $m = 3$ and 5) differ insignificantly (by a factor of only 1.6); for eigenmodes with larger poloidal numbers m, this difference is even smaller.

These considerations suggest that the use of poloidal and toroidal arrays of numerous probes to identify the eigenmodes experimentally does not appreciably

facilitate the diagnostics proposed. Moreover, these arrays are to be combined with the other diagnostic equipment, thereby substantially complicating the assembly of the diagnostic system.

In summary, we propose to detect the eigenmodes using only two probes installed in the same poloidal cross section of a tokamak and to identify them by means of numerical analysis.

As shown in Fig. 1, the probes should be installed in the poloidal cross section opposite to the antenna. Knowing the mode intensities measured experimentally at the antenna and measuring them by the probes in the cross section opposite to the antenna makes it possible to determine the even and odd toroidal numbers of the eigenmodes. To distinguish between the eigenmodes with even and odd poloidal numbers m, the two magnetic probes should be placed at diametrically opposite points of the same poloidal cross section.

3.2. The Way the Mode Numbers n and m Are Incorporated into the Code

In our numerical code, the mode numbers n and m were chosen from the following considerations:

(a) experiments and theory show that, for $\omega/\omega_{ci} < 0.5$, the only eigenmodes that can be excited in the plasma are those with $m/n > 0$;

(b) Collins *et al.* [10] showed that the intensities of the modes with the poloidal number $m = -1$ and toroidal numbers $n < 0$ are higher than the intensities of the remaining modes; and

(c) for tokamak plasmas with $\omega/\omega_{ci} \ll 1$ (e.g., for the T-10 plasma), the dispersion relation for the DAW spectrum can be written approximately as [5]

$$(\omega_{\mathrm{DAW}})_{n,m} \approx |n| F_1\left(\frac{m}{n}\right)\left[1 - m^{-2} F_2\left(\frac{m}{n}\right)\right], \qquad (3)$$

which implies that the (n, m) and $(-n, -m)$ modes have the same resonant frequencies.

3.3. Estimate of the Resonant Frequency of the Eigenmode

Analyzing experimental results raises the question of how the radial deviation of an eigenmode from $r_{\min}$ and the frequency shift between this mode and $\omega_{\min}$ depend on the ratio ω/ω_{ci}. In the estimates for T-10 in the case $\omega/\omega_{ci} \ll 1$, we can set $\omega_{ci} = 2 \times 10^8\ \mathrm{s}^{-1}$ and $\omega = 3 \times 10^7\ \mathrm{s}^{-1}$ to obtain that the eigenfrequency $\omega_{n,m,0}$ of the DAW spectrum differs from the minimum frequency $\omega_A(r_{\min})$ of the continuum by about 1% and that the radial deviation of the eigenmode with the frequency $\omega_{n,m,0}$ from the mode with the minimum frequency of the continuum is about 2 cm (or 3%). Consequently, to obtain rough estimates of the resonant frequency of the eigenmode of the DAW spectrum, we can use the minimum frequency of the continuum, which is found from dispersion relation (1) for the continuum.

In the limit $\omega/\omega_{ci} \ll 1$, the dispersion relation for the DAW spectrum was derived by Appert and Vaclavik [5]:

$$(\omega_{\mathrm{DAW}})_{n,m,0} = \omega_A(r_{\min})_{n,m}[l - \Delta_{n,m,l}], \qquad (4)$$

where $\omega_A(r_{\min})$ is the minimum in the Alfvén continuum and l is the radial mode number. Dispersion relation (4) contains a small correction,

$$\Delta_{n,m,l} = f\{L^2(r_{\min}), L_n(r_{\min}), L_q(r_{\min}), q(r_{\min})\},$$

which was found by Mahajan *et al.* [8] for $L^2 = 2\omega_A^2/(\omega_A^2)'$, $L_n = n_e/n_e'$, and $L_q = q/q'$, where the prime denotes the radial derivative.

3.4. Potentialities of the Numerical Code

As will be shown below, our numerical code can be applied

(i) to formulate the requirements for the antenna that excites the eigenmodes of the DAW spectrum in a plasma,

(ii) to investigate the possibility for auxiliary plasma heating by AWs, and

(iii) to provide recommendations for performing experiments in tokamaks (e.g., in T-10, TEXTOR, and ITER).

In comparison with the previous results reported elsewhere, the new results obtained with our code are as follows.

(a) Using theoretical formulas, we calculated the DAW spectrum for a deuterium plasma with the modes whose numbers take on all values from (–1, –1) to (–6, –2), i.e., the modes that contain information required to determine the radial profiles of q and A_{eff}.

(b) We computed radial profiles of the AW power deposited in the plasma for various eigenmodes with different mode numbers.

(c) A comparison between our numerical results and the relevant experimental data from TEXTOR showed that they are in good agreement.

(d) We compared numerical results obtained for cold and real plasmas.

(e) We formulated the requirements imposed on the antenna aimed at exciting the eigenmodes of the DAW spectrum in a tokamak plasma. From a practical standpoint, this is the main result of our work.

4. CLASSES OF CURRENT DENSITY PROFILES FOR WHICH THE *Q* PROFILE CAN BE RECONSTRUCTED

The radial profile of the safety factor $q(r)$ is governed by the current density profile $j(r)$. We applied our code to reconstruct the q profile from the following

class of monotonically decreasing current density profiles:

$$j(r) = j(0)\left[1 - \left(\frac{r}{a}\right)^2\right]^{\delta}. \quad (5)$$

Our code is capable of covering wide ranges of values of the parameters $q(a)$ and δ, which govern this class of profiles.

The q profile can also be reconstructed from other classes of current density profiles, specifically, those that may be approximated with good accuracy by analytic functions, for example, from the class of double-humped profiles

$$j(r) = C_1\left[1 - \left(\frac{r-\Delta_1}{a}\right)^2\right]^{\alpha} + C_2\left[1 - \left(\frac{r-\Delta_2}{a}\right)^2\right]^{\delta} + C_3, \quad (6)$$

where the parameters α, δ, Δ, C_1, C_2, and C_3 can be varied over broad ranges. The α and δ define how steep the slopes of the humps are; the Δ defines how much the humps are displaced from the plasma center; and C_1, C_2, and C_3 describe the relative heights of the humps.

The code determines the parameter values $q(0)$, $j(0)$, δ, and $q(a)$ that correspond to the real experiment, because the central value $q(0)$ of the safety factor and the parameter δ are related in a certain manner, depending on the current density profile. For example, for profiles (5), they are related by

$$q(0) = \frac{q(a)}{\delta + 1}. \quad (7)$$

This relationship follows from (5) after integrating the current density over the entire cross section of the plasma. A similar relationship for double-humped profiles (6) should obviously contain both α and δ.

The code also determines the resonant frequencies $\omega_{n,m}$ of the eigenmodes and their resonant radial positions $r_{n,m}$ (at which the intensities of AWs are observed to be maximum).

In simulations, the plasma density profiles were approximated by the experimental profiles obtained with the help of an interferometer.

For the T-10 tokamak, the electron density was approximated by a parabolic profile typical of most tokamaks,

$$n_e(r) = n_e(0)\left[1 - 0.95\left(\frac{r}{a}\right)^2\right]. \quad (8)$$

5. DETERMINATION OF $q(0)$ AND RECONSTRUCTION OF THE PROFILES OF THE SAFETY FACTOR $q(r)$ AND EFFECTIVE ION MASS $A_{\text{eff}}(r)$

Recall that, in order to reconstruct the radial profiles of $q(r)$ and $A_{\text{eff}}(r)$, it is necessary

(a) to experimentally measure the eigenfrequencies $\omega_{n,m}$ of the DAW spectrum,

(b) to identify the eigenmodes with the numerical code and to determine the mode numbers n and m, and

(c) to determine the plasma density profile $\rho(r)$ using the interferometry technique.

For fixed n and m, we can find $q(r_{\min})$, where $r_{\min}$ is the radius at which function (1) is minimum. The value $q(r_{\min})$ is determined graphically as follows. From formula (1), we can find $q(r)$ as a function of n, m, $\omega_{n,m}$, and $\rho(r)$. Then, we plot the experimental radial profile of the function q using the measured data on the plasma density $\rho(r)$ at fixed values of n, m, and $\omega_{n,m}$. Specifying the current density profile in the form of (5), we can express $q(r)$ as

$$q\left(\frac{r}{a}\right) = \frac{q(a)\left(\frac{r}{a}\right)^2}{1 - \left[1 - \left(\frac{r}{a}\right)^2\right]^{\delta+1}}. \quad (9)$$

Differentiating (1) with respect to radius, we can relate $q(r_{\min})$ to the ratio of the mode numbers m/n and the derivatives ρ' and q':

$$q(r_{\min}) = -\left(\frac{m}{n}\right)\left[\frac{2\rho' q}{\rho q'} + 1\right]. \quad (10)$$

Substituting the experimental radial profile of the plasma density and the derivative q' found from (9) into (10), we can obtain the analytical profile of $q(r_{\min}, \delta)$, where the form-factor δ serves as a parameter. The point at which the theoretical profile intersects the experimental one allows us to find $r_{\min}$, $q(r_{\min})$, and δ. Repeating this procedure for eigenmodes with other mode numbers, we can determine the q values at different radial positions.

The central value $q(0)$ is found using a somewhat different procedure. The $q(0)$ value is determined from the theoretical profiles of the resonant frequencies of the neighboring eigenmodes as functions of the form-factor δ. The eigenmodes are regarded as being neighboring if the absolute values of the sum of their mode numbers, $|n + m|$, are equal to each other. From the experimentally measured DAW spectrum, we find the frequency difference for the same neighboring eigenmodes and compare this difference with the theoretical one, thereby determining the quantity δ, which is uniquely related to $q(0)$ through (7).

The radial profile $A_{\text{eff}}(r)$ is calculated with allowance for the fact that, by virtue of the relationship $\omega_{\text{DAW}}(r_{\min}) \sim 1/\sqrt{A_{\text{eff}}(r_{\min})}$, the eigenmode frequencies are sensitive to the effective ion mass. The effective mass can be changed by injecting a small amount of impurity atoms. From the difference in the frequencies of the eigenmode that are measured before and after the injection, we can find the local value of $A_{\text{eff}}(r)$ [5].

Repeating this procedure for eigenmodes with other mode numbers, we can obtain the local values of $A_{\text{eff}}(r)$ at different radial positions.

6. NUMERICAL METHOD AND THE RESULTS OBTAINED

The numerical method was developed in several steps. First, we considered the simplified model of a cold plasma ($T_{i,e} = 0$). Then, we incorporated the temperature. Since the final version of the code is a modification of the simplified version (with $T_{i,e} = 0$), the simulation algorithm we will describe for the case $T_{i,e} = 0$ serves as the basis for the general computational scheme. The calculation accuracy was checked by comparing our test numerical results with the data from TEXTOR experiments.

In simulations, we modeled the antenna by a hollow circular cylinder of radius r_{ant}, which was coaxial with both an ideally conducting wall of radius r_{w} and a plasma column of radius a. The geometry of this model, which is valid for large-aspect-ratio tokamaks, is shown in Fig. 4. In formula (11) and in subsequent simulations, the antenna was assumed to be infinitely long, since the antenna length-to-radius ratio is large.

Antennas similar to that shown in Fig. 4 were treated in theoretical papers [6, 7], because the cylindrical axisymmetric geometry of the antenna is exceptionally convenient for calculations.

The waves are excited by an alternating antenna current J_{ant}, which has the following form in the cylindrical coordinates (r, ϑ, z) associated with the antenna axis:

$$J_{\text{ant}} = J_0\left[k\mathbf{e}_\vartheta - \frac{m}{r}\mathbf{e}_z\right] \times \delta(r - r_{\text{ant}})\cos(\omega t)\cos(kz + m\vartheta), \tag{11}$$

where $\delta(r - r_{\text{ant}})$ is the Dirac delta function, k and m are the axial and poloidal wavenumbers, and the vector $J_0[k\mathbf{e}_\vartheta - (m/r_A)\mathbf{e}_z]$ describes the surface density of the antenna current [6]. In all simulations, the current constant J_0 was set to be 0.1 A/cm.

All equilibrium quantities were assumed to be functions of r only. The quantities describing the wave were assumed to depend on time and the z-coordinate as

$$\exp\{i[kz + m\vartheta - (\omega + i\nu)]\}. \tag{12}$$

The plasma motion was described assuming that the oscillation amplitude was small.

6.1. The Case of a Cold Plasma

With the purpose of describing the DAW spectrum theoretically, we begin with the approximation of a cold, ideally conducting plasma in cylindrical geometry (which is valid for large-aspect-ratio tokamaks). Landau damping by electrons was taken into account as an imaginary correction to the frequency, $\omega \longrightarrow \omega + i\nu$, where (as in [6]) ν was set to be equal to 0.003ω.

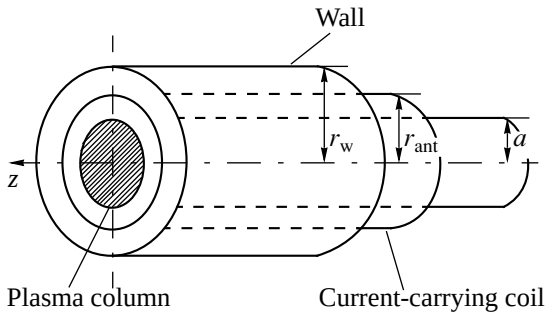

Fig. 4. Geometry of the theoretical model for calculating the DAW spectrum.

The motion of a cold plasma can be described by the linearized equation

$$\rho\frac{\partial \mathbf{v}}{\partial t} = \frac{1}{c}\{[\mathbf{j}, \mathbf{B}_0] + [\mathbf{j}_0, \mathbf{B}]\} \tag{13}$$

and by Ohm's law with allowance for the Hall effect,

$$\mathbf{E} + \frac{1}{c}[\mathbf{v}, \mathbf{B}_0] = \frac{m_i}{ec\rho}\{[\mathbf{j}, \mathbf{B}_0] + [\mathbf{j}_0, \mathbf{B}]\}. \tag{14}$$

Here, $\mathbf{B}_0$ and $\mathbf{j}_0$ are the equilibrium magnetic field and equilibrium current density, $\mathbf{B}$ and $\mathbf{j}$ are the perturbed magnetic field and perturbed current density, ρ is the equilibrium plasma density, c is the speed of light, and m_i is the mass of an ion.

The equilibrium tokamak magnetic field was assumed to be such that $B_{0z} \approx B_0 = \text{const}$ and $|B_{0\vartheta}/B_{0z}| \ll 1$. The problem was treated in a local orthogonal coordinate system with triply orthogonal unit vectors $\mathbf{e}_r$, $\mathbf{e}_\perp = [\mathbf{e}_r, \mathbf{e}_\parallel]$, and $\mathbf{e}_\parallel = \mathbf{B}_0/B_0$. From equations (13) and (14) and Faraday's law, we can obtain the following set of basic differential equations for the radial profiles of the quantities of interest to us:

$$A\frac{1}{r}\frac{d}{dr}(rE_\perp) = Gk_\perp E_\perp + \frac{i\omega}{c}\{A - k_\perp^2\}B_\parallel, \tag{15}$$

$$A\frac{dB_\parallel}{dr} = \frac{c}{i\omega}(G^2 - A^2)E_\perp - Gk_\perp B_\parallel, \tag{16}$$

where

$$A = \frac{(\omega/c_A)^2}{[1 - (\omega/\omega_{ci})^2]} - k_\parallel^2, \tag{17}$$

$$G = \left(\frac{\omega}{c_A}\right)\frac{\omega/\omega_{ci}}{[1 - (\omega/\omega_{ci})^2]} - \frac{2k_\parallel}{r}\frac{B_{0\vartheta}}{B_{0z}}. \tag{18}$$

Here, we assumed that $B_{0\vartheta} \simeq B_0\alpha r$ with α a small parameter. The derivation of these equations, which were integrated numerically in our code, was given in [12].

Since the denominator in the coefficient A is equal to $1 - (\omega/\omega_{ci})^2$, the singularity $A = 0$ occurs at the frequency $\omega = k_\parallel c_A(1 + k_\parallel^2 c_A/\omega_{ci}^2)^{-1/2}$ rather than at $\omega = k_\parallel c_A$.

The coefficient G describes the rate with which the AW energy is absorbed by the plasma and the spatial position of the resonant layer where the AW energy is deposited. Incorporating absorption into numerical analysis results in the appearance of peaks in the frequency spectra of the AW field components that correspond to the Alfvén eigenmodes.

Generally, equations (15) and (16) describe both magnetosonic waves and the DAW spectrum.

In vacuum, the wave field components E_z and B_z satisfy the modified Bessel equations

$$\frac{d^2E_z}{dr^2} + \frac{1}{r}\frac{dE_z}{dr} - \left[k^2 + \left(\frac{m}{r}\right)^2\right]E_z = 0, \quad (19)$$

$$\frac{d^2B_z}{dr^2} + \frac{1}{r}\frac{dB_z}{dr} - \left[k^2 + \left(\frac{m}{r}\right)^2\right]B_z = 0. \quad (20)$$

The remaining field components were expressed in terms of E_z and B_z through Maxwell's equations.

Equations (19) and (20) have the solutions

$$\begin{aligned} E_z &= C_1 I_m(|kr|) + C_2 K_m(|kr|) \\ B_z &= D_1 I_m(|kr|) + D_2 K_m(|kr|) \end{aligned} \quad r > r_{\text{ant}}, \quad (21)$$

$$\begin{aligned} E_z &= C_3 I_m(|kr|) + C_4 K_m(|kr|) \\ B_z &= D_3 I_m(|kr|) + D_4 K_m(|kr|) \end{aligned} \quad r < r_{\text{ant}}, \quad (22)$$

where I_m and K_m are the modified Bessel functions.

The constants C_{2-4} and D_{2-4} in (21) and (22) were found from the boundary conditions at the wall and at the antenna [7] and were expressed in terms of C_1 and D_1.

Integrating the differential equations just derived, we determined the eigenmodes that correspond to peaks in the frequency spectra of the AW field components.

We developed two subroutines, one of which calculates the radial profiles of the AW field components and the AW power deposited in the plasma for a given generator frequency ω, and the other determines the resonant frequencies for the prescribed eigenmodes by changing the frequency ω step by step in a given range. Also, for each frequency value in this range, the latter subroutine plots the aforementioned radial profiles, selects the peaks in them, and then repeats this procedure for the next frequency value.

6.1.1. Boundary conditions. The differential equations (15) and (16) for the field components $E_\perp$ and $B_\parallel$ were integrated numerically from the plasma center under the boundary conditions $E_\perp(0) = B_\parallel(0) = 0$ and $E_\perp'(0) = B_\parallel'(0) = 0$ (the latter is a consequence of the cylindrical symmetry of the problem). Such an approach resulted in the appearance of singularities of the 0/0 type at the plasma center. We overcame them in a standard way by approximating the functions at the center by

$$B_\parallel \sim \gamma_1(r)\left(\frac{r}{r_0}\right)^\lambda, \quad E_\perp \sim \gamma_2(r)\left(\frac{r}{r_0}\right)^{\lambda+1}, \quad r_0 = 1 \text{ cm}. \quad (23)$$

That these approximate expressions are of different orders in r stems from the fact that the orders of the functions $E_\perp$ and $B_\parallel$ in equations (15) and (16) differ by unity.

Passing over to the new functions

$$\tilde{E}_\perp(r) = \frac{E_\perp(r)}{\left(\frac{r}{r_0}\right)^{\lambda+1}\gamma_2(r)}, \quad \tilde{B}_\parallel(r) = \frac{B_\parallel(r)}{\left(\frac{r}{r_0}\right)^{\lambda}\gamma_2(r)}, \quad (24)$$

and substituting them into the basic equations (15) and (16), we obtain

$$\begin{aligned} \frac{d\tilde{E}_\perp}{dr} &= \tilde{E}_\perp\left(\frac{Gk_\perp}{A} - \frac{\lambda+2}{r}\right) - \frac{i\omega}{c}\frac{1}{r}\left(1 - \frac{k_\perp^2}{A}\right)\tilde{B}_\parallel \\ \frac{d\tilde{B}_\parallel}{dr} &= -\frac{ic}{\omega}\frac{G^2 - A^2}{A}\tilde{E}_\perp r - \tilde{B}_\parallel\left(\frac{A\lambda}{r} + Gk_\perp\right), \end{aligned} \quad (25)$$

with the new boundary conditions at $r = 0$,

$$\tilde{E}_\perp(0) = 1, \quad \tilde{B}_\parallel(0) = \gamma_3, \quad \gamma_3 = \frac{\gamma_1}{\gamma_2}. \quad (26)$$

Equations (25) with the boundary conditions (26) were integrated numerically by the Runge–Kutta method.

The expressions for the complex power index λ and for the ratio of the functions γ_1 and γ_2, which vary gradually with the radius, are presented in Appendix 2.

By virtue of (24), the components $E_\perp(r)$ and $B_\parallel(r)$ in the plasma are

$$E_\perp(r) = \tilde{E}_\perp(r)\left(\frac{r}{r_0}\right)^{\lambda+1}\gamma_2; \quad B_\parallel(r) = \tilde{B}_\parallel(r)\left(\frac{r}{r_0}\right)^{\lambda}\gamma_2. \quad (27)$$

The complex quantity γ_2 and the independent coefficients C_1 and D_1 in solutions (21) and (22) for the vacuum region were found by matching the solutions at the plasma–vacuum boundary $r = a$ (where a is the plasma radius) with the help of the four boundary conditions:

$$\begin{aligned} &\text{(a) the continuity of } E_\perp \text{ at } r = a, \\ &\text{(b) the continuity of } B_\parallel \text{ at } r = a, \\ &\text{(c) } j_r(a) = 0, \\ &\text{(d) the continuity of } B_r \text{ at } r = a. \end{aligned} \quad (28)$$

The continuity of B_r at $r = a$ follows from Faraday's law $\mathrm{curl}\mathbf{E} = -c^{-1}\partial\mathbf{B}/\partial t$ and the boundary condition $[\mathbf{e}_r, \mathbf{E}(a)]_-^+ = 0$.

As a result, the imaginary and real parts of the function γ_2 become

$$\mathrm{Im}\,\gamma_2 = \left[\mathrm{Im}\,E_\perp(a)\frac{c_3}{r\left(\frac{a}{r_0}\right)^{\mathrm{Re}\,\lambda}c_1} - \frac{\mathrm{Re}\,B_\parallel(a)}{\left(\frac{a}{r_0}\right)^{\mathrm{Re}\,\lambda}}\right]\frac{1}{c_5},$$
$$\mathrm{Re}\,\gamma_2 = \frac{\mathrm{Im}\,E_\perp(a)}{r\left(\frac{a}{r_0}\right)^{\mathrm{Re}\,\lambda}c_1} - \mathrm{Im}\,\gamma_2\frac{c_2}{c_1}, \quad (29)$$

where

$$c_1 = \mathrm{Im}\,\tilde{E}_\perp(a)\cos(\arg) + \mathrm{Re}\,\tilde{E}_\perp(a)\sin(\arg),$$
$$c_2 = \mathrm{Re}\,\tilde{E}_\perp(a)\cos(\arg) - \mathrm{Im}\,\tilde{E}_\perp(a)\sin(\arg),$$
$$c_3 = \mathrm{Re}\,\tilde{B}_\parallel(a)\cos(\arg) - \mathrm{Im}\,\tilde{B}_\parallel(a)\sin(\arg), \quad (30)$$
$$c_4 = \mathrm{Im}\,\tilde{B}_\parallel(a)\cos(\arg) + \mathrm{Re}\,\tilde{B}_\parallel(a)\sin(\arg),$$
$$c_5 = \frac{c_2c_3}{c_1} + c_4, \quad \arg = \ln\left(\frac{a}{r_0}\right)\mathrm{Im}\,\lambda.$$

The method for calculating the independent coefficients C_1 and D_1 in the solutions for the vacuum region and the boundary values of the field components $E_\perp(a)$ and $B_\parallel(a)$ is presented in Appendix 3.

6.1.2. Absorbed power. The energy deposited in unit plasma volume per unit time was expressed as the averaged (over the oscillation period) scalar product of the real parts of the complex vectors of the electric field and current density:

$$\frac{de}{dt} = \frac{1}{4}\sum_a (j_aE_a^* + E_aj_a^*), \quad (31)$$

where e is the energy density.

In our code, the absorbed energy was found from the dielectric tensor,

$$\frac{de}{dt} = \frac{1}{2}\frac{\omega}{4\pi}\sum_{a,b}\varepsilon_{ab}^{(an)}E_a^*E_b, \quad (32)$$

where $\varepsilon_{ab}^{(an)} = \frac{1}{2i}(\varepsilon_{ab} - \varepsilon_{ba}^*)$ is the anti-Hermitian part of the dielectric tensor, composed of the imaginary parts of the diagonal elements and the real parts of the off-diagonal elements.

In calculating the absorbed energy, Landau damping by electrons was taken into account as an imaginary correction $i\nu$ to the frequency.

Transforming the imaginary parts of the diagonal elements of the tensor ε in the proper manner yields

$$\mathrm{Im}\,\varepsilon_{rr} = \frac{c^2(\mathrm{Im}\,A\omega^2 - 2\mathrm{Re}\,A\omega\nu)}{\omega^4 + 4\omega^2\nu^2},$$
$$\mathrm{Im}\,\varepsilon_{\perp\perp} = \mathrm{Im}\,\varepsilon_{rr}, \quad (33)$$

where

$$\mathrm{Re}\,A = \frac{(\omega_{ci}/c_A)^2\omega^2(\omega_{ci}^2 - \omega^2 - 4\nu^2)}{(\omega_{ci}^2 - \omega^2)^2 + 4\omega^2\nu^2},$$
$$\mathrm{Im}\,A = \frac{2(\omega_{ci}/c_A)^2\omega_{ci}^2\omega\nu}{(\omega_{ci}^2 - \omega^2)^2 + 4\omega^2\nu^2} \quad (34)$$

are the real and imaginary parts of the coefficient A in the basic differential equations (15) and (16).

The real parts of the off-diagonal elements of the tensor ε are

$$\mathrm{Re}\,\varepsilon_{r\perp} = -\frac{c^2(\mathrm{Im}\,G\omega^2 - 2\mathrm{Re}\,G\omega\nu)}{\omega^4 + 4\omega^2\nu^2},$$
$$\mathrm{Re}\,\varepsilon_{\perp r} = -\mathrm{Re}\,\varepsilon_{r\perp}, \quad (35)$$

where

$$\mathrm{Re}\,G = \frac{(\omega_{ci}\omega/c_A^2)[\omega^2(\omega_{ci}^2 - \omega^2 - 4\nu^2) - 2\omega_{ci}^2\nu^2]}{(\omega_{ci}^2 - \omega^2)^2 + 4\omega^2\nu^2} + G_1,$$
$$\mathrm{Im}\,G = \frac{(\omega/c_A)^2\omega_{ci}\nu(3\omega_{ci}^2 - \omega^2 - 4\nu^2)}{(\omega_{ci}^2 - \omega^2) + 4\omega^2\nu^2} \quad (36)$$

are the real and imaginary parts of the coefficient G in equations (15) and (16).

The term G_1 in the real part of the coefficient G contains information on the equilibrium current density profile $\mathbf{j}_0(r)$. In local orthogonal coordinates, the expressions for the equilibrium current density components, $j_{0\vartheta} = 0$ and $j_{0z} = (c/(4\pi r))d(rB_{0\vartheta})/dr$, can be converted to the form

$$j_0 = j_{0z} = j(0)[1 - (r/a)^2]^\delta, \quad (37)$$

where $j(0) \equiv j(r = 0)$.

Integrating (36) over the radius, we find the field component $B_{0\vartheta}$ and the coefficient G_1:

$$B_{0\vartheta} = \frac{2\pi j(0)a^2}{cr(\delta + 1)}\{1 - [1 - (r/a)^2]^{\delta+1}\}, \quad (38)$$

$$G_1 = -4kj(0)[1 - (r/a)^2]^\delta\pi/(cB_0). \quad (39)$$

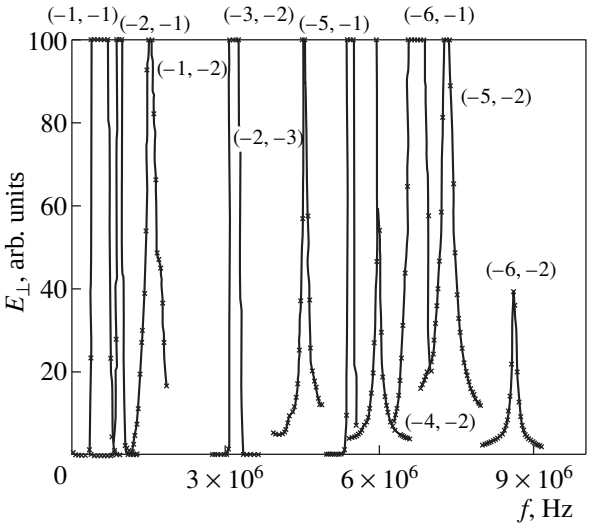

Fig. 5. Theoretical DAW spectrum calculated for the case of a cold deuterium plasma in T-10 (f is the generator frequency).

Consequently, the AW power deposited in unit plasma volume can be written as

$$\frac{de}{dt} = \frac{\omega}{8\pi}[\mathrm{Im}\,\varepsilon_r(\mathrm{Re}\,E_r^2 + \mathrm{Im}\,E_r^2) + \mathrm{Im}\,\varepsilon_{rr}(\mathrm{Re}\,E_\perp^2 + \mathrm{Im}\,E_\perp^2) + 2\mathrm{Re}\,\varepsilon_{r\perp}(\mathrm{Im}\,E_\perp \times \mathrm{Re}\,E_r - \mathrm{Re}\,E_\perp \times \mathrm{Im}\,E_r)]. \quad (40)$$

6.1.3. Numerical results for the case of a cold plasma. The eigenmodes manifest themselves as peaks in the frequency profiles of the AW field components, $E_\perp(f)$ and $B_\parallel(f)$, and the deposited power, $\mathcal{P}(f)$.

Figure 5 shows the theoretical DAW spectrum calculated numerically for the case of a cold deuterium plasma.

Recall that the calculation accuracy was checked by comparing the preliminary numerical results with the relevant experimental data from TEXTOR [5], in which case the input to the code included the parameter values characteristic of the TEXTOR plasma in those experiments (of course, except for the temperature, which was assumed to be zero). The results of the comparison are summarized in Table 1, which shows that our theory agrees fairly well with the experiment.

Table 1. Comparison between the theoretical and experimental results for the parameter values $I_p = 350$ kA, $n_{e0} = 2.8 \times 10^{13}$ cm^{-3}, $B_t = 2$ T, and $\delta = 3.5$

(n, m) mode	Resonant frequency, MHz	
	numerical code, theory	experiment
(–5, –2)	3.04	2.75
(–4, –2)	2.45	2.45
(–3, –2)	1.86	2.00

This agreement, first, confirms the previously known conclusion that, in the geometry adopted here, the eigenfrequencies of the DAW spectrum depend weakly on the temperature and are mainly governed by the plasma density and current density profiles and, second, makes it possible to justify the reliability of the model underlying the code by performing test simulations.

Under the above assumptions, we also obtained some important results for the T-10 tokamak.

The relative frequency width of the (–6, –1) eigenmode is about 7% and that of the (–5, –2) eigenmode is about 3%.

The intensity of AWs is highest in the resonant layer, in which the AW energy is deposited. The spatial position of the resonant layer depends on the ratio n/m of the mode numbers. The larger this ratio, the closer the resonant layer to the plasma center.

The radial profiles of the absorbed AW energy for four eigenmodes are shown in Figs. 6–9.

According to the theory, the resonant layer for the (–6, –1) mode ($|n/m| = 6 \gg 1$) should lie near the plasma center; this is confirmed by our test simulations. The resonant layer for the (–1, –1) mode, for which this ratio is equal to unity, occurs almost in the middle of the plasma column. For the (–2, –3) and (–1, –2) modes, the ratio n/m is smaller than unity, so that the energy of these eigenmodes is deposited at the plasma periphery.

The width of the resonant layers for all of these eigenmodes is about 1–2 cm.

Further modifications of the calculation scheme and numerical code made it possible to refine the previous results and obtain the new ones. In particular, we were able to determine the accuracy with which the central value $q(0)$ of the safety factor was computed.

6.2. The Case of a Real Plasma

Now, we consider a plasma with electron and ion temperatures typical for tokamaks (e.g., for T-10).

The effect of the thermal motion of electrons and ions was taken into account by supplementing the equations of plasma motion (13) and (14) with the terms that account for the pressure gradient:

$$\rho\frac{\partial \mathbf{v}}{\partial t} = \frac{1}{c}\{[\mathbf{j}_0, \mathbf{B}] + [\mathbf{j}, \mathbf{B}_0]\} - \nabla P_i - \nabla P_e, \quad (41)$$

$$\mathbf{E} + \frac{1}{c}[\mathbf{v}, \mathbf{B}_0] = \frac{m_i}{ec\rho}\{[\mathbf{j}, \mathbf{B}_0] + [\mathbf{j}_0, \mathbf{B}]\} - \frac{m_i}{e\rho}\nabla P_e. \quad (42)$$

To describe how the plasma pressure affects the waves, we must relate the pressure gradient to the

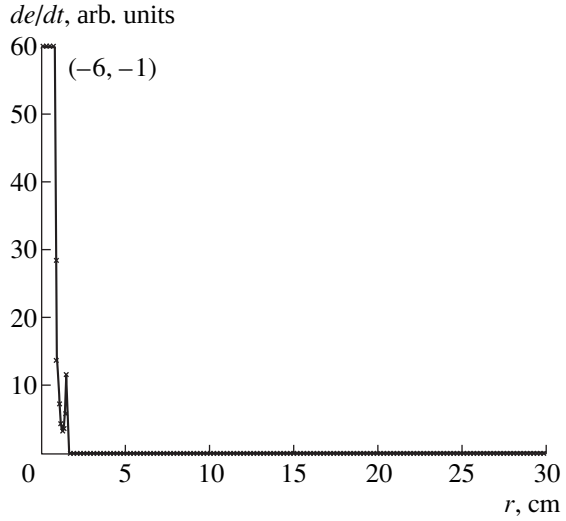

Fig. 6. Radial profile of the absorbed AW power for the (–6, –1) mode (*de*/*dt* is the AW power deposited in unit plasma volume).

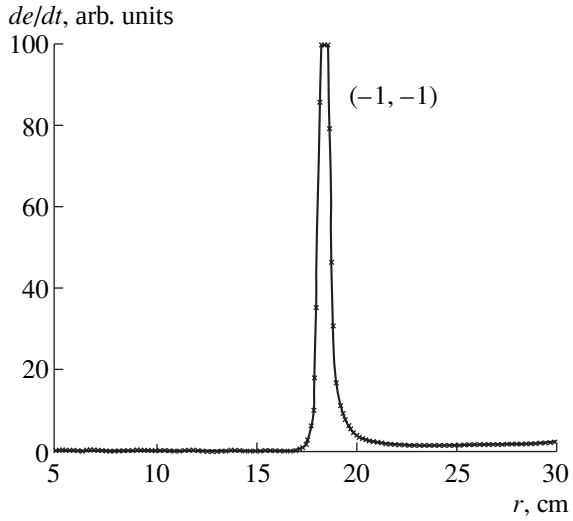

Fig. 7. Radial profile of the absorbed AW power for the (–1, –1) mode.

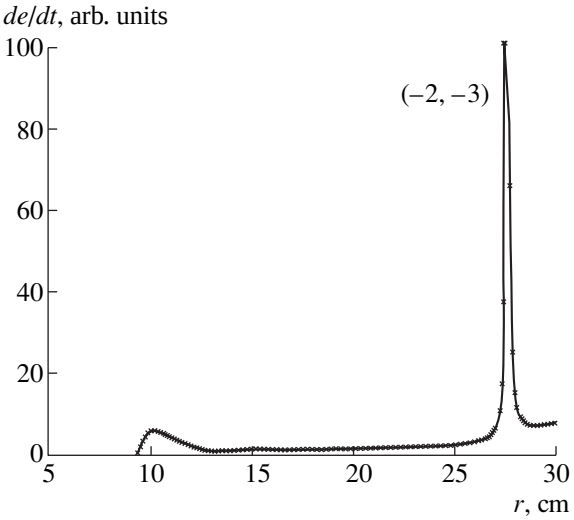

Fig. 8. Radial profile of the absorbed AW power for the (–2, –3) mode.

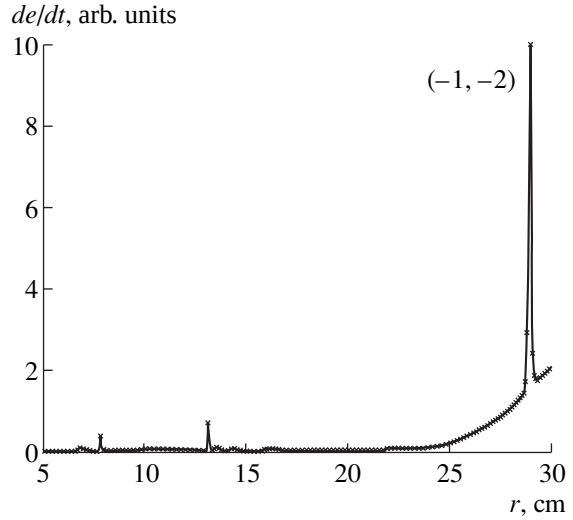

Fig. 9. Radial profile of the absorbed AW power for the (–1, –2) mode.

velocity of plasma motion. We assume that the plasma state changes adiabatically,

$$P \sim n^{\gamma},$$

where γ is the adiabatic power-law index. The evolution of the density n and the change in the velocity $\mathbf{v}$ are related by the continuity equation

$$\frac{\partial n}{\partial t} = -\mathrm{div}(n\mathbf{v}). \qquad (43)$$

In the linear approximation, equation (43) reduces to

$$\frac{\partial n'}{\partial t} \approx -n\,\mathrm{div}\,\mathbf{v}, \qquad (44)$$

where n' and n are the perturbed and unperturbed densities, respectively. In the case of a plane wave, the perturbed density gradient is

$$\nabla P = \left[\frac{i}{\omega}\mathbf{k}(\mathbf{kv}) + \frac{\mathbf{e}_r}{n}\frac{\partial n}{\partial r}\frac{(\mathbf{kv})}{\omega}\right]\gamma P, \qquad (45)$$

where

$$\nabla P = \nabla P_i + \nabla P_e,\ P = \gamma n(T_i + T_e),$$

$$\mathbf{kv} = -\frac{\dfrac{4\pi i c_A^2}{\omega c B_0}\left(1 + \dfrac{j_0 c k_\parallel}{B_0 \omega \omega_{ci}}\right)k_\perp B_\parallel}{1 + i\dfrac{P}{\omega^2 \rho}k^2}.$$

The electron density in (45) was calculated from the parabolic profile (8). The electron and ion temperatures were approximated by the following profiles typical of most present-day tokamaks:

$$T_{e,i} = T_{e,i}(0)\left[1-\left(\frac{r}{a}\right)^2\right]^2. \quad (46)$$

Inserting (45) into (41), we obtain the velocity of plasma motion in local coordinates:

$$\mathbf{v} = \frac{4\pi i c_A^2}{\omega c B_0}\left\{[\mathbf{j}\mathbf{e}_\parallel] + \frac{j_0}{B_0}[\mathbf{e}_\parallel B]\right\} - i\frac{\gamma P}{\omega^2\rho}\mathbf{k}(\mathbf{k}\mathbf{v}) - \frac{\gamma P}{\omega^2\rho}\frac{1}{n}\frac{\partial n}{\partial r}\mathbf{e}_r(\mathbf{k}\mathbf{v}). \quad (47)$$

We substitute (45) and (47) into the equations of plasma motion (41) and (42) and solve them together with Faraday's law in order to obtain a new set of differential equations for the AW field components $E_\perp$ and $B_\parallel$,

$$\frac{dE_\perp}{dr} = \left(A_1 k_\perp - \frac{1}{r}\right)E_\perp + \frac{i\omega}{c}\left(1-\frac{k_\perp}{G_1}\right)^2 B_\parallel, \quad (48)$$

$$\frac{dB_\parallel}{dr} = A_2 E_\perp + G_2 B_\parallel k_\perp, \quad (49)$$

where

$$A_1 = \frac{\varepsilon_{r\perp}\omega^2}{ic^2\left[\left(\frac{\omega}{c}\right)^2\varepsilon_{rr} - k_\parallel^2\right]}, \quad G_1 = \left(\frac{\omega}{c}\right)^2\varepsilon_{rr} - k_\parallel^2, \quad (50)$$

$$A_2 = i\frac{\omega}{c}\left[\varepsilon_{\perp\perp} - \frac{\varepsilon_{\perp r}\varepsilon_{r\perp}}{\varepsilon_{rr} - \left(\frac{c}{\omega}\right)^2 k_\parallel^2} - \left(\frac{c}{\omega}\right)^2 k_\parallel^2\right],$$
$$G_2 = -i\frac{\varepsilon_{\perp r}}{\varepsilon_{rr} - \left(\frac{c}{\omega}\right)^2 k_\parallel^2}. \quad (51)$$

Expressions for the elements of the dielectric tensor for a real plasma are given in Appendix 4.

As in the case of a cold plasma, solving the problem for a real plasma in the way just described resulted in the appearance of singularities of the 0/0 type at the plasma center. These singularities can be resolved by the method we have presented. The relevant change of the functions puts the resulting set of equations (with the boundary conditions imposed so as to perform numerical integration from the center) in the form

$$\frac{d\tilde{E}_\perp}{dr} = \tilde{E}_\perp\left[A_1 k_\perp - \frac{1}{r}(\lambda+2)\right] + \tilde{B}_\parallel\frac{1}{r}\frac{i\omega}{c}\left(1-\frac{k_\perp^2}{G_1}\right),$$

$$\frac{d\tilde{B}_\parallel}{dr} = \tilde{E}_\perp r A_2 + \tilde{B}_\parallel\left(G_2 k_\perp - \frac{\lambda}{r}\right), \quad (52)$$

$$\tilde{E}_\perp(0) = 1, \ \tilde{B}_\parallel(0) = \gamma_3(0), \ \left.\frac{d\tilde{E}_\perp}{dr}\right|_{r=0} = \left.\frac{d\tilde{B}_\parallel}{dr}\right|_{r=0} = 0.$$

The complex power index λ for a real plasma is evaluated in Appendix 5.

Equations (52) were integrated numerically from the plasma center to the plasma periphery in order to obtain the desired values of the functions $E_\perp$ and $B_\parallel$ at the plasma–vacuum boundary. These values were then used to integrate the basic equations (48) and (49) with coefficients (50) and (51) from the plasma boundary to the plasma center. As a result, the code plotted the radial profiles of the AW field components for each value of the frequency ω, which was varied with a given step within the prescribed range. The refined version of the code made it possible to determine the resonant frequencies more exactly for the same eigenmodes that were treated in the case of a cold plasma.

Landau damping by electrons was described by the following formula related to the case of an equilibrium thermal plasma [13]:

$$\nu = \frac{\sqrt{\pi}\omega_0}{2\sqrt{2}}u_{ph}^3\left(\frac{m_e}{T_e}\right)^{3/2}\exp\left\{-\frac{m_e u_{ph}^2}{2T_e}\right\}, \quad (53)$$

where $u_{ph} = \omega/k$ is the AW phase velocity and ω_0 is the electron plasma frequency.

Formula (53) can be applied only under the following two conditions. First, the damping time should be shorter than the period of electron and ion bounces in the potential wells of the wave electric field, $|\tau_{OSC}/\tau| > 1$, in order for the waves to damp completely before nonlinear effects come into play [14]. Here, τ is the damping time and τ_{OSC} is the estimated time interval during which the linear theory is applicable, $\tau_{OSC} \sim \sqrt{m/(ekE)}$, where m is the mass of a particle and E is the wave electric field. Second, when the time between collisions, τ_c, is shorter than the characteristic time interval over which the linear theory is valid ($|\tau_{OSC}/\tau_c| > 1$), Landau damping should be taken into account along with the conventional collisional damping.

Formula (53) is obtained in the lowest order in kv/ω and is valid only for weak damping, which depends on the wavenumber k.

6.2.1. Numerical results for the case of a real plasma. Our simulations confirm that the thermal electron motion affects the AW propagation in the plasma weaker than, e.g., particle–particle collisions, which are incorporated into our model through an imaginary correction to the frequency. However, taking into account nonzero temperatures $T_{i,e}$ corresponding to real experiments allowed us to achieve (in some cases) essentially complete agreement between the eigenfre-

quencies of the Alfvén modes that were computed from the above theoretical formulas and those measured experimentally. The numerical results presented below were obtained for the following parameter values corresponding to the T-10 tokamak: $I = 272.7$ kA, $B_t = 3$ T, $\delta = 3.5$, $n_{e0} = 10^{13}$ cm^{-3}, $T_{e0} = 1000$ eV, and $T_{i0} = 500$ eV.

As in the case of a cold plasma, we checked the reliability of the results by running the code with the input parameters relevant to the TEXTOR experiments (cf. Section 6.1.3), in which case the adiabatic power-law index was set to be equal to that for one-dimensional motion, $\gamma = 3$. The numerical results and experimental data are compared in Table 2, which shows that the best agreement between them is achieved when the thermal motion is taken into account.

The specific results presented below were obtained for the T-10 tokamak (as in the case of a cold plasma). However, the qualitative conclusions are also valid for other tokamaks.

Thermal motion manifests itself, in particular, in the fact that the eigenfrequencies of the neighboring modes (see Section 5) depend on the parameter δ, which governs the shape of the current density profile. If the difference between the eigenfrequencies of a given pair of neighboring modes is known from experiments, then the results obtained above make it possible to readily determine $q(0)$ using formula (7) (see Section 5). As an example, Fig. 10 shows the behavior of the frequency difference between the (–5, –2) and (–6, –1) modes.

Generally, an increase in δ leads to a corresponding increase in the difference between the frequencies of the neighboring eigenmodes. This circumstance simplifies the experimental detection of eigenmodes and provides more precise measurements of $q(0)$, which can be found directly from Fig. 10 in comparing the theoretical frequency difference with that recorded in experiments.

Table 2

(n, m) mode	Resonant frequency, MHz	
	numerical code	experiment
(–5, –2)	2.75	2.75
(–4, –2)	2.53	2.45
(–3, –2)	2.00	2.00

Analyzing the accuracy with which $q(0)$ can be determined, it will be useful to present δ-profiles of the frequency difference for several values of the damping rate ν. Recall that, as in [7], the imaginary correction ν to the frequency serves to take into account energy dissipation. Figures 11 and 12 show the frequency difference between the (–5, –2) and (–6, –1) modes as a function of δ for $\nu = 0.03\omega$, 0.003ω, and 0.0003ω. Comparing the profiles obtained for ν values that differ by an order of magnitude, we can estimate the amount by which $q(0)$ changes when the difference Δf_{res} ($\omega_{DAW} = 2\pi f_{\text{res}}$) is changed accordingly. For example, an error of 0.01 MHz in calculating Δf_{res} leads to an error of about 0.08 in calculating $q(0)$. According to Fig. 11, a change in Δf_{res} by 1% corresponds to a change in $q(0)$ by 3.6%. Consequently, the calculation accuracy should be very high. Our numerical scheme is capable of ensuring such accuracy. Accordingly, the fairly simple diagnostic equipment proposed here should ensure the required measurement precision.

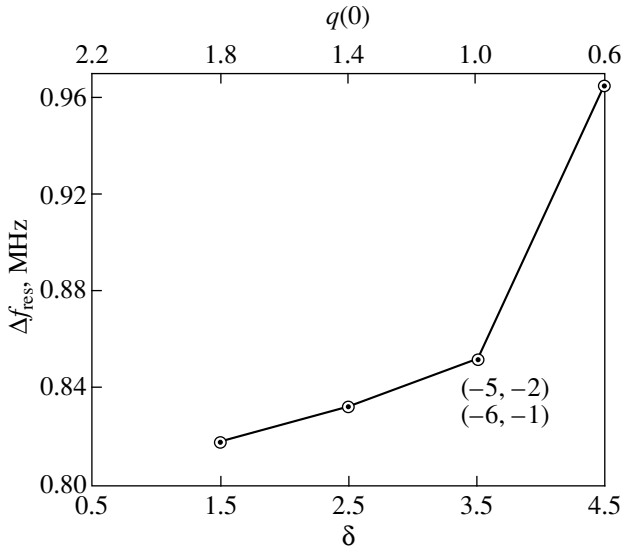

Fig. 10. Theoretical difference between the frequencies of the neighboring (–5, –2) and (– 6, –1) eigenmodes as a function of the parameter δ.

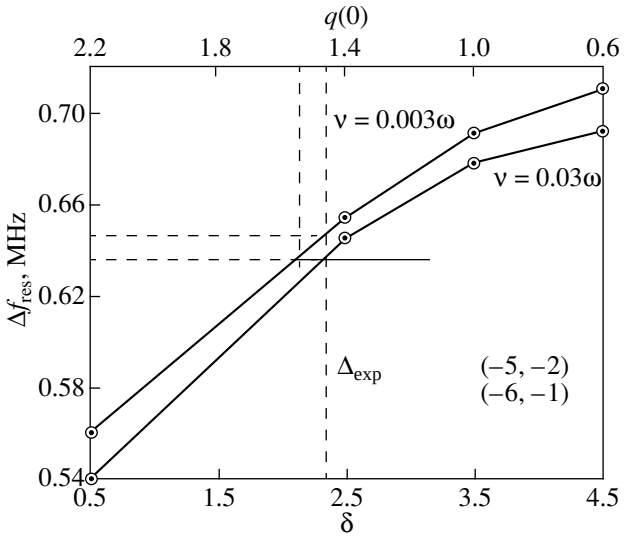

Fig. 11. Difference between the frequencies of the (–5, –2) and (–6, –1) eigenmodes as a function of δ for two different values of the damping rate $\nu = 0.03\omega$ and 0.003ω.

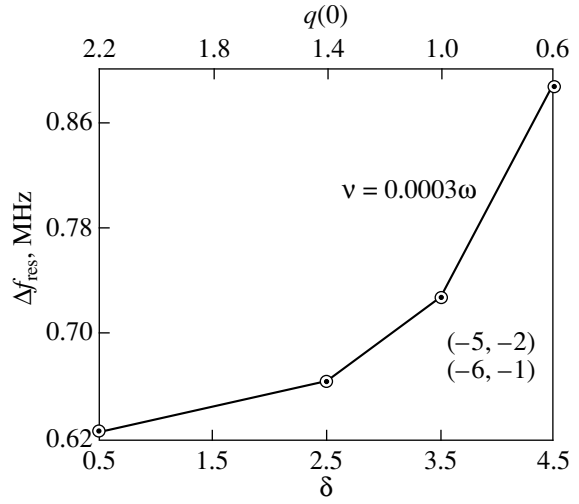

Fig. 12. Difference between the frequencies of the (–5, –2) and (–6, –1) eigenmodes for the damping rate $\nu = 0.0003\omega$.

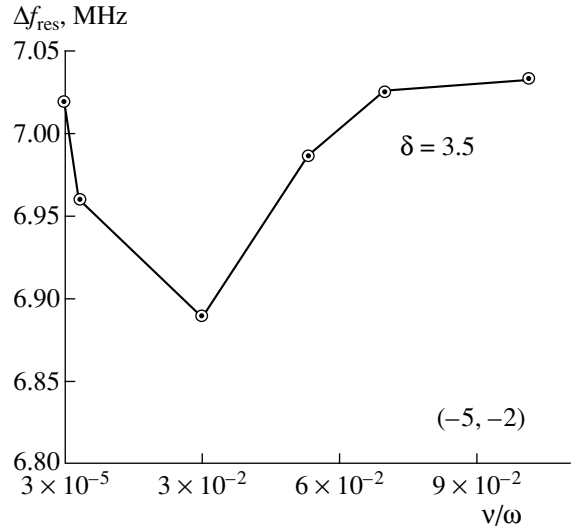

Fig. 13. Resonant frequency of the (–5, –2) eigenmode versus the damping rate for $\delta = 3.5$.

Since ν is mainly governed by collisional processes whose role, even at $\nu = 0.003\omega$, is great enough for energy exchange between the eigenmodes, the δ-profiles of the frequency difference are expected to change qualitatively at much lower damping rates, e.g., at $\nu = 0.0003\omega$ (Fig. 12). A comparison between Figs. 12 and 13 confirms this conclusion.

Our simulations revealed that the mode frequencies depend weakly on the damping rate. Figures 13 and 14 show the related profiles computed at a fixed parameter value $\delta = 3.5$. For the (–5, –2) mode, a change in ν by four (on average) orders of magnitude, from $3 \times 10^{-5}\omega$ to $10^{-1}\omega$, causes the resonant frequency to change by 0.13 MHz, i.e., by no more than 2%. For the (–6, –1) mode, a similar change in the damping rate, from $3 \times 10^{-5}\omega$ to $7 \times 10^{-1}\omega$, leads to almost the same change in the resonant frequency, i.e., 0.1 MHz (1.5%). We found that each of the eigenmode profiles has its own extreme point.

Our simulations also showed that the frequency shift for each mode is much more sensitive to the parameter δ (which governs the shape of the current density profile) than to the damping rate. For example, for the eigenfrequency to change by 0.13 MHz, the parameter δ should be changed by only 4, while ν should be changed by a factor of 3330. In other words, in real experiments, the resonant frequency f_{res} of any eigenmode will change by no more than 4×10^{-4} MHz if the damping rate changes by an order of magnitude. The estimate just presented implies that it is possible to choose the optimum electron and ion temperatures for which the eigenmode frequencies can be assumed to be independent of the damping rate. This, in turn, ensures both the stability of the plasma–antenna system to variations of such a parameter as ν and the reliability of information obtained about the plasma with the help of the DAW spectrum.

Our analysis revealed that the plasma is quite stable against variations of the external (with respect to the plasma) antenna parameters. For example, we carried out additional test simulations for the (–1, –1) mode in order to examine the stability of the plasma–antenna system against variations of the shape and dimensions of the antenna (specifically, the antenna radius). The antenna was assumed to be positioned either at the plasma boundary, $r_{ant} = a = 30$ cm, or at the wall, $r_{ant} = r_w = 39$ cm. The test computations showed that both the resonant frequency $f_{res} = 8.454 \times 10^5$ Hz and the radial position of the resonant layer, $r_{res} = 20.8$ cm, do not change, while the AW power deposited in the plasma

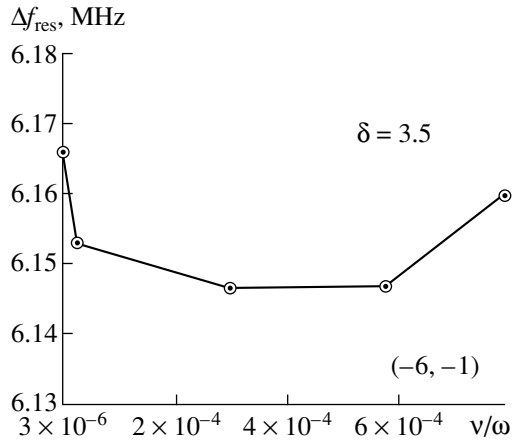

Fig. 14. Resonant frequency of the (–6, –1) eigenmode versus the damping rate for $\delta = 3.5$.

per unit length changes insignificantly and is equal to $\mathcal{P} \approx 8.3 \times 10^{-1}$ W/cm.

Hence, our simulations confirm that the method proposed makes it possible to obtain information about the plasma parameters rather than about the external equipment used to excite AWs in the plasma.

It is also of interest to analyze the AW power absorbed by the plasma as a function of the toroidal number n at the fixed poloidal number $m = -1$ (Fig. 15). The profile in Fig. 15 was obtained by processing the numerical results for the four modes indicated. The power of the modes with small numbers n is absorbed almost completely. As n increases, the absorbed power falls off sharply by many orders of magnitude. The profile in Fig. 15 agrees qualitatively and quantitatively with similar profiles computed by Ross *et al.* [6] for other values of the plasma parameters.

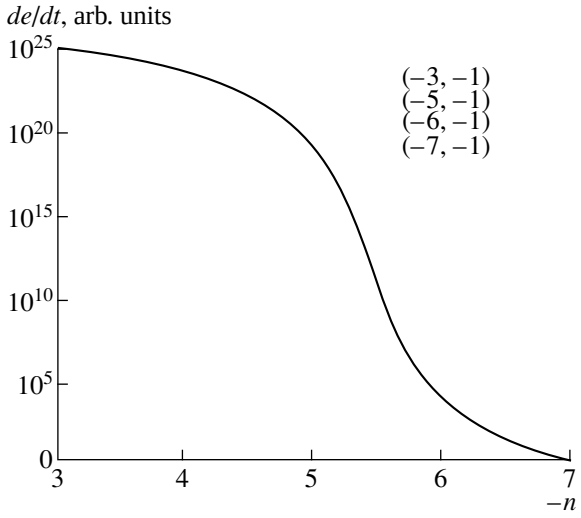

Fig. 15. AW power deposited in the plasma versus the toroidal number n for the fixed poloidal number $m = -1$.

In summary, we again outline the main steps in developing the code (recall that the reliability of our preliminary numerical results was checked by comparing them with the experimental data from TEXTOR).

First, we developed a simplified version of the code in cylindrical geometry on the basis of the model of a cold, ideally conducting plasma ($T_{i,e} = 0$). This simplified version was also created in several steps.

At the first step, we took into account only one mechanism for energy exchange between the eigenmodes, specifically, toroidal feedback coupling, in which case, however, we failed to obtain the entire DAW spectrum, and the AW field components computed with the simplest version of the code were found to contradict those measured experimentally in TEXTOR.

After we supplemented the code with another mechanism for energy exchange, namely, Landau damping, which was taken into account through the imaginary correction $i\nu$ to the frequency [6], we succeeded in calculating the entire DAW spectrum. However, at this step, we again failed to achieve agreement between the theoretical and experimental eigenfrequencies of the DAW spectrum.

We significantly raised the calculation accuracy when we switched from integration of the basic set of differential equations from the plasma center to the plasma boundary to integration in the opposite direction. To do this, we obtained the initial conditions at the plasma boundary by integrating the basic equations from the plasma center. Such an artificial approach allowed us to apply the geometrical-optics approximation (which implies that the wavelength is much shorter than the characteristic dimension of the system) over most of the plasma column (including the plasma boundary). As a result, our physical model became even more reliable, which was confirmed by simulations. Using this approach, we achieved not only qualitative but also quantitative (to some extent) agreement between the theoretical and experimental results.

Note that, in order to resolve singularities at the center, the basic set of differential equations integrated from the plasma center was transformed by changing the functions in the proper manner.

The final step in refining the calculation scheme was to take into account the thermal motion of electrons and ions. The correction ν was specified from the explicit expression for the Landau damping rate [13] rather than in a model form. As a result, we arrived at an essentially complete agreement between the computed and experimental DAW spectra.

7. CONCLUSION

We have described a numerical method developed for use in the diagnostics proposed for determining the parameter q and effective ion mass from the DAW spectrum in tokamak plasmas. Estimates of the parameters of the diagnostic system for most tokamaks (TEXTOR, T-10, ITER, etc.) show that the desired characteristics can be obtained with a high accuracy using simpler (in comparison with other diagnostics) equipment with fairly moderate technical parameters. We have developed a computer code appropriate for determining the parameters of the eigenmodes of the DAW spectrum such as the frequency and amplitude of AW fields, their intensities, and so on.

We have applied our code to investigate the plasma stability against variations of the antenna parameters in order to formulate the requirements for the antenna: the shape of the antenna, its position inside the discharge chamber, the generator frequency, etc.

The code can be used to choose the optimum electron and ion temperatures (which affect the damping rate of the eigenmodes of the DAW spectrum) and the current density profile (which governs the AW eigen-

frequencies), thereby making it possible to provide recommendations for experiments in tokamaks (in particular, in T-10).

Since the mechanisms for energy conversion from AWs to the plasma are incorporated into the code, it can also be used to study the possibility of auxiliary plasma heating by AWs.

APPENDIX 1

JUSTIFICATION OF THE CHOICE OF THE ANTENNA AND ESTIMATION OF ITS MAIN PARAMETERS APPLIED TO T-10

A1.1. Choice of the Toroidal Mode Numbers n for Measurements

Experimental measurements of the DAW spectrum in TEXTOR (Fig. 3) showed that the larger the toroidal number n, the larger the difference between the frequencies of the neighboring eigenmodes (n_1, m_1) and (n_2, m_2) and the stronger the dependence of the resonant frequency of each of the modes on the $q(0)$ value [5]. These circumstances make the frequency difference for the modes with large n easier to record experimentally.

Also, each of the modes with large toroidal numbers is characterized by its own resonant layer (see Section 2), which occurs near the plasma center ($r_{n,m} \approx 0$). Such modes allow the central value $q(0)$ to be determined more exactly in comparison with that obtained from the modes whose resonant layers lie far away from the center [5].

Consequently, it is expedient to find $q(0)$ using eigenmodes with large n. The modes with $n \sim 1$ make it possible to determine the radial profile $q(r)$ at $r > 0$, because their resonant layers, which can occur at radii $r_{n,m}$ far away from the plasma center, characterize the quantities $q(r_{n,m})$ at these radial positions.

Hence, it is expedient to work with a sufficiently broad spectrum of toroidal numbers n such as $0 \le n \le 8$.

A1.2. How the Poloidal Length of the Antenna Influences the Mode Intensities

From (1), we can see that, if the antenna is relatively long, then the intensity of eigenmodes with the largest m decreases in proportion to $\sin(m\vartheta_A)/m$.

Our analysis shows that the antenna with the poloidal angle span $2\vartheta_{ant} = 135°$ excites the broadest spectrum of eigenmodes with the poloidal numbers m. However, the modes with $m > 4$ are more difficult to detect experimentally, because their intensities decrease as m increases (in the proportion just indicated). Since the method for measuring $q(0)$ in TEXTOR from the frequency difference between the neighboring eigenmodes [5] does not involve the modes with $m > 3$, the antenna with the poloidal angle span $2\vartheta_{ant} = 90°$ (which corresponds to 57.7 cm) is quite suitable for our purposes. Such an antenna does not excite modes whose poloidal numbers are multiples of 4, whereas the modes with $m = 0$ and toroidal numbers 1, 2, and 3 will dominate in the antenna spectrum, in which case the eigenmodes are much easier to identify experimentally. Also, this antenna is simpler from a technological standpoint.

A1.3. Choice of the Antenna Width in the Toroidal Direction

Since the antenna width in the toroidal direction is much less than the toroidal circumference of the torus, then, according to dispersion relation (1), the antenna width has essentially no effect on the intensity of eigenmodes with $n \le 8$ or even with larger toroidal numbers. Consequently, it is more expedient to use antennas with a large width in the toroidal direction. In this case, the antenna inductance becomes lower, because the linear inductance L_p of a two-strip line is related to the strip width b by the simple relationship

$$L_p = \mu_0 h/b, \qquad \text{(A1.1)}$$

where h is the distance between the strips. For a given radiation power deposited in the plasma, the wider the antenna, the lower the high-frequency potential at the antenna.

The sizes of the diagnostic ports in T-10 are such that the antenna can be no wider than 5 cm, which corresponds to about 1.9°.

A1.4. Necessity to Screen the Antenna

In T-10, the characteristic plasma density near the antenna is $n \sim (7–8) \times 10^{12}$ cm^{-3}. The capacitance that is formed by the direct-current and reverse-current conductors of a loop antenna can shunt the loop through the plasma. The impedance of the plasma-filled gap is calculated from the formula

$$X_c = 1/(\omega C_v l_{ant} \varepsilon), \qquad \text{(A1.2)}$$

where C_v is the linear capacitance of a loop antenna in vacuum, l_{ant} is the antenna length, and ε is the permittivity of a cold plasma.

The permittivity ε can be estimated as [13]

$$\varepsilon = c^2/c_A^2, \qquad \text{(A1.3)}$$

where c is the speed of light and c_A is the Alfvén velocity. For the toroidal field $B_t = 2$ T and the density $n \sim 7.5 \times 10^{12}$ cm^{-3}, the permittivity ε is $\varepsilon \approx 709$. The capacitance of a loop antenna in vacuum is estimated as $C_v l_{ant} \approx 35$ pF; consequently, for the maximum frequency of a sweep band (8 MHz), the capacitive reactance of the plasma-filled gap is $X_c \approx 1.1\ \Omega$. Consequently, the antenna loop should be screened in order for the plasma not to flow into the gap between the conductors.

A1.5. Minimum and Maximum Frequencies of a Sweep Band

In order to excite the number of eigenmodes that would be sufficient for diagnostic purposes, it is necessary that the eigenfrequencies of the (n, m) modes to be detected lie within the sweep band of a generator whose frequency increases linearly from a minimum value to a maximum value during a certain time interval in the course of discharge.

The maximum and minimum values of the frequency band are determined from dispersion relation (1) for AWs. The antenna geometry chosen for T-10 experiments implies that, in the DAW spectrum, the most complete information will be obtained from eigenmodes with the toroidal numbers $0 \le n \le 8$ and poloidal numbers $0 \le m \le 3$. Since the T-10 tokamak operates with a deuterium plasma, we obtain from dispersion relation (1) that, for the density $n_{e0} = 4 \times 10^{13}$ cm^{-3} and the maximum toroidal field $B_t = 2.9$ T, the maximum frequency is $f \approx 8$ MHz. For the highest density $n_{e0} = 5 \times 10^{13}$ cm^{-3} recorded in T-10 experiments and $B_t = 2$ T, we obtain that the minimum frequency is $f_{\min} \approx 0.8$ MHz.

A1.6. Radiation Impedance of a Screened Antenna

The radiation impedance of an antenna was calculated using the method proposed by Weynants *et al.* [15] to analyze the coupling between an antenna and a plasma in experiments on ion cyclotron heating.

Weynants *et al.* [15] derived the wave field distribution around an antenna that is not screened in vacuum and showed that the transverse (with respect to the toroidal direction) electric and magnetic components are of utmost importance. They also considered the effect of the screen and showed that it can suppress waves with different polarizations of the field **E** in a plasma.

In order to simplify the model, we assume that the current distribution in the antenna strip is uniform,

$$J(k_\parallel) = I\sin(k_\parallel w)/(k_\parallel w), \qquad \text{(A1.4)}$$

where I is the net current in the antenna and w is its half-width. The wave vector component $k_\parallel$ parallel to the equilibrium magnetic field was calculated from the formula

$$k_\parallel^2 = (\omega/c_A)^2[1 + \omega/\omega_{ci}]^{-1}. \qquad \text{(A1.5)}$$

In the approximation at hand, the radiation impedance R_{rad} was defined as

$$R_{rad} = [1/(2\pi|I|^2)]\int_0^{k_\parallel^{(\max)}} g(k_\parallel)|J(k_\parallel)|^2 dk_\parallel, \qquad \text{(A1.6)}$$

where the function $g(k_\parallel)$ was specified graphically in [15]. To estimate the function $g(k_\parallel)$ from the plot presented in [15], we specify the position of the antenna as follows:

(a) the distance between the antenna and the bellow (wall) is 1.5 cm,

(b) the distance between the antenna and the plasma center is 36.75 cm, and

(c) the distance between the antenna and the plasma boundary is 0.75 cm.

The quantity $k_\parallel$ was determined from formula (A1.5) with the maximum (central) plasma density. At a frequency of 6 MHz, we have $k_\parallel^{(\max)} \approx 5.01$ m^{-1}, so that formula (A1.6) for the radiation impedance gives $R_{\rm rad} \approx 4.8 \times 10^{-1}\ \Omega$.

A1.7. Frequency Profiles of the Antenna Current and Voltage

For the output stage of a broadband power amplifier to be installed in T-10, the length $l_{\rm cab}$ of the cable between the output stage and a loop antenna should be no shorter than several meters. For the frequency sweep band discussed in Section A1.5, the cable should be a distributed parameter line, which is calculated using the methods of the theory of long lines.

Under the assumption that losses in the cable are absent, the basic equations of a uniform line yield the following expression for the antenna current $I_{\rm ant}$:

$$I_{\rm ant} = I_0 W/[W\cos(kl_{\rm cab}) + Z_{\rm ant}\sin(kl_{\rm cab})], \qquad \text{(A1.7)}$$

where $k = 2\pi/\lambda$ is the wavenumber, W is the wave impedance, and I_0 is the current at the input of a long line. The load impedance $Z_{\rm ant}$ can be divided into resistive and reactive parts,

$$Z_{\rm ant} = R_{\rm ant} + R_{\rm rad} + i\omega L_{\rm ant}. \qquad \text{(A1.8)}$$

Below, we will show that the antenna resistance $R_{\rm ant}$ is low in comparison with both $R_{\rm rad}$ and the inductive reactance $\omega L_{\rm ant}$ (where $L_{\rm ant}$ is the inductance of the antenna loop); consequently, in calculating the desired frequency profiles of the antenna current and voltage, we can neglect the antenna resistance.

The main contribution to the antenna impedance comes from the antenna inductance, which was estimated from formula (A1.1) in which the length of a two-strip line was taken to be $l_{\rm ant} \approx 57.7$ cm.

For the antenna current $I_{\rm ant}$ to be frequency independent, the reactive part $i\omega L_{\rm ant}\sin(kl_{\rm cab})$ of the impedance should be small. This can be achieved only under the condition $kl_{\rm cab} \ll 1$. From these considerations and from the requirement that the design be as easy as possible, we choose the cable length to be $l_{\rm cab} = 5$ m.

For this cable length, the ratio of the antenna current to the current at the beginning of the line is maximum at the maximum frequency of a sweep band:

$$I_{\rm ant}/I_0 \approx 1.66 \ \text{ at } \ f = 6\ \text{MHz}. \qquad \text{(A1.9)}$$

Table 3

f, MHz	0.8	2	3	4	5	6
λ_{cab}, m	247.13	98.85	65.9	49.43	39.54	32.95
kl_{cab}, rad	1.27×10^{-1}	3.18×10^{-1}	4.77×10^{-1}	6.36×10^{-1}	7.95×10^{-1}	9.53×10^{-1}
I_{ant}, A	14.53	15.14	16.18	17.81	20.25	23.9
U_{ant}, V	17.38	42.06	66.89	97.9	139	197.5
Z_{ant}, Ω	$4.8 \times 10^{-1} + i \times 1.1$	$4.8 \times 10^{-1} + i \times 2.74$	$4.8 \times 10^{-1} + i \times 4.11$	$4.8 \times 10^{-1} + i \times 5.5$	$4.8 \times 10^{-1} + i \times 6.85$	$4.8 \times 10^{-1} + i \times 8.22$

Let us find the current at the input of the long line. First, we estimate the required power deposited in a plasma. In the TEXTOR experiments [5], this power was equal to 200 W. For T-10, the radiation power can be estimated by comparing the working volumes of the tokamaks: $V_{T\text{-}10}/V_{TEXTOR} \approx 0.5$. Consequently, the radiation power in T-10 can be estimated as $\mathcal{P}_{rad} = R_{rad}I \approx 100$ W, so that the current I_0 at the beginning of the long line is about 14.4 A.

For a current of 14.4 A at the input of the long line and a frequency of 6 MHz, the high-frequency potential U_l at the antenna is 197.5 V.

The magnitudes of the high-frequency current and potential at the antenna for some frequencies from the sweep band and a current of 14.4 A at the input of the line are summarized in Table 3.

A1.8. Resistance of the Antenna

The resistance of the antenna is estimated from the following two simple expressions for (a) the electric conductivity of copper and stainless steel,

$$\sigma_{st} = \sigma_{Cu}/40; \tag{A1.10}$$

and (b) the skin depth of a metal as a function of frequency,

$$\delta_{sk} \sim 1/\sqrt{f\sigma}. \tag{A1.11}$$

It is also well known that the skin depth δ_{Cu} for copper at a frequency of 1 kHz is equal to 2 mm.

Using relationships (A1.10) and (A1.11) and taking into account the fact that the entire length of the loop antenna is about 117 cm, we can estimate the resistance of the antenna at a frequency of 6 MHz as $R_{ant} \approx 0.05$ Ω.

APPENDIX 2

CALCULATION OF THE COMPLEX POWER INDEX λ AND THE RATIO OF THE GRADUALLY VARYING FUNCTIONS $\gamma_1(r)$ AND $\gamma_2(r)$ FOR A COLD PLASMA

In the limit $r \longrightarrow 0$, the basic set of equations reduces to

$$\frac{dE_\perp}{dr} = \left(\frac{mG}{A} - 1\right)\frac{E_\perp}{r} + \frac{i\omega}{c}\left[1 - \frac{(m/r)^2}{A}\right]B_\parallel,$$
$$\frac{dB_\parallel}{dr} = -\frac{ic}{\omega}(G^2 - A^2)\frac{E_\perp}{A} - \frac{mG}{Ar}B_\parallel, \tag{A2.1}$$

where A and G are the coefficients in basic equations (14) and (15). Substituting expressions (22) into equations (A2.1), we arrive at the following two algebraic equations for λ, γ_1, and γ_2:

$$(\lambda + 1)\gamma_2 = \gamma_2\left(\frac{mG}{A} - 1\right) + \frac{i\omega}{c}\left[1 - \frac{(m/r)^2}{A}\right]\gamma_1^2,$$
$$\lambda\gamma_1 = -\frac{ic}{\omega}(G^2 - A^2)\frac{\gamma_2 r^2}{A} - m\frac{G}{A}\gamma_1. \tag{A2.2}$$

We divide both of these equations by γ_2 to obtain the following two equations for λ and $\gamma_3 = \gamma_1/\gamma_2$:

$$\lambda = \frac{mG}{2} - 2 + \frac{i\omega}{c}\left[1 - \frac{(m/r)^2}{A}\right]\gamma_3,$$
$$\frac{i\omega}{c}\left[1 - \frac{(m/r)^2}{A}\right]\gamma_3^2 + 2\left(\frac{mG}{A} - 1\right)\gamma_3 \tag{A2.3}$$
$$+ \frac{ic}{\omega}(G^2 - A^2)\frac{r^2}{A} = 0.$$

We can see that λ is a complex quantity. Solving the quadratic equation for γ_3 gives

$$\gamma_3 = -\frac{Acr^2/(i\omega)}{m^2}\left\{-\left(\frac{mG}{A} - 1\right)\right.$$
$$\left. + \sqrt{\left(\frac{mG}{A} - 1\right)^2 - \frac{m^2(G^2 - A^2)}{A^2}}\right\}.$$

As a result, we find the power index λ:

$$\lambda = -1 + \sqrt{\left(\frac{mG}{A} - 1\right)^2 - \frac{m^2(G^2 - A^2)}{A^2}}. \tag{A2.4}$$

Performing the necessary manipulations, we can reduce λ to the form

$$\lambda = rm_1 - 1 + irm_2, \tag{A2.5}$$

where

$$rm_1 = \sqrt{(rm + \mathrm{Re}\,q_1 - \mathrm{Re}\,q_2)/2},$$

$$rm_2 = \sqrt{(rm + \mathrm{Re}\,q_2 - \mathrm{Re}\,q_1)/2},$$

$$rm = \sqrt{(\mathrm{Re}\,q_1 - \mathrm{Re}\,q_2)^2 + (\mathrm{Im}\,q_1 - \mathrm{Im}\,q_2)^2},$$

$$\mathrm{Re}\,q_1 = \left[\frac{(\mathrm{Re}\,G \times \mathrm{Re}\,A + \mathrm{Im}\,G \times \mathrm{Im}\,A)m}{\mathrm{Re}\,A^2 + \mathrm{Im}\,A^2} - 1\right]^2$$

$$- \frac{(\mathrm{Im}\,G \times \mathrm{Re}\,A - \mathrm{Im}\,A \times \mathrm{Re}\,G)^2 m^2}{(\mathrm{Re}\,A^2 + \mathrm{Im}\,A^2)^2},$$

$$\mathrm{Im}\,q_1 = \frac{2m(\mathrm{Im}\,G \times \mathrm{Re}\,A - \mathrm{Im}\,A \times \mathrm{Re}\,G)}{\mathrm{Re}\,A^2 + \mathrm{Im}\,A^2}$$

$$\times \left[\frac{m(\mathrm{Re}\,G \times \mathrm{Re}\,A + \mathrm{Im}\,G \times \mathrm{Im}\,A)}{\mathrm{Re}\,A^2 + \mathrm{Im}\,A^2} - 1\right],$$

$$\mathrm{Re}\,q_2 = m^2 \frac{\mathrm{Re}(G^2 - A^2) \times (\mathrm{Re}\,A^2 - \mathrm{Im}\,A^2) + 2\mathrm{Re}\,A \times \mathrm{Im}\,A \times \mathrm{Re}(G^2 - A^2)}{(\mathrm{Re}\,A^2 - \mathrm{Im}\,A^2)^2 + 4\mathrm{Re}\,A^2 \times \mathrm{Im}\,A^2},$$

$$\mathrm{Im}\,q_2 = m^2 \frac{\mathrm{Im}(G^2 - A^2) \times (\mathrm{Re}\,A^2 - \mathrm{Im}\,A^2) - 2\mathrm{Re}\,A \times \mathrm{Im}\,A \times \mathrm{Re}(G^2 - A^2)}{(\mathrm{Re}\,A^2 - \mathrm{Im}\,A^2)^2 + 4\mathrm{Re}\,A^2 \times \mathrm{Im}\,A^2}.$$

APPENDIX 3

INDEPENDENT COEFFICIENTS C_1 AND D_1 IN THE SOLUTIONS FOR THE VACUUM REGION AND THE AW FIELD COMPONENTS $E_\perp(a)$ AND $B_\parallel(a)$ AT THE PLASMA–VACUUM BOUNDARY

The condition that the component $E_\perp$ be continuous at $r = a$ gives

$$\begin{aligned}\mathrm{Re}\,E_\perp &= \mathrm{Re}\,C_1 \times CH_{10} + \mathrm{Im}\,D_1 \times CH_4 B_{0z}/B_{0\vartheta}(a),\\ \mathrm{Im}\,E_\perp &= \mathrm{Im}\,C_1 \times CH_{10} + J_0 CH_{11} \\ &\quad - \mathrm{Re}\,D_1 \times CH_4 B_{0z}/B_{0\vartheta}(a).\end{aligned} \tag{A3.1}$$

The condition that the component $B_\parallel$ be continuous at $r = a$ yields

$$\begin{aligned}\mathrm{Im}\,D_1 &= \mathrm{Im}\,B_\parallel/CH_8,\\ \mathrm{Re}\,D_1 &= (\mathrm{Re}\,B_\parallel + J_0 CH_9)/CH_8.\end{aligned} \tag{A3.2}$$

From the condition that the radial component of the current density be equal to zero at the plasma–vacuum boundary, we obtain

$$\begin{aligned}\mathrm{Re}\,B_\parallel \times CH_{15} &= \mathrm{Im}\,E_1 \times CH_{16},\\ \mathrm{Im}\,B_\parallel \times CH_{15} &= -\mathrm{Re}\,E_1 \times CH_{16},\end{aligned} \tag{A3.3}$$

and, from the condition that the component B_r be continuous, we find

$$\begin{aligned}\mathrm{Im}\,E_\perp &= CH_{14} \times (J_0 \times CH_{12} + \mathrm{Re}\,D_1 \times CH_{13}),\\ \mathrm{Re}\,E_\perp &= -CH_{14} \times \mathrm{Im}\,D_1 \times CH_{13}.\end{aligned} \tag{A3.4}$$

The coefficients CH_{1-16} in equations (A3.1) and (A3.4) can be evaluated as

$$CH_1 = I_m(|kr_w|)/K_m(|kr_w|),$$

$$CH_2 = I'_m(|kr_w|)/K'_m(|kr_w|),$$

$$CH_3 = I_m(|kr_{ant}|)K'_m(|kr_{ant}|) - I'_m(|kr_{ant}|)K_m(|kr_{ant}|),$$

$$CH_4 = \frac{\omega}{ck^2}\frac{B_{0\vartheta}}{B_0}[K_m(|ka|)CH_2 - I'_m(|ka|)],$$

$$CH_5 = \frac{k_\parallel}{k}[I_m(|ka|) - CH_1 K_m(|ka|)],$$

$$CH_6 = \frac{4\pi m\omega}{ckr_{ant}}\frac{k_\parallel}{CH_3}[K_m(|kr_{ant}|)I_m(|ka|) - I_m(|kr_{ant}|)K_m(|ka|)],$$

$$CH_7 = \frac{4\pi\omega B_\vartheta}{ckCH_3 B_0}[K'_m(|kr_{ant}|)I'_m(|ka|) - I'_m(|kr_{ant}|)K'_m(|ka|)], \tag{A3.5}$$

$$CH_8 = \frac{k_\parallel}{k}[K_m(|ka|) - CH_2 K_m(|ka|)],$$

$$CH_9 = \frac{4\pi k_\parallel}{CH_3}[I'_m(|kr_{ant}|)K_m(|ka|) - K'_m(|kr_{ant}|)I_m(|ka|)],$$

$$CH_{10} = CH_5\frac{k_\perp}{k_\parallel}, \quad CH_{11} = CH_6\frac{k_\perp}{k_\parallel} + CH_7\frac{B_{0z}}{B_{0\vartheta}},$$

$$CH_{12} = \frac{4\pi k}{CH_3}[K'_m(|kr_{ant}|)I'_m(|ka|) - I'_m(|kr_{ant}|)K'_m(|ka|)],$$

$$CH_{13} = I'_m(|ka|) - CH_2K'_m(|ka|), \quad CH_{14} = \frac{\omega}{ck_\parallel k},$$

$$CH_{15} = k_\perp(a)[1-\varepsilon_{rr}(a)],$$

$$CH_{16} = \operatorname{Im}\varepsilon_{rr}(a)\left[\frac{\omega}{c} - \frac{c}{\omega}k_\parallel^2(a)\right].$$

Equations (A3.2)–(A3.4) yield the following expression for the real part of the component $B_\parallel$:

$$\operatorname{Re}B_\parallel(a) = \frac{J_0\left[\frac{CH_9}{CH_8} + \frac{CH_{12}}{CH_{13}}\right]}{\frac{CH_{15}}{CH_{16}CH_{14}CH_{13}} - \frac{1}{CH_8}}. \quad \text{(A3.6)}$$

We insert (A3.6) into the second equation in (A3.2) to obtain the real part of the coefficient D_1:

$$\operatorname{Re}D_1 = \frac{J_0\left[\frac{CH_9}{CH_8} + \frac{CH_{12}}{CH_{13}}\right]\frac{1}{CH_8}}{\frac{CH_{15}}{CH_{16}CH_{14}CH_{13}} - \frac{1}{CH_8}} + J_0\frac{CH_9}{CH_8}. \quad \text{(A3.7)}$$

Solving the first equation in (A3.4) together with the second equation in (A3.1), we find the imaginary part of C_1:

$$\operatorname{Im}C_1 = \operatorname{Re}D_1CH_{17} + J_0\frac{CH_{14}CH_{12} - CH_{11}}{CH_{10}}, \quad \text{(A3.8)}$$

where

$$CH_{17} = \frac{1}{CH_{10}}\left[CH_{14}CH_{13} + CH_4\frac{B_{0z}}{B_{0\vartheta}}\right].$$

Substituting (A3.6) into the first equation in (A3.3) gives the following expression for $\operatorname{Im}E_\perp$:

$$\operatorname{Im}E_\perp(a) = \frac{J_0\left[\frac{CH_9}{CH_8} + \frac{CH_{12}}{CH_{13}}\right]\frac{CH_{15}}{CH_{16}}}{\frac{CH_{15}}{CH_{16}CH_{14}CH_{13}} - \frac{1}{CH_8}}. \quad \text{(A3.9)}$$

To determine the remaining coefficients in the expressions for $\operatorname{Im}D_1$ and $\operatorname{Re}C_1$, we must first find the complex quantity γ_2 at the plasma–vacuum boundary. To do that, we transform expressions (26) for $E_\perp(r)$ and $B_\parallel(r)$ to

$$\operatorname{Re}E_\perp(r) = \Big[(\operatorname{Re}\tilde{E}_\perp\operatorname{Re}\gamma_2 - \operatorname{Im}\tilde{E}_\perp\operatorname{Im}\gamma_2)$$

$$\times\cos\left(\ln\left(\frac{r}{r_0}\right)\operatorname{Im}\lambda\right) - (\operatorname{Im}\tilde{E}\operatorname{Re}\gamma_2 \quad \text{(A3.10)}$$

$$+ \operatorname{Re}\tilde{E}_\perp\operatorname{Im}\gamma_2)\sin\left(\ln\left(\frac{r}{r_0}\right)\operatorname{Im}\lambda\right)\Big]r\exp\left(\ln\left(\frac{r}{r_0}\right)\operatorname{Re}\lambda\right),$$

$$\operatorname{Im}E_\perp(r) = \Big[(\operatorname{Im}\tilde{E}_\perp\operatorname{Re}\gamma_2 + \operatorname{Re}\tilde{E}_\perp\operatorname{Im}\gamma_2)$$

$$\times\cos\left(\ln\left(\frac{r}{r_0}\right)\operatorname{Im}\lambda\right) + (\operatorname{Re}\tilde{E}_\perp\operatorname{Re}\gamma_2 \quad \text{(A3.11)}$$

$$- \operatorname{Im}\tilde{E}_\perp\operatorname{Im}\gamma_2)\sin\left(\ln\left(\frac{r}{r_0}\right)\operatorname{Im}\lambda\right)\Big]r\exp\left(\ln\left(\frac{r}{r_0}\right)\operatorname{Re}\lambda\right),$$

$$\operatorname{Re}B_\parallel(r) = \Big[(\operatorname{Re}\tilde{B}_\parallel\operatorname{Re}\gamma_2 - \operatorname{Im}\tilde{B}_\parallel\operatorname{Im}\gamma_2)$$

$$\times\cos\left(\ln\left(\frac{r}{r_0}\right)\operatorname{Im}\lambda\right) - (\operatorname{Re}\tilde{B}_\parallel\operatorname{Re}\gamma_2 \quad \text{(A3.12)}$$

$$- \operatorname{Im}\tilde{B}_\parallel\operatorname{Im}\gamma_2)\sin\left(\ln\left(\frac{r}{r_0}\right)\operatorname{Im}\lambda\right)\Big]\exp\left(\ln\left(\frac{r}{r_0}\right)\operatorname{Re}\lambda\right),$$

$$\operatorname{Im}B_\parallel(r) = \Big[(\operatorname{Im}\tilde{B}_\parallel\operatorname{Re}\gamma_2 + \operatorname{Re}\tilde{B}_\parallel\operatorname{Im}\gamma_2)$$

$$\times\cos\left(\ln\left(\frac{r}{r_0}\right)\operatorname{Im}\lambda\right) + (\operatorname{Re}\tilde{B}_\parallel\operatorname{Re}\gamma_2 \quad \text{(A3.13)}$$

$$- \operatorname{Im}\tilde{B}_\parallel\operatorname{Im}\gamma_2)\sin\left(\ln\left(\frac{r}{r_0}\right)\operatorname{Im}\lambda\right)\Big]\exp\left(\ln\left(\frac{r}{r_0}\right)\operatorname{Re}\lambda\right),$$

where $r_0 = 1$ cm. The expressions for $\operatorname{Im}E_\perp(a)$ and $\operatorname{Re}B_\parallel(a)$ were derived above.

Now, we find the remaining parts of the components $E_\perp$ and $B_\parallel$ at $r = a$:

$$\operatorname{Re}E_\perp(a) = (\operatorname{Re}\gamma_2c_2 - \operatorname{Im}\gamma_2c_1)a^{\operatorname{Re}\lambda+1},$$
$$\operatorname{Im}B_\parallel(a) = (\operatorname{Re}\gamma_2c_4 + \operatorname{Im}\gamma_2c_3)a^{\operatorname{Re}\lambda}. \quad \text{(A3.14)}$$

The parts $\operatorname{Im}D_1$ and $\operatorname{Re}C_1$ can be represented as

$$\operatorname{Im}D_1 = \frac{\operatorname{Im}B_\parallel(a)}{CH},$$
$$\operatorname{Re}C_1 = -\operatorname{Im}D_1 \times CH_{17}. \quad \text{(A3.15)}$$

The radial profiles of the AW field components were determined from formulas (26). Finally, these formulas can be written as

$$\operatorname{Re}E_\perp(r) = \Big[(\operatorname{Re}\tilde{E}_\perp\operatorname{Re}\gamma_2 - \operatorname{Im}\tilde{E}_\perp\operatorname{Im}\gamma_2)$$

$$\times\cos\left(rm_2\ln\left(\frac{r}{r_0}\right)\right) - (\operatorname{Re}\tilde{E}_\perp\operatorname{Im}\gamma_2 - \operatorname{Im}\tilde{E}_\perp\operatorname{Re}\gamma_2)$$

$$\times\sin\left(rm_2\ln\left(\frac{r}{r_0}\right)\right)\Big]r\exp\left[(rm_1-1)\ln\left(\frac{r}{r_0}\right)\right],$$

$$\operatorname{Im}E_\perp(r) = \Big[(\operatorname{Im}\tilde{E}_\perp\operatorname{Re}\gamma_2 + \operatorname{Re}\tilde{E}_\perp\operatorname{Im}\gamma_2)$$

$$\times \cos\left(rm_2 \ln\left(\frac{r}{r_0}\right)\right) + (\mathrm{Re}\,\tilde{E}_\perp \mathrm{Re}\,\gamma_2 - \mathrm{Im}\,\tilde{E}_\perp \mathrm{Im}\,\gamma_2)$$

$$\times \sin\left(rm_2 \ln\left(\frac{r}{r_0}\right)\right)\Bigg] r \exp\left[(rm_1 - 1)\ln\left(\frac{r}{r_0}\right)\right], \quad \text{(A3.16)}$$

$$\mathrm{Re}\,B_\parallel(r) = \Bigg[(\mathrm{Re}\,\tilde{B}_\parallel \mathrm{Re}\,\gamma_2 - \mathrm{Im}\,\tilde{B}_\parallel \mathrm{Im}\,\gamma_2)$$

$$\times \cos\left(rm_2 \ln\left(\frac{r}{r_0}\right)\right) - (\mathrm{Re}\,\tilde{B}_\parallel \mathrm{Im}\,\gamma_2 - \mathrm{Im}\,\tilde{B}_\parallel \mathrm{Re}\,\gamma_2)$$

$$\times \sin\left(rm_2 \ln\left(\frac{r}{r_0}\right)\right)\Bigg] \exp\left[(rm_1 - 1)\ln\left(\frac{r}{r_0}\right)\right],$$

$$\mathrm{Im}\,B_\parallel(r) = \Bigg[(\mathrm{Im}\,\tilde{B}_\parallel \mathrm{Re}\,\gamma_2 + \mathrm{Re}\,\tilde{B}_\parallel \mathrm{Im}\,\gamma_2)$$

$$\times \cos\left(rm_2 \ln\left(\frac{r}{r_0}\right)\right) + (\mathrm{Re}\,\tilde{B}_\parallel \mathrm{Re}\,\gamma_2 - \mathrm{Im}\,\tilde{B}_\parallel \mathrm{Im}\,\gamma_2)$$

$$\times \sin\left(rm_2 \ln\left(\frac{r}{r_0}\right)\right)\Bigg] \exp\left[(rm_1 - 1)\ln\left(\frac{r}{r_0}\right)\right],$$

with rm_1 and rm_2 taken from Appendix 2.

Note that the eigenmodes can be evaluated by a number of methods. However, only some of them can be applied to solve the problem under discussion in arbitrary geometry.

For example, one of these methods involves WKB analysis [8], which restricts the class of the desired functions to those describing plane waves, $\exp(ik_r r)$, where k_r is the radial wavenumber (which, in turn, is expressed in terms of the radial mode number l). The plane wave approximation cannot be used to calculate the resonant frequencies of eigenmodes whose intensities are maximum at the plasma center. In this case, the approximate dispersion relation for the DAW spectrum fails to hold [5]. For eigenmodes whose resonant layers occur near the plasma periphery, the WKB method requires that the boundary conditions be modified in such a manner that this dispersion relation gives more or less accurate results [8]. The WKB technique also cannot be used to determine the AW power deposited in unit plasma volume. Consequently, this approach is inappropriate for studying auxiliary plasma heating by Alfvén and magnetosonic waves or for determining the width of the resonant peaks in the DAW spectrum (i.e., for estimating their quality factors) [8].

APPENDIX 4

DIELECTRIC TENSOR ELEMENTS WITH ALLOWANCE FOR THE ELECTRON AND ION TEMPERATURES

Substituting (45) into (42), we obtained the vector equation, which was then solved together with Faraday's law. As a result, we arrived at the following expressions for the elements of the dielectric tensor $\hat{\varepsilon}$:

$$\varepsilon_{rr} = 1 + \frac{(4\pi/\omega)[\lambda - (\omega/\omega_{ci})\beta]}{1 - (\omega/\omega_{ci})^2},$$

$$\varepsilon_{\perp r} = \frac{i(4\pi/\omega)[\beta - (\omega/\omega_{ci})\alpha]}{1 - (\omega/\omega_{ci})^2},$$

$$\varepsilon_{r\perp} = \frac{4\pi}{\omega}\Bigg\{\xi\Bigg[i\left(\frac{1}{n}\frac{\partial n}{\partial r}\frac{m_i}{e} - \theta\frac{B_0 k_\perp}{\omega c}\right.$$

$$\left. + \frac{\omega}{\omega_{ci}}\left(\frac{1}{n}\frac{\partial n}{\partial r}\frac{B_0}{\omega c} - \frac{m_i k_\perp}{e}\right)\right) - \left(\frac{\omega}{\omega_{ci}}\left(\frac{1}{n}\frac{\partial n}{\partial r}\frac{B_0}{\omega c} + \theta\frac{m_i k_\perp}{e}\right)\right.$$

$$\left.\left. - \frac{\theta}{n}\frac{\partial n}{\partial r}\frac{m_i}{e} - \frac{B_0 k_\perp}{\omega c}\right)\Bigg] + i\left(\alpha\frac{\omega}{\omega_{ci}} - \beta\right)\Bigg\} \Big/ \left[1 - \left(\frac{\omega}{\omega_{ci}}\right)^2\right], \quad \text{(A4.1)}$$

$$\varepsilon_{\perp\perp} = 1 + \frac{4\pi}{\omega}\Bigg\{\xi\Bigg[i\left(\frac{1}{n}\frac{\partial n}{\partial r}\frac{B_0}{\omega c} + \theta\frac{m_i k_\perp}{e}\right.$$

$$\left. - \frac{\omega}{\omega_{ci}}\left(\frac{\theta}{n}\frac{\partial n}{\partial r}\frac{m_i}{e} + \frac{B_0 k_\perp}{\omega c}\right)\right) + \frac{\theta}{n}\frac{\partial n}{\partial r}\frac{B_0}{\omega c} - \frac{m_i k_\perp}{e}$$

$$\left. + \frac{\omega}{\omega_{ci}}\left(\frac{1}{n}\frac{\partial n}{\partial r}\frac{m_i}{e} - \theta\frac{B_0 k_\perp}{\omega c}\right)\right] + \alpha - \frac{\omega}{\omega_{ci}}\beta\Bigg\} \Big/ \left[1 - \left(\frac{\omega}{\omega_{ci}}\right)^2\right],$$

where $\alpha = \dfrac{\omega c^2}{4\pi c_A^2} + \dfrac{j_0}{B_0}\dfrac{ck_\parallel}{\omega_{ci}}$, $\beta = \dfrac{j_0}{B_0}\dfrac{ck_\parallel}{\omega}$,

$\theta = \dfrac{\gamma n_e (T_e + T_i)k^2}{\omega^2 \rho}$, $\xi = \dfrac{\gamma n_e}{\omega\rho}\dfrac{\dfrac{c^2}{\omega B_0}\left(1 + \dfrac{j_0}{B_0}\dfrac{ck_\parallel}{\omega\omega_{ci}}\right)k_\perp k_\parallel}{1 + \dfrac{\gamma^2 n_e^2 (T_e + T_i)^2}{\omega^4 \rho^2}k^4}$,

and γ is the adiabatic power-law index.

APPENDIX 5

CALCULATION OF THE COMPLEX POWER INDEX λ AT $T_{i,e} \neq 0$

In the limit $r \longrightarrow 0$, we have $E_\perp(0) = B_\parallel(0) = 0$; and $\nabla P' \longrightarrow 0/0$. Consequently, expression (45) contains singularities of the 0/0 type at the plasma center. We assume that, at $r \longrightarrow 0$, the field components have the form

$$B_\parallel \sim \gamma_1(r) r^\lambda, \quad E_\perp \sim \gamma_2(r) r^{\lambda+1}, \quad \text{(A5.1)}$$

where $\gamma_1(r)$ and $\gamma_2(r)$ are gradually varying functions of r. We insert expressions (A5.1) into (48) and (49) to

arrive at the following two algebraic equations for two unknowns, λ and $\gamma_3 = \gamma_1/\gamma_2$:

$$\lambda = A_1 m - 2 + \frac{i\omega}{c}\left[1 - \frac{(m/r)}{G_1}\right]\gamma_3, \qquad \gamma_3\lambda = A_2 r^2 + G_2 m\gamma_3. \tag{A5.2}$$

Solving (A5.2) gives the complex power index λ:

$$\lambda = mA_1 - 2 + \frac{1}{2}\left\{m(G_2 - A_1) + 2 + \sqrt{[m(A_1 - G_2) - 2]^2 + \frac{4i\omega}{c}A_2\left(r^2 - \frac{m^2}{G_1}\right)}\right\}. \tag{A5.3}$$

REFERENCES

1. K. McCormick, R. Bartiromo, H. S. Bosch, *et al.*, in *Proceedings of 12th European Conference on Controlled Fusion and Plasma Physics, Budapest, Hungary, 1985* [ECA **9F**, 199 (1985)].
2. F. M. Levinton, Rev. Sci. Instrum. **63**, 5157 (1992).
3. F. M. Levinton, R. J. Fonck, G. M. Gammel, *et al.*, Phys. Rev. Lett. **63**, 2060 (1989).
4. H. Soltwisch, W. Stodieck, J. Manickam, *et al.*, in *Proceedings of 11th IAEA Conference on Plasma Physics and Controlled Nuclear Fusion Research, Kyoto, Japan, 1986* [Nucl. Fusion Suppl. **1**, 263 (1987)].
5. K. Appert and J. Vaclavik, Plasma Phys. **25**, 551 (1983).
6. D. W. Ross, G. L. Chen, and S. M. Mahajan, Phys. Fluids **25**, 652 (1982).
7. P. Descamps, G. V. Wassenhove, R. Koch, *et al.*, Phys. Lett. A **143**, 311 (1990).
8. S. M. Mahajan, D. W. Ross, and G. L. Chen, Phys. Fluids **26**, 2195 (1983).
9. K. Appert, G. A. Collins, F. Hofmann, *et al.*, Phys. Rev. Lett. **54**, 1671 (1985).
10. G. A. Collins, F. Hofmann, B. Joye, *et al.*, Phys. Fluids **29**, 2260 (1986).
11. B. Joye, A. Lietti, J. B. Lister, *et al.*, Preprint No. LRP 196/81 (Centre de Recherches en Physique des Plasmas, Lausanne, 1981).
12. A. Yu. Novikov, Preprint No. 5740/7, IAE (Kurchatov Institute of Atomic Energy, Moscow, 1994).
13. D. A. Frank-Kamenetskiĭ, *Course of Plasma Physics* (Atomizdat, Moscow, 1964).
14. T. Stiks, *The Theory of Plasma Waves* (McGraw-Hill, New York, 1962; Atomizdat, Moscow, 1965).
15. R. R. Weynants, A. M. Messiaen, C. Leblud, *et al.*, in *Proceedings of 2nd Joint Grenoble–Varenna International Symposium on Heating in Toroidal Plasmas, Grenoble, 1980* (Centre D'Etudes Nucleaires, Grenoble, 1980), Vol. 1, p. 487.

Translated by G. V. Shepekina